PARTICLE DYNAMICS AND RESISTIVITY CHARACTERISTICS IN BIFURCATED CURRENT SHEETS

by

Tushar Andriyas

A dissertation submitted in partial fulfillment
of the requirements for the degree

of

DOCTOR OF PHILOSOPHY

in

Electrical Engineering

Approved:

Dr. Edmund Spencer Major Professor	Dr. Robert Schunk Committee Member
Dr. Charles Swenson Committee Member	Dr. Jacob Gunther Committee Member
Dr. Bedri Cetiner Committee Member	Dr. Mark R. McLellan Vice President for Research and Dean of the School of Graduate Studies

UTAH STATE UNIVERSITY
Logan, Utah

2013

Abstract

Particle Dynamics and Resistivity Characteristics in Bifurcated Current Sheets

by

Tushar Andriyas, Doctor of Philosophy

Utah State University, 2013

Major Professor: Dr. Edmund Spencer
Department: Electrical and Computer Engineering

Charged particle chaos and its collective effects in different magnetic geometries are investigated in a sequence of various numerical experiments. The fields generated by the particles as a result of interaction with the background electric and magnetic fields is not accounted for in the simulation. An X-line is first used to describe the geometry of the magnetotail prior to magnetic reconnection and a study of the behavior of charged particles is done from a microscopic viewpoint. Another important geometry in the magnetotail prior to substorm onset is Bifurcated Current Sheet. The same analysis is done for this configuration. The existence of at least one positive Lyapunov exponent shows that the motion of the particles is chaotic. By using statistical mechanics, the macroscopic properties of this chaotic motion are studied. Due to particles being charged, an electric field (perpendicular to the magnetic field in weak magnetic field region) accelerates the particles on average. Finite average velocity in the direction of electric field gives rise to an effective resistivity even in a collisionless regime such as solar corona and the magnetotail.

Starting from initial velocities that are chosen randomly from a uniform distribution, the evolution of these distributions tends to a Maxwellian by the end of the simulation that is somewhat analogous to collisions in a Lorentz gas model. The effective resistivity due to such collisions is estimated. Ohmic heating is found to occur as a result of such

an effective resistivity. Such collisions due to collective particle effects are essentially a different mechanism from classical collision notion. These experiments are done for two types of ions found in the plasma sheet prior to substorm onset, viz., protons and oxygen ions. Observational evidence of oxygen ions in the central plasma sheet, which flow out along open field lines from the ionosphere, were also simulated in the same manner. Oxygen ions have been found to influence the bifurcation of the current sheet and are also important in reconnection and other nonohmic instabilities, such as Kelvin Helmholtz instability, due to their mass.

It is found that acceleration in X-line scales with the mass of ion species and the resistivity remains constant for different electric field strengths. In a Bifurcated Current Sheet, the acceleration scales with the square of mass of ion species and the resistivity scales with the electric field. Also, the overall resistivity values found in a Bifurcated Current Sheet are an order of magnitude lower than that found in an X-line.

(208 pages)

Public Abstract

Particle Dynamics and Resistivity Characteristics in Bifurcated Current Sheets

by

Tushar Andriyas, Doctor of Philosophy

Utah State University, 2013

Major Professor: Dr. Edmund Spencer
Department: Electrical and Computer Engineering

Charged particle chaos, which manifests as a result of nonlinearity in model equations and its collective, fluid like effects in different magnetic geometries, is investigated in a sequence of various numerical experiments. The fields generated by the particles as a result of interaction with the background electric and magnetic fields are not accounted for in the simulation. An X-line is first used to describe the geometry of the magnetotail prior to magnetic reconnection, in which magnetic fields of opposite polarity can merge in presence of finite dissipation, and a study of the behavior of charged particles is done from a microscopic viewpoint. Another important geometry in the magnetotail prior to substorm onset is Bifurcated Current Sheet. The same analysis viz., calculating for macroscopic quantities such as resistivity, temperature, etc., is done for this topology. The existence of at least one positive Lyapunov exponent, which is an indication of chaos in a system, shows that the motion of the particles is chaotic. By using statistical mechanics, the macroscopic properties of this chaotic motion is studied. Due to particles being charged, an electric field (perpendicular to the magnetic field in weak magnetic field region) accelerates the particles in an average (macroscopic) sense. A finite average velocity in the direction of electric field gives rise to an effective resistivity even in a collisionless regime (where collisions are so rare

that macroscopic dissipation cannot be accounted for through such a mechanism) such as solar corona and the magnetotail.

Starting from initial velocities that are chosen randomly from a uniform distribution, the evolution of these distributions tends to Maxwellians by the end of the simulation that is somewhat analogous to collisions in a Lorentz gas model. The effective resistivity due to such process is estimated. Ohmic heating is found to occur as a result of such an effective resistivity perpendicular to the direction of the electric field. Such collisions due to collective particle effects are essentially a different mechanism from classical dissipation due to collisions notion. These experiments are done for two types of ions found in the plasma sheet prior to substorm onset, viz., protons and oxygen ions. Observations suggest that oxygen ions flow out along open field lines from the ionosphere, ending up in the central plasma sheet. These ions were also simulated in the same way as protons. Oxygen ions have been found to influence the bifurcation of the current sheet and are also important in reconnection and other nonohmic instabilities such as Kelvin Helmholtz instability due to their mass.

It is found that acceleration in X-line scales (increases) with the mass of ion species and the resistivity remains constant for different electric field strengths. In a Bifurcated Current Sheet, the acceleration scales with the square of mass of ion species and the resistivity scales with the electric field. Also, the overall resistivity values found in a Bifurcated Current Sheet are an order of magnitude lower than that found in an X-line.

To God Almighty, my parents - Mithlesh and Fredrick Andriyas, sister - Sanyogita, pet parrot- Fulki, my grandparents, and all my friends back in India....

Acknowledgments

I would take this opportunity to express my gratitude to my major professor, Dr. Edmund Spencer, for his never-ending support, help, patience, and guidance throughout the course of this work. My gratitude is also due to Dr. Schunk for helping us in this project and giving us valuable information about the area through his suggestions and hilarious yet informative lectures on plasma physics. I would also like to deeply thank my committee members, Drs. Swenson, Gunther, and Cetiner, for taking time out from their hectic time table along with their help time and again. I would also not forget to mention our ECE staff, especially Trent and Mary Lee, who helped me get through the endless lot of paperwork and deadlines. I would also acknowledge the help of Joan Rudd, Steve Beck, Emma Torres, and Nakaiya Stucki from the School of Graduate Studies. Staying away from home would have been difficult without the unending mental support from my sister, Sanyogita Andriyas. I am highly obliged to my parents, Mithlesh and Fredrick Andriyas, who made countless sacrifices to see me where I am today. Their encouragement in times of distress and intrepid faith in my strengths was a huge motivation to continue my studies. There were many hard times and it was the "Great I am" who helped me with double the strength and confidence to run through the walls of weakness and despair. It was He who gave me health and mind to accomplish this work. I would like to express my gratitude towards Deepak, Shashi Kant, and Shantanu for taking care of me when I came to the US. I would also like to thank my very close friends Levan, Udara, and Dumindu, and their families for providing warmth and happiness whenever I needed it. I would thank Fawad, a brother from my sister country. Last, but in no sense the very least, I would like to acknowledge my badminton and tennis buddies, specially Yot, Yao, Thomas, Oscar, Shantanu, Swad, Varun, Shree, Xing, Gawli, Chandu, Yi, Nisa, Prajwal, Ashish, Ravi, Vishal, and many others for providing a stress buster on Fridays, which I always longed for every week.

Tushar Andriyas

Contents

List of Tables

List of Figures

Chapter 1

Introduction

Electric and magnetic fields pervade all of the known universe. From stars to planets to dying stars to stars gone wild, magnetic field plays a major role in the interaction of the body with the surrounding space. Solar system itself is made up of planets that do and do not have their own internal magnetic field. The Sun also produces its own magnetic field through the motion of conductive plasma inside the star. This motion is created through convection, which is a form of energy transport involving the physical movement of material. Contrary to prior beliefs, it has been found through theory validated by satellite observations that the space between planets called the interplanetary space is not empty but is filled with a rare, magnetized plasma that constantly streams out of the sun. This stream of particles and magnetic field is called the solar wind. The solar wind is a stream of charged particles ejected from the upper atmosphere of the Sun. It mostly consists of electrons and protons. These particles can escape the Sun's gravity because of their high kinetic energy and the high temperature of the corona. Parker [7] first showed that the solar corona must expand, and called the outward streaming coronal gas as solar wind. Typical values of solar wind parameters are given in Table 1.1. As seen in the table, the parameters vary vastly depending on Sun's activity (minimum or maximum). During a maxima, the interplanetary space is filled with transient bursts called Coronal Mass Ejections (CMEs) while during a minima, quasi-periodic structures with repeated fast and slow wind phases called Corotating Interaction Regions (CIRs) are found. In the absence of this solar wind,

Table 1.1: Typical solar wind parameters measured at the Earth's orbit.

Parameter	Minimum	Maximum	Average
Velocity (Km/s)	200	900	400
Density (cm^{-3})	0.4	50-100	6.5
B (nT)	0.2	80	6

the magnetic field around a planet would look like that of a dipole as shown in fig. 1.1. The picture is completely different when the solar wind is present. It compresses the dayside (the part of the planetary magnetic field facing the Sun) and stretched the nightside into a cavity called the magnetosphere (fig. 1.2). This cavity shelters the surface of the planet from the high energy particles of the solar wind. The different regions of the magnetosphere can be seen in fig. 1.3. The outer boundary of the magnetosphere is called the magnetopause. In front of the dayside magnetopause another boundary called the bow shock is formed because the solar wind is supersonic. The region between the bow shock and the magnetopause is called the magnetosheath. At low-altitude limit, magnetosphere ends at the ionosphere. The magnetosphere is filled with plasma that originates both from the ionosphere and the solar wind.

1.1 Solar Wind Interaction with the Earth's Magnetosphere

In the open magnetosphere model initially suggested by Dungey [8], reconnection (or merging) of the interplanetary and geomagnetic field lines partially opens Earth's magnetic field to the solar wind. For this to happen, the field lines must be oppositely directed. A Southward interplanetary magnetic field (IMF) is thus needed to open Earth's closed dayside magnetic fields [9]. The antisunward magnetospheric convection is produced when the reconnected, open field lines are swept over the polar caps at the solar wind speed. This can be seen in fig. 1.4, which depicts the merging of a Southward turned solar wind field line with the magnetospheric field and traces the line down to the ionosphere with the red dots. The magnetic flux is returned back to the dayside once merging has occurred on the nightside. It is then said that a geomagnetic storm has occurred, the intensity of which is mentioned in Table 1.2. When the Northern and Southern hemispheric field lines are stretched into a magnetic tail by the solar wind, they eventually reconnect with each other deep in the antisunward region. This magnetic geometry has a tension that exerts a force on the plasma. Together with the pressure gradient and the potential difference applied across the magnetosphere by the flowing solar wind, these forces produce motion of the magnetospheric plasma on closed field lines towards the Sun and an associated dawn dusk

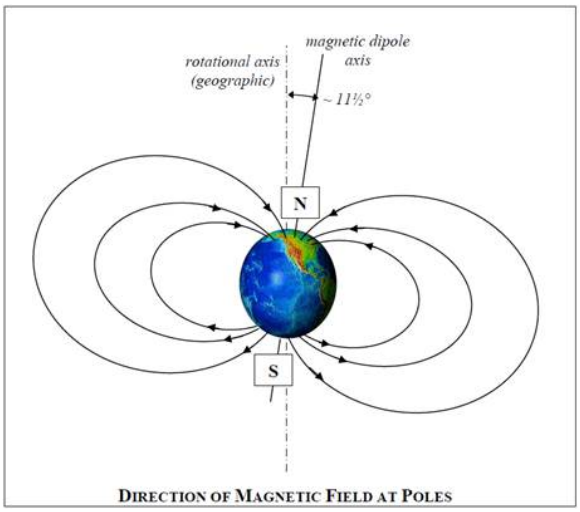

Fig. 1.1: Earth's magnetic field which is has dipole as the dominant contribution. This would be the field structure in absence of solar wind. Note the tilt of the magnetic axis w.r.t. the geographic axis.

magnetospheric electric field in the tail.

1.1.1 Geomagnetic Storms

The solar wind remains steady for most of the time but due to changes in the magnetic topology on the Sun, fast transients like a CME [10] can accompany the slow solar wind. Such a transient expanding in the interplanetary space is called a magnetic cloud. A schematic of a CME is shown in fig. 1.5.

A CME carries charged particles and magnetic field along with it. Since the CME travels faster than the ambient solar wind, a shock is formed on the leading edge which compresses the plasma and the magnetic field. The related enhancements of solar wind velocity accompanied by Southward IMF direction result into Sudden Storm Commencements (SSC) when a storm is said to be initiated. The interaction of this Southward field with the geomagnetic field increases convection. Hence, storms are initiated when enhanced energy transfer from the solar wind leads to intensification of the ring current [11] (fig. 1.3). Such intensifications are recorded as Dst enhancements on the ground. The Dst is a geomagnetic index which monitors the world wide magnetic storm level [11]. It is constructed by averaging the horizontal component of the geomagnetic field from mid-latitude and equatorial

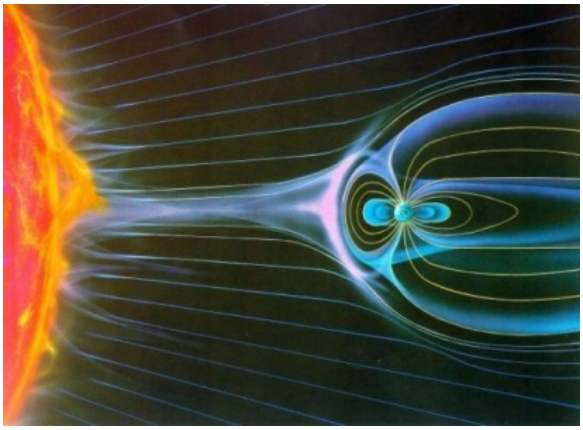

Fig. 1.2: Compression on the dayside (the side facing the Sun) and expansion/stretching in the nightside (side opposite to the Sun) of the Earth's magnetic field as a result of interaction with the solar wind. Close to the Earth around geosynchronous distances, the field is dipolar as it would have been in the absence of solar wind.

magnetograms from all over the world. Negative Dst values indicate a magnetic storm is in progress, the more negative Dst is the more intense the magnetic storm. The negative deflections in the Dst index are caused by the storm time ring current which flows around the Earth from East to West in the equatorial plane. The ring current results from the differential gradient and curvature drifts of electrons and protons in the near Earth region and its strength is coupled to the solar wind conditions. Only when there is an Eastward electric field in the solar wind which corresponds to a Southward interplanetary magnetic field (IMF) is there any significant ring current injection resulting in a negative change to the Dst index. Thus, by knowing the solar wind conditions and the form of the coupling function between solar wind and ring current, an estimate of the Dst index can be made. Geomagnetic storms can last for days with large amounts of energetic particle injections into the magnetosphere. The coupling between solar wind and the magnetosphere is studied through the convection electric field which is the product of solar wind velocity and the North South magnetic field component (B_z). Depending on the strength of the solar wind parameters, the geomagnetic storms can be categorized as shown in Table 1.2.

A very intense geomagnetic storm occurred on April, 2002. Solar wind velocity V_x, IMF B_z, proton density N_p, and the Dst are shown in fig. 1.6. The right panel depicts

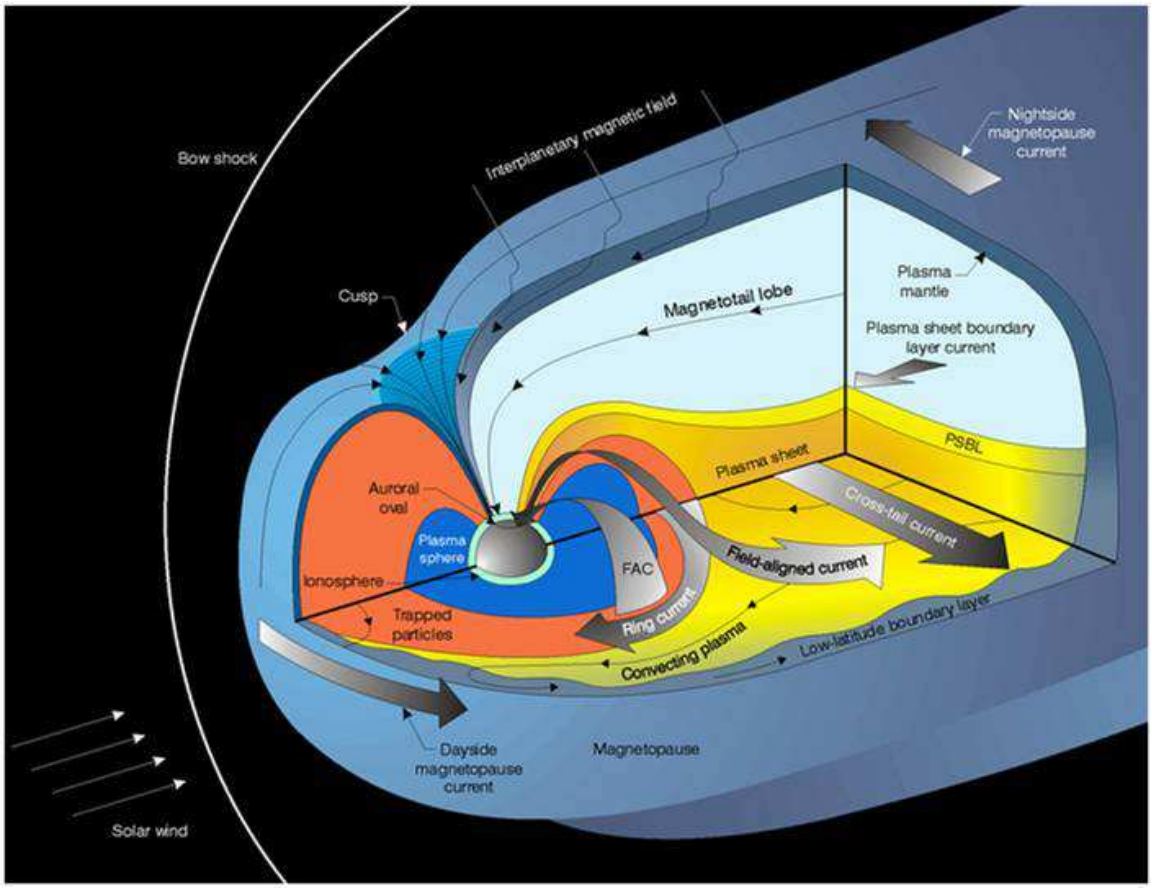

Fig. 1.3: Pictorial representation of the different parts of the Earth's magnetosphere, the cocoon within which Earth's magnetic field resides. As a result of the interaction with solar wind, different boundary layers with varying thickness are formed, the most prominent being the bow shock where the solar wind slows down to subsonic speeds and the magnetopause which separates the solar wind from the magnetosphere.

the substorm activity through AL intensifications (fig. 1.7). As seen in the left panel, the ring current activity intensifies once the IMF B_z turns negative (Southward). Shocks (rapid jumps in the parameters) can also be seen specially in V_x. It can be seen that the magnetospheric activity is driven by solar wind magnetic field and velocity. The compression through dynamic pressure enhancement leads to a positive spike prior to a storm onset.

1.1.2 Geomagnetic Substorms

A geomagnetic substorm is a brief disturbance in the Earth's magnetosphere that causes energy to be released from the "tail" of the magnetosphere and injected into the

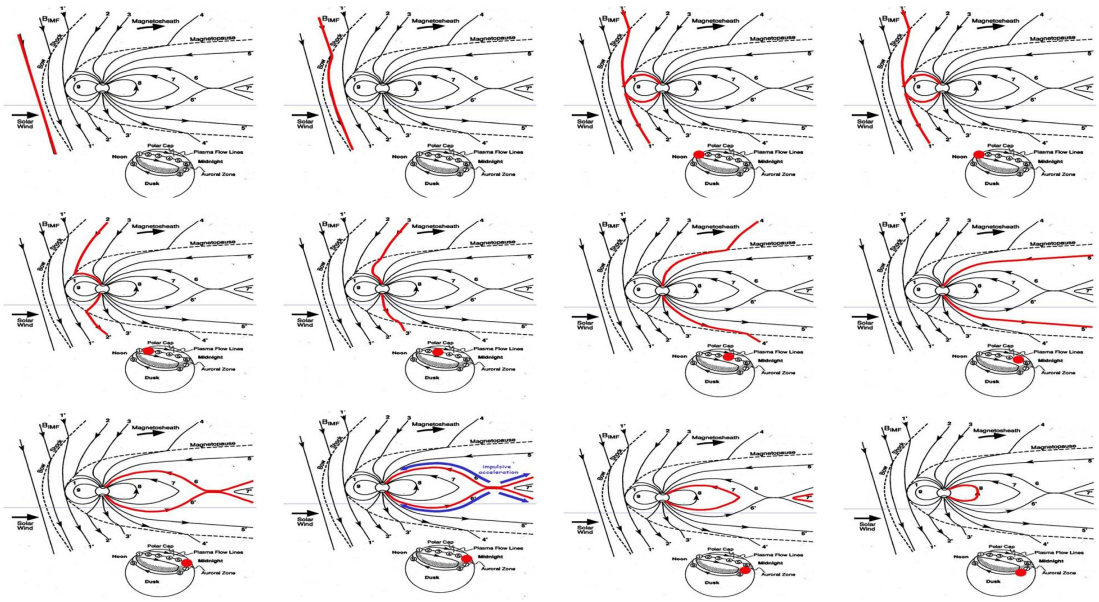

Fig. 1.4: Interaction of the solar wind magnetic field with the Earth's magnetic field leading to convection in the magnetosphere. This convection is specially strong when the solar wind magnetic field in the North South direction (z direction in GSM coordinates) points in the South direction which then leads to magnetic merging at the magnetopause. Energy is hence transferred from the solar wind to the magnetosphere.

Table 1.2: Storm intensities (ring current strength in Dst) according to the strength of B_z.

Strength	Dst (nT)	B_z (nT)
Intense (CME driven)	-100	-10
Moderate	-50	-5
Small (CIR driven)	-30	-3

high latitude ionosphere [12, 13]. There are three phases in a substorm (see fig. 1.8).

Growth phase starts with the Southward turning of the interplanetary magnetic field (IMF B_z) [14]. It remains for an hour with an increase in the tail lobe field leading to compression of the plasma sheet. The cross-tail current (fig. 1.3) also intensifies leading to stretching of the magnetic field lines in the magnetotail [15]. Expansion phase is characterized by Earthward high speed plasma flows within the near-Earth plasma sheet and plasmoids in the far tail which can last anywhere from 10 minutes to 2 hours [16]. Current disruption occurs in the near Earth tail with the interrupted current flowing through the ionosphere with the formation of a substorm current wedge. The stretched field lines also

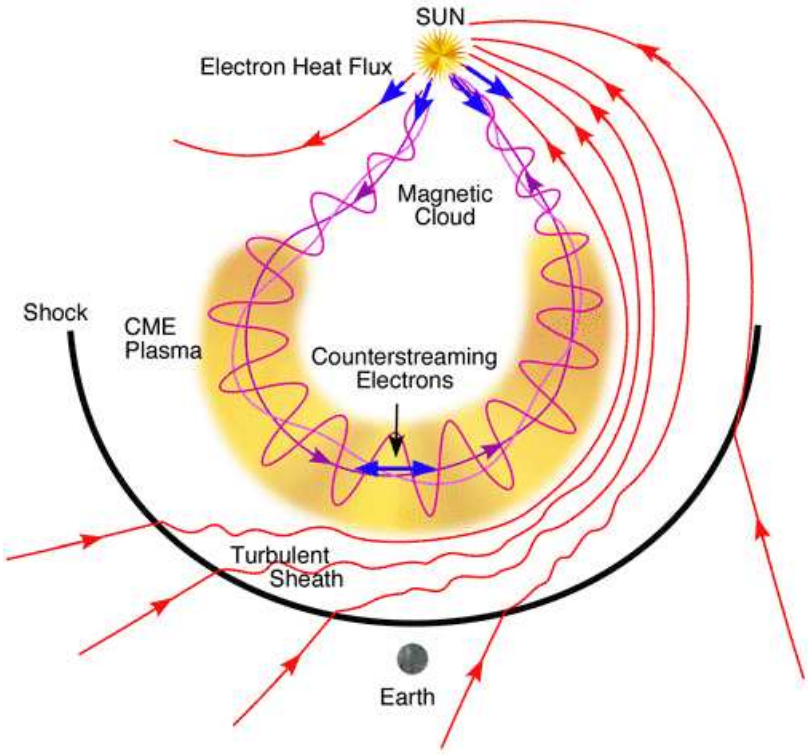

Fig. 1.5: Figure showing the different regions of a CME in the interplanetary space called an interplanetary CME or ICME. Since the ICME travels at speeds faster than the ambient solar wind, it creates a traveling shock which has a shocked part called the sheath. Energetic particles are detected at the shock. Counter streaming electrons can be detected inside the cloud that arrives after the shock.

relax to a more dipolar configuration as a result of the reconnection which is called dipolarization. During the recovery phase the magnetosphere returns to its quiet state [17]. Just as the strength of *Dst* indicates the level of geomagnetic storm activity, similarly a substorm can be detected through another geomagnetic index called the AL index. A number of stations located in latitude which is typical of Northern hemisphere auroral zone measure the North South magnetic perturbation H as a function of universal time. A superposition of these data gives a lower bound or maximum negative excursion of the H component to be determined called the AL index. Similarly, an upper bound or maximum positive excursion in H is called the AU index. The difference between AU and AL indices is called the AE index [18]. Sample AL index for the Bastille day event can be seen in the bottom panel of fig. 1.7. As can be seen in the figure, AL follows a certain trend with a sharp decrease

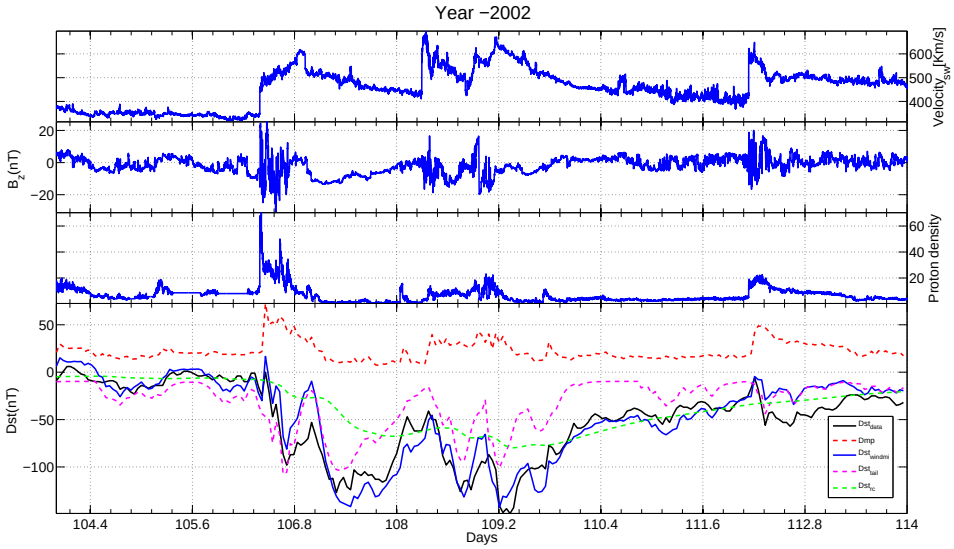

Fig. 1.6: Solar wind V_x, B_z, and N_p along with ring current Dst (left panel) and AL (right panel) index for the April, 2002 event. The top three panels are satellite data taken from the ACE satellite `http://www.srl.caltech.edu/ACE/ASC/level2/index.html` and are the solar wind velocity in the radial direction, magnetic field in the North South direction, and solar wind density, respectively. Multiple shocks (almost sudden enhancements of V_x and N_p and compression of B_z) can be seen in the data. Geomagnetic response to the solar wind is shown in the last panel along with fits from the WINDMI model. The lowest panel also shows contribution from various current systems mainly the magnetopause current (D_{mp}) and magnetotail (Dst_{tail}).

during the storm and slow recovery after that.

1.2 Magnetospheric Models

Four basic types of models are used to model the space plasmas [19]. Kinetic (statistical) models regard a plasma as made up of charged particles like ions and electrons in random motion. They view the plasma as a collection of electrons and ions whose positions and velocities are described by an assumed probability density function. Fluid (continuum) models regard a plasma as a substance or a set of interacting substances passing through and interacting with one another. They assume a Gaussian distribution of particle velocities, meaning that the particles have reached a thermal equilibrium. Fluid approximation reduces the dimensionality of the governing dynamical equations from seven in

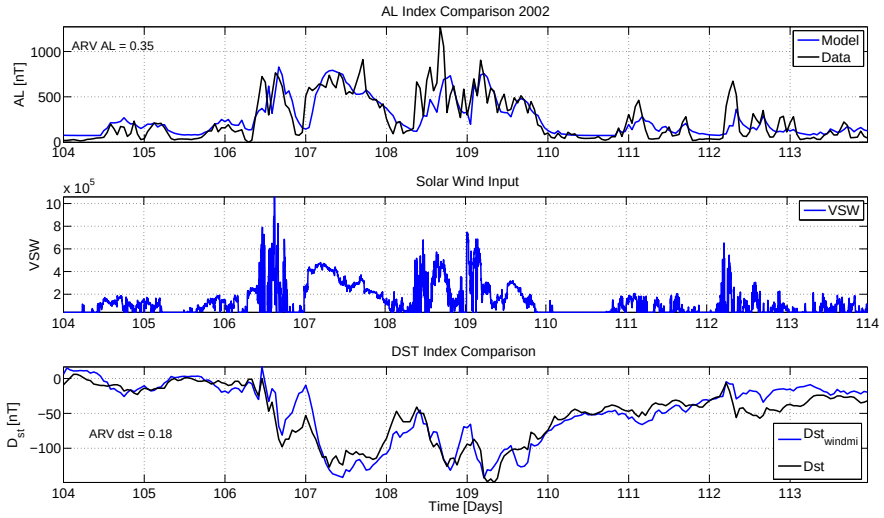

Fig. 1.7: AL index for the April, 2002 event. These currents are found in the auroral latitudes in and around the polar regions. Fit to the data is shown in blue for both AL and Dst. Solar wind rectified driver is also shown for reference in the middle panel.

the kinetic case (time, three spatial dimensions, and three velocity dimensions) to four in the fluid case (time and three spatial dimensions). Fluid models can be further subdivided into two-fluid (or more generally multi-fluid) and one-fluid (magnetohydrodynamic (MHD)) models. Two-fluid models apply separate evolution equations to each type of species (e.g., electrons, ions, neutrals, etc.), which are coupled to each other through various interaction terms. Magnetohydrodynamic (MHD) models reduce the two-fluid model by simplifying the interaction terms between the electrons and ions, resulting in a single set of evolution equations. The main assumption that leads to such a formulation is quasi-neutrality. Due to the re-neutrality assumption, one-fluid models remove the fastest wave in the two-fluid system, which is often referred to as the whistler wave. Hence, numerical methods based on one-fluid models are less computationally expensive than two-fluid models. On the other hand, a two-fluid model can accurately model conditions where one-fluid models fail. A third type of models sandwiched between kinetic and MHD (fluid) regimes known as hybrid are also used. This modeling assumes one species, typically the electrons in space plasma applications, as treated as fluid, while the other species is treated kinetically. Computa-

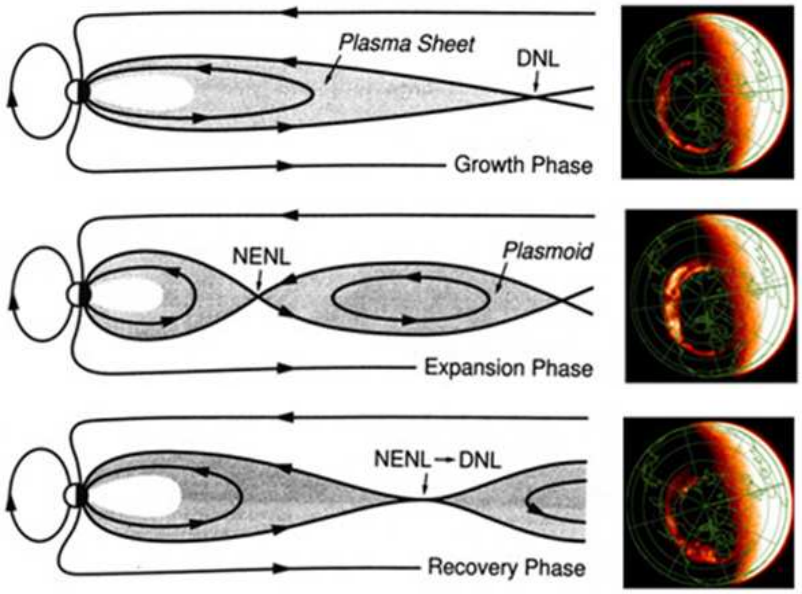

Fig. 1.8: The three phases of a typical substorm. The growth phase starts with the Southward turning of the interplanetary magnetic field (IMF), tail lobe increases leading to compression of the plasma sheet, and cross-tail current enhances leading to stretching of the magnetotail field lines. During the expansion phase, Earthward high speed plasma flows are observed within the near-Earth plasma sheet, and plasmoids are detected in the far tail, part of near Earth cross-tail current vanishes, which is called current disruption, and magnetic field lines as a result of disruption relax to a more dipolar configuration, called dipolarization. Magnetosphere returns to a quiet state during the recovery phase.

tionally, such models are less expensive than kinetic but more expensive than fluid models. All the model types used some coupling between particles and fields (through Maxwell's equations). Finally, there are global low-dimensional nonlinear dynamical models such as WINDMI (section 1.3), and also equation based models such as Wang-Sheeley-Arge model of the coronal magnetic field. These models are fast compared to the above mentioned models with plasma behavior modeled by a set of differential/integral/integro-differential equations.

1.3 The WINDMI Model of the Nightside Magnetosphere

WINDMI is a low-dimensional model of the energy transfer from the solar wind through the magnetosphere and into the ionosphere [20]. The model uses the analogy of electric

circuitry (capacitances, resistances, inductances) to describe with a set of nonlinear ordinary differential equations the response of the magnetosphere-ionosphere system to solar wind driving. The electric driving voltage applied by the solar wind is described either by the Rectified, Siscoe, or Newell coupling function. These input drivers are functions of solar wind parameters such as velocity, magnetic field, and proton density. The major outputs of the model are the energy of the ring current (Dst index) and the AL index of geomagnetic activity. The model can be put in differential form as follows.

$$
\begin{aligned}
L\frac{dI}{dt} &= V_{sw} - V + M\frac{dI_1}{dt}, && (1.1)\\
C\frac{dV}{dt} &= I - I_1 - I_{ps} - \Sigma V, && (1.2)\\
\frac{3}{2}\frac{dp}{dt} &= \frac{\Sigma V^2}{\Omega_{cps}} - u_0 p\sqrt{K_{||}}\Theta(u) - \frac{pVA_{eff}}{\Omega_{cps}B_{tr}L_y} - \frac{3p}{2\tau_E}, && (1.3)\\
\frac{dK_{||}}{dt} &= I_{ps}V - \frac{K_{||}}{\tau_{||}}, && (1.4)\\
L_I\frac{dI_1}{dt} &= V - V_1 + M\frac{dI}{dt}, && (1.5)\\
C_I\frac{dV_I}{dt} &= I_1 - I_2 - \Sigma_I V_I, && (1.6)\\
L_2\frac{dI_2}{dt} &= V_I - (R_{prc} + R_{A2})I_2, && (1.7)\\
\frac{dW_{rc}}{dt} &= R_{prc}I_2^2 + \frac{pVA_{eff}}{B_{tr}L_y} - \frac{W_{rc}}{\tau_{rc}}. && (1.8)
\end{aligned}
$$

The nonlinear equations of the model trace the flow of electromagnetic and mechanical energy through eight pairs of transfer terms [20]. The remaining terms describe the loss of energy from the magnetosphere-ionosphere system through plasma injection, ionospheric losses, and ring current energy losses. In the differential equations the coefficients are physical parameters of the magnetosphere-ionosphere system. The quantities L, C, Σ, L_1, C_I, and Σ_I are the magnetospheric and ionospheric inductances, capacitances, and conductances, respectively. A_{eff} is an effective aperture for particle injection into the ring current, that on the dusk side merges with what is known as the Alfven layer. The Alfven layer is defined to be the separatrix between two sets of drift trajectories, one comprising open drift paths extending from the magnetospheric tail to the dayside magnetopause and another, nearer

set consisting of closed drift paths, encircling the Earth. The resistances in the partial ring current and region 2 current, I_2 are R_{prc} and R_{A2}, and L_2 is the inductance of the region 2 current [20]. The coefficient u_0 in eq. (1.3) is a heat flux limiting parameter. The energy confinement times for the central plasma sheet, parallel kinetic energy and ring current energy are τ_E, τ_k, and τ_{rc}, respectively. The effective width of the magnetosphere is L_y and the transition region magnetic field is given by B_{tr}. The pressure gradient driven current is given by $I_{ps} = L_x(p/\mu_0)^{1/2}$, where L_x is the effective length of the magnetotail. The output of the model are the AL and Dst indices, in addition to the magnetospheric field aligned currents. The parameters of the model are the physical coefficients of the equations obtained by volume integration of the partial differential equations. They can be estimated using semi analytical techniques or they can be considered as variables that need to be optimized within physically allowable ranges to fit the data for a given storm. Some parameters, e.g., Ω_{cps}, L, have been approximated analytically using the Tsyganenko magnetic field model and then allowed to vary over a physically reasonable range of values as explained by Spencer and Horton [21]. The current I_1 used in the model is that portion of the field aligned region 1 current that maps to the nightside central plasma sheet and is considered to be part of the substorm current wedge that produces the Westward auroral electrojet. The auroral AL index now follows as a magnetic field perturbation $\triangle B_{AL}$ from the ambient terrestrial field due to the Westward electrojet current that flows in the E-layer (between 90 to 120 Kms) in the nightside ionosphere. The portion of the Dst index due to plasma energy stored in the ring current W_{rc} is given by the Dessler-Parker-Sckopke (DPS) [22, 23] relation:

$$Dst_{rc} = \frac{\mu_0 W_{rc}(t)}{2\pi B_E R_E^3}, \tag{1.9}$$

where B_E is the Earth's surface magnetic field along the equator. The ring current energy (W_{rc}) injection terms in the WINDMI model are the first and second terms on the right hand side of eq. (1.8). The current I_2 is a region 2 current that leaves the ionosphere on the dawn side, closes in the ring current and returns to the ionosphere on the dusk side. This secondary loop of current has a self-inductance L_2 and drives a current through the partial

ring current resistance R_{prc} as well as the resistance of the region 2 current loop footprint R_{A2}. The Joule heating through the resistance R_{prc} energizes the ring current particles. The particles injected across the effective aperture A_{eff} is another source of ring current energy. The ring current energy in the model is assumed to be lost by particles drifting out of orbit or by charge exchange processes at a rate proportional to τ_{rc}. The major current systems that are considered to contribute to the total Dst in the magnetosphere are: (1) the magnetopause currents shielding Earth's dipolar magnetic field; (2) the symmetric ring current; (3) the partial ring current; and (4) the cross-tail current along with the closure currents on the magnetopause. All these currents cause magnetic perturbations on the Earth's surface. We add the magnetopause current and cross-tail current contributions in addition to the WINDMI ring current in order to calculate the complete simulated Dst index. The quiet time values for each current system is included in the WINDMI model calculations. Following Spencer et al. [20] we have lumped together the effects of the region one and two currents, I_1, I_2, and the geotail current and proceed to use αI of the geotail current to represent both. The contributions from the magnetopause and tail current systems are given by

$$Dst_{mp} = a * \sqrt{P_{dyn}}, \tag{1.10}$$

$$Dst_t = \alpha I(t), \tag{1.11}$$

where Dst_{mp} is the perturbation due to the magnetopause currents and Dst_t is the magnetic field contribution from the tail current $I(t)$ which is modeled by WINDMI as I. P_{dyn} is the dynamic pressure exerted by the solar wind on the Earth's magnetopause. The simulated Dst is then given by

$$Dst_{windmi} = Dst_{rc} + Dst_{mp} + Dst_t. \tag{1.12}$$

In eq. (1.2), the parameter Σ represents a collisionless conductivity. This conductivity is derived from the MHD momentum equation as given in Spencer [24]. The divergence of the off-diagonal momentum stress tensor $\vec{\pi}$ is given by the chaotic scattering of the ions

in large orbits from the sharp field curvature in the central plasma sheet where the field magnitude is weak and current density high. Horton and Tajima [25] give the volume integrated effect of this large gyro radius effect as

$$\nabla \cdot \vec{\pi} = \rho \nu_{\text{eff}} \vec{v_E}, \tag{1.13}$$

where ν_{eff} the effective collision frequency. The projection of this collisionless magnetic viscosity in the normal direction of $\nabla\Psi$ gives

$$\frac{\nabla\Psi \cdot (\nabla \cdot \vec{\pi})}{B^2} = -\frac{\rho \nu_{\text{eff}} E_y}{B^2}. \tag{1.14}$$

The value of this term is an important driver in substorm dynamics modeled in WINDMI [21]. Such resistivity can be found by studying many single particle trajectories ($\vec{E}$ and $\vec{B}$ are not calculated self-consistently) and calculating resistivities based on particle chaotization inside the current sheet (section 2.3). The plasma sheet conductivity is a complex theoretical calculation due to the chaotic orbits of the protons and oxygen ions that have a gyro radius comparable to the thickness of the heating layer. Inside this layer the theory of Horton and Tajima [25] shows that

$$\Sigma = 0.1 \frac{L_x L_z}{L_y} \left(\frac{en}{B_n}\right) \left(\frac{\rho_i}{R_c}\right)^{1/2}. \tag{1.15}$$

1.4 Purpose and Objectives of the Study

The aim of this research is to calculate the resistivity values in different configurations of magnetic shears called current sheets. Before a substorm onset (subsection 1.1.2), the current sheet thins and bifurcates. We would like to calculate resistivity values for such configuration and also for different times during the growth phase when the sheet thickness can vary depending on the amount of tail field stretching and also for symmetric and asymmetric sheets. Such a model will help in putting a more realistic values of Σ in eq. (1.2), and hence a more closer modeling of substorms in the WINDMI model (section 1.3). During the particle traversal through a current sheet, it experiences inadiabatic motion.

In certain parameter ranges and initial conditions (section 3.6), the particle trajectory can lead to an increase of entropy leading to an increase in the conductivity. Exponential fits to number of particles in the current sheet as a function of time (fig. 6.3) show that the behavior exhibits a double exponential rather than single exponential decay as indicated by Numata and Yoshida [6]. Hence, the resistivity values might need reinterpretation which would also be a subject of investigation. Resistivity values are important specially during reconnection events since it determines the reconnection rate. This is important for the energy budget of the system, which in this case is the magnetotail. A special class of reconnection process is the tearing mode which happens at very low frequencies. Horton et al. [26] describe such a geometry to calculate AC conductivity based on a slow time varying magnetic field profile which through the Maxwell's first curl equation produce an electric field. The study would also look at such configurations for different types of current sheets.

During substorms and even quiet times, the magnetotail field as seen in the observations deviates from the so called modified Harris sheet. Two such observed geometries in the literature are the X-line [6] and the Bifurcated Current Sheet (which from now on will be referred to as BCS) [27]. The fields lines by the virtue of being in such configurations store energy which must be released in some form for the field lines to return to a relaxed state. Such reconfigurations in reversed magnetic fields is called reconnection and can occur both in collisional (laboratory plasmas) and collisionless plasmas (space plasmas). Finite resistivity is needed for such releases which in turn results from finite number of collisions. This results in resistive breaking of field lines. But for space plasmas this is not the case and some other mechanisms are needed. Since the number of collisions is very rare in space plasmas, although reconnection occurs but at a very slow scale. Retaining terms in Ohm's law for scales smaller than global and larger than electron gyro scales do seem to eradicate the impulsive nature of reconnection but at a higher computational cost. This study tries to find a colliosionless resistivity analogous to the collisional resistivity used in laboratory plasmas as a substitute in the Ohm's law which in turn should give a faster reconnection rate but at a lower computational cost. This is valid specially in the magnetotail where

single particle like instead of fluid like features have been seen in the observed distributions functions. Electric fields found in solar corona is to strong for fuid theory to hold in the reconnection sites in the corona. Hence, this study tries to find a link between the kinetic (on the proton diffusion scale) and the macroscopic (fluid scales) through a mesoscopic model of the average velocity inside the chaos region (see section 6.3).

Chapter 2

Magnetotail Current Sheet Models

As indicated in Chapter 1, the Sun flings out plasma continuously along with magnetic field that is said to be frozen-in to the plasma called the solar wind. This wind is super-magnetosonic (i.e., traveling faster than any of the wave modes in a magnetized plasma). Planets on the other hand may or may not have their own magnetic field. When the solar wind hits the magnetized planets, a shock is formed (as the information about the obstacle can be conveyed only at characteristic speeds, the fastest amongst them being the magnetosonic speed), and it is decelerated to submagnetosonic speeds behind the shock flows around the obstacle analogous to water flowing around rocks. Since the wind is slowed down, according to continuity equation, it is compressed and heated. Such mass and momentum flow around the Earth causes the dipole field to be compressed on the dayside and stretched on the nightside. Close to the Earth, field lines are still dipolar. Much of the magnetospheric dynamics is governed by this region with charged particles being often energized. Visual indicators of storms and substorms are auroras that occur in the polar region.

2.1 Tail Lobes

Much of the the tail is made up of two large volumes of nearly parallel magnetic field lines. The bundle North of the equator points Earthwards, while the Southern bundle points away from Earth. Plasma density in this region is very rare as seen in Table 2.1. These two volumes are linked to Northern and Southern polar regions, respectively. This region extends far in nightside with distances close to 220 R_E recorded by satellites and can be seen in fig. 2.1.

As suggested by the table, such low density means that connection to the solar wind

Table 2.1: Plasma density in different regions of the magnetosphere.

Region	N_p (cm^{-3})
Solar wind in front of Bow Shock	6
Magnetosheath	1
Plasma Sheet	$0.3 - 0.5$
Tail lobes	.01

down the tail leads to charged particle escape along the field lines, somewhere far downstream from Earth. Very few solar wind ions (high energy) can oppose the wind's average flow (which is downtail) and head upstream, towards Earth.

2.2 Plasma Sheet

As seen in fig. 1.3, the two tail lobes are separated by a region of fairly weak magnetic field and of much denser plasma. This region is called the plasma sheet. Its thickness ranges from 2-6 R_E (Earth radii). Also, the field line reversal and stretching means that a current system called the cross-tail current flows in the dawn dusk direction or out of the page in fig. 1.3. Like every steady electric current, this current closes onto the magnetopause current that separates the solar wind plasma from the magnetospheric plasma, and the closing occurs in two branches that follow the magnetopause around either tail. Also, as seen in fig. 1.3, the core plasma sheet is separated from the lobes by Plasma Sheet Boundary Layer (PSBL). Most particles are energized to KeVs. Wave turbulence ranging from electrostatic to electron cyclotron frequency is also observed in the plasma sheet [28]. As mentioned before, plasma sheet plays in storms and substorms. Periods of superdense plasma sheet can be an important preconditioning to the onset of a geomagnetic storm [29]. Also O^+ can also flow from the ionosphere to dominate the inner magnetosphere just before storm and substorm onset [30].

2.3 Current Sheets

As seen in fig. 1.3, on the nightside, the solar wind stretches the Earth's magnetic field into what is called the magnetotail. The Northern and Southern lobes contain magnetic

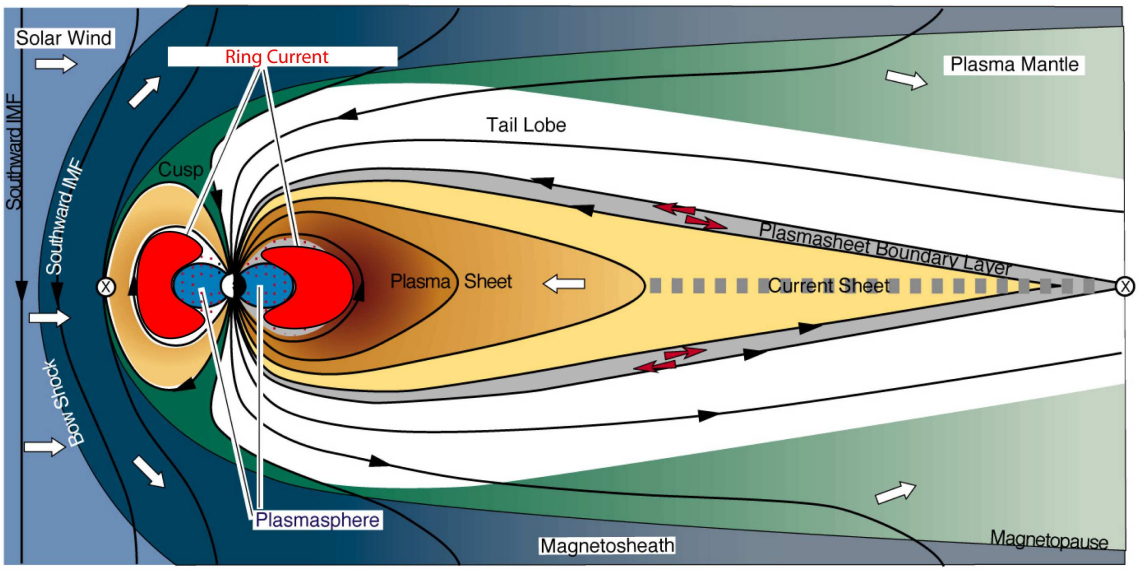

Fig. 2.1: A slice of fig. 1.3 taken through the plane $y = 0$ showing the location of current sheet in the magnetotail. Deep in the tail around $12 - 16\ R_E$, the field lines are stretched as a result of solar wind convection. This stretching of oppositely directed field lines causes the strengthening of cross-tail current (coming out of the board).

fields that go into and come out of the Earth. A North South view of the magnetosphere is shown in fig. 2.1. Close to where the magnetic field configuration changes from Northern to Southern lobe, a current needs to flow to support this change [31]. As discussed previously, as a result of the interaction of solar wind with the geomagnetic field, the tail is stretched. Also, reconnection on the dayside leads to transport of magnetic flux to the nightside. The stored magnetic energy is released frequently through merging in the nightside which relaxes the configuration. This section will discuss a few magnetic field line models used to analyze the dynamics in the magnetotail.

2.3.1 Harris Sheet

A current sheet is the region within the plasma sheet wherein the magnetic field rapidly changes from tailward to Sunward orientation. If we assume the magnetic field is antisymmetric about the current sheet center, the hyperbolic tangent current sheet model of Harris is a good approximation to the profile of the current sheet. The Harris model is a simple

analytical description of a 1D current sheet model and is self-consistent using either MHD or kinetic theory. The magnetic field, plasma thermal pressure, and current density are given by Dusenbery et al. [32]

$$B_x = B_0 tanh(z/L), \tag{2.1}$$

$$p_T = p_o sech^2(z/L), \tag{2.2}$$

$$j = \frac{B_0}{\mu_0 h} sech^2(z/L), \tag{2.3}$$

where B_0 is the lobe field, z is the distance between the observation point and the current sheet center, and L is the current sheet half thickness. The sheet is shown in the top panel of fig. 2.2.

2.3.2 Parabolic Sheet

When a normal magnetic field component (finite B_z) is added to the Harris sheet, magnetic field lines look like parabolas [32]. The middle panel of fig. 2.2 shows that a particle with sufficiently large gyro radius (either due to large initial perpendicular velocity or large mass) can loose adiabaticity in such a geometry. Sample particle trajectories in model current sheets will be discussed in section 3.6.

2.3.3 X-line and Associated Topologies

Although reconnection occurs naturally in nature for example in Solar corona, Earth's magnetopause etc., the Harris sheet equilibrium discussed in subsection 2.3.1 is unsuitable to study steady reconnection problem. One then needs to a priori force an X-line configuration of the magnetic field. Such a geometry is shown in the left panel of fig. 2.3.

The magnetic field configuration for a Y-line can be put mathematically as [6]

$$\vec{\mathbf{B}} = \left[B_0 \left(\frac{y \mp l_y}{l_x} \right), B_0 \frac{x}{l_x}, 0 \right], (|y| > l_y), \tag{2.4}$$

$$\vec{\mathbf{B}} = \left[0, B_0 \left(\frac{x}{l_x} \right), 0 \right], (|y| \leq l_y), \tag{2.5}$$

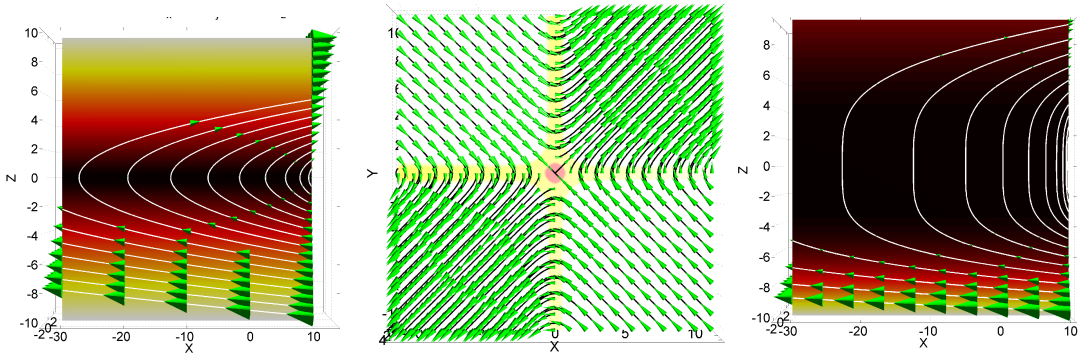

Fig. 2.2: Current sheet models used to study particle dynamics. The top panel shows the magnetic field topology for a modified Harris ($B_z \neq 0$) sheet. The middle panel depicts a reconnection geometry with oppositely directed field lines convecting in from top and bottom to merge in the middle. This topology only occurs for a fast Petschek-type reconnection. During substorms, magnetotail can have a bifurcated structure due to fast Earthward flows in the central plasma sheet and given that frozen-in condition holds, the field lines are dragged in the center but are left behind in the lobes.

where B_0, l_x, and l_y are constants and signify the magnitude of the magnetic field far from the neutral sheet ($x = 0, |y| \leq l_y$), and the extent of bending or curvature in the magnetic field, respectively. If one were to substitute $l_y = 0$ in the above equations, we would get an X-line as seen in fig. 2.3.

2.3.4 Bifurcated Current Sheet (BCS)

Before the substorm onset, during the late growth phase, observations of the magnetotail have shown that the current sheet is far from looking like a Harris sheet [33]. The process which leads to bifurcation is still widely debated with many instabilities that might lead to it such as lower hybrid drift (LHDI) and kink mode or velocity shear driven instability [34]. The shape of the sheet magnetic field can be seen in last panel of fig. 2.2. Using the model equations [35, 36]

$$B_x = \frac{B_0}{2}\left(tanh\left(\frac{z+z_c}{L_{left}}\right) + tanh\left(\frac{z-z_c}{L_{right}}\right)\right), \tag{2.6}$$

$$B_y = 0, \tag{2.7}$$

$$B_z = B_n, \tag{2.8}$$

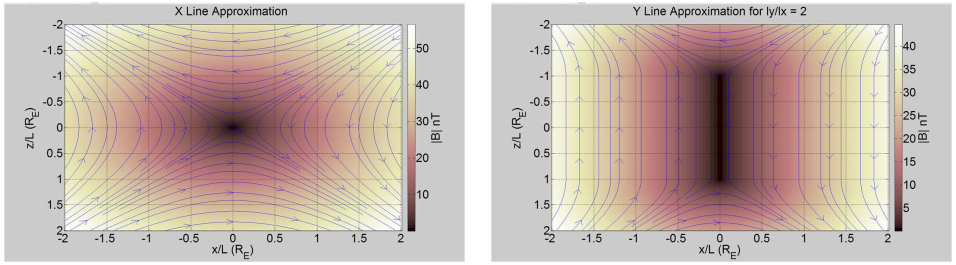

Fig. 2.3: X-line and associated magnetic field geometries. X-lines are needed for fast Petschek-type reconnection while Y-lines tend to have very low Sweet-Parker rate of merging. Rate of reconnection depends on the aspect ratio (length to width ratio) which is comparable to unity for an X-line and very large for Y-line.

where $B_0, B_n, L_{right}, L_{left}$, and z_c are all constants in appropriate units, we can derive different sheet configurations. For $L_{right} = L_{left}$ and $z_c = 0$, we get the Harris sheet configuration as shown on the left panel of fig. 2.4. With $L_{right} = L_{left}$ and $z_c \neq 0$, the current sheet bifurcates into a symmetric current sheet as seen in the middle panel of fig. 2.4 while for $L_{right} \neq L_{left}$ and $z_c \neq 0$, the current density strengths in the peaks becomes unequal and it is called an asymmetric current sheet (fig. 2.4 right panel). The type of particle orbits found in such sheets is the same as found for the parabolic configuration. Transient, quasi-periodic, and chaotic orbits are therefore found in the BCS, also. But depending on whether or not the sheet is asymmetric (fig. 2.4), these orbits can exist for a range of parameters. The current sheet which is not centered in the equatorial plane as is the case for Harris sheet.

2.4 Reconnection

2.4.1 Introduction

We have seen in Chapter 1 that storage of magnetic energy leads to geomagnetic storms and substorms in the magnetotail [3, 37]. This stored energy is released in the form of heat and kinetic energy of the particles (conservation of energy) and the process is called magnetic reconnection. Magnetic reconnection is the fundamental process by which magnetic fields in conductive fluids topologically rearrange themselves while moving to a

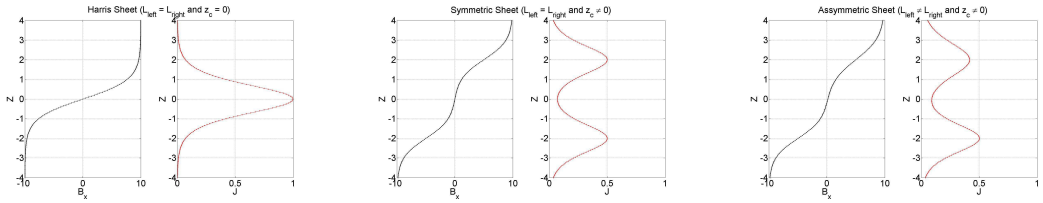

Fig. 2.4: Magnetic field configurations with respective current densities (J) using different values of L_{left}, L_{right}, and z_c in eq. (2.6). The leftmost panel is a 1D plot of the Harris sheet ($B_z = 0$) with the variation of B_x w.r.t. z shown and the associated current sheet in the center. The middle panel shows the variation of B_x w.r.t. z for a BCS when the scale over which the field varies being equal ($L_{left} = L_{right}$) which leads to a symmetric current sheet which is located off center. Similarly when $L_{left} \neq L_{right}$, the two current sheets are of different strengths and vary across different scales, the so called asymmetric current sheet.

lower energy state. Stress on oppositely directed field lines is reduced by merging of these flux tubes. The magnetic energy converted into kinetic energy of the fluid is accelerated out of the reconnecting layer. Theories provide good macroscopic descriptions of reconnection, the actual physical mechanism for reconnection at the microscopic scale remains unknown. Figure 2.5 shows two examples of where reconnection plays a dominant role in converting magnetic energy in sheared fields into kinetic and thermal energies. A simple model that mimics this process is shown in fig. 2.5(c). Magnetic reconnection plays an important role in the dynamics of solar flares and CMEs and may be the primary heating mechanism in the solar corona. Reconnection in the Earth's magnetotail causes particles to be accelerated Earthward with speeds up to 1000 Km/s (close to the Alfven speed in the region) [38–40]. Figures 2.5(a) and 2.5(b) show example regions where reconnection takes place. Figure 2.5(a) depicts reconnection in solar corona and fig. 2.5(b) shows reconnecting field lines in the geomagnetic tail. Figure 2.5(c) shows the geometry of the reconnecting fields which is asymptotically called an X-line (the dotted lines).

2.4.2 Generalized Ohm's Law

Forces on charged particles in a plasma are primarily due to electric and magnetic fields which might be externally imposed or self-produced. The basic microscopic dynamics of

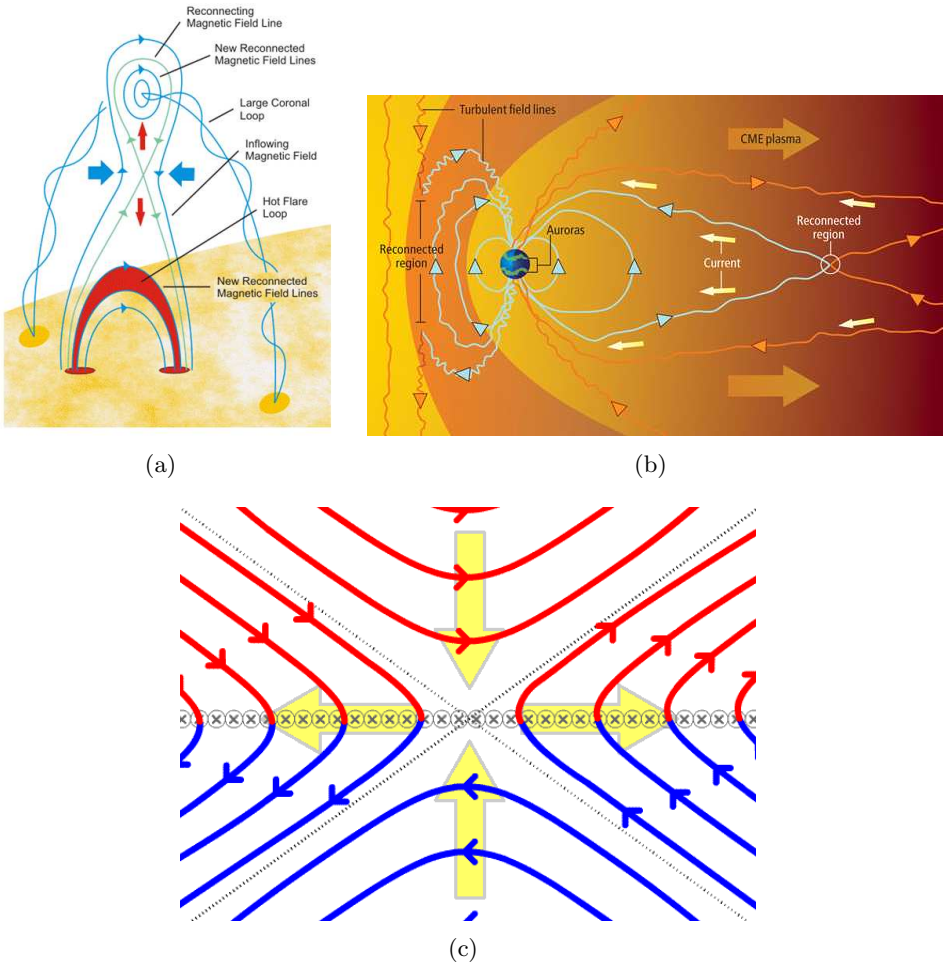

Fig. 2.5: Reconnection as a mechanism to reduce stress on sheared magnetic fields. Figures 2.5(a) and 2.5(b) show example regions where reconnection takes place. Figure 2.5(a) depicts reconnection in solar corona and fig. 2.5(b) shows reconnecting field lines in the geomagnetic tail. Figure 2.5(c) shows the geometry of the reconnecting fields which is asymptotically called an X-line (the dotted lines). Red and blue lines denote fields of opposite polarity. Yellow arrows denote the incoming and outgoing plasma. Courtesy: `http://en.wikipedia.org/wiki/Magnetic_reconnection`

a charged particle is governed by the Newton-Lorentz equation and is discussed in detail in Chapter 3. Here we discuss the macroscopic motion of these charged particles as a fluid continuum with fast time scales averaged out. Considering the macroscopic motion of charged particles say ions and electrons, the total time time rate of change ($\frac{\partial}{\partial t} + \vec{u}_i \cdot \vec{\nabla}$, i being the species, ion or electron) is equal to the sum of all forces acting on the system (which is the Lorentz force plus other body forces like gravitation). Electric and magnetic

fields influence a charged particle through the Lorentz force given by

$$\vec{F}_{Lorentz} = q(\vec{E} + \vec{v} \times \vec{B}), \tag{2.9}$$

$\vec{v}$ being the velocity of the particle, $\vec{E}, \vec{B}$ the electric and magnetic fields experienced by the particle, and q is the charge on the particle. The Lorentz force is discussed in detail in Chapter 3. In absence of perpendicular electric fields or any inhomogeneities in the fields, the particles are forced to move along the magnetic field lines or they are frozen-in to the field. Inhomogeneity in particle density or temperature or both will cause pressure gradients on the fluid level. This gradient will act to decelerate the particles and is given by

$$\vec{F}_{press} = -\vec{\nabla} \cdot \prod, \tag{2.10}$$

where $\prod$ is the pressure tensor ($\prod = p\mathbf{I} + \pi$). p is one-third the trace of the diagonal of the pressure tensor, the off-diagonal terms (π) being the viscous part of the tensor which can be due to relative shear between adjacent layers [41]. $\mathbf{I}$ is the unity tensor. Collisions between unlike particles also tends to change the velocity of the system. This force provides the conductivity in a plasma. This force can be written as [37, 41, 42]

$$\vec{F}_{col} = mn\langle\nu_c\rangle(\vec{v}_p - \vec{v}_e), \tag{2.11}$$

where ν_c is the collision frequency. Ignoring any anisotropic effects (which means that the pressure or temperature along and across the magnetic field can be different due to the fact that the particle is free to move along but not across the magnetic field), we can now formulate the dynamical equation for ions and electrons. Space plasmas behave on multiple spatial and temporal scales. For either species i (which can be multiple ions (both of solar wind and ionospheric origin) and electrons at different temperatures), the total rate of change of momentum is given by

$$m_i n_i \frac{d\vec{v}_i}{dt} = \sum \vec{F}, \tag{2.12}$$

where $\vec{F}$ are the forces mentioned above in eqs. (2.9), (2.10), and (2.11). Close to planetary bodies, gravity would also be included in the list of forces. Hence, we have

$$m_i n_i \frac{d\vec{v}_i}{dt} = m_i n_i \left(\frac{\partial \vec{v}_i}{\partial t} + (\vec{v}_i \cdot \vec{\nabla})\vec{v}_i \right) = q_i n_i (\vec{E} + \vec{v}_i \times \vec{B}) - \vec{\nabla} p_i - m_i n_i \langle \nu_{ij} \rangle (\vec{v}_i - \vec{v}_j), \quad (2.13)$$

where ν_{ij} is the collision frequency between species i and j. Experimentally, v_i, the species bulk speed is difficult to measure. On the other hand, it is much simpler to measure the bulk speed (total speed of fluid as a whole) and the differential speed (the electric current). Hence, a magnetohydrodynamic formulation is done in which it is assumed that under equilibrium conditions, individual species densities are equal ($n_p \approx n_e$). Secondly, due to the mass difference between electrons and an ion species, the bulk velocity is mostly ion velocity ($\vec{v} \approx \vec{v}_i$). The current density is then defined as

$$\vec{J} = \sum_i n_i q_i \vec{v}_i. \quad (2.14)$$

For ions and electrons, adding and subtracting species momentum equations (eq. (2.13)) will give a momentum equation and a current equation. The current equation called the generalized Ohm's law is given as [41]

$$\vec{E}' = \underbrace{\eta \vec{J}}_{\text{Resistive term}} + \underbrace{\frac{1}{ne}\vec{J} \times \vec{B}}_{\text{Hall term}} - \underbrace{\frac{1}{ne}\vec{\nabla} p_e}_{\text{Electron pressure term}} + \underbrace{\frac{m_e}{ne^2}\frac{\partial \vec{J}}{\partial t}}_{\text{Electron inertia term}}, \quad (2.15)$$

where $\vec{E}' = \vec{E} + \vec{u} \times \vec{B}$ is the electric field in the frame moving with fluid velocity $\vec{v}$. The relation $mn\langle \nu_{ij} \rangle = \eta q_i^2 n^2$ was used in the first term on the right hand side.

The terms on the right represent the resistive, Hall, electron pressure gradient and electron inertial term and is also called the nonideal contribution in the Ohm's law (since the equation no longer indicates that charged species are bound to the magnetic field lines) which break oppositely directed field lines. Only pressure anisotropies can lead to field line breaking and merging. This is due to the fast that the curl of the gradient of scalar pressure is identically zero. Equation (2.15) was derived assuming that $m_i >> m_e$ (since the proton

is three orders of magnitude heavier than the electron).

2.4.3 Magnetic Induction

Equation (2.15) contains terms that are important on various time scales. As a simplification, if the plasma is very dense ($1/n \to 0$). Then eq. (2.15) is reduced to the so called resistive limit as

$$\vec{E} + \vec{u} \times \vec{B} = \eta \vec{J}. \tag{2.16}$$

Using the Maxwell's equations, we can further manipulate the Ohm's law. They are

$$\vec{\nabla} \times \vec{E} = -\frac{\partial \vec{B}}{\partial t}, \tag{2.17}$$

$$\vec{\nabla} \times \vec{B} = -\mu_0 \vec{J}, \tag{2.18}$$

$$\vec{\nabla} \cdot \vec{E} = \frac{\rho}{\epsilon_0}, \tag{2.19}$$

$$\vec{\nabla} \cdot \vec{B} = 0. \tag{2.20}$$

In the above equations, the displacement current term ($\epsilon_0 \mu_0 \frac{\partial \vec{E}}{\partial t}$) has been neglected since we are interested to study time scales that are of low frequency [41]. An order of magnitude calculation shows that for a plasma process time scale of τ and on spatial scale L, the ratio of the conductive to the displacement current is

$$\frac{\mu_0 \vec{J}}{\epsilon_0 \mu_0 \frac{\partial \vec{E}}{\partial t}} \approx \frac{\mu_0 \vec{J}}{\epsilon_0 \mu_0 \frac{\eta \vec{J}}{\tau}} = \frac{c^2 \mu_0 \tau}{\eta} = \frac{c^2 \mu_0 \tau L^2}{\eta L^2} = \frac{\tau}{\tau_{light}^2} \frac{\mu_0 L^2}{\eta} = \frac{\tau \tau_{diff}}{\tau_{light}^2} \gg 1, \tag{2.21}$$

where the resistive approximation to Ohm's law was used in the second step. Even with $\tau = \tau_{light}$, the conducting current remains larger than the displacement current. By using the Ampere's law we can reduce the resistive Ohm's law to

$$\vec{E} = -\vec{u} \times \vec{B} + \frac{\eta}{\mu_0} \vec{\nabla} \times \vec{B}, \tag{2.22}$$

$$\frac{\partial \vec{B}}{\partial t} = \vec{\nabla} \times (\vec{u} \times \vec{B}) + \frac{\eta}{\mu_0} \nabla^2 \vec{B} \text{ (curl of eq. (2.22) + eq. (2.17))}. \tag{2.23}$$

This equation is called the magnetic induction equation and it implies that the magnetic field at a particular point in space can change due to the bulk movement of magnetized fluid (convection) or due to a decay of the fields in the plasma (diffusion) [41, 43]. The diffusion of magnetic field in the magnetic induction equation is due only to the resistive decay of currents that support the magnetic fields. The remaining terms in the Ohm's law such as electron inertia, pressure, and Hall terms can also contribute to the change in the magnetic field.

A quick order of magnitude calculation reveals that the ratio of the convection to the diffusion term in eq. (2.23) which is defined as the magnetic Reynold's number (R_m) is given by

$$R_m \equiv \left| \frac{\vec{\nabla} \times (\vec{u} \times \vec{B})}{\frac{\eta}{\mu_0} \nabla^2 \vec{B}} \right| \approx \frac{\mu_0 v B L^2}{\eta B L} = \frac{\mu_0 v L}{\eta}. \tag{2.24}$$

For $R_m \gg 1$, the plasma flow dominates over the diffusion and the magnetic field is said to be frozen-in to the plasma [41, 43, 44]. In the limit when $R_m \ll 1$, the plasma and magnetic field motion is completely decoupled and the two are free to diffuse through each other.

2.4.4 Magnetic Diffusion and Reconnection

As discussed in subsection 2.4.1, reconnection is the topological rearrangement of oppositely directed magnetic fields in which the stored magnetic energy is released as thermal and kinetic energy of the plasma [3]. In the limit of when the conductivity being very high ($\eta \to 0$ being the case for many astrophysical plasmas [43]), eq. (2.23) reduces to

$$\frac{\partial \vec{B}}{\partial t} = \vec{\nabla} \times (\vec{u} \times \vec{B}). \tag{2.25}$$

Magnetized plasmas such as the solar wind and that in the magnetospehere when in contact cannot diffuse through because they are highly conducting and collisionless (mean free path $\gg$ spatial scales in the system), and so the ideal Ohm's law (eq. (2.25)) governs the dynamics. Other terms in the generalized Ohm's can also contribute to the diffusion when the conductivity is high [3]. Various other mechanisms apart from these such as

anomalous resistivity from turbulence [45], wave-particle interaction, or through chaotic particle motion [6] can produce resistivity required for the reconnection in plasmas where collisional resistivity is too low to account for the fast merging seen in space plasmas. An example model proposed separately by Sweet [2] and Parker [1] will shed more light into the problem of reconnection in collisionless plasmas.

2.4.5 Sweet-Parker Model

The Sweet-Parker model explains the dynamics of a system in equilibrium where convection is balanced by diffusion ($R_m = 1$). It is centered on the role of resistivity in the conversion of stored magnetic field energy into plasma thermal and kinetic energy.

Plasma flows into the current layer at some relatively small inflow velocity V_{in} as seen in fig. 2.6. It then accelerates along the layer and shoots from the ends of the magnetic diffusion layer with a relatively large exit velocity $V_{out} = V_A$ as seen in fig. 2.7. The Sweet-Parker model was the first model to show how localized reconnection of field lines can cause the observed macroscopic changes. The model was far too slow, however, to account for the fast reconnection observed in the solar system. For example, the energy release in solar flares observed to occur in minutes would take tens of days according to the model.

The main assumption of the model is incompressibility (fluid density stays constant on time scales of interest). Without resistivity, the oppositely directed field lines in fig. 2.6 would stay without mixing for infinite time. But on small length scales (e.g., current layers), resistivity can and does become important allowing the two layers on the either side of the current layer to mix. To find out the inflow and outflow velocities, we know that the energy is conserved. Hence, the magnetic energy of the inflowing plasma is equal to the bulk kinetic energy of the outflowing plasma [37].

$$\frac{1}{2}\rho u^2 = \frac{B_x^2}{2\mu_0}, \tag{2.26}$$

$$v_{out} = \frac{B_x}{\sqrt{\rho\mu_0}} \equiv V_A, \tag{2.27}$$

where as from fig. 2.7, the magnetic field is mainly in the x direction which implies that to

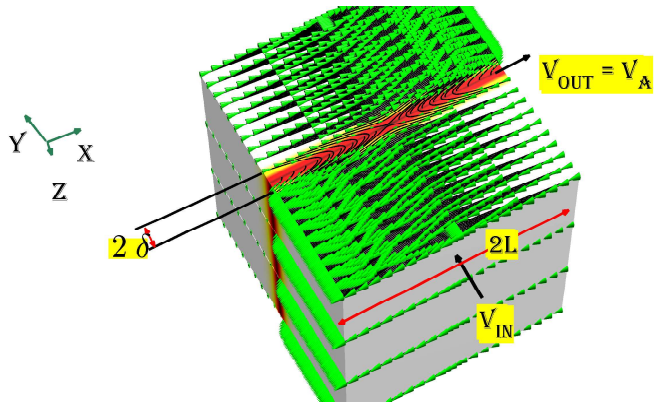

Fig. 2.6: Sweet-Parker model of magnetic reconnection. Frozen-in plasma and magnetic field convect towards the current layer (weak magnetic field in red color) at a fraction of the Alfven speed and get annihilated to be ejected from the sides at Alfven speed [1–3]. Black lines are the magnetic field streamlines and the green cones indicate the polarity of the magnetic field.

support the reversal, the current is in the z direction. To get an expression for the inflow speed, we know that ideal conditions hold outside far from the diffusion region (fig. 2.6). Hence, the current is zero and the Ohm's law is reduced to $E_z - v_{in}B_x = 0$ outside the diffusion region and $\hat{x} \times \hat{(} - y) = -\hat{z}$. Using Amperes law around the current layer, we get

$$B_x(4L) = \mu_0 4L\delta J_z, \tag{2.28}$$

since the sides of the pillbox do not contribute as the $B_x \perp dy$. Inside the current layer, since the plasma stagnates before being accelerated, $u = 0$ and the Ohm's law is written as $E_z = \eta J_z$. Hence, we can calculate the inflow velocity as [37] $v_{in} = \frac{E_z}{B_x} = \frac{\eta J_z}{\mu_0 \delta J_z} = \frac{\eta}{\mu_0 \delta}$. Now using the condition for incompressibility, we can calculate the length scaling for the model.

$$2\delta u_{out} = 2L u_{in}, \tag{2.29}$$

$$\delta\left(\frac{B_x}{\sqrt{\rho\mu_0}}\right) = L\left(\frac{\eta}{\mu_0\delta}\right), \tag{2.30}$$

$$\delta = \frac{L}{\sqrt{S}}, \tag{2.31}$$

where S is the Lundquist number which is the magnetic Reynold's number with $v = v_A$.

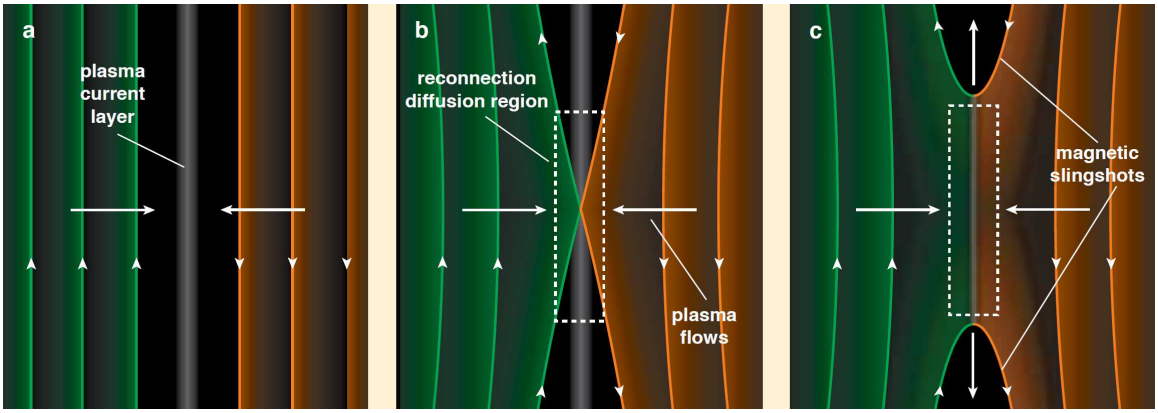

Fig. 2.7: Magnetic reconnection in oppositely directed magnetic fields in a 2D view. The field strength is weak in the current layer where the frozen-in condition is broken. The second figure depicts the plasma inflow and the third shows the plasma and magnetic field outflow. Courtesy `http://mms.space.swri.edu/AmSci-Reconnection.pdf`.

Hence, eq. (2.31) implies that the diffusion layer thickness δ is inversely proportional to the Lundquist number. Plasmas with high numbers should then have a very thin current layer. But it is observed in experiments and even in space plasmas (where the collisional resistivity η is very small) that the current layer remains wide on a macroscopic scale. This led to the community looking at other sources of resistivity and eventually to a model of collisionless reconnection discussed next.

2.4.6 Collisionless Reconnection

As discussed in subsection 2.4.4, the diffusion layer thickness scales inversely with the Lundquist number. But such scaling is not found in either experiments and space plasma observations. Other terms in the Ohm's law could then be important in the dynamics of reconnection. Theory of such process was put forth by Biskamp et al. [46], Biskamp [47], and worked upon numerically by Shay et al. [48]. Returning back to the generalized Ohm's law from eq. (2.15), we need to again to an order of magnitude comparison. Before that, we normalize the equation so that every term becomes unit less. We scale the velocity by Alfven speed v_A, spatial scale by L, so that time is scaled by the Alfven transit time $\tau_A = L/v_A$, magnetic field by B_0 (some asymptotic field in the system). Denoting the

unitless variables (say C) by $\hat{C}$, we then have

$$v \to v_A \hat{v}, B \to B_0 \hat{B}, t \to \tau_A \hat{t}, x \to L\hat{x}. \tag{2.32}$$

We can then write the current density J and the electric field E in terms of the above unitless variables as

$$J \to \frac{B_0}{\mu_0 L}\hat{J}, E \to \frac{B_0 L}{\tau_A}\hat{E}. \tag{2.33}$$

These normalizations when substituted in the Ohm's law give

$$\frac{B_0 L}{\tau_A}\vec{\hat{E}} + v_A B_0 \vec{\hat{v}} \times \vec{\hat{B}} = \frac{\eta B_0}{\mu_0 L}\vec{\hat{J}} + \frac{B_0^2}{\mu_0 L n e}\vec{\hat{J}} \times \vec{\hat{B}} - \frac{p_0}{neL}\vec{\hat{\nabla}}\hat{p}_e + \frac{B_0 m_e}{\mu_0 L n e^2 \tau_A}\frac{\partial \vec{\hat{J}}}{\partial \hat{t}},$$

$$\vec{\hat{E}} + \vec{\hat{v}} \times \vec{\hat{B}} = \underbrace{\frac{\eta B_0}{\mu_0 L v_A B_0}}_{\text{term 1}}\vec{\hat{J}} + \underbrace{\frac{B_0^2}{\mu_0 L n e v_A B_0}}_{\text{term 2}}\vec{\hat{J}} \times \vec{\hat{B}} - \underbrace{\frac{p_0}{neL v_A B_0}}_{\text{term 3}}\vec{\hat{\nabla}}\hat{p}_e + \underbrace{\frac{B_0 m_e}{\mu_0 L n e^2 \tau_A v_A B_0}}_{\text{term 4}}\frac{\partial \vec{\hat{J}}}{\partial \hat{t}},$$

where $v_A B_0$ was divided out from the equation.

It can be shown that the first two terms and the third last term $\rho E/ne$ can be ignored when the spatial scale length is much greater than the electron inertial length (c/ω_{pe}). The last two terms in can be ignored when the scale length is much greater than the ions' inertial length (c/ω_{pi}). The terms on the left correspond to the ideal Ohm's law which says that the magnetic field and the plasma morph as a single entity (twist, stretch, and break). The terms 1 to 4 simplify to

$$\begin{aligned}
\textbf{term 1} &= \frac{\eta}{\mu_0 L v_A} = \frac{1}{S} \text{ (Lundquist number , i.e., eq. (2.24) with } v = v_A), \\
\textbf{term 2} &= \frac{B_0}{\mu_0 L n e v_A} = \frac{B_0}{n e \mu_0 L \frac{B_0}{\sqrt{m_i n \mu_0}}} = \frac{1}{L\sqrt{\frac{ne^2}{m_i \epsilon_0}\mu_0 \epsilon_0}} = \frac{c}{\omega_{pi} L} = \frac{\delta_i}{L}, \\
\textbf{term 3} &= \frac{p_0}{neLv_A B_0} = \frac{p_0}{enL\frac{B_0^2}{\sqrt{m_i n \mu_0}}} = \frac{p_0}{\sqrt{\frac{e^2 n}{m_i \mu_0}} L B_0^2} = \frac{p_0}{\omega_{pi}\sqrt{\frac{\epsilon_0}{\mu_0}} L B_0^2} = \frac{p_0 c}{\omega_{pi} L \frac{B_0^2}{\mu_0}} = \frac{\beta \delta_i}{L}, \\
\textbf{term 4} &= \frac{B_0 m_e}{\mu_0 L n e^2 \tau_A v_A B_0} = \frac{m_e}{\mu_0 L n e^2 \frac{L}{v_A} v_A} = \frac{1}{\frac{ne^2}{m_e \epsilon_0}\epsilon_0 \mu_0 L^2} = \frac{c^2}{\omega_{pe}^2 L^2} = \frac{\delta_e^2}{L^2},
\end{aligned}$$

where $\omega_p = \sqrt{\frac{ne^2}{m\epsilon_0}}$ is the plasma frequency for ion and electron, δ is the skin depth (scales on which the particle inertia dominates), and β is the ratio of the plasma thermal pressure p to the magnetic pressure $B_0^2/2\mu_0$. Also, the Alfven speed was substituted for as $v_A = \frac{B_0}{\sqrt{m_i n \mu_0}}$ and the electron pressure p_e was scaled according to some asymptotic pressure p_0.

Hence, the generalized Ohm's law can be written in normalized form as

$$\hat{\vec{E}} + \hat{\vec{v}} \times \hat{\vec{B}} = \frac{1}{S}\hat{\vec{J}} + \frac{\delta_i}{L}\hat{\vec{J}} \times \hat{\vec{B}} - \frac{\delta_i}{L}\beta\hat{\vec{\nabla}}\hat{p}_e + \left(\frac{\delta_e}{L}\right)^2 \frac{\partial \hat{\vec{J}}}{\partial t}. \tag{2.34}$$

According to eq. (2.34), it is only when we are dealing with large spatial scales ($L \gg c/\omega_{pi}$) when the resistive approximation holds. On the order of ion inertial scales, the Hall and pressure gradient term begin to dominate. Hall term tends to decouple the electrons and ions so that electrons are still frozen in to the magnetic field but the ions get demagnetized [43]. The decoupling makes the ions to move at much slower pace than electrons and this drag produces the Hall current that points out of the plane [48]. To support this current the ions also have to move out of the plane.

On the electron inertial scales, even the electrons get demagnetized as seen in fig. 2.8. The frozen-in condition of the magnetic induction equation is broken and the field lines can merge. Electrons are accelerated out of the diffusion region at super-Alfven speeds. But as the electrons try accelerate further the an electric field builds up to pull the ions into the diffusion region and then accelerated out from the region [3]. The Hall currents produced alter the magnetic field topology on ion inertial scales as seen in fig. 2.8. A question arises as to at what scale does the magnetic field morph? At the electron inertial scale, the frozen-in condition is totally broken. There exists a thin current sheet on the order of the electron inertial scale c/ω_{pe}, but the thin width implies that the out of plane current contribution is very small. On the other hand, although the ion current is much smaller, it exists over a larger area of width $2c/\omega_{pi}$. The morphology of the fields therefore occur at these scales. Simulations of collisionless reconnection also indicate that this does in fact happen [48].

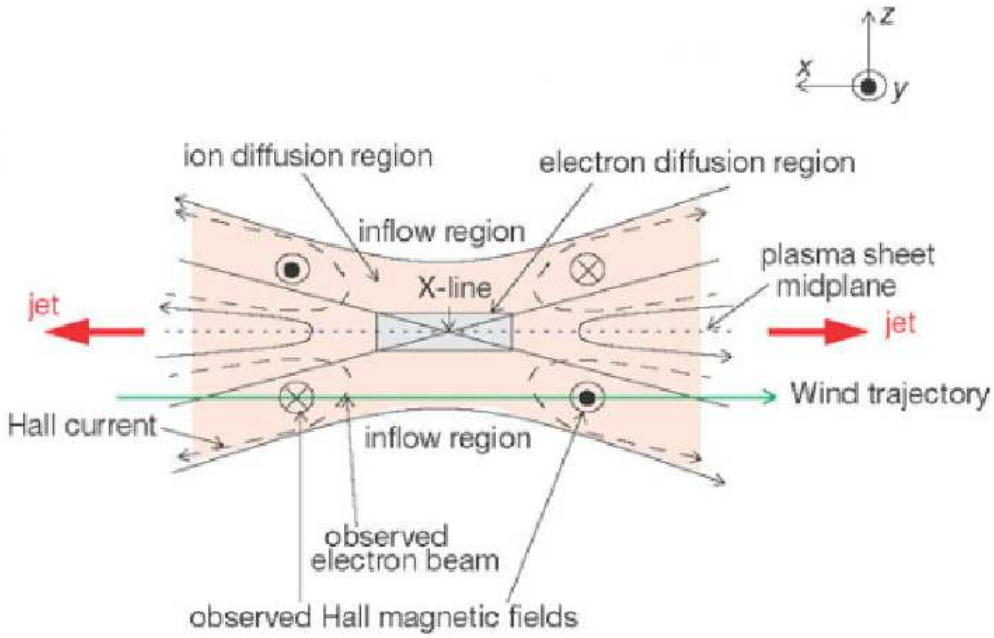

Fig. 2.8: Geometry of collisionless reconnection with the depiction of ion and electron diffusion regions (δ_i and δ_e, respectively). Electron diffusion length is smaller than that of an ion (because of its mass) and the demagnetization occurs over smaller scales. Courtesy: Oieroset et al. [4].

Chapter 3

Charged Particle Motion in Electric and Magnetic Fields

3.1 Single Particle Motion

It is known that a charged particle experiences a force while going through electric and magnetic fields. This force is called the Lorentz force and can be mathematically written as

$$\vec{F} = q(\vec{E}(\vec{r}) + \vec{v} \times \vec{B}(\vec{r})), \tag{3.1}$$

where $\vec{E}$, $\vec{B}$, and $\vec{v}$ are the external electric and magnetic fields (which might be spatially inhomogeneous and hence the $\vec{r}$ dependence) and the particle velocity. In absence of electric field, a particle gyrates around the magnetic field. The frequency, frequently called the gyro frequency ($\frac{qB}{m}$) is the angular frequency of the particle in the plane perpendicular to the magnetic field. When an electric field is imposed, the particle along with gyrating drifts in a direction perpendicular to both electric and magnetic field (fig. 3.1), called the $E \times B$ drift. When the magnetic field varies slowly over a gyro radius (the ratio of perpendicular particle velocity to the gyro frequency), a particle can also experience a gradient drift. In the presence of curvatures in field lines [31], a curvature drift also appears. In practical situations, the magnetic field always has a curvature and gradient with the added electric fields. As a result, a charged particle experiences all types of drifts as it moves along the magnetic field. An example of combination of such drifts can be seen in the Earth's magnetic field in the inner magnetosphere where the field structure is dipolar and has not been stretched by the solar wind. As seen in figs. 3.2(a) and 3.2(b), a charged particle exhibits three motions, gyration around a field line, bounce motion about the mirror points where the magnetic field is strong enough to reflect the particle, and East West drift which produces the ring current. Proton trajectory in 3D and in the equatorial plane are plotted

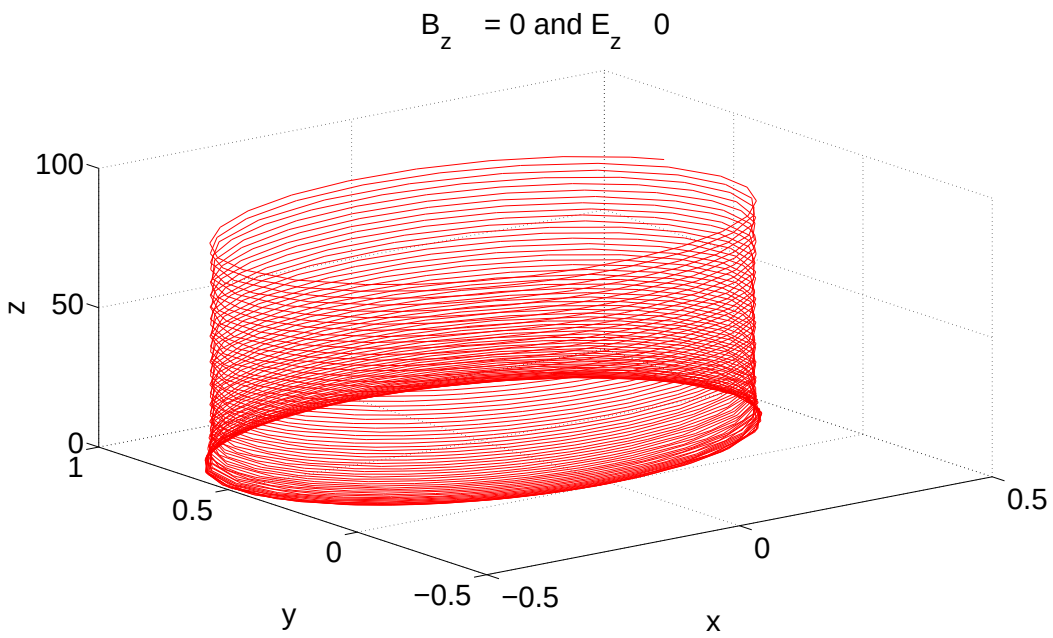

Fig. 3.1: Gyration and drift of a charged particle in a static electric and magnetic field. Magnetic field was taken to be along the z direction with no electric field. The Newton-Lorentz system was solved using Matlab ODE solver and the charged particle (proton) trajectory was plotted after a few gyration periods. The particle gyrates around the magnetic field and makes a helical pattern because of nonzero initial parallel velocity.

in figs. 3.2(c) and 3.2(d). When a fast motion like that of a gyrating particle is accompanied by slower motion such as bounce between the mirror points, invariants of the motion can be found. These are called the adiabatic invariants and remain approximately constant for a slowly varying field. Such approximation is valid when the length scale of the field variation L is very large compared to the gyro radius. It will be seen in section 2.3, such an approximation is broken in a current sheet where the particle can exhibit transient nongyrating orbits. With the field variation on a scale very large compared to particle gyro radius, a further improvement in simulating charged particles in spatially varying magnetic fields can be made. This approximation is called the Guiding Center Motion (section 3.2).

3.2 Guiding Center Motion

In previous Chapters, it was seen that the Earth's magnetic field is dipolar and that the solar wind drags the field on the nightside and compresses it on the dayside so that

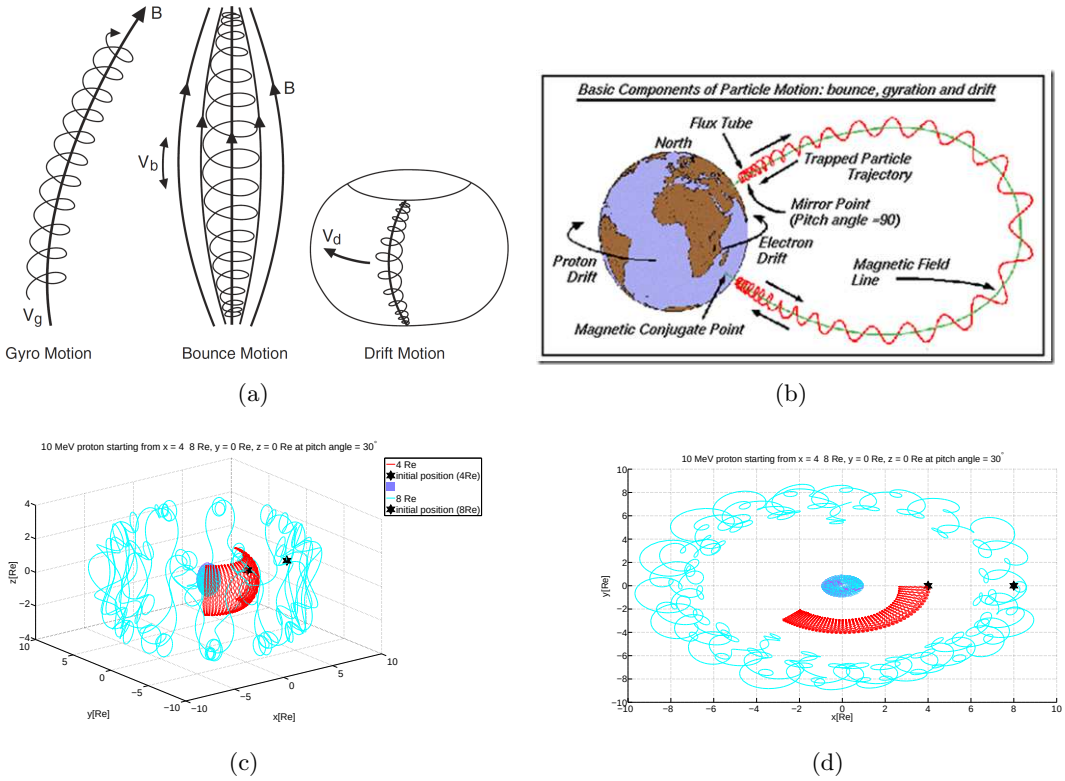

Fig. 3.2: Three types of motion of a charged particle in a dipolar magnetic field. Figures 3.2(a) and 3.2(b) show the three types of adiabatically invariant motions, gyration transverse to a magnetic field line, bounce motion between mirror points, and azimuthal drift due to curvature in the field lines. Figures 3.2(c) and 3.2(d) show the trajectory of a 10 MeV proton which was started of at $x = 4$ and 8 R_E (Earth radius) denoted by a black stars. The plots were generated by solving the Newton-Lorentz system with a dipolar magnetic field (eq. (3.5)). After solving the equations for a few hundred gyrations, the coordinate solutions were plotted using plot3 command.

after a few Earth radii (R_E), the field is no more dipolar. In this section, charged particle motion in the dipole field lines close to the Earth ($\approx 3 - 4\ R_E$) is discussed. Located on these closed field lines are the Van Allen radiation belts where particles can be energized to energies very close to MeVs (fig. 3.3). Such particles can only escape the magnetic field when they interact with waves (wave-particle interaction) that can send them plummeting into the high latitude polar ionosphere to form the diffuse aurora. Hence, the interaction that produces this feature is more subtle and involves the combined magnetic fields of the Sun and the Earth to trap and accelerate the particles.

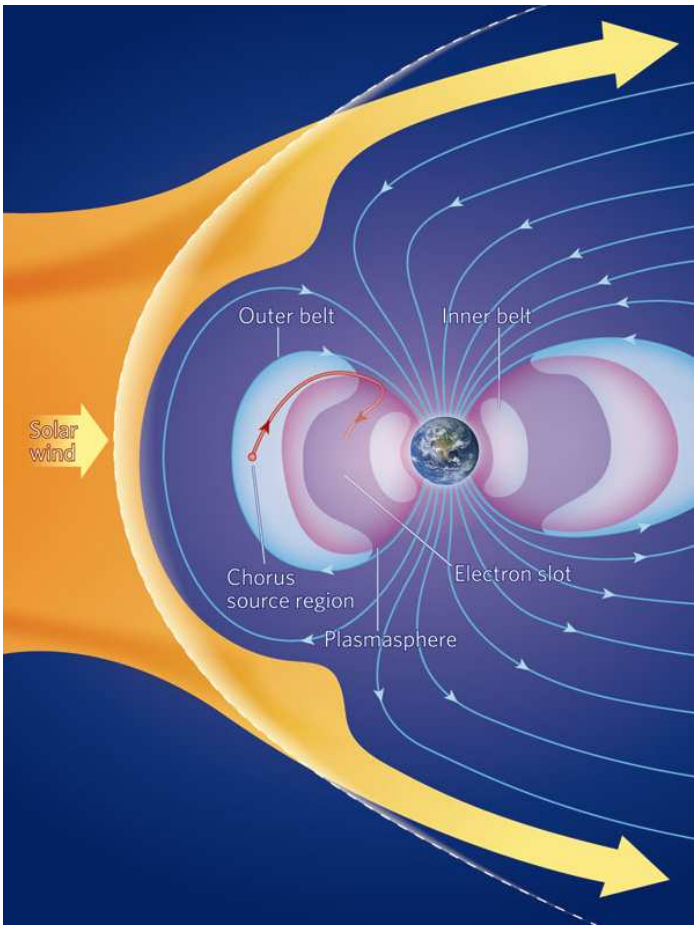

Fig. 3.3: Van Allen radiation belts which are located in the dipole field lines. Charged particles trapped on these field lines can wreck havoc on satellites and are potential health hazards for astronauts. Courtesy: `http://www.universetoday.com/60674/`.

3.2.1 Charged Particle Dynamics in Dipolar Fields

Particle behavior in electric and magnetic fields can be studied by using Newton's equation of motion with the acceleration provided by the electric and magnetic fields. This will eventually lead to bulk drift as shown in fig. 3.4. Mathematically for a particle of mass m and charge q the equation is written as [44]

$$m\frac{d\vec{v}}{dt} = \vec{F}, \tag{3.2}$$

where $\vec{F}$ is given by eq. (3.1). It is assumed that the particle velocity is nonrelativistic (in that case the Lorentz factor, $\gamma = 1/\sqrt{(1 - v^2/c^2)}$ would have been multiplied into the left

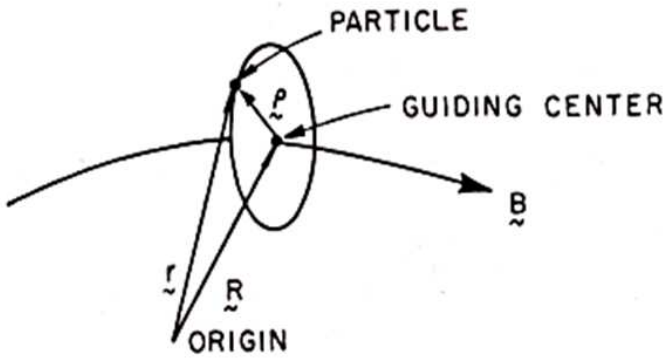

Fig. 3.4: The figure used to illustrate the vector addition $\vec{r} = \vec{R} + \vec{\rho}$ associated with gyro motion and the guiding center approximation [5].

hand side in the differential operator). Time dependence on fields requires that one uses a self-consistent simulation such as Particle in Cell or a hybrid code which further complicates the situation since the self-fields produced by the particle can cause other effects to creep in. As seen in fig. 3.1, if the fields are spatially uniform, the particle executes helical motion. This gyration has a frequency of $\Omega = qB/m$ and a radius of gyration $\rho = v_\perp/\Omega$, where $v_\perp$ is the velocity perpendicular to the magnetic field. It can be seen that an addition of electric field parallel to the magnetic field ($E_{||}$) will cause the particle to accelerate in the direction of the magnetic field removing the particle from the region. This implies that trapped particles inside the Van Allen belts experience negligible $E_{||}$, and hence the name trapped. A perpendicular electric field will on the other hand cause the particle to drift slowly perpendicular to both the electric and magnetic field called the E cross B drift. This can be seen neglecting the left hand side of eq. (3.2) as this produces fast gyro motion, and taking the cross product of the remaining equation with $\vec{B}$ to get the $\vec{E} \times \vec{B}$ drift as [41, 43, 44]

$$\vec{v}_{E\times B} = \frac{\vec{E} \times \vec{B}}{B^2}. \tag{3.3}$$

This drift is independent of charge and mass, and all types of charged particles will experience the same amount of drift. As mentioned before, the averaging over particle gyro radius will lead to faster simulation and lead to fig. 3.5. This guiding center drift will be discussed in detail in subsection 3.2.3.

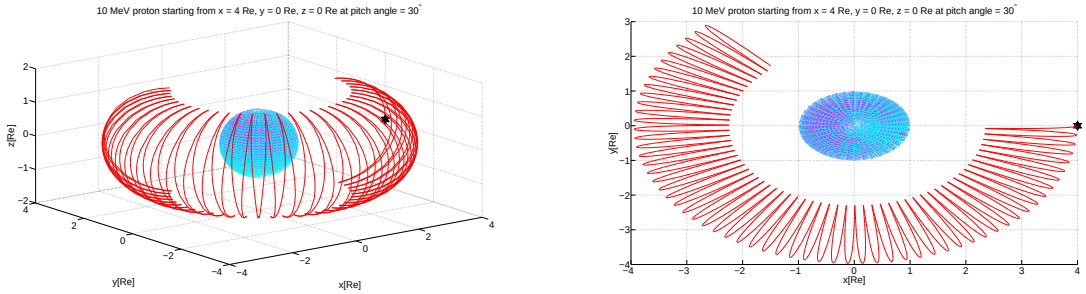

(a) (b)

Fig. 3.5: Guiding center approximation to the Newton-Lorentz equation. Figures 3.5(a) and 3.5(b) show the trajectory of a 10 MeV proton which was started of at $x = 4\ R_E$ (Earth radius) denoted by a black star. Instead of integrating the full Newton-Lorentz set of ODEs, which in turn need a small enough timestep to account for the fast gyrations around the magnetic field, eqs. (3.23) and (3.24) are solved. Since we are not concerned with the individual particle motion, and only in the average slow drift, these equations can be integrated quickly to yield the slower motions, viz., bounce between mirror points and azimuthal drift. The equations were solved in Matlab using ODE solver and the spatial coordinates were plotted after a few hundred timesteps.

The magnetic field generated by a dipole with a magnetic moment $\vec{M}$ Am^2 located at $\vec{r}$ can be written as [49]

$$\vec{B}(\vec{r}) = \frac{\mu_0}{4\pi r^3}\left[3(\vec{M}\cdot\hat{r})\hat{r} - \vec{M}\right], \tag{3.4}$$

where $\vec{r} = x\hat{x} + y\hat{y} + z\hat{z}$, $r = |\vec{r}|$, and $\hat{r}$ is the unit vector pointing in the direction $\vec{r}$. For Earth, since the geographic poles are of opposite polarity to the magnetic poles, $\vec{M} = -M\hat{z}$.

Using R_E as units of spatial measurement, at the equator $(x = R_E, y = 0, z = 0)$, the magnetic field measured is $B_0 \approx 3 \times 10^{-5}$T. The factor $\mu_0 M/4\pi$ can be written as $B_0\ R_E^3$. Then in Cartesian coordinates we can write the field as [43, 50]

$$\vec{B} = -\frac{B_0 R_E^3}{r^5}\left[3z(x\hat{x} + y\hat{y}) + (2z^2 - x^2 - y^2)\hat{z}\right]. \tag{3.5}$$

Using eqs. (3.2) and (3.5), a proton was simulated starting at the equator on [4 R_E,0,0] and [8 R_E,0,0] with the same energy, same pitch angle, and for the same time. As seen in figs. 3.2(c) and 3.2(d), the proton moves in a helical trajectory (not the case for reversed field seen in fig. 3.6) with two other periodic (of very large period) motions called the bounce

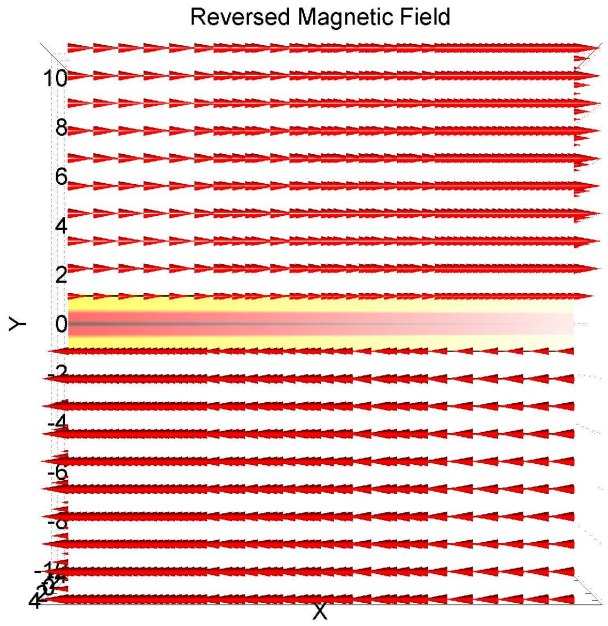

Fig. 3.6: Reversed magnetic field with color showing the magnetic field intensity. In the center lies a current sheet where the magnetic topology reverses in polarity. Equation (3.29) was used as an input into the Matlab streamline function to plot streamlines of the field. The coordinate y would be z in magnetospheric coordinates (GSM). The colorbar represents the magnetic field intensity which is the weakest in the current sheet.

and drift motion. These motions are slow compared to the gyro motion of the particle which leads to them being not a Constant of Motion (COM) (section 3.3) but an adiabatic invariant. This invariance resulted from the fact that these slow motions were superimposed on a very fast oscillation. In other words, when the scale length of the system is very large compared to the spatial scales of dynamics, there are adiabatic invariants in the system.

The bounce motion leads the particle being trapped in the field lines with bounce action occurring close to where the field strength is strong. The drift occurs across the field lines and as seen in fig. 3.2(d), a particle in weak field (8 R_E) (since dipole field reduces by $1/R_E^3$) drifts faster than the one closer to the stronger field (4 R_E).

3.2.2 Adiabatic Invariants

If the spatial and temporal scales of a system vary slowly compared to the frequencies of oscillation, there exist adiabatic invariants in the system [51]. The invariant in Hamiltonian

dynamics (section 3.3) can be written as the action [43, 51]

$$J = \oint_{H=E} p \cdot \dot{q}, \tag{3.6}$$

where q, p are the generalized coordinate and momentum with the integral performed over a cycle on a given energy shell ($H = E$). Three adiabatic invariants exist for the motion of a charged particle in a dipole magnetic field. The total canonical momentum for the system is $m\vec{v}_q\vec{A}$, $\vec{A}$ being the vector potential due to the magnetic field. The first invariant due to gyro motion J_1 can be obtained as [43]

$$J_1 = \oint (m\vec{v} + q\vec{A}) \cdot \vec{dl}, \tag{3.7}$$

$\vec{dl}$ being a differential element of the trajectory. Using Stokes' Theorem, we get

$$\oint q\vec{A} \cdot \vec{dl} = \int q\nabla \times \vec{A} \cdot d\vec{\sigma}, \tag{3.8}$$

where the area integral on the right hand side is taken over the closed path of left hand side. By using the identity $\vec{B} = \vec{\nabla} \times \vec{A}$, J_1 can be simplified as

$$J_1 = 2\pi\rho m v_\perp - q\pi\rho^2 B, \tag{3.9}$$

$$= \frac{\pi m^2 v_\perp^2}{qB}, \tag{3.10}$$

ρ being the gyro radius, and hence the path length and area covered in one gyro period is $2\pi\rho$ and $\pi\rho^2$, respectively. Also, over the period, $\vec{B}$ is assumed to be constant and since the particle gyrates in a sense that opposes the external field, a negative sign appears before the second expression. Equation (3.10) apart from some constant factors is the magnetic moment $\mu = mv_\perp^2/2B$. It is the moment of the current generated by a gyrating particle.

The adiabatic invariance of μ leads to the existence of mirror points. As the particle approaches region of strong magnetic field (poles in the dipolar field), in order to keep μ invariant, the $v_\perp$ should also increase. But the total energy of the particle is bounded since

$v_\perp = 2m\sqrt{E - mv_{||}^2/2}$ and its maximum value is when $v_{||}$ or the velocity parallel to the magnetic field is zero. This point is the mirror point and the particle is said to bounce back.

The second invariant is associated with the bounce motion between the mirror points. The action parallel to the magnetic field is [43, 44, 52]

$$J_2 = \oint [\vec{p} + q\vec{A}] \cdot \vec{dl}, \tag{3.11}$$

$$= \oint \vec{p} \cdot \vec{dl}, \tag{3.12}$$

$$= \oint p_{||} ds, \tag{3.13}$$

$p_{||}$ being the momentum parallel to the field. $\vec{A}$ does not contribute to the integral as no flux is closed parallel to the magnetic field. Using the pitch angle, $p_{||} = mv\cos(\alpha)$. Using the fact that the magnetic moment remains constant along a field line so that the pitch angle varies to 90° at the mirror point, we can get the invariant as

$$I = \frac{J_2}{2mv} = \frac{1}{2}\oint \sqrt{1 - \frac{B(s)}{B_m}} ds, \tag{3.14}$$

where B_m is the magnetic field strength at the mirror point.

The third invariant is associated with the slow azimuthal drift (drift in the xy plane for the dipole field). This can be formulated as the action

$$J_3 = \oint (m\vec{v} + q\vec{A}) \cdot \vec{dl}, \tag{3.15}$$

$$= \oint q\vec{A} \cdot \vec{dl}, \tag{3.16}$$

where p along $\vec{dl}$ is assumed negligible owing to the slow drift velocity [5]. Using Stokes' theorem eq. (3.16) is reduced to

$$J_3 = q \oint \vec{B} \cdot \vec{ds} = q\Phi, \tag{3.17}$$

where Φ is the flux enclosed in the azimuthal direction.

3.2.3 Guiding Center Formulation

Guiding center is the center of the gyro motion. It moves with constant velocity in uniform magnetic field. It lends itself well to the visualization and quick calculation of the average motion of the particle. For numerical calculations, the time step needs to be a fraction of the fastest time scale which is the gyro period for the present case. For lighter particles such as electrons, this can get very small implying that the simulation takes a long time to complete. The main assumption for such a formulation is that the magnetic field should vary slowly on the spatial scale of gyro radius [43, 52], i.e.,

$$\rho << \frac{|\vec{B}|}{|\delta B|}. \tag{3.18}$$

Following Northrop [5], the motion of the guiding center can be accounted by substituting for the particle position $\vec{r}$ by $\vec{r} = \vec{R} + \vec{\rho}$ and Taylor expanding the magnetic field about the guiding center $\vec{R}$ (under the assumption)

$$\vec{R} >> \vec{\rho}, \tag{3.19}$$

(see fig. 3.4), we get

$$\vec{B}(\vec{r}) = \vec{B}(\vec{R}) + (\vec{\rho} \cdot \vec{\nabla})\vec{B}. \tag{3.20}$$

Noting that $\vec{\rho} = \hat{i} \sin\phi + \hat{j} \cos\phi$ for magnetic field in z direction (ϕ is the gyro phase), averaging over the gyro motion, and noting that $\langle\vec{\rho}\rangle = \langle\dot{\vec{\rho}}\rangle = \langle\ddot{\vec{\rho}}\rangle = 0$ gives [5, 52]

$$\ddot{\vec{R}} = \frac{q}{m}\left(\dot{\vec{R}} \times \vec{B}(\vec{R})\right) - \frac{\mu}{m}\vec{\nabla}\vec{B}(\vec{R}). \tag{3.21}$$

Motion parallel to the magnetic field can be found by taking the dot product of eq. (3.21) with the magnetic field unit vector $\hat{b}$. The first term on the right side vanishes and the remaining equation is given by [52]

$$\ddot{\vec{R}}_{||} = -\frac{\mu}{m}\hat{b} \cdot \vec{\nabla}\vec{B}, \tag{3.22}$$

which simplifies to

$$\frac{dv_{||}}{dt} = \frac{d^2 s_{||}}{dt^2} = -\frac{\mu}{m}\frac{\partial B(s)}{\partial s}, \tag{3.23}$$

where s is the distance along a magnetic field line. As mentioned before, this is the bounce motion between the mirror points with the right side acting as a potential along the field lines, the negative sign indicating acceleration in weaker fields and vice versa. Similarly, perpendicular to the field, the drift is given by [5, 52]

$$\vec{R_\perp} = \frac{m}{qB^2}\vec{B} \times \vec{\dot{R}} + \frac{\mu}{qB^2}\vec{B} \times \vec{\nabla}\vec{B}. \tag{3.24}$$

The terms on the right hand side pertain to curvature and gradient drifts, respectively. Charge dependence in these drifts implies that oppositely charged particles will create currents, for example the ring current (fig. 1.3).

Under such approximations, the trajectories in fig. 3.2 with this approximation were simulated and are shown in fig. 3.5 (figs. 3.5(a) and 3.5(b) are the same orbit viewed in 3D and equatorial plane, respectively). It should be noted that this approximation is valid only under the condition $\vec{R} \gg \vec{\rho}$. In presence of magnetic null or weak magnetic field (as seen in Chapter 2), this approximation is not valid. Even for a highly energetic particles, the Larmor radius might become comparable or larger than the length scale of the magnetic field in which case the guiding center approximation is again invalidated.

3.3 Hamiltonian Dynamics, Constants of Motion, and Integrability

In classical mechanics, majority of systems can be classified into two categories, Hamiltonian and dissipative systems. Loosely speaking, suppose that $H(\vec{q}, \vec{p})$ is a smooth function of the generalized coordinates ($\vec{q}$) and their conjugate momenta ($\vec{p}$). Then we can define a Hamiltonian system as

$$\dot{q}_i = \frac{\partial H}{\partial p_i}, \tag{3.25a}$$

$$\dot{p}_i = -\frac{\partial H}{\partial q_i}, \tag{3.25b}$$

$i = 1, 2, ..., N$ being the the number of degrees of freedom. The dimension of state space is said to be $2N$. A COM is some quantity that is conserved throughout the dynamics of a system, which constrains the motion of the system. For example, the Hamiltonian is a COM which can be proved by taking the time derivative of the Hamiltonian (and noting that $\vec{p}$ and $\vec{q}$ are functions of time), we get

$$\begin{aligned} \dot{H} &= \sum_{i=1}^{n} \frac{\partial H}{\partial q_i}\dot{q}_i + \frac{\partial H}{\partial p_i}\dot{p}_i, \\ &= \sum_{i=1}^{n} \frac{\partial H}{\partial q_i}\frac{\partial H}{\partial p_i} - \frac{\partial H}{\partial p_i}\frac{\partial H}{\partial q_i} = 0, \end{aligned} \tag{3.26}$$

where eqs. (3.25b) and (3.25b) were used in the second step.

For mechanical systems, the Hamiltonian is also called the total energy of the system. The Hamiltonian is a conserved quantity for closed (no external forcing) systems. A very simple example is that of a mechanical spring as a 1D harmonic oscillator which has one degree of freedom (dof). A dof is the number of pairs of $[q, p]$. The Hamiltonian of the system can be written as

$$H(q, p) = \frac{1}{2}kq^2 + \frac{p^2}{2m}, \tag{3.27}$$

where q, p are the generalized coordinate and corresponding conjugate momentum. Since the Hamiltonian is a COM for the system, fixing it initially will essentially restrict the motion of the oscillator to a given energy shell and the curves in phase space (q, p space) will be closed. As a general rule for integrability, a system is said to be integrable if it has COMs equal to the number of degrees of freedom. For the simple harmonic oscillator, this is the case since dof is one and so is COM which the Hamiltonian itself. In general for N dofs, their must be N COMs but for integrability, these constants should also be in involution, meaning that they should commute with regards to the Poisson bracket which is written for two COMs say A and B (which are functions of generalized coordinates and momenta) as

$$A, B = \sum_i \left[\frac{\partial A}{\partial q_i}\frac{\partial B}{\partial p_i} - \frac{\partial A}{\partial p_i}\frac{\partial B}{\partial q_i}\right] = 0. \tag{3.28}$$

The independent constants of motion restrict an integrable system on an N dimension surface in the phase space. For integrable systems, a transformation called the canonical transformation can then be used to change variables from the generalized coordinates and momenta to $action - angle$ variables. In such coordinates, the actions are constants, and the angles just depend on time. This can be visualized as actions being some constant radii of an N dimension torii and the angles being the frequency of oscillation around the N coordinates multiplied by time. Hence, this surface is topologically equivalent to an N dimension torus. The above equation just means that A and B are actual COMs and that A is not some combination of B in which case the right hand side would not have been zero.

3.4 Example: Reversed Magnetic Field (Harris Sheet)

The analysis done in the previous section can be applied to a current sheet. Figure 3.6 shows a magnetic field that reverses in the mid plane (close to $y = 0$). Mathematically, this can be written as (locally would be a linear approximation or the first term of the Taylor series but here it is valid for the whole domain)

$$B_x = tanh(y/L) \approx \frac{y}{L}, \tag{3.29}$$

to account for the variations in the y direction and

$$B_y = 0, \tag{3.30}$$

$$B_z = 0. \tag{3.31}$$

The Hamiltonian for this system can be written as

$$H = \frac{(\vec{p} - q\vec{A}) \cdot (\vec{p} - q\vec{A})}{2m}, \tag{3.32}$$

where q and $\vec{A}$ are the charge on the particle and the magnetic vector potential of the system. We have not considered electric fields which if included will lead to addition of scalar potential to the Hamiltonian. Also, the electric field is assumed homogeneous throughout

the domain. For the magnetic field model of a modified Harris sheet (without the addition of a small B_z) given by eq. (3.29), $\vec{A} = A_z[y^2/2L]$, and hence the Hamiltonian can be written as

$$H(y, p_x, p_y, p_z) = \frac{p_x^2}{2m} + \frac{p_y^2}{2m} + \frac{(p_z - \frac{qy^2}{2})^2}{2m}, \tag{3.33}$$

which indicates that for the system which has three dofs, we have p_x, p_z, and H as the COMs. It can be shown that the these COMs are in involution which makes this problem integrable. When one cannot find sufficient COMs, the system is said to behave in a very unpredictable fashion. Chaos is the study of such systems.

3.5 Chaos

Chaos with regards to dynamical systems refers to the sensitive dependence on initial conditions. Also known as the butterfly effect, if two initial conditions which start off very close to each other, diverge after certain time. This can be understood from the famous Lorenz model proposed by Edward Lorenz in 1963. He was studying the convection in the atmosphere with a set of three coupled first order differential equations which read as

$$\begin{aligned} \frac{dx}{dt} &= \sigma(y - x), \\ \frac{dy}{dt} &= x(\rho - z) - y, \\ \frac{dz}{dt} &= xy - \beta z, \end{aligned} \tag{3.34}$$

where x, y, and z are the so called phase space variables with σ, ρ, and β being the system parameters. Physically x is the convective flow, y is the horizontal temperature distribution, and z is the vertical temperature distribution and the parameters are σ is the ratio of viscosity to thermal conductivity, ρ is the temperature difference between the top and bottom of the slice, and β is the width to height ratio of the slice. The system is a complex nonlinear dynamical system since the evolution of the phase space vector ($\mathbf{x} = [xyz]^T$) depends nonlinearly on the variable values in previous time step and three parameters. To find the sensitive dependence on initial conditions, the parameters σ and β are fixed at 10

and 8/3 and the last parameter ρ is varied to study chaos. At $\rho = 28$, it is found that the system has a chaotic solution which is depicted in fig. 3.7. As seen in the figure, after a certain time, the two solutions which started out mimicking each other diverge and if run for a large time, will lead to a completely different solution. The difference in the initial conditions can be thought of as the uncertainty in measurements taken by the measuring device. The time evolution can be thought of as trying to predict the state of a system at a particular instant in the future. Since all measuring devices have a finite accuracy, the prediction from the two initial conditions would be rendered useless after a certain time.

Poincare surface of section (SOS) is also a tool used to study what parameters are responsible for chaos in a system. By studying the different trajectories of the respective initial conditions, a plane can be found through which all the trajectories pass. A cut of the phase space through the plane then gives a set of points as time evolves. Other tools include fractal and correlation dimension and studying the dynamics in reduced state space called iterated maps.

3.5.1 Lyapunov Exponents

Chaos can be quantified in many ways. As was discussed, two initial conditions depart after a given time for a chaotic system. This can be seen for the case of Lorenz system in the right panel of fig. 3.8. If they diverge at an exponential rate, we can define a divergence in terms of a Lyapunov exponent. Hence, after some given time two initial conditions that started infinitesimally close to each other with a separation δZ_0 will separate out at a rate given by

$$|\delta Z(t)| \approx e^{\lambda t}|\delta Z_0|, \tag{3.35}$$

with λ being the exponent. Considering the initial conditions to be distributed in an error sphere of radius ϵ, over a period of time, the sphere will morph into an ellipsoid with the length of the largest axis being the maximum rate of divergence in any direction.

Lyapunov exponents play an important role in the theory of both Hamiltonian and dissipative dynamical systems. They provide a computable, quantitative measure of the

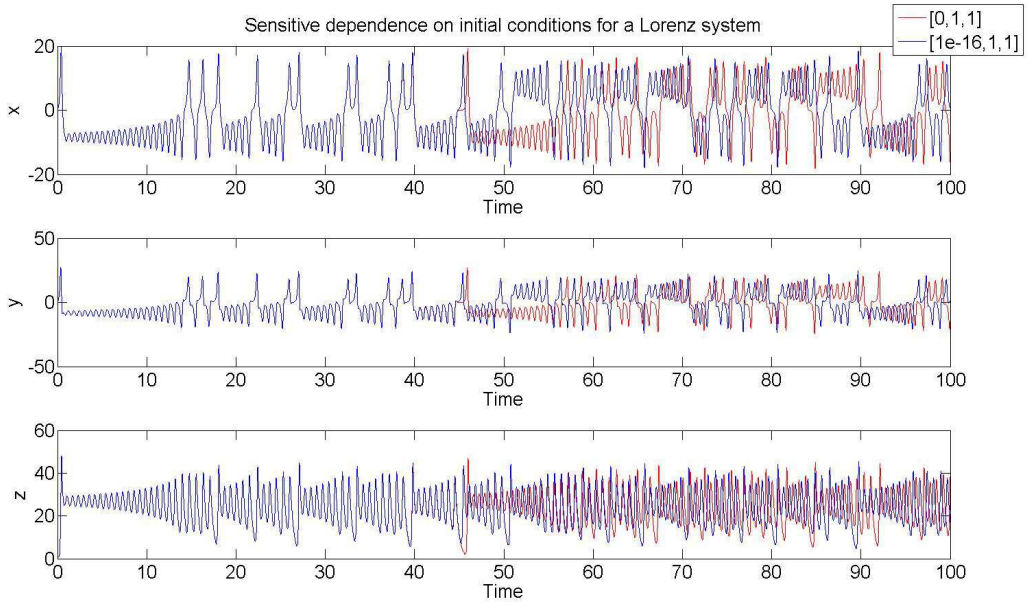

Fig. 3.7: Time series of two initial conditions (shown in the legend) implying sensitive dependence on initial conditions for the Lorenz system. As seen in the legend, a small error (see legend for values) in the initial condition which might be thought of as the resolution of a measuring instrument, results in the deviation of the two solutions after approximately 45 time steps. The plot was generated by integrating eq. (3.34) using Matlab ODE solver and the integrated solutions for the three variables were plotted using the plot command.

degree of stochasticity for a trajectory. In addition, there is a close link between Lyapunov exponents and other measures of randomness such as the Kolmogorov-Sinai entropy, correlation dimension, and the fractal dimension. The procedure for computing the Lyapunov exponents was developed by Benettin et al. [53]. We can define the Lyapunov exponents for the flow $\vec{x}(t)$ generated by the smooth vector field $\vec{f}$ in $2N+1$ (for space and momentum coordinates and possibly time if the vector field is time dependent) dimension phase space as $\frac{d\vec{x}}{dt} = \vec{f}(\vec{x}(t), t)$. For a trajectories initially started off at $\vec{x}_0$ and $\vec{x}_1$ which are $\vec{\delta}x$ apart (i.e., $|\vec{x}_0 - \vec{x}_1| = \vec{\delta}x$ called a hypersphere in phase space which can be an error hypersphere due to measured inaccuracy or due to finite number of computer bits which implies finite precision), the evolution of the this sphere is governed by

$$\frac{d\vec{\delta}x}{dt} = \vec{M}(\vec{f}(t))\vec{\delta}x, \tag{3.36}$$

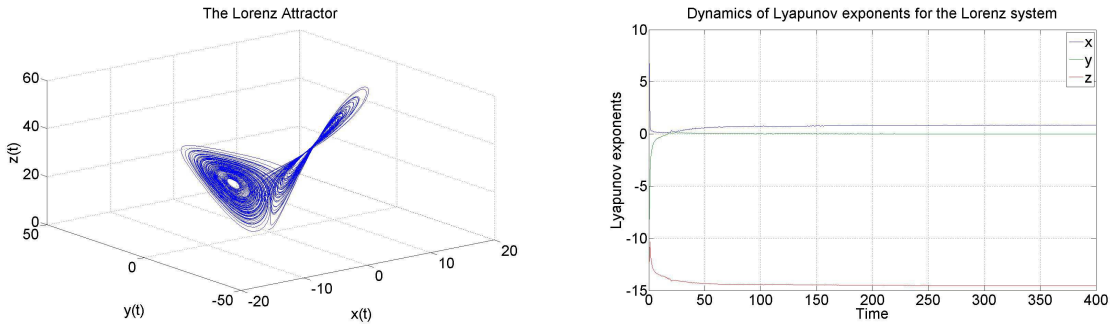

Fig. 3.8: Sample phase space trajectory and Lyapunov exponents for the Lorenz system. The solutions plotted in fig. 3.7 were used again to plot the figure in left panel using plot3 command of Matlab. The plot in the right panel was generated using the code downloaded from `http://www.math.rsu.ru/mexmat/kvm/matds/` and described in Appendix A. Lyapunov exponents in the three directions are shown and since the system is dissipative, the sum of the exponents is not zero. Also note that the presence of a positive exponent indicates the presence of chaos in the system. The exponents quantify the strength of chaos already found in fig. 3.7.

where $\vec{M}$ is the Jacobian of the vector field. As defined in eq. (3.35), a mean divergence rate between the two trajectory can be defined as

$$\lambda(\vec{x}_0, \vec{\delta x}) = \lim_{t\to\infty} \frac{1}{t} log\left(\frac{N(\vec{x}_0, t)}{N(\vec{x}_0, 0)}\right), \tag{3.37}$$

where N is an appropriate norm. For a chaotic system, at least one of the Lyapunov exponents must be positive. Also, the phase space variables determine the number of Lyapunov exponents which are three for the case of the Lorenz system. For an N^{th} order system, there are a spectrum of Lyapunov exponents which are in some increasing order with the largest being called the maximum Lyapunov exponent. For an even order system (space and velocity or momentum), the total of the Lyapunov exponents should be almost close to zero since the trajectories can be run for only a finite time. Also, because of Liouville's theorem, which states that Hamiltonian flow is incompressible, all Lyapunov exponents do not increase at the same time. The evolution occurs in such a way to conserve the phase space volume. Some directions expand while others contract in order to keep the volume constant. For dissipative systems, the volume shrinks with time and reduces to a ball of

measure zero in all directions.

3.5.2 Gram-Schmidt Orthonormalization

Calculation of Lyapunov exponent requires frequent orthonormalization as the principle axis that one starts with can increase in magnitude and rotate through time even for the linearized set (eq. (3.36)). As a result, the calculation of Lyapunov exponent needs some renormalization and reorthogonalization at some predetermined instants of time of the so called $fiducial$ trajectory in phase space as seen in fig. 3.9.

These two problems can be easily gotten rid of by the iterative use of the Gram-Schmidt reorthonormalization (GSR) procedure. Let the initial condition at $t = t_p$ for linearized eq. (3.36) be $[\vec{\delta}x_i(t_p)]$ (i being the dimension of the phase space), which is a set of orthonormal vectors spanning the surface of an infinitesimal hypersphere. The set of vectors evolve to $[\vec{\delta}x_i^{'}(t_{p+1})]$ after $t_{p+1}-t_p$ steps. After the reorthonormalization using GSR, old unnormalized and nonorthogonal set of vectors is replaced by the new set of orthonormal vectors

$$\delta x_1 = \frac{\delta x_1^{'}}{|\delta x_1^{'}|}, \tag{3.38}$$

$$\delta x_2 = \frac{\delta x_2^{'} - (\delta x_2^{'} \cdot \delta x_1)\delta x_1}{|\delta x_2^{'} \cdot \delta x_1)\delta x_1|}, \tag{3.39}$$

and so on till the i^{th} axis is orthonormalized. Each vector x_i tends to point to the direction of most rapid growth in decreasing order, and because first vector is always the basis on which other orthogonal vectors are built, this vector seeks out the most rapidly growing direction and so on. The Lyapunov exponents obtained this way are ordered from largest to smallest. As before, the sum of the Lyapunov exponents provides a time derivative of the volume of an infinitesimal phase space. While the sum of the Lyapunov exponents reduces in dissipative systems, it is preserved in conservative systems. For an autonomous (no explicit time dependence) Hamiltonian system with Hamiltonian H, we have

$$\frac{d}{dt}\begin{pmatrix}\vec{q}\\ \vec{p}\end{pmatrix} = \begin{pmatrix}\frac{\partial H}{\partial \vec{q}}\\ -\frac{\partial H}{\partial \vec{p}}\end{pmatrix}, \tag{3.40}$$

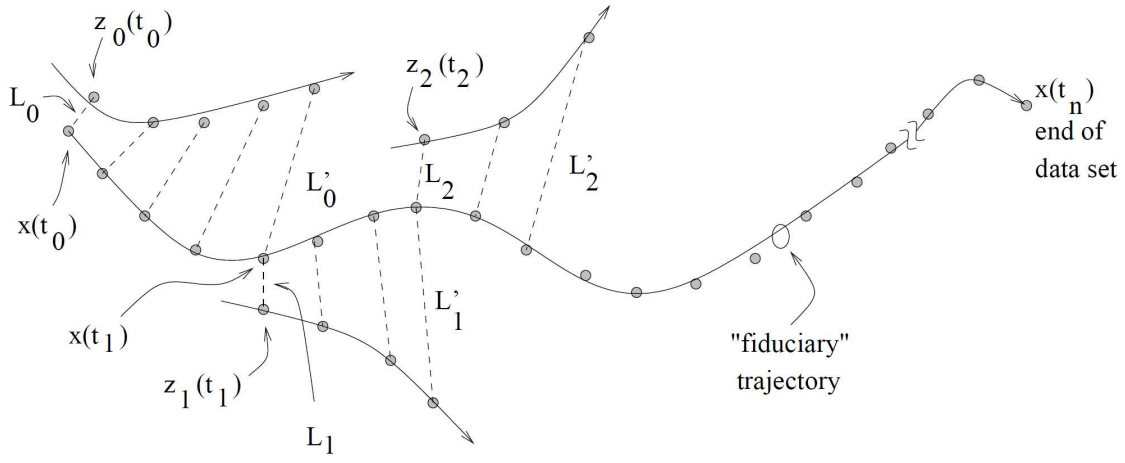

Fig. 3.9: Calculation of Lyapunov exponent according to initial condition $\vec{x}(t_0)$ and subsequent renormalization and reorthogonalization at t_1, t_2, etc. Starting with an initial condition $x(t_0)$, the set of ODEs including the variational ODEs are solved using the Matlab ODE solver. After a predetermined number of timesteps (denoted here by L_1 ...), the equations are reorthonormalized using Gram-Schimdt method and the simulation carries on for a few hundred timesteps.

q, p being the generalized coordinate and its conjugate momentum. The rate of change of the volume V in phase space can be found from the Lie derivative as

$$\frac{1}{V}\frac{dV}{dt} = \frac{\partial \dot{\vec{q}}}{\partial \vec{q}} + \frac{\partial \dot{\vec{p}}}{\partial \vec{p}} = 0. \tag{3.41}$$

As an end remark, chaos is reflected in the systems that contain at least one positive Lyapunov exponent.

3.5.3 Surface of Section (SOS)

Numerical calculation of the time evolution of a dynamical system is just the first step towards understanding that system. A qualitative understanding can yield important insights of the motion. For given system, instead of looking at hundreds of thousands of phase space trajectories, by throwing away virtually all but some calculated information about the trajectory, we can gain information about its evolution and its relation to other

trajectories. One such tool that extracts the essence by throwing away information is called the Poincare SOS. A SOS can be generated by recording successive intersections of a set of trajectories with a given predetermined plane in the phase space. The plane is spanned by a coordinate axis and the canonically conjugate momentum axis. Many important properties of an SOS make it an important tool in the analysis of a dynamical system.

The SOS technique was used to good measure in the 1964 landmark paper by astronomers Michel Henon and Carl Heiles. They found that trajectories behaved in a manner dependent on where they were started in the phase space. Some trajectories were chaotic, whereas other trajectories were regular. An essential characteristic of the chaotic motion is that initially nearby trajectories separate exponentially with time (section 6.2) while regular trajectories separate linearly. They observed that these two types of trajectories were clustered in the phase space into regions of regular motion and ocean of chaotic motion.

The phase plane chosen for SOS should be such that most of the trajectories should intersect with it in transverse direction as seen in fig. 3.10. For example say we have a Hamiltonian given by

$$H(\vec{q},\vec{p}) = \frac{1}{2}(p_x^2 + p_y^2) + \phi(x,y), \tag{3.42}$$

which has two dofs, mass is normalized to 1, and ϕ is some general potential in the system. Hamiltonian being one of the COMs implies that a given value $H = E$ restricts the motion to from a 4D to 3D hyper space which can be understood as the intersection of the energy surface E with the 4D phase space. Let it be called D_3. Lets assume that most of the trajectories intersect the $y = 0$ plane and that we record the crossing when $\dot{y} > 0$ to remove the crossing with oppositely directed velocity as shown in fig. 3.11. We can then construct an SOS for the system by recording when the trajectories intersect the $y = 0$ plane and also the value of x, p_x at the time. After many such trajectories are run through for a sufficient time periods, the accumulated points show regions of transient, periodic, quasi-periodic, and chaotic orbits. This tool, although does not quantify chaos, can be a very useful indicator of the behavior of the system in phase space where it can be ergodic for much of the space but only in a few places is it integrable. An example of a driven pendulum will illustrate

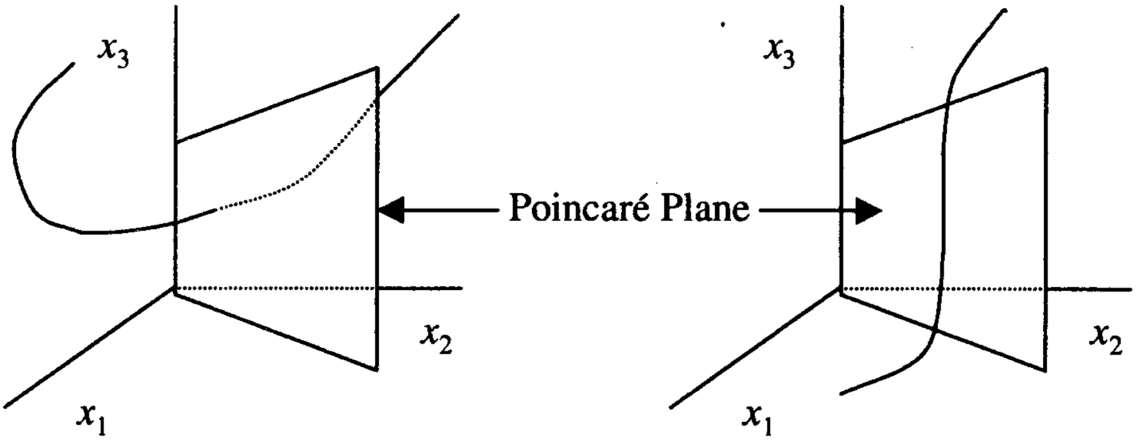

Fig. 3.10: Selecting a suitable plane in a 3D phase space to build a SOS. The phase space trajectory which is the solution to the set of ODE equations, should intersect the plane which is to be chosen as the plane on which the values of other phase space of the reduced set (see Appendix A) are to be saved. The left plane is fine for an SOS but the right one is not since it runs parallel to the trajectory.

the procedure.

3.5.4 Simple Pendulum with External Driving and Dissipation

For a given simples pendulum shown in fig. 3.12 and Table 3.1, which is being driven by a harmonic external driving, the equation of motion can be written as

$$\frac{d^2\theta}{dt^2} = -\frac{g}{l}\sin(\theta) - F_v\frac{d\theta}{dt} + F_d\sin(\omega_d t), \tag{3.43}$$

where as shown in fig. 3.12, θ is the angular displacement from the vertical, l is the length of the pendulum, g the acceleration due to gravity, F_v is the viscous damping force amplitude (force modeled as proportional to angular velocity), and ω_d is the frequency of external driving. As the differential equation has $\sin(\theta)$, the problem is highly nonlinear. Normalizing the equation to ω_d, we get

$$\frac{d^2\theta}{dt^2} = -\omega^2\sin(\theta) - f_v\frac{d\theta}{dt} + f_d\sin(t), \tag{3.44}$$

where $\omega^2 = g/l\omega_d^2$, $f_v = F_v/\omega_d$, and $f_d = F_d/\omega_d^2$, respectively. Reducing the number of

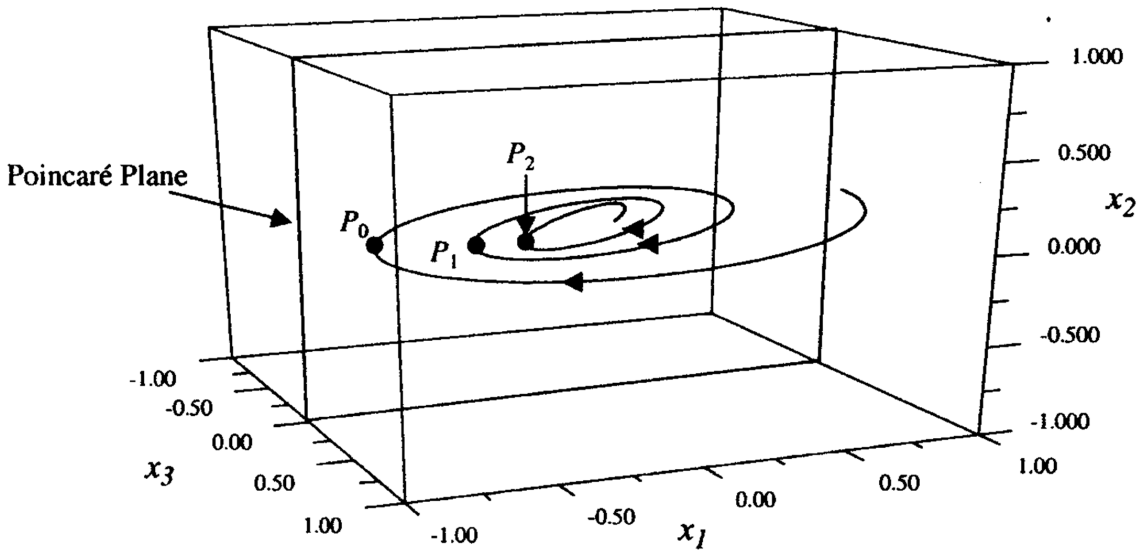

Fig. 3.11: Section through a 3D phase space with the crossing of a trajectory recorded when it crosses the $x_3 = 0$ plane. As the solution evolves with given initial conditions, the trajectory can be seen to intersect the plane $x_3 = 0$ at $P_0, P_1 \ldots$.

free parameters, we analyze what happens when the amplitude of the external force f_d is changed keeping other two constant. With different values of f_d, the solution is shown in figs. 3.13(a)-3.13(i). The motion is periodic for such values of the forcing amplitude. But when the amplitude is increased further to 2.7, the motion becomes chaotic which can be seen in figs. 3.14(a) and 3.14(b). Hence, periodic orbits will show up as a set of finite points on the section and a chaotic orbit will have an infinite set of points (when run for a long time), with self-similar structure. As will be seen in subsection 3.6.2, new orbits can be found such as quasi-periodic and transient which are a result of an interaction between two frequencies on fast and slow scales.

3.6 Sample Particle Trajectories in Parabolic Field

3.6.1 Normalization

While numbers with units are easy to comprehend and make sense of, at times while modeling physical phenomena, these numbers can become too small or too large. Computers

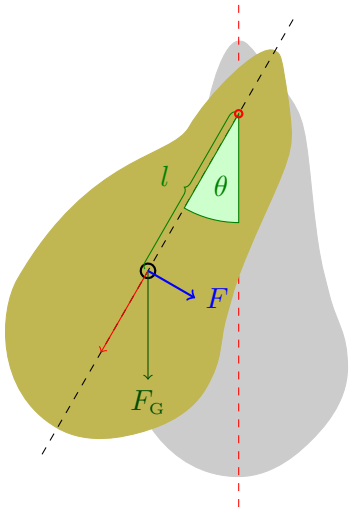

Fig. 3.12: A simple pendulum of length l and mass m displaced at an angle of θ from the vertical.

are notorious with such numbers with regards to rounding off errors. To mitigate such errors and to make a code more efficient, equations to be modeled are normalized first according to temporal and spatial scales of interest along with scales at which forces act (for a magnetotail current sheet, the parameters used for normalization are indicated in Table 3.1). For the equation of motion for a charged particle in electric and magnetic fields, which can be written as

$$m\frac{d\vec{v}}{dt} = q(\vec{E} + \vec{v} \times \vec{B}), \tag{3.45}$$

$$\frac{d\vec{x}}{dt} = \vec{v}, \tag{3.46}$$

such normalizations are found as follows. Spatial scale can be taken as the inhomogeneity scale of the magnetic field. Parabolic current sheet can be used as an example.

Parabolic field structure for the magnetotail was introduced in subsection 2.3.2. Close

Table 3.1: Normalizing parameters for the parabolic current sheet.

Space	Time	Magnetic field	Charge	Mass
L Scale of Magnetic field variation	Ω_{cp}^{-1} Inverse proton cyclotron frequency	B_0 Field value at $z = L$	Z Normalized to proton charge	M Normalized to proton mass

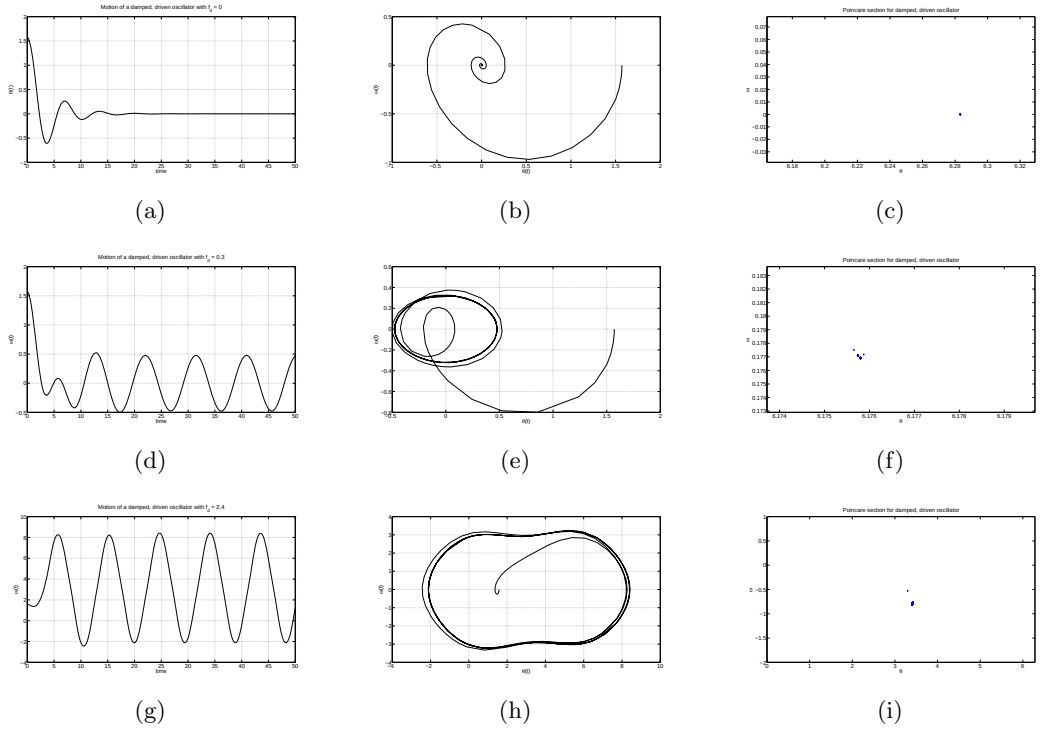

(a) (b) (c)

(d) (e) (f)

(g) (h) (i)

Fig. 3.13: Effect of external driving force amplitude on the dynamics of a damped pendulum with $f_d = 0, .3,$ and 2.4, respectively. The phase space plot in fig. 3.13(b) shows that the trajectory is attracted to point. The presence of an attractor implies that all trajectories will be in finite time attracted to it and that dissipation implies the existence of this feature. As the external force is turned on, figs. 3.13(d) and 3.13(g) show that the solution settles into a periodic motion. Figures 3.13(c), 3.13(f), and 3.13(i) are the respective Poincare SOS.

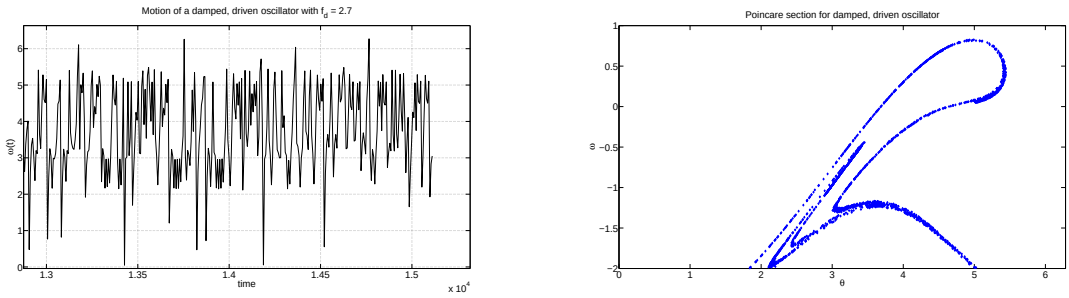

(a) (b)

Fig. 3.14: Appearance of chaos in the driven damped pendulum. Figure 3.14(a) shows the solution for the angular displacement θ (mod 2π). The Poincare section shows that the attractor does not have a random structure but self-similar structure. As seen in fig. 3.14(a), the signal appears to be highly chaotic. The system also show ergodicity in the sense that most of the phase space in fig. 3.14(b) is traversed by the trajectory. The plots were generated similarly to fig. 3.13 using Matlab and its ODE solvers.

to the current sheet (where the magnetic field magnitude goes very small (fig. 2.2)), parabolic field can be approximated *locally* by the following magnetic field configuration [32]

$$\begin{aligned} B_x &= B_0 \frac{z}{L}, \\ B_y &= 0, \\ B_z &= B_n, \end{aligned} \tag{3.47}$$

where B_0 and B_n are constants and L is the length of the field variation.

The normalization of the equations is done as follows (since computers are very bad with very small or very large numbers). The space coordinates will be normalized by L. Let time be normalized by τ. In due course of normalization, τ will be found to be equal to inverse of cyclotron frequency. With space and time normalized, the velocity can also be normalized to the ratio of L/τ. Let the mass m be normalized by Mm_p where m_p is the mass of a proton and $M = 1$ for proton. Similarly, charge q in eq. (A.6) can be normalized by Ze, Z being the charge number on the respective species. for example, for electron $Z = -1$ and for singly charged oxygen ion, $Z = 1$. Magnetic and electric fields are normalized to B_0 and $L/\tau B_0$, respectively. With these normalizations and after simplification, eq. (A.6)

reads

$$M\frac{m_p}{eB_0\tau}\frac{d\vec{v}^{\,\prime}}{dt^{\prime}} = Z(\vec{E}^{\prime} + \vec{v}^{\,\prime} \times \vec{B}^{\prime}), \tag{3.48}$$

$$\frac{d\vec{x}^{\,\prime}}{dt^{\prime}} = \vec{v}^{\,\prime}, \tag{3.49}$$

where $^{\prime}$ represents the normalized variables. The normalizing parameters are mentioned in Table 3.1.

Recognizing eB_0/m_p as proton cyclotron frequency (Ω_{cp}), $\tau = {\Omega_{cp}}^{-1}$ will simplify the differential equation even further. Such normalization reduces the number of parameters in the problem from say L, B_0, B_z etc., to just $L, b_n = B_z/B_0$. When converting back to real world units, proper scales are needed according to observations. For the case of the magnetotail, Table 3.2 shows the values of the normalizing parameters.

Sample particle trajectories and the respective SOS plots will be discussed in this section.

3.6.2 Analysis of Parabolic Sheet Dynamical System

Three types of particle orbits can be found for such a system. The trajectories are shown in fig. 3.15.

The leftmost panel of fig. 3.15 shows that for certain initial conditions, the particle oscillates between the two turning points (where the kinetic energy goes to zero) called the bounce motion while gyrating weakly around B_z. Such an orbit when seen in SOS looks like a drift ring that is the particle never comes back to the initial condition. This orbit is different from a period n orbit which would intersect the SOS plane n number of times only. The second orbit type can be called a quasi-resonant orbit since the particle comes

Table 3.2: Values for the normalizing parameters with regards to the magnetotail current sheet.

L	6400 (Km)
B_0	$3.1 \times 10^{-5}(T)$
Ω_{cp}^{-1}	$\approx 10^{-4}(s)$

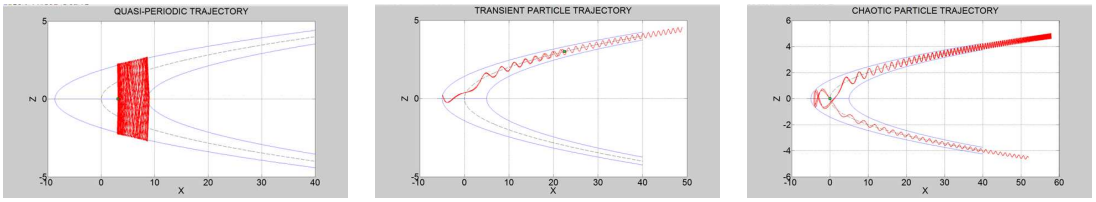

Fig. 3.15: Sample trajectories of a proton in a parabolic magnetic field with $L = 1, B_z/B_x = .2$. The leftmost panel depeicts the trajectory of a quasi-periodic orbit where the fast bounce and slow drift motions are incommensurate and the motion happens on a 2D torus. This type an orbit will be evident in the SOS plot by a circle of points. The middle panel is a plot of transient orbit because of the fact that the orbit traces back to the point where it was initially started. This type of an orbit is caused by a very large parallel velocity which leads to the particle being lost from the current sheet for a very long time. Empty spaces in a SOS plot is caused by such orbits. The last panel is of a chaotic orbit which interacts with the current sheet multiple number of times between its bounce motion between the mirror points in the lobes. This figure was obtained by plotting the solution of Newton-Lorentz system of ODEs with magnetic field given by eq. (3.47) in absence of any electric field. The result was plotted using Matlab plot command.

into the current sheet and then retraces its orbit as it moves out and never comes back to visit the neutral sheet. This happens when the particle has a sufficient velocity parallel to the asymptotic magnetic field (B_0). Of course at some point in space, the magnetic field would strong enough to mirror the particle.

Periodic, quasi-periodic, transient, and chaotic trajectories would show up as points as shown in fig. 3.16. This technique will be further explored in section 3.6. The last panel shows a chaotic orbit which starts out being adiabatic far from the neutral sheet but as the particle gets close to the neutral sheet ($z = 0$), it becomes demagnetized and exits the sheet in either direction to come back again after being mirrored far from the sheet. Figure 3.16 shows the SOS for the three trajectories. When a large number of initial conditions were tested in the harris sheet, structure could be seen in the behavior. As seen in fig. 3.17 shows that there are regions in phase space which are empty. These are the transient regions due to resonant trajectories (see middle panel of fig. 3.15) which have a very small initial pitch angle. They are reflected back after a very long time and so the phase space that they correspond to is mostly empty. Quasi-periodic initial conditions were not picked and so that region is also empty and is not due to it being another resonant region. The

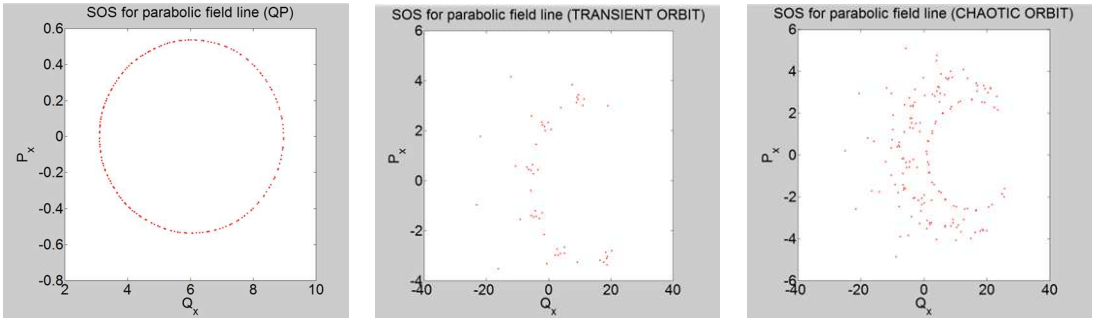

Fig. 3.16: SOS for different particle orbits for $L = 1, B_z/B_x = .2$. The different behaviors in phase space is due to the particle initial conditions being different for the three orbits. The three panels correspond to the three types of orbits found in the text and depicted in fig. 3.15. Quasi-periodic orbits turn out as bunch of points on a circle, with no point on the circle being visited more than once (incommensurate frequency ratio). Transient orbits cross the current sheet plane ($z = 0$) a finite number of times, and hence the phase space (v_x, x or p_x, q_x in generalized momentum and coordinate) is mostly empty when compared to a chaotic orbit. The figures were generated using Matlab by solving the reduced set of ODEs and plotting the coordinate x against velocity v_x when the trajectory crosses the $z = 0$ plane.

SOS for different strengths of B_z are plotted in figs. 3.18(a)-3.18(c). The SOS is regarded as a very useful tool in analyzing the nature of a nonlinear dynamical system. Without analyzing the SOS, one cannot go further in the exploration of a given nonlinear dynamical system. It does not quantify chaos but can tell important information about integrable and chaotic or ergodic parts of the phase space as seen in fig. 3.18 where the chaos parameter is b_n.

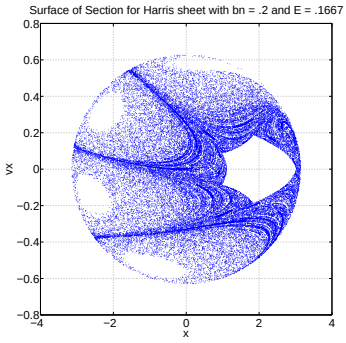

Fig. 3.17: SOS for different particle orbits for $L = 1, B_z/B_x = .2$. 4000 initial conditions with normalized energy $E = .1667$ were run with the outputs taken for when the trajectory crossed $z = 0$. As in fig. 3.16, knowing that there exist three types of orbits, 4000 initial conditions were used to evolve the reduced set of ODEs and the system was solved for a few hundred time steps (w.r.t. gyro period). The solution in x, v_x plane was plotted using Matlab. The empty four spaces around the circumference correspond to transient orbits, while the inner topological circle indicates quasi-periodic trajectory. Existence of chaotic orbits is confirmed by the rest of phase space (ergodic).

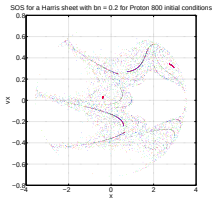

(a)

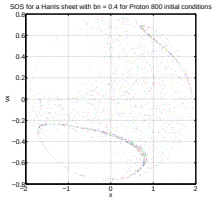

(b)

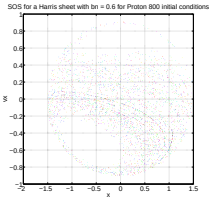

(c)

Fig. 3.18: Appearance of chaos in the parabolic current sheet. Figures 3.18(a)-3.18(c) are SOS for the normalized $B_z = .2, .4$, and $.6$, respectively. As B_z increases, the regions of quasi-periodic orbits disappear and the phase space is filled with chaotic (Speiser type) and transient (empty space) orbits. The normal magnetic field (B_z) was increased from top to bottom plots. Increasing the strength led to the quasi-periodic orbits vanishing and transient regions merging together. Phase mixing can be seen to occur when moving to stronger field strengths. Eight hundred initial conditions were plotted in all the graphs using Matlab to solve and plot the solutions.

Chapter 4

Simulation to Study Particle Chaos in Magnetotail Magnetic Field Configurations

4.1 Introduction

As seen in Chapter 2, magnetotail is quite a dynamic place due to the interaction of the geomagnetic field with the solar wind. This leads to surges in various current systems around the magnetosphere. Maxwell's equations show that such increase will result in morphing of the magnetic field geometry. Hence, close to the Earth, the field is dipolar and has three adiabatic invariants (see Chapter 3), and so guiding center approximation works for the geometry which in turn eases the load on numerical computation. Such an approximation is valid under eq. (3.19). But the field far from the Earth around $10 - 30$ R_E is far from being dipolar. In this chapter, we will analyze the degree to which the X-line and BCS is chaotic using the Lyapunov exponents enumerated in the earlier chapters.

4.2 Lyapunov Exponents for X-line

As seen in the previous chapter, Lyapunov exponents are a powerful to study the presence of chaos. A positive exponent indicates chaos in the dynamical system. For even ordered Hamiltonian systems such as the Newton-Lorentz model, using the exponents, one can define an effective collision frequency by noting that the units of the exponents are s^{-1} [6]. The effect of imposed fields can also be analyzed using the exponents.

For an X-line, figs. 4.1(a) and 4.2(a) are plots of the six exponents in the six directions of phase space. Both protons and oxygen ions experience chaos in an X-line which can be concluded by the positive value of exponent. For varying electric fields, figs. 4.1(b) and 4.2(b) show that the amount of chaos on the particles increases with an increasing electric

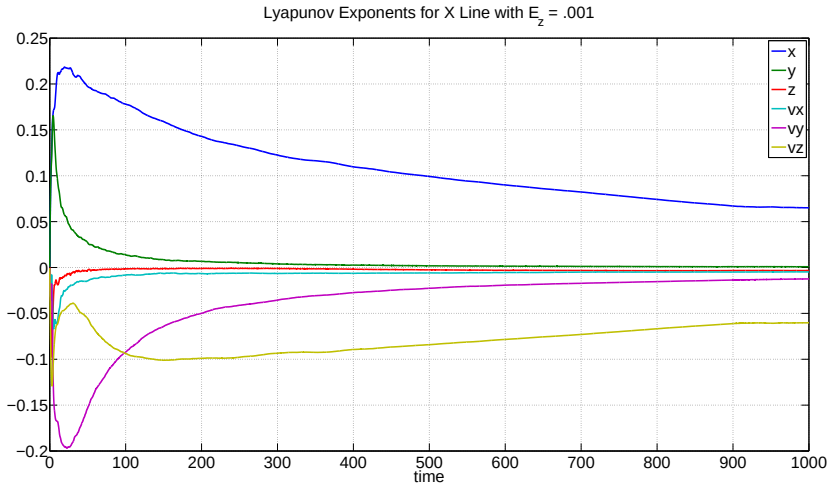

(a)

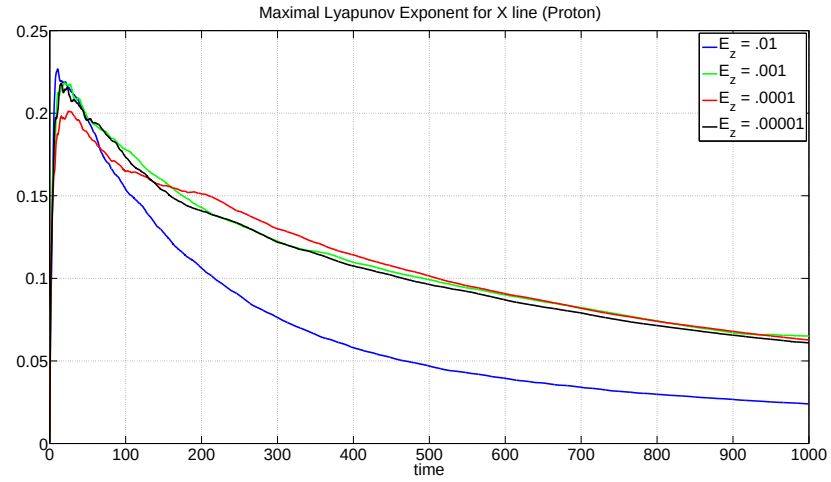

(b)

Fig. 4.1: Lyapunov exponents for proton in an X-line shown in fig. 4.1(a). Indication of at least on positive exponent indicates the presence of chaos. Figure 4.1(b) indicates the maximal Lyapunov exponents for different values of electric field. For the set of six ODEs for the evolution of x, y, z, v_x, v_y, and v_z, the exponents for the evolution are shown in different colors (see legend). The extended set of equations (explained in Appendix A) were solved using the ODE solver of Matlab. Also important to note is that the Newton-Lorentz system is conservative in the sense that the phase space volume is conserved according to Louville's theorem. In fig. 4.1(b), the exponents with maximum positive values (indicating chaos) are shown for varying strengths of electric field shown in the legend. The y axis corresponds to the exponents in the six directions. As can be seen, increasing the electric field tends to reduce chaos since the particles are swept away from the accelerating region before they can acquire sufficient velocity.

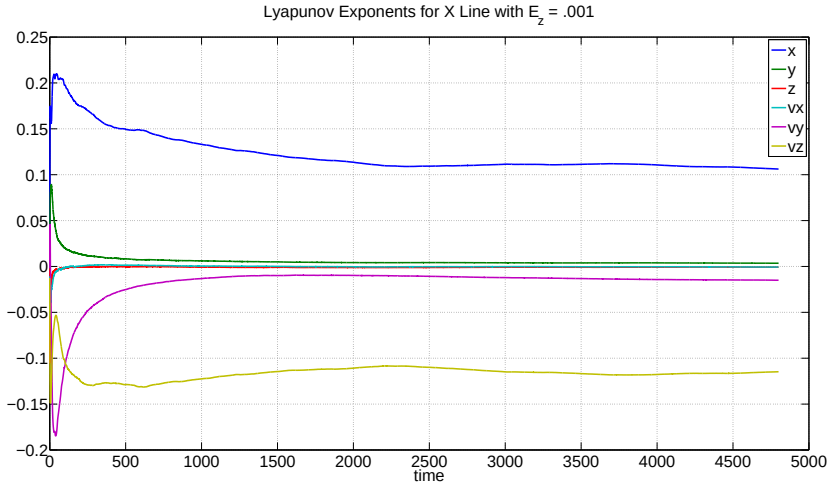

(a)

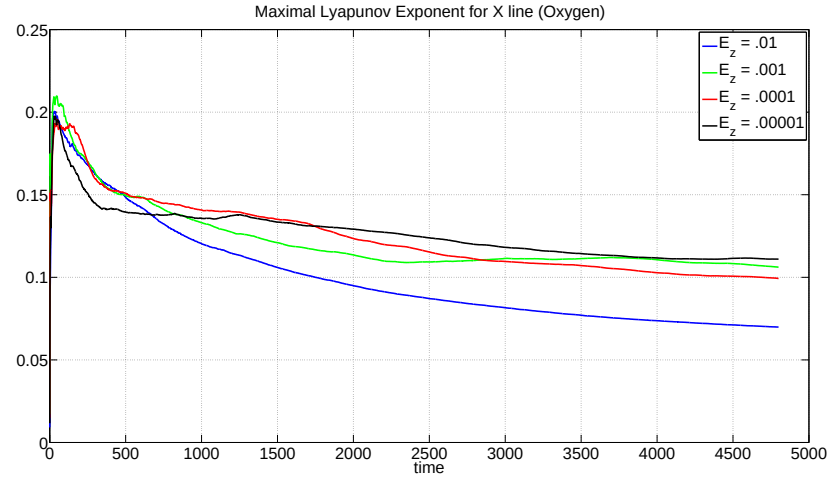

(b)

Fig. 4.2: Lyapunov exponents for oxygen ion in an X-line shown in fig. 4.2(a). Indication of at least on positive exponent indicates the presence of chaos. Figure 4.2(b) indicates the maximal Lyapunov exponents for different values of electric field. An oxygen ion with single charge is more chaotic in a given electric field than a proton (approximately two times more chaotic). The gyro radius is larger (due to larger mass) compared to a proton and since we are interested in the proton diffusion region, oxygen ions are removed from the chaos region before being accelerated by the electric field. For the set of six ODEs for the evolution of x, y, z, v_x, v_y, and v_z, the exponents for the evolution are shown in different colors (see legend). The extended set of equations (explained in Appendix A) were solved using the ODE solver of Matlab.

field.

4.3 SOS for X-line with Varying $\zeta = B_{0x}/B_{0z}$

As noted for a parabolic sheet, as the normal magnetic field is increased, the amount of chaos increases (fig. 3.18). Starting from $b_n = .2$ where the phase space is divided amongst transient (empty spaces), quasi-periodic (semi closed orbits), and chaotic (uniformly distributed points) orbits, as b_n gets stronger, the phase space is filled with chaotic and transient orbits. Following the same premise, SOS with different values of the ratio $\zeta = B_{0x}/B_{0z}$ are plotted in figs. 4.3(a)-4.3(c). The ratio does not have any effect on the dynamics in phase space and it is filled with only chaotic and transient orbits.

4.4 Lyapunov Exponents for BCS

Lyapunov exponents for a BCS are shown for for protons (figs. 4.4(a) and 4.4(b)) and oxygen ions (figs. 4.5(a) and 4.5(b)). For a given electric field, the charged particle experiences a constant amount of chaos as indicated by at least one positive exponent. Particle trapping in the normal magnetic field, B_z results in nearly the same amount of chaos in across different strengths of electric field. On the other hand, as was noted in previous chapters, the normal magnetic field induces chaos into a current sheet (without a normal magnetic field, a reversed magnetic field has integrable orbits only and has no chaos). The same argument works for the BCS where varying the strength of normal magnetic field varies the amount of chaos a particle experiences inside the current sheet. This can be seen in figs. 4.6(a) and 4.6(b).

4.5 SOS for BCS with Varying $b_n = B_{0z}/B_{0x}$

As noted for a parabolic sheet, as the normal magnetic field is increased, the amount of chaos increases (fig. 3.18). Starting from $b_n = .1$ where the phase space is divided amongst transient (empty spaces), quasi-periodic (semi closed orbits), and chaotic (uniformly distributed points) orbits, as b_n gets stronger, the phase space is filled with chaotic orbits with a very small space filled with quasi-periodic (adiabatic) orbits. Following the same premise,

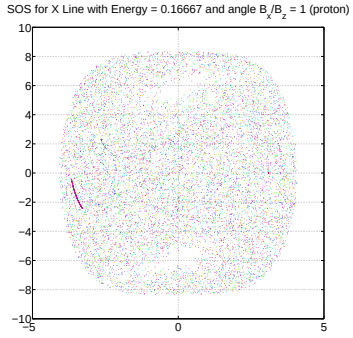

(a)

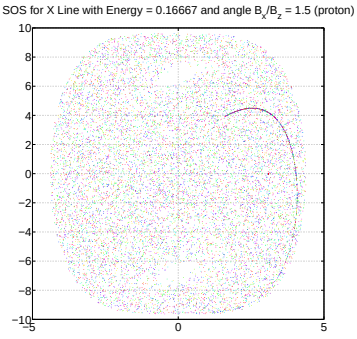

(b)

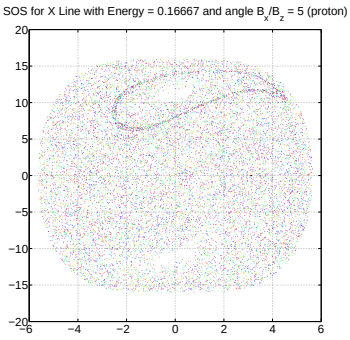

(c)

Fig. 4.3: SOS for an X-line with varying the ratio B_{0x}/B_{0z}. Figures 4.3(a)-4.3(c) are plots for $\zeta = B_{0x}/B_{0z} = 1, 1.5$, and 5, respectively. Compared to SOS for the modified Harris sheet (fig. 3.18), the ratio has little effect on the overall behavior of the system with only transient (empty spaces) and chaotic orbits existing for an X-line. Only protons were run for the section. The x and y axis are x and v_x, respectively. The energy was kept constant and the ratio of the lobe to normal magnetic field (B_{0x}/B_{0z}) was varied across the three plots. Absence of quasi-periodic orbits indicates that the X-line is more chaotic than a modified Harris sheet. The graphs were plotted using the procedure outlined in Appendix A and the resulting crossings in the x, v_x plane were plotted using Matlab.

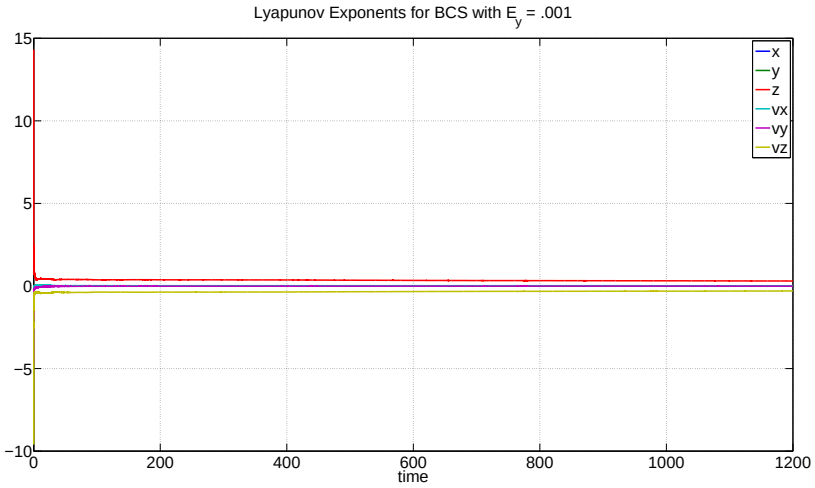

(a)

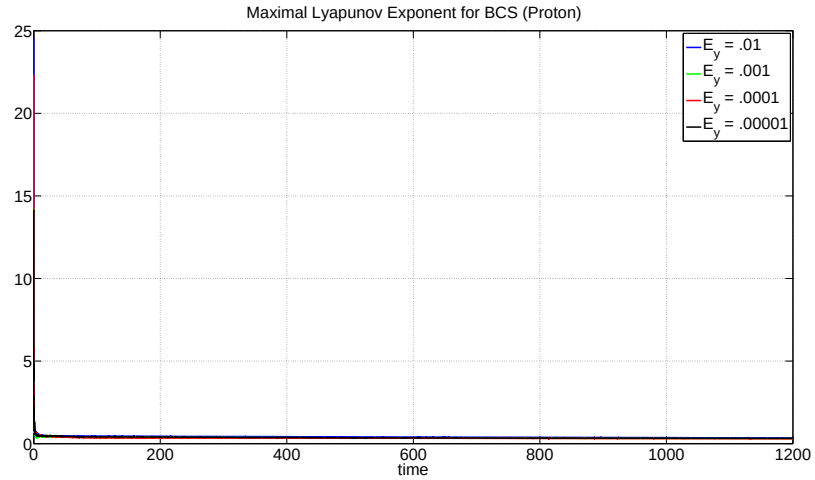

(b)

Fig. 4.4: Lyapunov exponents for proton in an BCS shown in fig. 4.4(a). Indication of at least on positive exponent indicates the presence of chaos. Figure 4.4(b) indicate the maximal Lyapunov exponents for different values of electric field. The values range from $.29-.32s^{-1}$. For the set of six ODEs for the evolution of x, y, z, v_x, v_y, and v_z, the exponents for the evolution are shown in different colors (see legend). The extended set of equations (explained in Appendix A) were solved using the ODE solver of Matlab. Compared to an X-line, the BCS is more chaotic for a given electric field strength. Also as for the X-line, the system is conservative (incompressible flow in phase space). As indicated by fig. 4.4(b), changing the electric field does seem to change the amount of chaos as given by the steady state values ranging in $.29 - .32s^{-1}$.

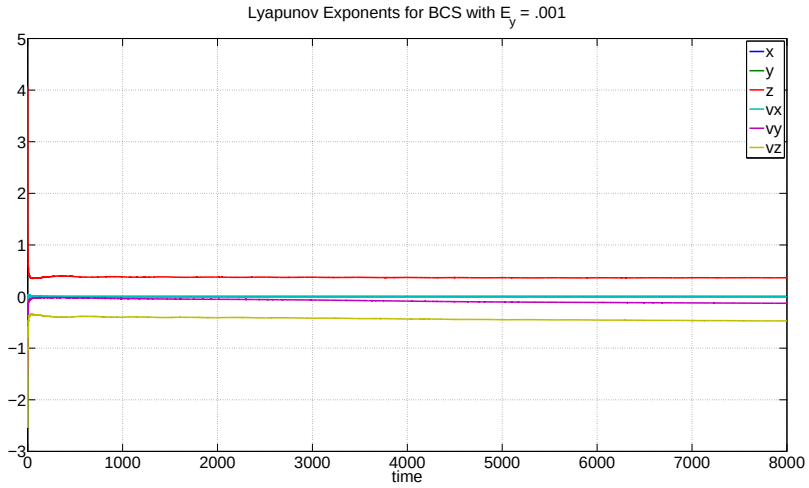

(a)

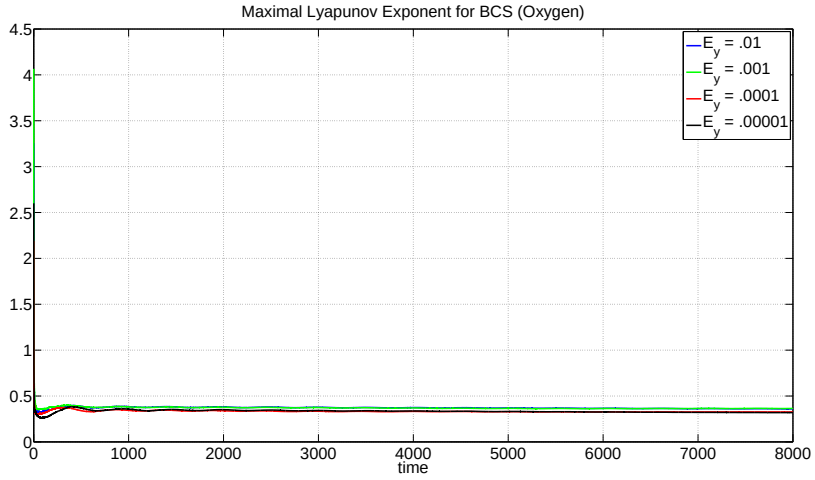

(b)

Fig. 4.5: Lyapunov exponents for oxygen ion in BCS shown in fig. 4.5(a). Indication of at least on positive exponent indicates the presence of chaos. Figure 4.5(b) indicates the maximal Lyapunov exponents for different values of electric field. The values range from $.32 - .36 s^{-1}$. As was the case for X-line, the oxygen ion is more chaotic than proton (around 1.12 times). For the set of six ODEs for the evolution of x, y, z, v_x, v_y, and v_z, the exponents for the evolution are shown in different colors (see legend). Compared to an X-line, the BCS is more chaotic for a given electric field strength. Also as for the X-line, the system is conservative (incompressible flow in phase space). The extended set of equations (explained in Appendix A) were solved using the ODE solver of Matlab.

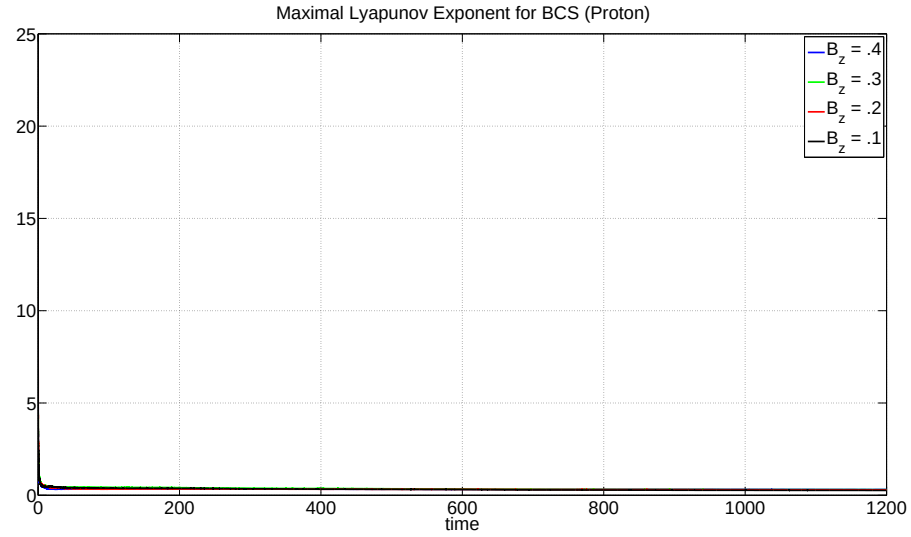

(a)

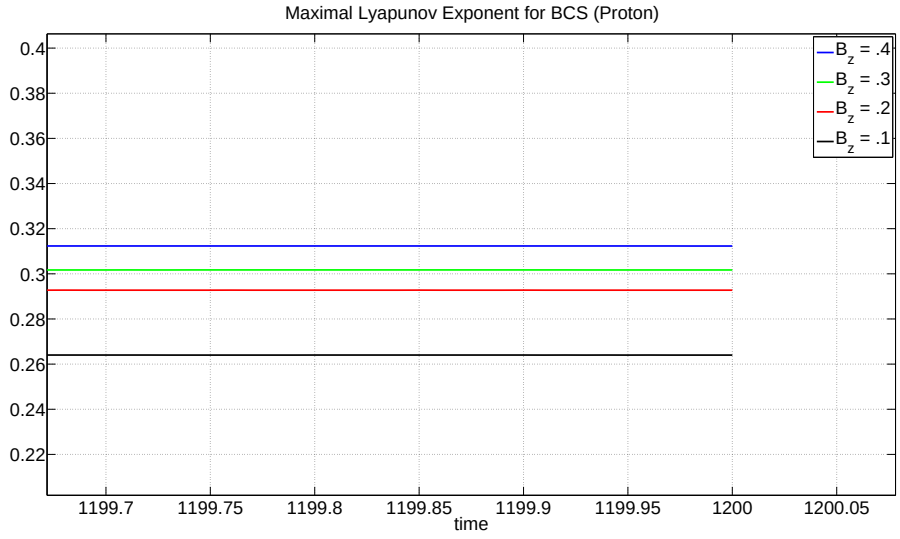

(b)

Fig. 4.6: Maximal Lyapunov exponents for proton in an BCS for different values of B_z. Figure 4.6(b) shows that the final values range from $.26 - .31 s^{-1}$. As for the modified Harris sheet, an addition of a small normal magnetic field component increases chaos. For the set of six ODEs for the evolution of x, y, z, v_x, v_y, and v_z, the exponents for the evolution are shown in different colors (see legend). The extended set of equations (explained in Appendix A) were solved using the ODE solver of Matlab. The figures indicate that since the BCS is not a neutral but a quasi-neutral inside the current sheet (finite B_z) compared to a very weak overall field strength in case of X-line, B_z is a chaos parameter.

SOS with different values of the ratio $\zeta = B_{0x}/B_{0z}$ are plotted in fig. 4.7. As the strength of b_n was increased, it led to change in the overall behavior of the current sheet with the decrease and disappearance of quasi-periodic orbits (regions corresponding to circular regions) as one goes from fig. 4.7(a) to fig. 4.7(d). The energy was kept constant and the ratio of the lobe to normal magnetic field (B_{0z}/B_{0x}) was varied across the three plots. The fact that this model behaves in a manner similar to the modified Harris sheet can be seen by the emergence of chaos (ergodicity) in the phase space for strong b_n with the invariant tori corresponding to adiabatic motion being broken and the phase space occupied by chaotic orbits only.

4.6 Summary of the Study

This chapter mainly focused on finding the behavior of particles in phase space for the two current sheet configurations in question, viz., X-line and BCS. It was found in sections 4.3 and 4.5 that the two models behaved differently with regards to types of orbits that could exist in the geometries. As seen in fig. 4.3, the phase space is occupied by a small transient space (empty regions) and a large chaotic region. Also, the ratio ζ was not a chaos parameter in that the phase space behavior remained the same for any value of ζ. But as seen in fig. 4.7, the ratio b_n was a chaos parameter as also implied in fig. 3.18 and that quasi-periodic orbits disappeared from phase space with an increase in the parameter. Having found that chaos exists in such magnetic fields where the magnetic field varies over a gyro radius, sections 4.2 and 4.4 quantified this chaos by the use of Lyapunov exponents. The procedure to calculate them can be found in Appendix A. The fact that Newton-Lorentz system was conservative (i.e., flow was incompressible in phase space) was indicated by the sum of all the six Lyapunov exponents. From figs. 4.1 and 4.2, it was concluded that chaos scales with the strength of electric field and that a very strong electric field can eject particles from the chaos region reducing the chaos. Also, oxygen ions experience more chaos than protons in an X-line. The same can be concluded for a BCS with the maximal Lyapunov exponent varying on a much smaller scale for both protons and oxygen ions compared to X-line.

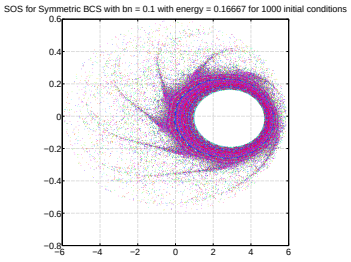

(a)

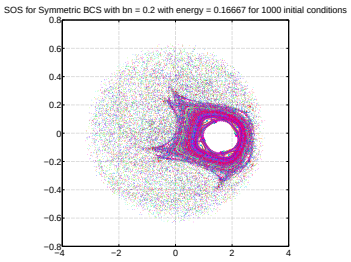

(b)

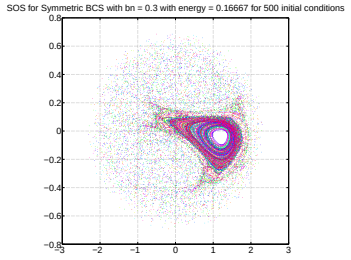

(c)

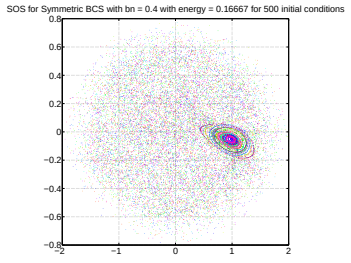

(d)

Fig. 4.7: SOS for BCS with varying the ratio $B_{0z}/B_{0x} = .1, .2, .3$, and $.4$ in figs. 4.7(a)-4.7(d), respectively. The graphs were plotted using the procedure outlined in Appendix A and the resulting crossings in the x, v_x plane were plotted using Matlab. Compared to SOS for the modified Harris sheet (fig. 3.18), the ratio has a significant effect on the overall behavior of the system with transient (empty spaces) and chaotic orbits existing for $b_n = .1$. Only protons were run for the section. The x and y axis are x and v_x, respectively.

Chapter 5

Velocity Distributions and Temperatures Inside X-line and BCS

From statistical mechanics, it is known that to derive macroscopic quantities such as bulk velocity, temperature, pressure, etc., many particles are invoked in the simulation. The initial conditions for each particle is derived from a uniform distribution (to eliminate any initial bias) and the particle is run through the magnetic and electric fields for a time determined by the maximal Lyapunov exponent (i.e., a plateau in the exponent). For the BCS, 10000 particles were run in this manner and this chapter discusses result of the runs with regards to the velocity distribution functions and temperatures in different directions.

5.1 X-line

Using the procedure outlined in Appendix A, charged particles were run in an X-line with magnetic field geometry discussed in Chapter 2. From Chapter 4, having quantified chaos in X-line, we found that chaos was strong in weak magnetic field region, the so called neutral current sheet. Using this information, we used the particle runs to find the x, y, and z directed velocity at prescribed time steps which were in the chaos region. The next two subsections describe the distribution functions and temperature profiles.

5.2 Velocity Distribution and Temperature for Protons and Oxygen Ions

Figures 5.1(a)-5.6(c) graph the evolution of the velocity distribution function in x, y, and z directions for protons and oxygen ions in an X-line. As mentioned, the simulations were started with uniform distributions in all the three directions. As seen in the figures, the distributions tend to isotropize to Maxwellians with finite temperatures with passage of time.

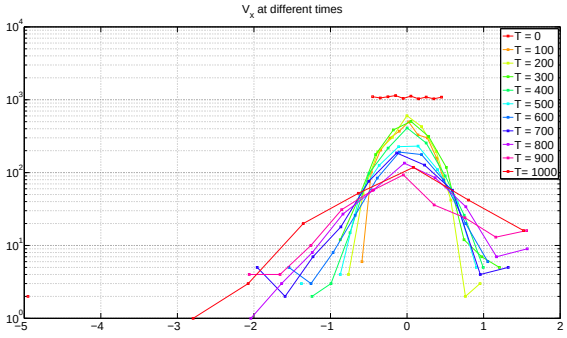

(a)

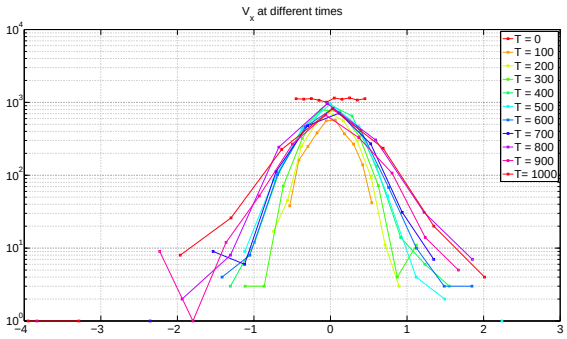

(b)

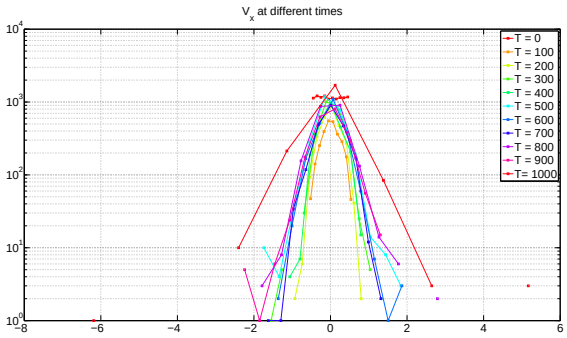

(c)

Fig. 5.1: Velocity distribution for protons in the x (Sun-Earth) direction for an X-line. Figures 5.1(a)-5.1(c) are functions for the three values of electric field $E_y = .001, .0001$, and $.00001$. $E_y = .01$ was too strong and the particles were ejected from the chaos region before being accelerated. Starting from a uniform distribution, the velocity distribution in the x direction shapes into a Maxewllian with the passage of time. The x and y axis are the particle velocity normalized to the Alfven speed and the number of particles in the chaos region. The plots were generated by accumulating the number of particles in the chaos region at a given time step and then Matlab hist command was used to generate the final viewgraphs. The plot has a log scale on the y axis (using semilogy command).

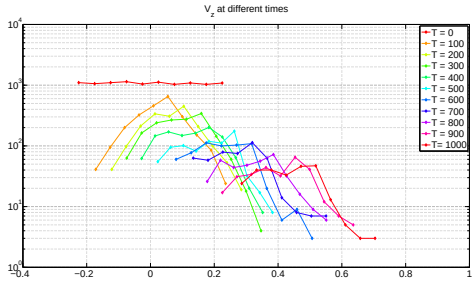

(a)

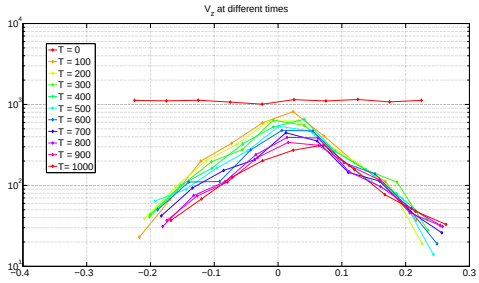

(b)

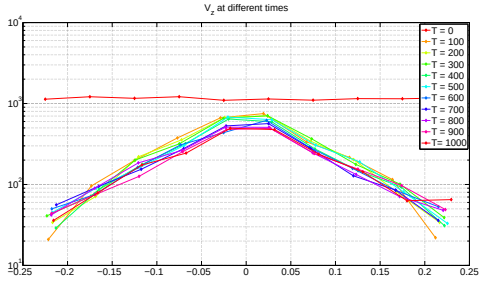

(c)

Fig. 5.2: Velocity distribution in the y (dawn dusk direction) direction for an X-line. Figures 5.2(a)-5.2(c) are functions for the three values of electric field $E_y = .001, .0001$, and $.00001$. $E_y = .01$ was too strong and the particles were ejected from the chaos region before being accelerated. Starting from a uniform distribution, the velocity distribution in the x direction shapes into a Maxewllian with the passage of time. The colors indicate the distribution function at different times during the simulation. For the strongest electric field strength shown in fig. 5.2(a), the particles develop an average drift along with the isotropization of the distribution. The same can be seen for weaker fields but the acceleration for the weakest field seems to be very small. The plots were generated by accumulating the number of particles in the chaos region at a given time step and then Matlab hist command was used to generate the velocity bins and the number of particles in the bins.

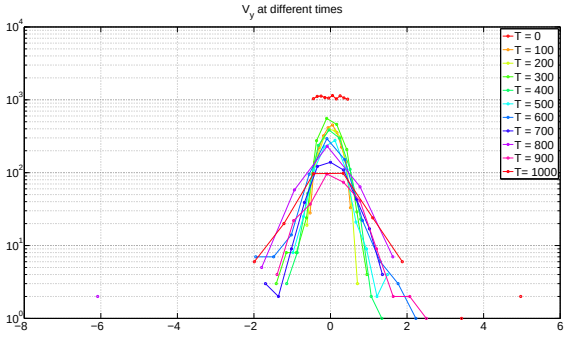

(a)

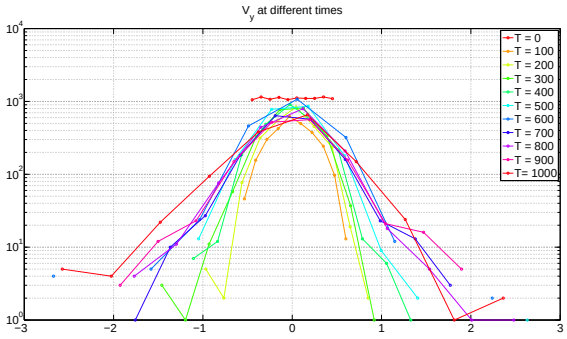

(b)

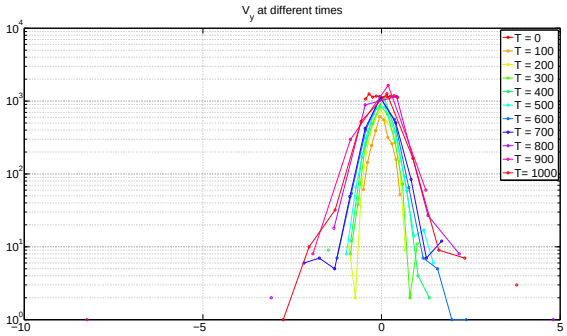

(c)

Fig. 5.3: Velocity distribution in the z (perpendicular to current sheet) direction for a X-line. Figures 5.3(a)-5.3(c) are functions for the three values of electric field $E_y = .001, .0001$, and .00001. As with fig. 5.1, the distributions evolve in to Maxwellians as time goes by. This is in part due to particles being ejected from the chaos region. The evolution into Maxwellian does look like a collisional process. The plots were generated by accumalating the number of particles in the chaos region at a given time step and then Matlab hist command was used to generate the velocity bins and the number of particles in the bins. The plot has a log scale on the y axis (using semilogy command).

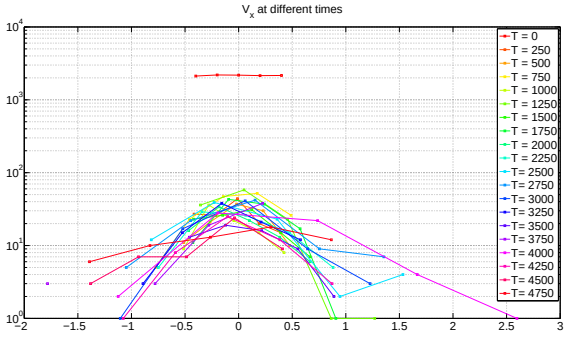

(a)

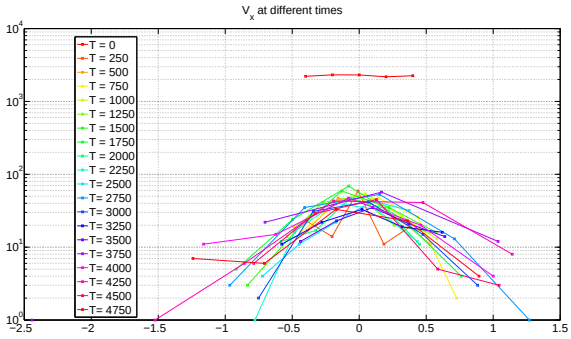

(b)

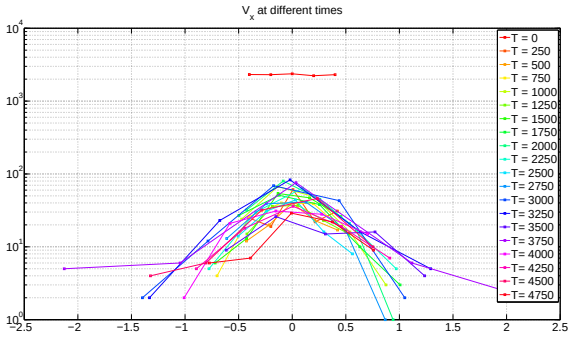

(c)

Fig. 5.4: Velocity distribution in the x (Sun-Earth) direction for a X-line for oxygen. Figures 5.4(a)-5.4(c) are functions for the three values of electric field $E_y = .001, .0001$, and $.00001$. Since the size of the chaos region has not been changed (still on proton inertial scale), the isotropization occurs much faster when compared to protons. Although jagged, the distributions have an overall Maxwellian nature. The plots were generated by accumulating the number of particles in the chaos region at a given time step and then Matlab hist command was used to generate the velocity bins and the number of particles in the bins. The plot has a log scale on the y axis (using semilogy command).

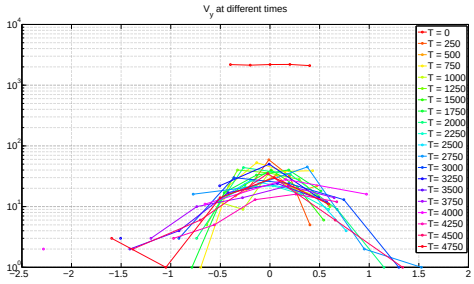

(a)

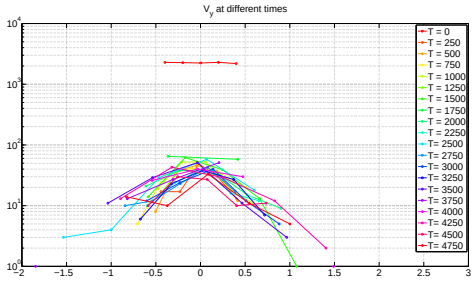

(b)

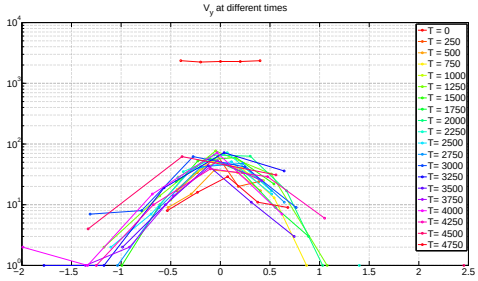

(c)

Fig. 5.5: Velocity distribution in the z (perpendicular to current sheet) direction for a X-line for oxygen. Figures 5.5(a)-5.5(c) are functions for the three values of electric field $E_y = .001, .0001$, and $.00001$. The colors indicate the distribution function at different times during the simulation. The times at which the distribution function was sampled is shown in the legends. The x and y axis are the particle velocity normalized to the Alfven speed and the number of particles in the chaos region. The plots were generated by accumulating the number of particles in the chaos region at a given time step and then Matlab hist command was used to generate the velocity bins and the number of particles in the bins. The plot has a log scale on the y axis (using semilogy command). Because of the oxygen ions being heavier (16 times) than the proton, they attain much lower speeds on the order of the Alfven speed as seen by the values on the x axis.

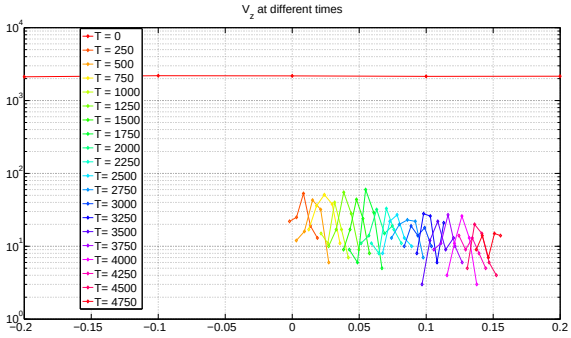

(a)

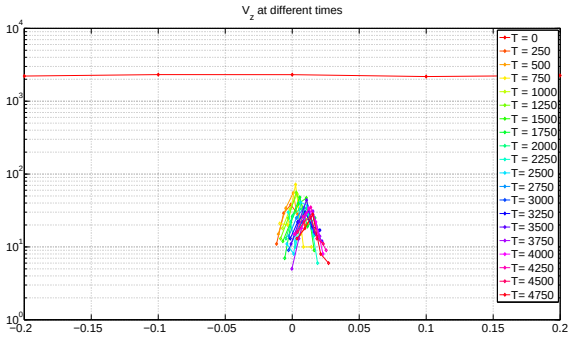

(b)

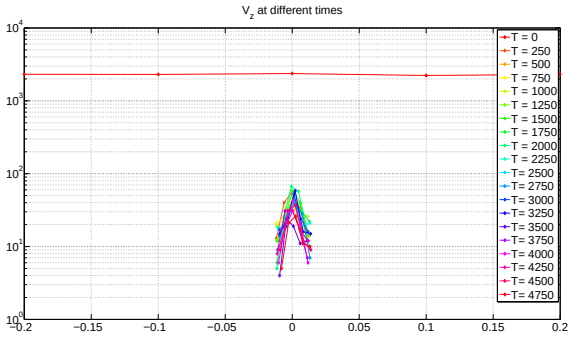

(c)

Fig. 5.6: Velocity distribution in the y (dawn dusk) direction for a X-line for oxygen. Figures 5.6(a)-5.6(c) are functions for the four values of electric field $E_y = .001, .0001$, and $.00001$. As seen in fig. 5.6(a), there are hardly any particles left in the chaos region (since the diffusion region has been scaled according to proton inertial length), but for weaker field strengths, distributions tend to isotropize in the direction of electric field. The x and y axis are the particle velocity normalized to the Alfven speed and the number of particles in the chaos region. The plots were generated by accumulating the number of particles in the chaos region at a given time step and then Matlab hist command was used to generate the velocity bins and the number of particles in the bins.

The distribution in the direction of electric field tends to have an average drift which weakens with decrease in electric field strength. Such drift is not that evident in fig. 5.6 as it is heavier than a proton. For both the charged species, $E_y = .01$ is too strong for the particles to remain in the chaos region and they are ejected from the chaos region. Since no particles remained in the chaos region by the end of the simulation, the plots for $E_y = .01$ are not shown.

Figures 5.7(a)-5.8(c) show the temperature profiles in the three directions for protons and oxygen ions, respectively. Since the particles drift with an average speed in the direction of electric field (y direction), the temperature in that direction goes down as more of the chaotic motion (which leads to increase in disorder, entropy, and temperature) is changed to ordered motion, a drift in y direction. Also, the temperatures at the end of the simulation vary with the electric field in the case of protons but saturates for weaker electric fields in the case of oxygen ions ($E_y = .0001, .00001$).

5.3 BCS Statistics

Using the procedure outlined in Appendix A, charged particles were run in a BCS with magnetic field geometry discussed in Chapter 2. From Chapter 4, having quantified chaos in BCS, we found that chaos was strong in weak magnetic field region where the Sun-Earth (x) component was negligible and only the North South (z) component was present which led to the quasi-neutral sheet. The presence of this component led to some interesting features in the velocity distribution functions and temperatures. Using this information, we used the particle runs to find the x, y, and z directed velocity at prescribed time steps which were in the chaos region. The next two subsections describe the distribution functions and temperature profiles.

5.3.1 Velocity Distribution for Protons and Oxygen Ions

The y directed distribution seems to have an elongated tail. Asymmetry in the structure also indicates that there might be a higher order moment (heat flow) in the direction of electric field primarily due to the more heavier oxygen ion. The z directed distribution

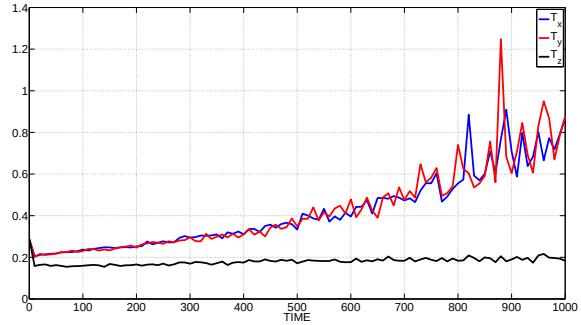

(a)

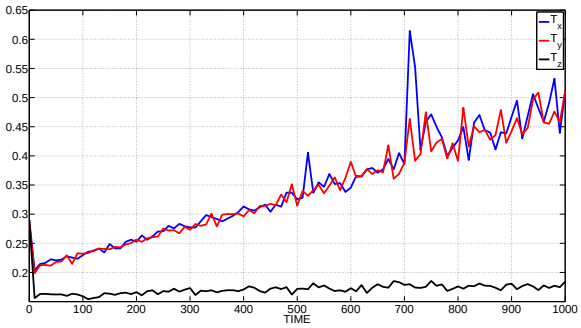

(b)

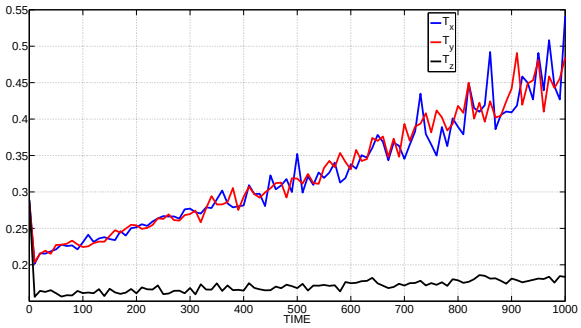

(c)

Fig. 5.7: Proton temperature in a X-line for different values of $E_y = .001, .0001$, and $.00001$ in figs. 5.7(a)-5.7(c), respectively. Blue, black, and red colors represent the temperatures in x, y, and z directions, respectively. The temperature in the direction of electric field (y direction in magnetospheric coordinates but z direction in the simulation) reduces drastically in the beginning and remains lower than that in the direction perpendicular to the electric field. This indicates that since the particles have an average velocity in the direction of electric field, the amount of randomness or temperature is reduced (also found by Numata and Yoshida [6]). The plot was generated by finding the second moment of the distributions found previously and these were plotted at specific times in the simulation.

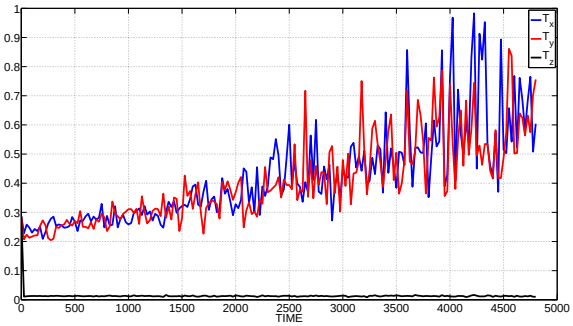

(a)

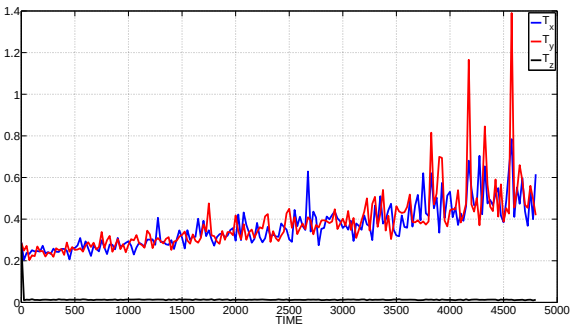

(b)

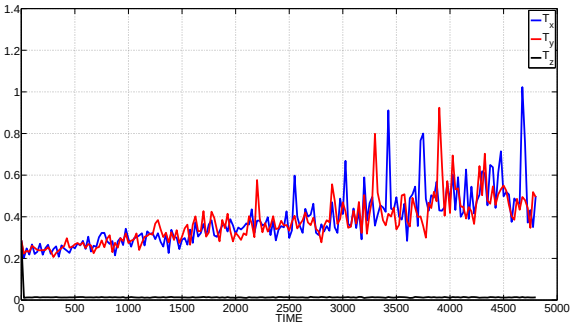

(c)

Fig. 5.8: Oxygen ion temperature in a X-line for different values of $E_y = .001, .0001$, and .00001 in figs. 5.8(a)-5.8(c), respectively. The plot was generated by finding the second moment of the distributions found previously and these were plotted at specific times in the simulation. Much higher temperatures can be seen for the oxygen ion since it is the inertia in the ion can cause a much higher chaotic motion when compared to the proton. As in the case of protons, the temperature (in normalized units) in the direction of electric field (y direction in magnetospheric coordinates but z direction in the simulation) reduces drastically in the beginning and remains lower than that in the direction perpendicular to the electric field.

has a structure somewhat to functions found in the solar wind, i.e., a thermal core and a nonthermal edge (the x directed distributions for both the species suggests that a good fit to the distribution might have two Maxwellians with different temperatures figs. 5.9(a)-5.10(d)). Figures 5.11(a)-5.12(d) represent the evolution of distribution function in the z direction for the two charged species. Similarly, figs. 5.13(a)-5.14(d) represent the evolution of distribution function in the y direction.

Along the magnetic field in the current sheet, the proton velocity reaches to around $4 - 5\ V_A$ (fig. 5.13). In the direction of electric field proton velocities reach $\approx 10 - 15\ V_A$ due to the influence of the electric field. However, the particle also $E \times B$ drifts in the x direction.

For oxygen ions, distribution along the magnetic field seems to develop a bifurcation as seen in fig. 5.14. The tail of the y velocity distribution is evidently elongated which could be the action of electric field in that direction trying to accelerate the particle but magnetic field pulling it back after some gyro periods. The heavier oxygen ion does not seem to be accelerated by the electric field significantly as the particle speed suggests the values around $1 - 1.5\ V_A$. The z directed distribution does look like a thermal distribution as the temperature graphs.

5.3.2 Proton and Oxygen Ion Temperatures

Proton and oxygen temperatures are shown in figs. 5.15(a)-5.16(d). Initially, because the distribution is uniform in all the three directions, temperatures in all cases and in both species start at the same number $\approx .3$ (normalized units). Since the distributions are sampled inside the quasi-neutral sheet, in which z direction is parallel to the ambient magnetic field, T_z is therefore the temperature in the parallel direction. In all the graphs, this temperature is lower than either of the perpendicular temperatures T_x and T_y. Protons achieve a much higher temperature (an order of magnitude higher than oxygen).

Diverging values of T_x and T_y suggest that the distribution in the direction perpendicular to the magnetic field can be nonthermal. Ratio of perpendicular to parallel temperatures are around ≈ 3 while the two perpendicular temperatures are almost equal. Contrary to

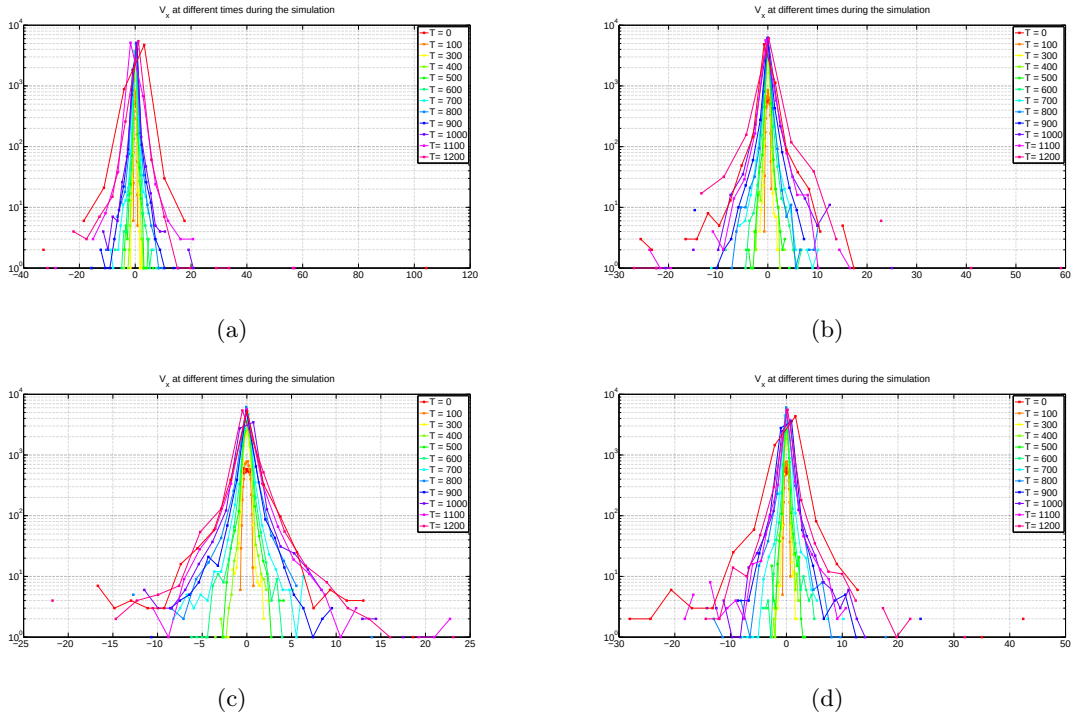

Fig. 5.9: Velocity distribution in the x (Sun-Earth) direction for a BCS. Figures 5.9(a)-5.9(d) are functions for the four values of electric field $E_y = .01, .001, .0001$, and $.00001$, respectively. The colors indicate the distribution function at different times during the simulation. Similar to the X-line, particles in BCS tend to isotropize due to particles being lost from the chaos region (which macroscopically looks like a collision process). The x and y axis are the particle velocity normalized to the Alfven speed and the number of particles in the chaos region. The plots were generated by accumulating the number of particles in the chaos region at a given time step and then Matlab hist command was used to generate the velocity bins and the number of particles in the bins. The plot has a log scale on the y axis (using semilogy command).

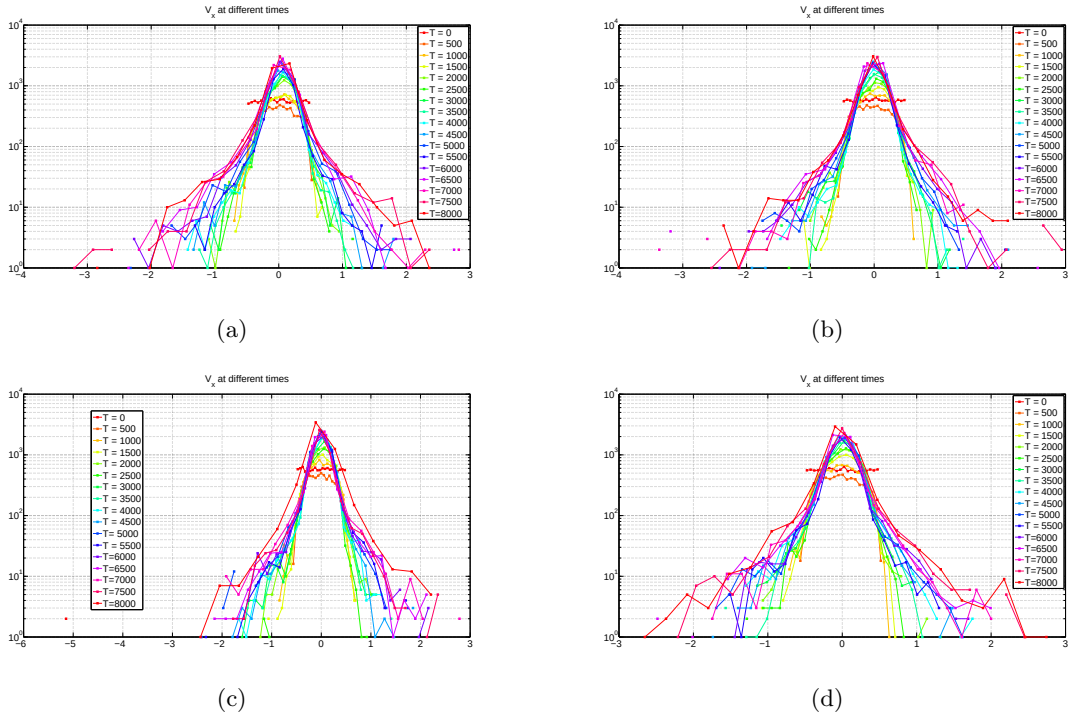

(a) (b)

(c) (d)

Fig. 5.10: Velocity distribution in the x (Sun-Earth) direction for a BCS for oxygen. Figures 5.10(a)-5.10(d) are functions for the four values of electric field $E_y = .01, .001, .0001$, and .00001, respectively. A very clear two temperature distribution can be seen for all the field strengths. Similar to the X-line, particles in BCS tend to isotropize due to particles being lost from the chaos region (which macroscopically looks like a collision process). The x and y axis are the particle velocity normalized to the Alfven speed and the number of particles in the chaos region. The plots were generated by accumulating the number of particles in the chaos region at a given time step and then Matlab hist command was used to generate the velocity bins and the number of particles in the bins.

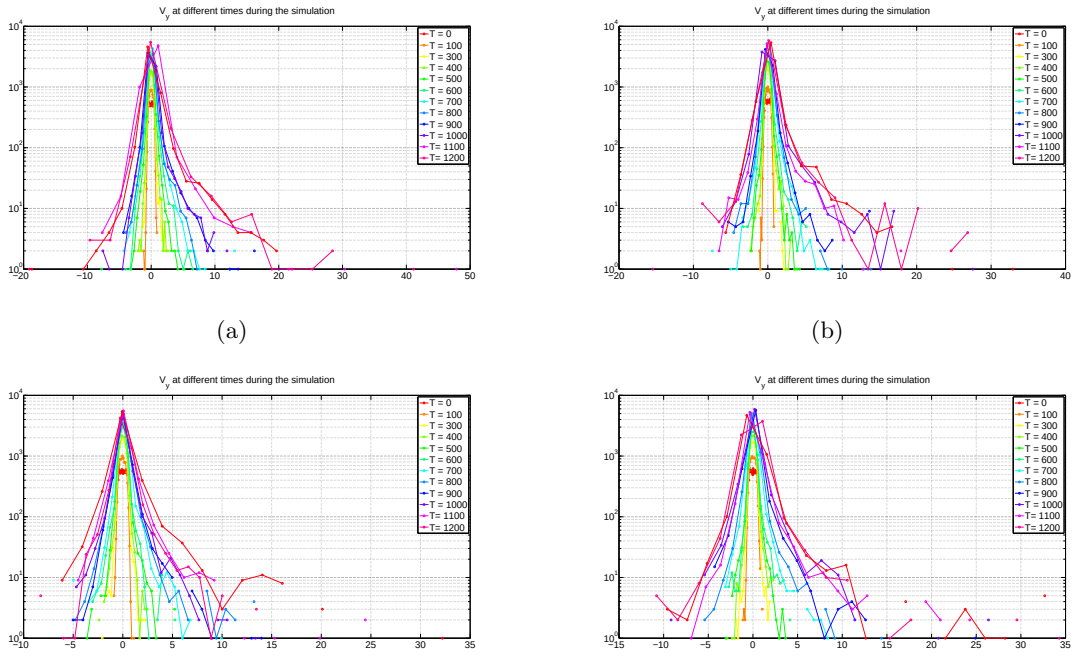

Fig. 5.11: Velocity distribution in the y (dawn dusk) direction for a BCS. Figures 5.11(a)-5.11(d) are functions for the four values of electric field $E_y = .01, .001, .0001$, and $.00001$, respectively. The colors indicate the distribution function at different times during the simulation. The distributions seem to have a fat tail and a different temperature in the core (where most particle velocities are binned). The x and y axis are the particle velocity normalized to the Alfven speed and the number of particles in the chaos region. The plots were generated by accumulating the number of particles in the chaos region at a given time step and then Matlab hist command was used to generate the velocity bins and the number of particles in the bins. The plot has a log scale on the y axis (using semilogy command).

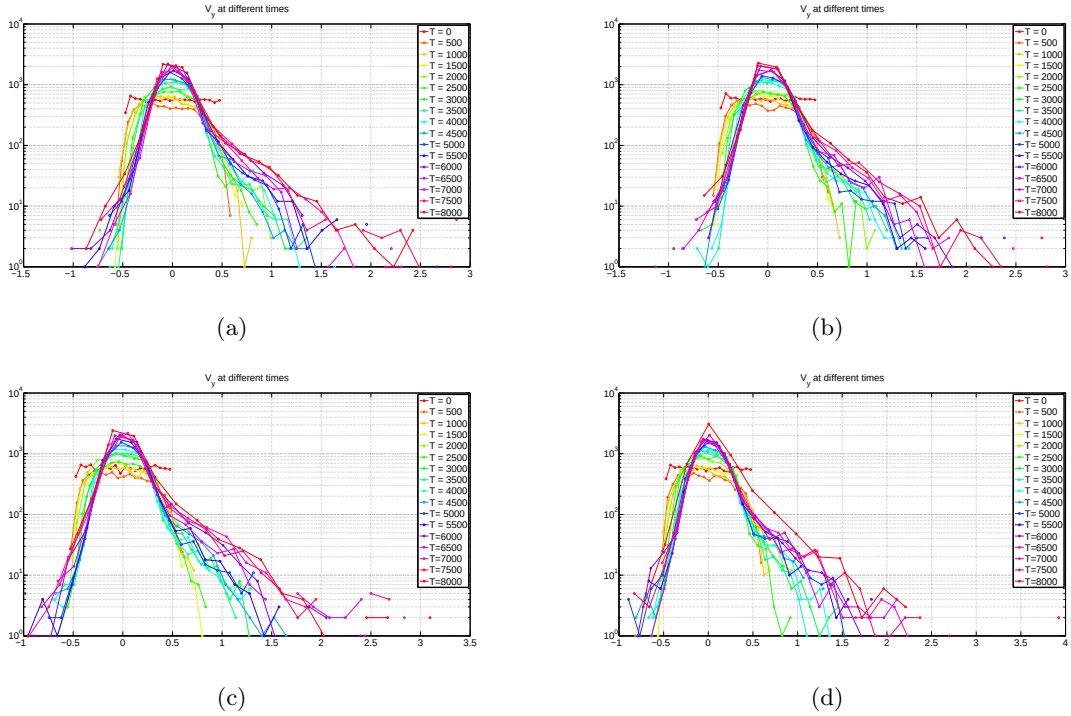

(a) (b)

(c) (d)

Fig. 5.12: Velocity distribution in the y (dawn dusk) direction for a BCS for oxygen. Figures 5.12(a)-5.12(d) are functions for the four values of electric field $E_y = .01, .001, .0001, .00001$, respectively. The x and y axis are the particle velocity normalized to the Alfven speed and the number of particles in the chaos region. The plots were generated by accumulating the number of particles in the chaos region at a given time step and then Matlab hist command was used to generate the velocity bins and the number of particles in the bins. The plot has a log scale on the y axis (using semilogy command). As for the protons, the distribution function in this direction has a fat tail with a core Maxwellian.

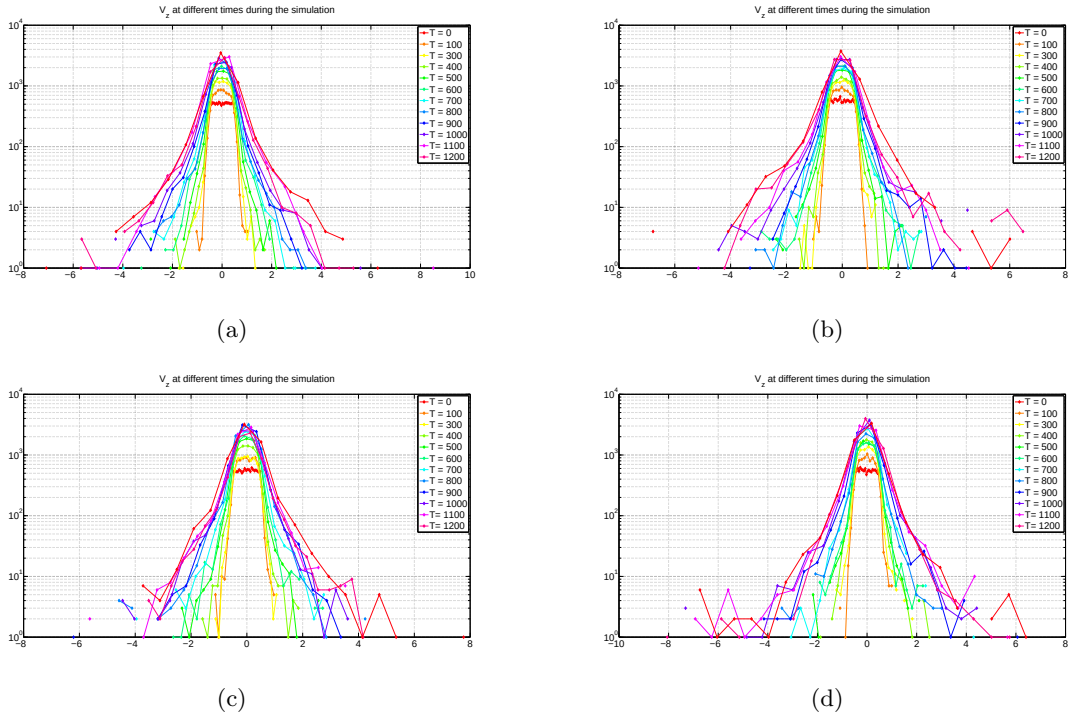

(a) (b)

(c) (d)

Fig. 5.13: Velocity distribution in the z (perpendicular to current sheet) direction for a BCS. Figures 5.13(a)-5.13(d) are functions for the four values of electric field $E_y = .01, .001, .0001,$ and .00001, respectively. The plot has a log scale on the y axis (using semilogy command). The colors indicate the distribution function at different times during the simulation. It can be seen clearly that the distributions have two temperatures (core and flank widths are different) and is consistently found for all field strengths. The x and y axis are the particle velocity normalized to the Alfven speed and the number of particles in the chaos region.

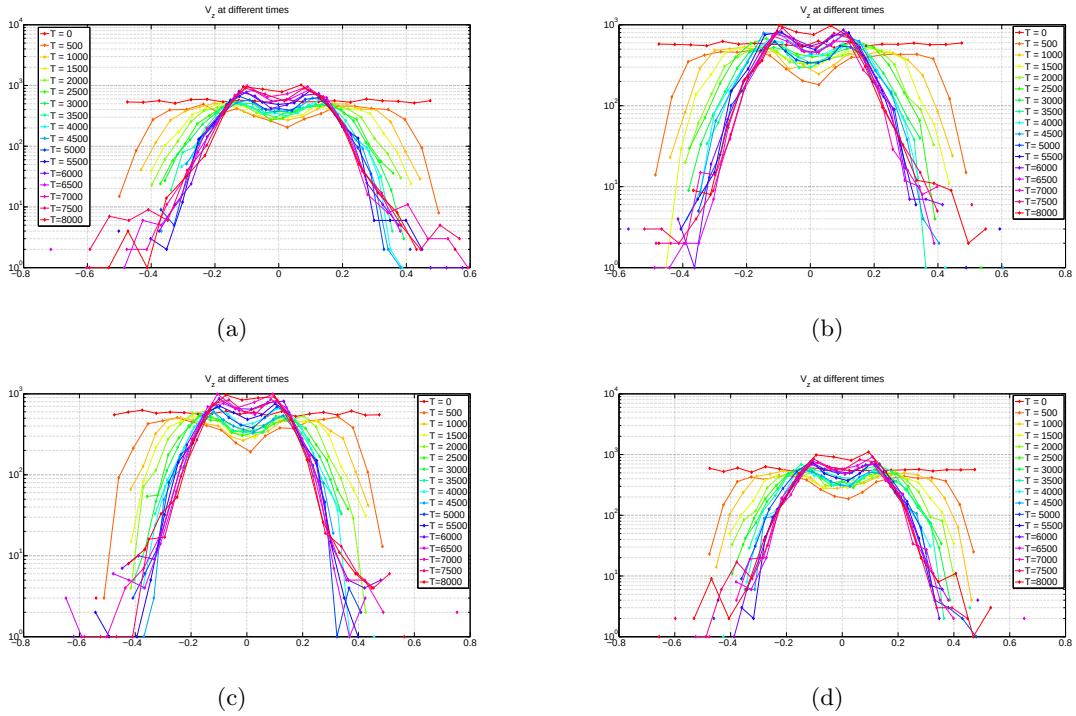

Fig. 5.14: Velocity distribution in the z (perpendicular to current sheet) direction for a BCS for oxygen. Figures 5.14(a)-5.14(d) are functions for the four values of electric field $E_y = .01, .001, .0001$, and $.00001$, respectively. The x and y axis are the particle velocity normalized to the Alfven speed and the number of particles in the chaos region. The plots were generated by accumulating the number of particles in the chaos region at a given time step and then Matlab hist command was used to generate the velocity bins and the number of particles in the bins. The plot has a log scale on the y axis (using semilogy command). The colors indicate the distribution function at different times during the simulation. The distributions although Maxwellian seem to have a bifurcated beam like distribution. Compared to protons, oxygen ions are accelerated to lower velocities owing to their heavier mass.

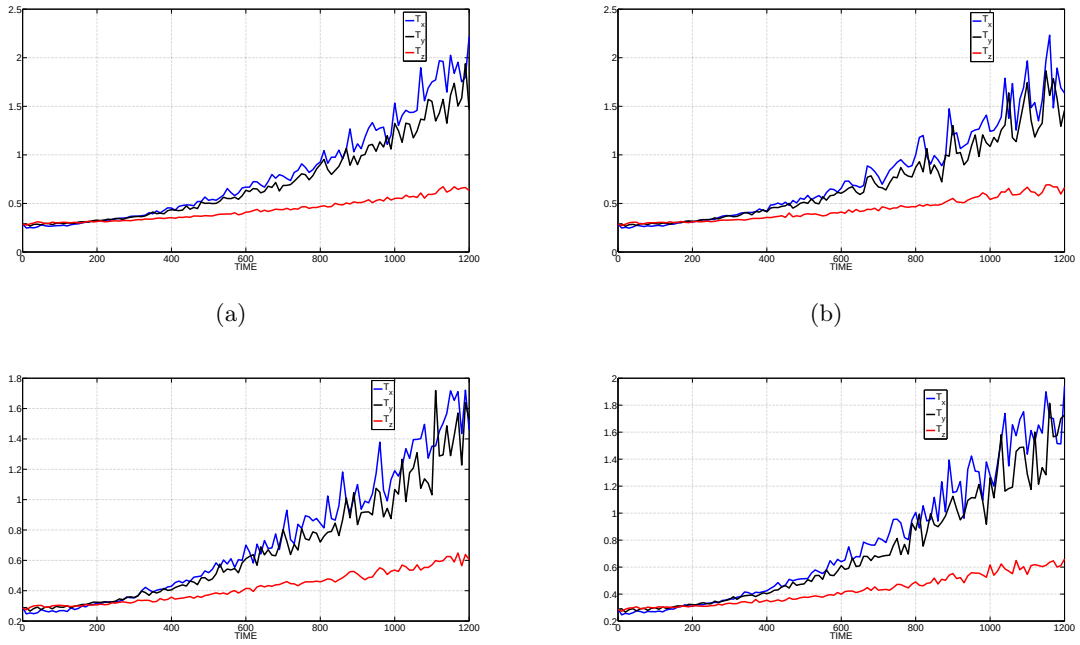

(a) (b)

(c) (d)

Fig. 5.15: Proton temperature in a BCS for $E_y = .01, .001, .0001$, and $.00001$ in figs. 5.15(a)-5.15(d), respectively. Blue, black, and red colors represent the temperatures in x, y, and z directions, respectively. Unlike the X-line, temperatures in all the directions tend to increase with time. This might be due to the fact that there exists a nonzero magnetic field (B_z) that controls the dynamics and along with E_y, makes the particles drift in x direction. Also, the temperatures are much higher than X-line. The plot was generated by finding the second moment of the distributions found previously and these were plotted at specific times in the simulation. The fluctuations are caused by statistical noise.

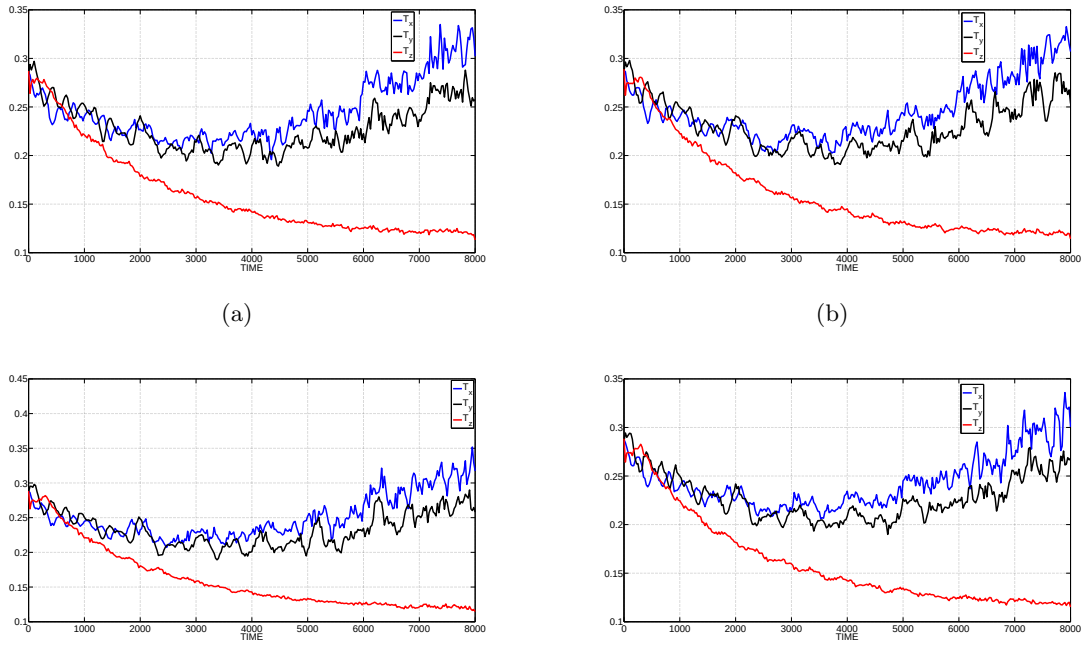

(a) (b) (c) (d)

Fig. 5.16: Oxygen ion temperature in a BCS for $E_y = .01, .001, .0001$, and .00001 in figs. 5.16(a)-5.16(d), respectively. Blue, black, and red colors represent the temperatures in x, y, and z directions, respectively. The plots were generated by accumulating the number of particles in the chaos region at a given time step and then Matlab hist command was used to generate the velocity bins and the number of particles in the bins. The plot has a log scale on the y axis (using semilogy command). Contrary to protons in BCS, the temperature in direction perpendicular to the weak magnetic field (z) decreases and then increases but in the direction of magnetic field decreases with time. This is also in contrast to what was found for an X-line where the direction of temperature decrease was the direction of electric field rather than the magnetic field.

results found by Numata and Yoshida [6], where the temperature along the direction of electric field decreased with time due to energy being transferred to accelerating the particle, BCS behaves in a somewhat different fashion. The temperature in the direction of magnetic field reduces and in the other two directions increases due to nonthermal features in the velocity distribution function.

5.4 Summary of the Study

This chapter focused on the study of velocity distributions and temperatures in X-line and BCS with varying the electric field in sections 5.1 and 5.3, respectively. For both the field geometries, we found that starting from an initial uniform distribution of velocities, the final distributions indicated Maxwellian features in figs. 5.1-5.6 for an X-line and figs. 5.9-5.14 for a BCS. Also, such isotropization occurred on a very fast scale. This is analogous to isotropization of distributions due to collisions in a Lorentz gas. But for the present case, the Maxwellian features are due to particles being lost from the chaos region, with particles with small velocities not being able to escape, and hence the higher number in the chaos region. Temperatures in the three directions for different electric fields tended to be the same in the direction perpendicular to the electric field. Also, due to bulk drift (evident for protons than for oxygen ions) in an X-line, the temperature (randomness) reduced in the direction of electric field and the temperatures in the other two directions were almost equal (see figs. 5.7 and 5.8). For a BCS, the distributions tend to have a two temperature profile with a stronger core temperature. Tails were found in the direction of electric field (fig. 5.11 for protons and fig. 5.12 for oxygen ions). The behavior in a BCS is different since the presence of a North South z component along with the electric field in y direction produces a drift in the x direction. Hence, the bulk acceleration is not evident in both protons and oxygen ions. The distribution along the magnetic field z tends to show a beam like distribution for oxygen ions. Contrary to the X-line, the temperatures in the three directions tend to increase with time with temperature being different in the z direction along B_z rather than the electric field E_y (figs. 5.15 and 5.16). The temperatures in the direction perpendicular to magnetic field B_z are equal for BCS.

Chapter 6

Resistivity Calculation from Multi-Particle Runs

6.1 Modeling

Spatial variations in electric and magnetic fields lead to nonlinearity in charged particle dynamics. Chaotic motion of particles is an important mechanism of producing resistivity in an almost collisionless plasma [54]. Strongly inhomogeneous magnetic fields (scale variation on or close to particle gyro radius) including null points breaks the conservation of adiabatic invariants mentioned in Chapter 3. When there are no COMs in the equations of motion, the degree of freedom increases and can result in chaotic motion of particles (depending on initial conditions). The mixing effect of chaos brings about rapid increase of the kinetic entropy in a collisionless plasma, which, however, is not sufficient to yield a diffusion-type dissipation. When a test particle is confined in a bounded domain of the phase space, the second cumulant of the velocity distribution saturates after the initial mixing phase, and hence, the diffusion constant (the time derivative of the second cumulant) diminishes to zero [6]. However, in an open system where particles can convect into/out a chaotic region of the phase space (either through coordinate or momentum axes), particles are heated locally during a certain staying time in the chaos region, and continuous dissipation process is achieved [54].

In this chapter, we study the motion of particles in an magnetic fields of X-line and BCS topology with perpendicular electric field (fig. 2.2 middle panel). Particles far from magnetic null point are magnetized and perform the usual $\vec{E} \times \vec{B}$ drift. The motion of particles becomes chaotic in the vicinity of null points. By analyzing motion of many particles (we consider independent particles ignoring collisions), we observe collisionless heating of particles in the chaos region in a statistical sense. This is contrary to the motion of magnetized

particles which cannot gain energy from a stationary electric field because of the periodicity of motion (gyration around a magnetic field line). When the particles are demagnetized in the neighborhood of null points, the particles have a net velocity in the direction parallel to electric field. We can then estimate an effective collisionless resistivity using the arguments of Ohm's law. This theory can be applied to various collisionless magnetic diffusion phenomena, such as fast magnetic reconnections leading to changes of magnetic topologies [25, 26, 54]. Wave-particle interactions (through lower hybrid drift instabilities) [34] or stochasticity of magnetic field lines have been studied as a source of particle nonadiabaticity leading to enhanced resistivities. The magnetic null points and quasi-neutral current sheets that demagnetize charged particles cause highly chaotic motion.

The standard normalization of Newton's equation of motion shows that the particle inertial effect (kinetic effect) works in a length scale of the skin depth [6]. The chaos region and amount of chaos is introduced by using the Lyapunov exponent discussed in Chapter 3. Nonlinearity in the equation of motion is implied from the spatial inhomogeneity in the magnetic field and chaos is found to be strongest near the null point where the particle is demagnetized and accelerated by the electric field [6]. The chaos-induced resistivity is scaled by the applied electric field (or Mach number) while it does not depend on plasma temperature. It is found that the collisionless resistivity can be orders of magnitude larger than the usual Spitzer/collisional resistivity [6].

6.2 Particle Trajectories and Lyapunov Exponents for X-line Configuration

Sample trajectories were calculated using Matlab ODE function and initial conditions picked to be in the neutral sheet and velocities uniformly distributed in a given interval. Shown in fig. 6.1 are 40 such trajectories showing that in and close to the neutral sheet, the particle does behave nonadiabatically [6]. To find if it is the case that there is chaos in the particle motion, Lyapunov exponents were calculated for $\approx$ 10000 particles. As seen in fig. 6.2, there is a positive exponent indicating to chaos [6]. The panels shows that with a constant electric field E_z of normalized value .001, 01, and.1, the Lyapunov exponent decreases with increasing electric field because of the fact that the particle is

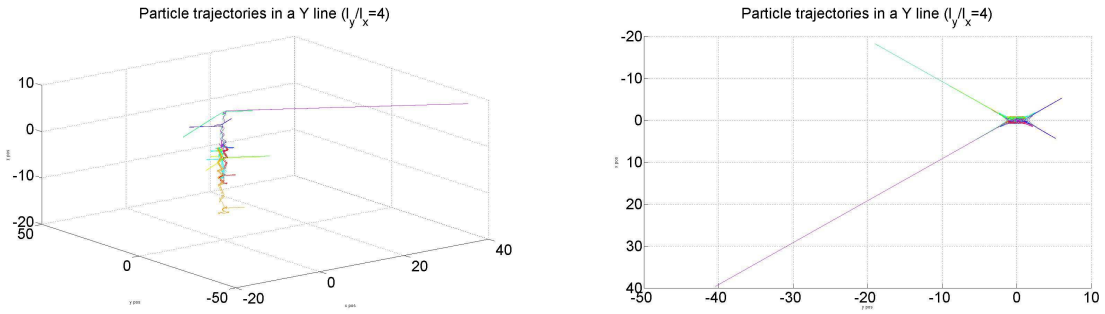

Fig. 6.1: Sample particle trajectories in a Y-line with $l_y/l_x = 4$. The different colors represent particles started at different initial positions and with different velocities. The right hand panel is a 2D projection of the left panel onto the $x - y$ plane. The trajectories were generated by solving the Newton-Lorentz system of ODEs with no electric field and Y-line as the magnetic topology and plotted with plot3 and plot commands in Matlab. As can be seen that far away from the chaos region (from the Y-line), the particles perform guiding center motion and drift into the chaos region where they interact with the neutral sheet and are ejected from it. After going out some distance into the lobes, the particle again mirror back into the sheet after sometime.

ejected (accelerated) away from the neutral sheet before being sufficiently randomized and so does not contribute to the resistivity significantly [6].

For different particle species (protons and oxygen ions), with different strengths of electric field, for an X-line are plotted in Appendix B.

6.3 Collisionless Resistivity

Collisionless resistivity is calculated from the acceleration of the particles in the direction of external electric field (which for the present case is in the z direction). Knowing that the particle is demagnetized inside the chaos region where the electric field monotonically accelerates the particle (fig. 6.3 left panel), resistivity can be derived using the equations used by Numata and Yoshida [6]. To calculate the average velocity, velocity of the particles in chaos region (which is determined from the maximum Lyapunov exponent) are averaged over the number of particles in the region (fig. 6.4(a)). Assuming a monotonic acceleration in this region, one may write the average microscopic velocity as

$$\hat{\bar{v}}_z(\hat{t}) \approx \alpha \hat{t}. \tag{6.1}$$

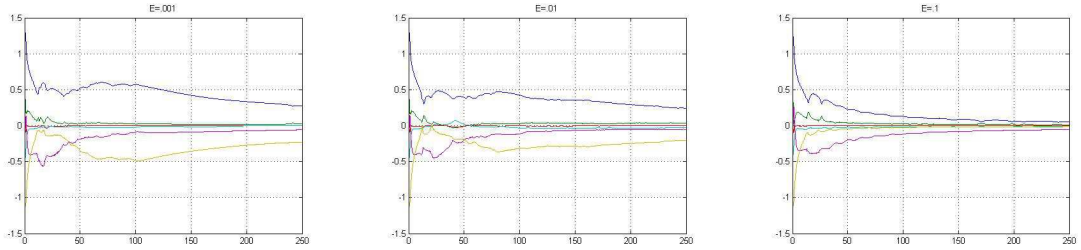

Fig. 6.2: Lyapunov exponents for $E = .001, .01$, and .1. Positive Lyapunov exponents indicate chaotic behavior (sensitive dependence to initial conditions) with an increasing electric field tending to reduce the amount of chaos (from left to right). Since the electric field tends to accelerate the particles out of the chaos region, the chaotic nature should reduce which is indicated by the reduction of the maximal Lyapunov exponent with increasing electric field strength. The extended set of ODEs (Appendix A) were solved using Matlab solvers and the resulting exponents in the six directions were plotted. Again, since the sum of the exponents is a very small number (in fact if run for a sufficient time is of the order of 10^{-9}), the system is conservative, i.e., volume conserving flow in phase space.

As noted from figs. 6.4(b) and 6.4(c) the particles are simultaneously ejected from the chaos region which is indicated by a reduction in the number particles in the chaos region. As found by Numata and Yoshida [6], this number decreases exponentially and is modeled by a single exponential with negative exponent as

$$n(\hat{t}) = n_o \exp(-\beta \hat{t}), \tag{6.2}$$

where β is the decay exponent. In principle, we can assume a convecting system in which particles with zero intial average velocity are injected and accelerated subsequently in the direction of the electric field. Using eqs. (6.1) and (6.2), we get [6],

$$\hat{\bar{U}}_z \;=\; \frac{\alpha}{\beta}\left(1 - \exp(-\beta \hat{t})\right), \tag{6.3}$$

where α and β are constants determined from the fitting tool which represent the slope of acceleration in the z direction and the exponent of the decay of particles in the chaos region which for ≈ 10000 particles were found to be 0.0004515 and 0.00341 as can be seen in fig. 6.4 and the 2^{nd} row of Table 6.1. An important fact is that although particles are

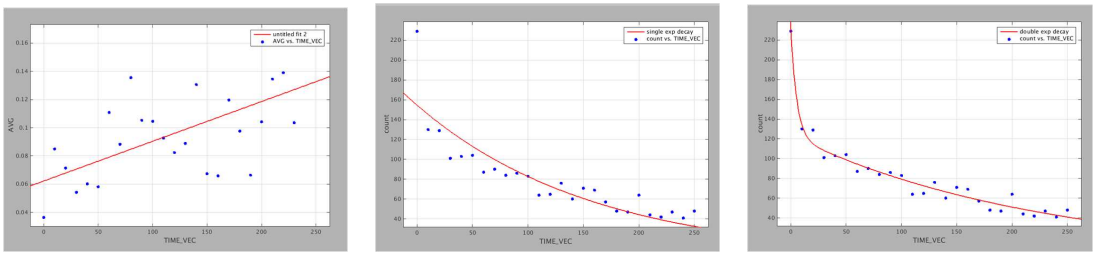

Fig. 6.3: Average particle velocity and exponential fits (middle panel single and right panel double) to the decay in the number of particles in the neutral sheet as a function of time for the X-line. A sample of 240 particles was used with $E_y = .001$ (normalized to $V_A B_0$) were used. A more finely resolved (in time) plots and the respective fits are shown in the next few sections. The particles are accelerated in the chaos region and at the same time are lost from the region. This looks similar to collisions where in the demagnetization is caused by the physical collision. A linear acceleration rate is then found by fitting the dots with the the fitting toolbox of Matlab. The numbers come very close to what Numata and Yoshida [6] obtained. Also as seen in the middle and right panel, a double exponential fit does fit the decay very well according to the goodness of fit numbers seen in the toolbox. The plots were generated by using the procedure outlined in Appendix A and plotting and fitting the result in Matlab.

run individually and hence there is no mutual interaction and self-fields, they still show collective effects.

To get to a macroscopic equation which represents a collective behavior and that relates the acceleration in the direction of electric field, a fluid type momentum equation can be written as [6]

$$\hat{\rho}_{eff} \frac{d\hat{\bar{U}}_{z1}}{d\hat{t}} = \hat{E}_z - \hat{\nu}_{eff} \hat{\bar{U}}_{z1}, \tag{6.4}$$

where $\hat{\bar{U}}_{z1}$ is the average velocity in the direction of electric field normalized by the Alfven speed and $\hat{\rho}_{eff}$ is the effective mass normalized by particle mass. This can be thought of as a collective fluid type mass that is accelerated by the electric field. $\hat{\nu}_{eff}$ is the effective collision frequency due to particle interacting with the inhomogeneous magnetic field normalized to the particle cyclotron frequency ω_c. From eq. (6.4), we can get saturation level of the average velocity as

$$\hat{\bar{v}}_{sat} = \frac{\hat{E}_z}{\hat{\nu}_{eff}}, \tag{6.5}$$

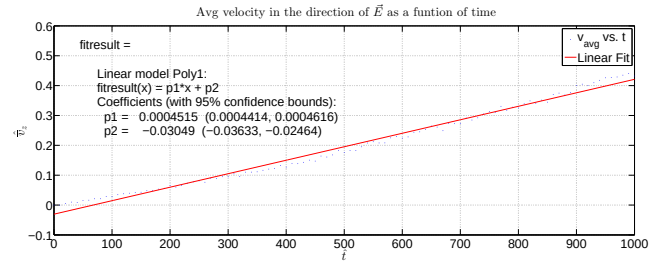

(a)

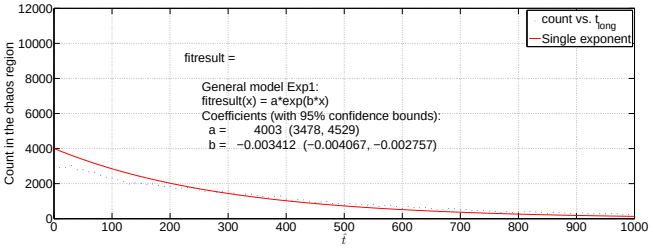

(b)

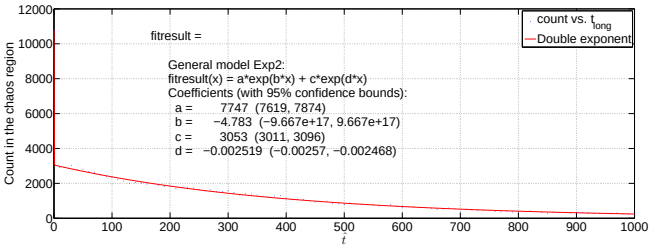

(c)

Fig. 6.4: Acceleration of protons in the direction of electric field ($E_y = .001$) in the case of an X-line. Figure 6.4(a) shows a linear fit to the acceleration and the fitted values can be seen on the left hand side. Figures 6.4(b) and 6.4(c) are single and double exponential fits to the decay of the number of protons inside the chaos region determined by the maximal Lyapunov exponent (fig. 4.1(b)). These numbers correspond to row 2 of Table 6.1. Figure 6.4(a) indicates that the acceleration in the direction of electric field can be modeled linearly. The fit results are indicated in the figures themselves. The decay of particles from the chaos region is graphed in figs. 6.4(b) and 6.4(c). Particles decay exponentially as found by Numata and Yoshida [6] also, but a double exponent seems to do a better job at fitting the decay as indicated by the goodness of fit numbers. The plots were generated using Matlab by following the procedure outlined in Appendix A and the results were fitted by utilizing the curve fitting toolbox of Matlab.

Table 6.1: Results for starting with uniformly distributed velocity distributions for an X-line with varying strengths of E_z. This table is for when $B_{0x}/B_{0y} = \beta = 1$. The double exponent numbers are for fast initial and slow final decay. The last column is the resistivity value calculated from the collisionless model and that from Spitzer's formula for collisional resistivity. η_{spit}, the Spitzer resistivity for the plasma sheet is 5.4×10^{-6} Ω/m. η_{eff}, η_{eff1} are collisionless resistivities of single and double exponential decays. $B_0 = 3.1 \times 10^{-8}$ T, $N_p = 2 \times 10^6 = N_e$ m^{-3}, $N_{O^+} = 4 \times 10^5$ m^{-3}(storm time).

Particle	B	E_z	Slope (α)	Exp (β)		$\eta_{eff}, [\eta_{eff1}, \eta_{eff2}]$ $\times 10^4$ (Ω/m)
				Single exponent	Double exponent	
Proton	X-line	.01	0.005153	-0.08631	NaN	1.6226 , [NaN]
Proton	X-line	.001	0.0004515	-0.00341	-4.783 , -0.002519	0.0732, [102.63,.05405]
Proton	X-line	.0001	3.775e-05	-0.00109	-2.332 , -0.0008186	0.0280, [59.84, 0.02101]
Proton	X-line	.00001	3.252e-06	-0.0006641	-0.5562, -0.0004385	0.0198 , [16.57, 0.0131]
Oxygen	X-line	.01	0.0003123	-0.1718	-9.436 ,-0.001866	266.46, [14635, 2.8942]
Oxygen	X-line	.001	3.127e-05	-0.1764	-10.49 , -0.0002303	273.25, [16249, 0.3567]
Oxygen	X-line	.0001	3.13e-06	-0.1829	-1.085 , -0.000106	283.04, [1679, 0.1640]
Oxygen	X-line	.00001	3.149e-07	-0.177	-1.145 , -0.0001056	272.26, [1761, 0.1624]

which can be translated to

$$\frac{\bar{v}_{sat}}{V_A} = \frac{E_z}{V_A B_0 \hat{\nu}_{eff}}, \tag{6.6}$$

in macroscopic (physical) units (i.e., from $\hat{A}$ to A where A can be any of the plasma variables). Using the resistive Ohm's law (section 2.4), we have [6]

$$E_z = \eta_{eff} J_z = \eta_{eff} n q \bar{v}_{sat}, \tag{6.7}$$

in which η_{eff} is the effective collisionless resistivity that we want to calculate. Using eq. (6.6), we can get a numerical expression of η_{eff} as

$$\eta_{eff} = \hat{\nu}_{eff} \frac{B_0}{nq}, \tag{6.8}$$

$$\eta_{eff} = \hat{\nu}_{eff} \frac{m B_0^2}{nmq B_0}, \tag{6.9}$$

$$\frac{\eta_{eff}}{\mu_0} = \hat{\nu}_{eff} \frac{B_0^2}{\mu_0 nm\omega_c}, \tag{6.10}$$

$$\frac{\eta_{eff}}{\mu_0} = \hat{\nu}_{eff} \frac{V_A^2 \omega_c}{\omega_c^2}, \tag{6.11}$$

$$\frac{\eta_{eff}}{\mu_0} = \hat{\nu}_{eff} \delta^2 \omega_c, \tag{6.12}$$

where $\omega_c = qB_0/m$ is the particle cyclotron frequency, $V_A = B_0/\sqrt{mn\mu_0}$ is the Alfven velocity, and $\delta = V_A/\omega_c$ is the particle inertial length, respectively [6].

Nonlinear fitting tool of Matlab was used to find the slope of acceleration (fig. 6.4) and to find the decay rate of the number of charged particles in the chaos region. Table 6.1 shows the result of fitting and the values of collisionless resistivity pertaining to plasma sheet parameters. As found by Numata and Yoshida [6], the resistivity values are 5-6 orders of magnitude larger than the collisional counterpart (Spitzer resistivity). Table 6.2 indicates that in an X-line most of the particles are lost from the chaos region. For a BCS, the case will be a different one where it will be seen that since the dissipation region (which is on the scale of protons and not oxygen ions) is very small compared to proton gyro radius.

Table 6.2: Percentage particles remaining in the chaos region at the end of simulation as compared to the number in the starting of the simulation (≈ 10000) for an X-line.

Particle	B	E_y	Count
Proton	X-line	.01	0 %
Proton	X-line	.001	2.35 %
Proton	X-line	.0001	12.11 %
Proton	X-line	.00001	17.47 %
Oxygen	X-line	.01	0 %
Oxygen	X-line	.001	0.45 %
Oxygen	X-line	.0001	0.85 %
Oxygen	X-line	.00001	0.97 %

6.4 Results for X-line with Varying Electric Field

To see what effect the electric field has on the particle trajectory and chaos, the same initial conditions were run with different values of electric field. The result is shown in figs. 6.5(a)-6.5(d). The particle staying time in chaos region varies with the electric field strength. For weak fields, the particle stays for a longer time in the region as compared to that in a strong field. This is also indicated by the Lyapunov exponents (fig. 4.1(a)), i.e., a stronger electric field tends to reduce chaos by removing particles from the chaos region. Table 6.2 also indicates the same conclusion. Experiments with different initial distribution functions and varying magnetic field topologies are discussed in Appendix C. Particle decay rates, bulk acceleration and final distribution functions are also discussed.

Starting with a uniformly distributed velocity space [6], in an X-line, the effect of electric field in the dawn dusk direction (y) can be seen in the particle average velocity as given in Table 6.1. As seen from the first four rows (colored in yellow, green, gray, and cyan), protons on average accelerate linearly in the direction of electric field. Also, the acceleration indicated by the slope α also increases with increasing electric field strength.

As seen in fig. 6.5, protons accelerate in the direction of the applied electric field. The slope of this acceleration as given in the fourth column of Table 6.1 is weaker when compared to free acceleration in absence of a magnetic field (blue lines in fig. 6.5), which indicates that the magnetic field acts to slow down the particle. This process can be modeled as an effective collision frequency and ultimately a collisionless resistivity [6]. The values of such a resistivity have been found to be orders of magnitude higher than the conventional

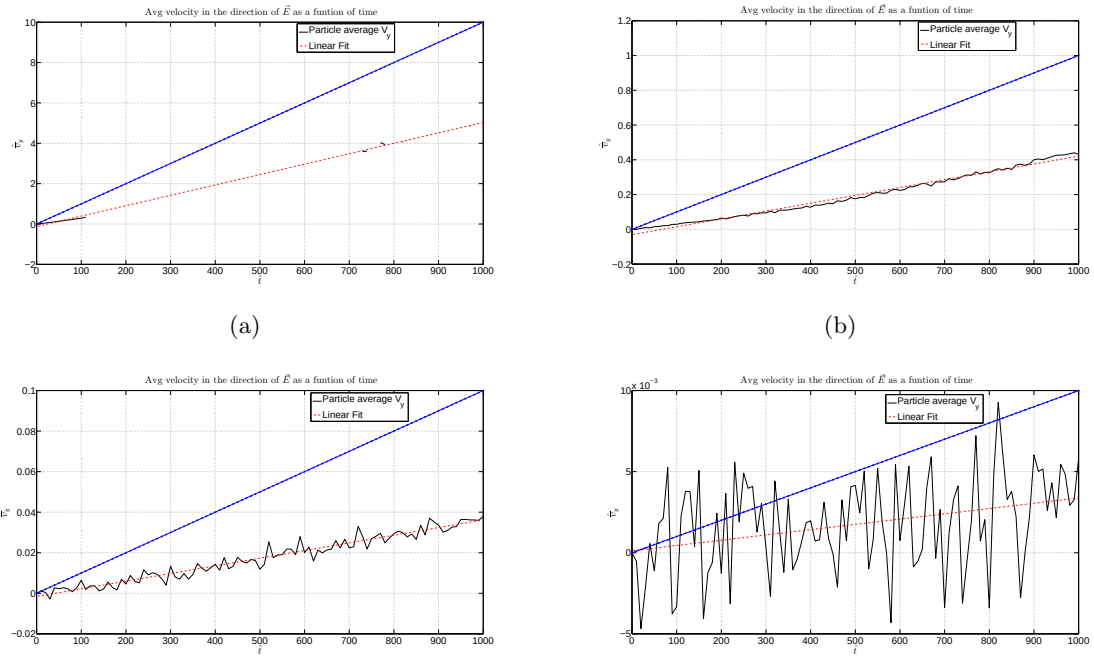

Fig. 6.5: Individual proton velocities averaged over the number of particles remaining in the chaos region at a certain time step in the direction of applied electric field for the case of X-line. Figures 6.5(a)-6.5(d) are graphs for when $E_y = .01, .001, .0001$, and $.00001$, respectively. As the numbers suggest in Table 6.2, the particle acceleration is dependent on the electric field strength. The blue lines indicate free acceleration in absence of a magnetic field. The red lines are linear fits to the given velocity data. The plots were generated using Matlab by following the procedure outlined in Appendix A and the results were fitted by utilizing the curve fitting toolbox included in Matlab. Figure 6.5(a) indicates that $E_y = .01$ is very strong and barring a few particles (see Table 6.2), most of the particles are lost. Still the fitting seems to suggest that there is a scaling of acceleration as it should with varying electric field (see Table 6.1 for the numbers). As the field gets weaker, more number of particles stay and exhibit chaotic motion in the prescribed region. Figure 6.5(d) suggests that the free acceleration lies inside the statistical noise of the model data.

Spitzer resistivity. The values calculated for the X-line with a varying electric field are given in the last column of Table 6.1. The same dynamics is observed for a oxygen ion (figs. 6.6(a)-6.6(d)). Since the ion is 16 times heavier than a proton, the acceleration is reduced by an order. Another important point to note is as indicated in Table 6.2, starting with the same number of particles in the chaos region, the number of oxygen ions left at the end of the simulation is two orders of magnitude less than that for a proton for weaker electric fields. Fits to single and double exponentials for protons and oxygen ions are given in figs. 6.7(a)-6.10(d), respectively.

6.5 Results for BCS with Varying Electric Field

As indicated by figs. 6.11(a)-6.12(d), compared to unimpeded acceleration in absence of magnetic field, the acceleration is significantly reduced due to an effective drag force due to magnetic field. The decay of protons in a BCS is plotted in figs. 6.13(a)-6.13(c). This force is effective in cases when E_y is large. For weaker electric fields (figs. 6.11(c)-6.12(d)), the action of magnetic field makes the acceleration nonlinear instead of linear as in the case of X-line. The slope of acceleration as seen in Table 6.3, is independent of the strength of the electric field. As in the case of an X-line, the heavier oxygen ion experiences an acceleration which is an order of magnitude lower than that for proton.

Figure 6.11 suggests that the free acceleration of protons is larger than that in presence of magnetic field, but for weaker electric field, the acceleration has a crossover after which the particles on average accelerate faster than free acceleration. This can also be seen in fig. 6.12, where for a heavier oxygen ion, the acceleration remains in the linear regime although one can still see the crossover. As for the X-line, experiment with different distribution functions and varying magnetic field topologies are discussed in Appendix D.

When compared to the number of particles remaining in the chaos region at the end of simulation, Tables 6.2 and 6.4 suggest that particles tend to be trapped in a BCS as compared to the X-line. This might happen because of the presence of a fairly weak but nonzero B_z for the case of BCS. The particles can be accelerated by the y directed electric field. This acceleration occurs during a small gyro period during which the particle gyrates

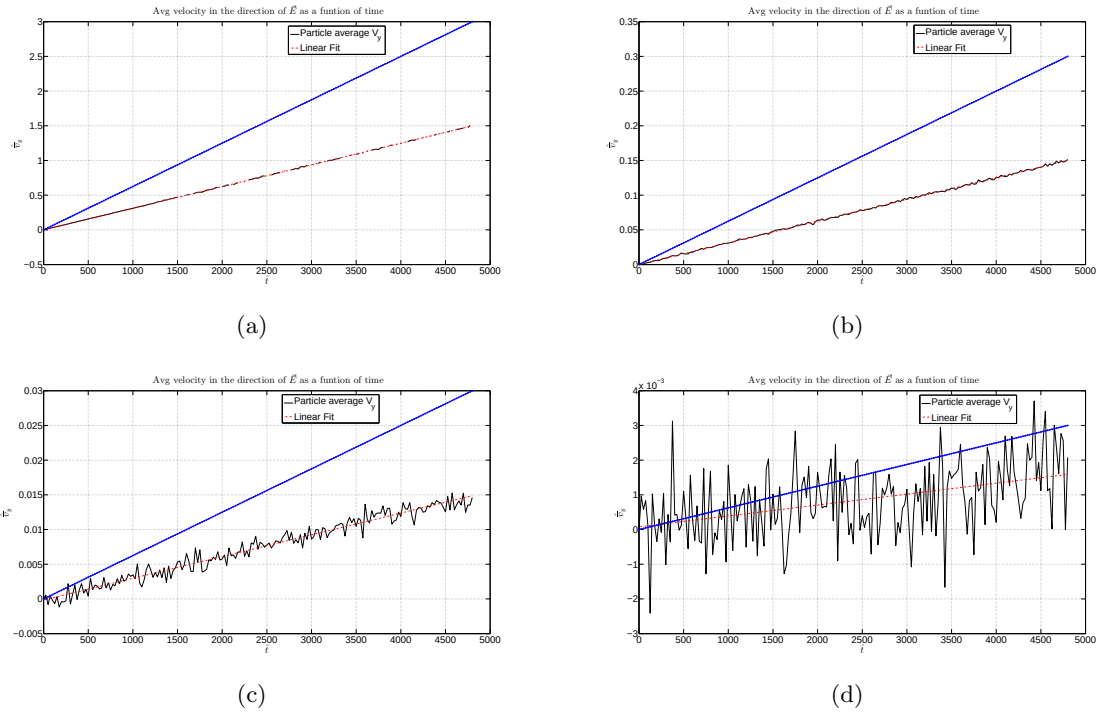

Fig. 6.6: Oxygen ion velocity in the direction of applied electric field for the case of X-line. Figures 6.6(a)-6.6(d) are graphs for when $E_y = .01, .001, .0001$, and .00001, respectively. As the numbers suggest in Table 6.2, the particle acceleration is dependent on the electric field strength. The blue lines indicate free acceleration in absence of a magnetic field. The red lines are linear fits to the given velocity data. Figure 6.6(a) again suggests that $E_y = .01$ is very strong and barring a few particles (see Table 6.2), most of the particles are lost. Still the fitting seems to suggest that there is a scaling of acceleration as it should with varying electric field (see Table 6.1 for the numbers). The plots were generated using Matlab by following the procedure outlined in Appendix A and the results were fitted by utilizing the curve fitting toolbox included in Matlab. As for protons, in fig. 6.6(d), the free acceleration line lies inside the statistical noise of average velocity but is still above the linear fit derived from the fitting tool.

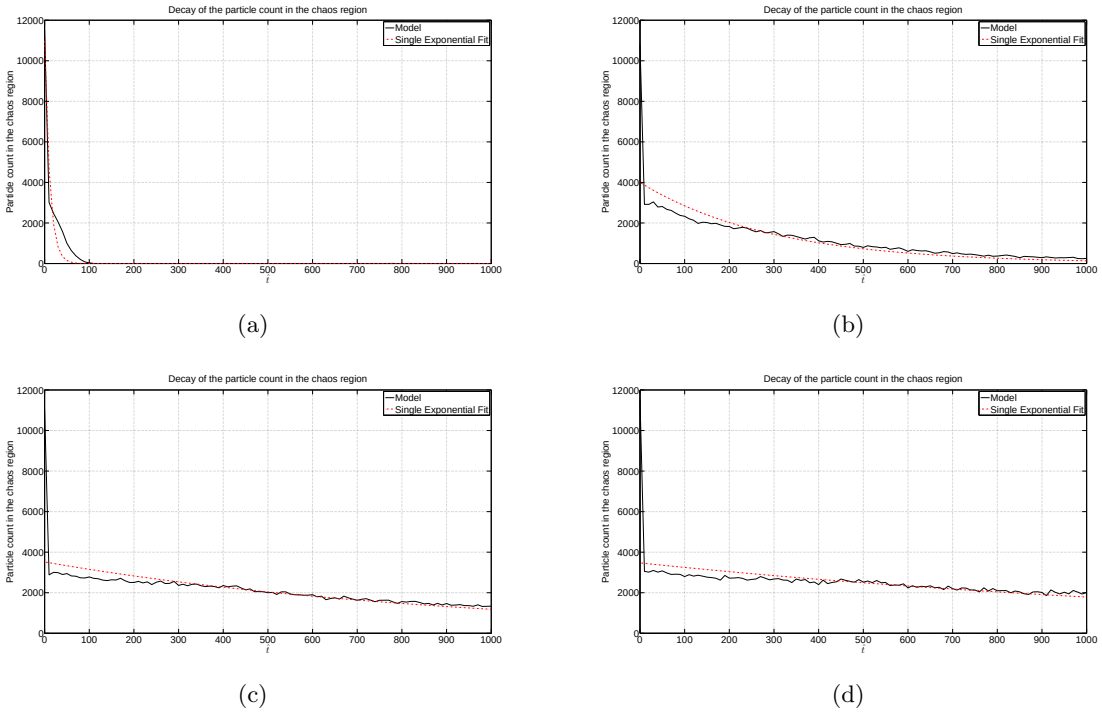

Fig. 6.7: Decay of protons inside the chaos region. The simulation is started with ≈ 10000 particles. Figures 6.7(a)-6.7(d) are plots for varying electric field E_y. The red curve is a single exponential fit to the data, the fitted numbers of which are given in column 5 of Table 6.1. The fact that the number of particles inside the chaos region are very small (0 for $E_y = .01$) is indicated by fig. 6.7(a). The decay is significantly fast in the initial time steps where the number of particles decay from approximately 10000 to around 3000 for the weaker fields. Numbers from single fit to the decay is given in Table 6.1. The plots were generated using Matlab by following the procedure outlined in Appendix A and the results were fitted by utilizing the curve fitting toolbox included in Matlab.

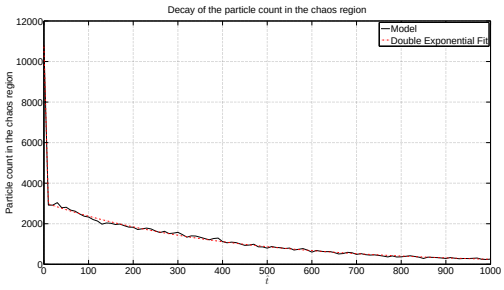

(a)

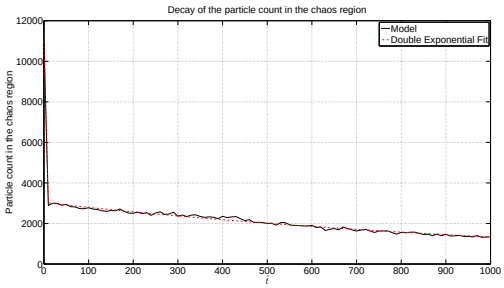

(b)

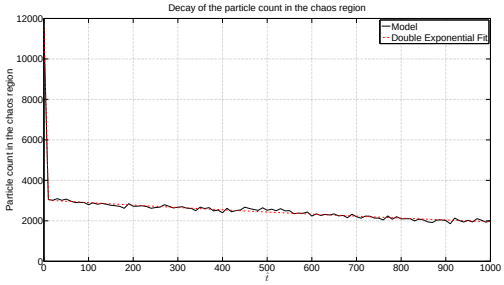

(c)

Fig. 6.8: Decay of the number of protons fitted with a double exponential. Figures 6.8(a)-6.8(c) are plots for varying electric field E_y. The red curve is a double exponential fit to the data, the fitted numbers of which are given in column 6 of Table 6.1. The first exponent is a fast intial decay and the later slow decay is fitted by the second exponent. The double exponential fit as indicated in Table 6.1 gives around the same numbers as the decay exponents as the single decay model. The plots were generated using Matlab by following the procedure outlined in Appendix A and the results were fitted by utilizing the curve fitting toolbox included in Matlab.

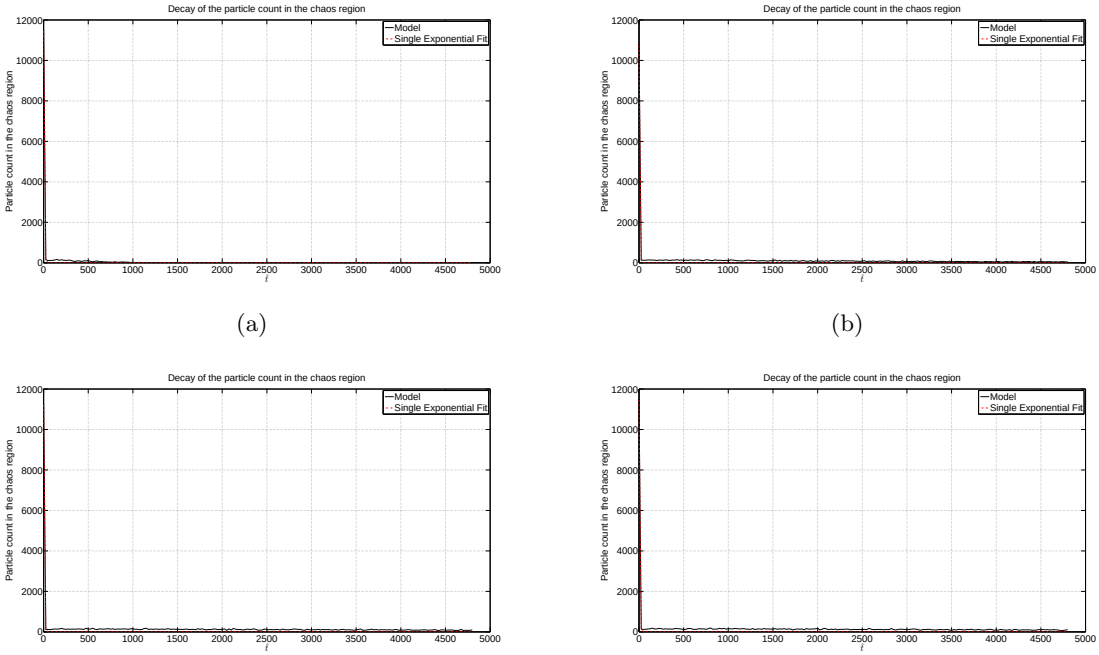

Fig. 6.9: Decay of the number of oxygen ions inside the chaos region. The simulation is started with ≈ 10000 particles. Figures 6.9(a)-6.9(d) are plots for varying electric field E_y. The red curve is a single exponential fit to the data, the fitted numbers of which are given in column 5 of Table 6.1. The plots were generated using Matlab by following the procedure outlined in Appendix A and the results were fitted by utilizing the curve fitting toolbox included in Matlab. The decay was fitted by a single exponent and as the Table 6.1, the single fit seems to be too fast a decay rate and gives resistivity orders of magnitude higher than what can be expected. This suggests that a double fit is needed for the oxygen ion.

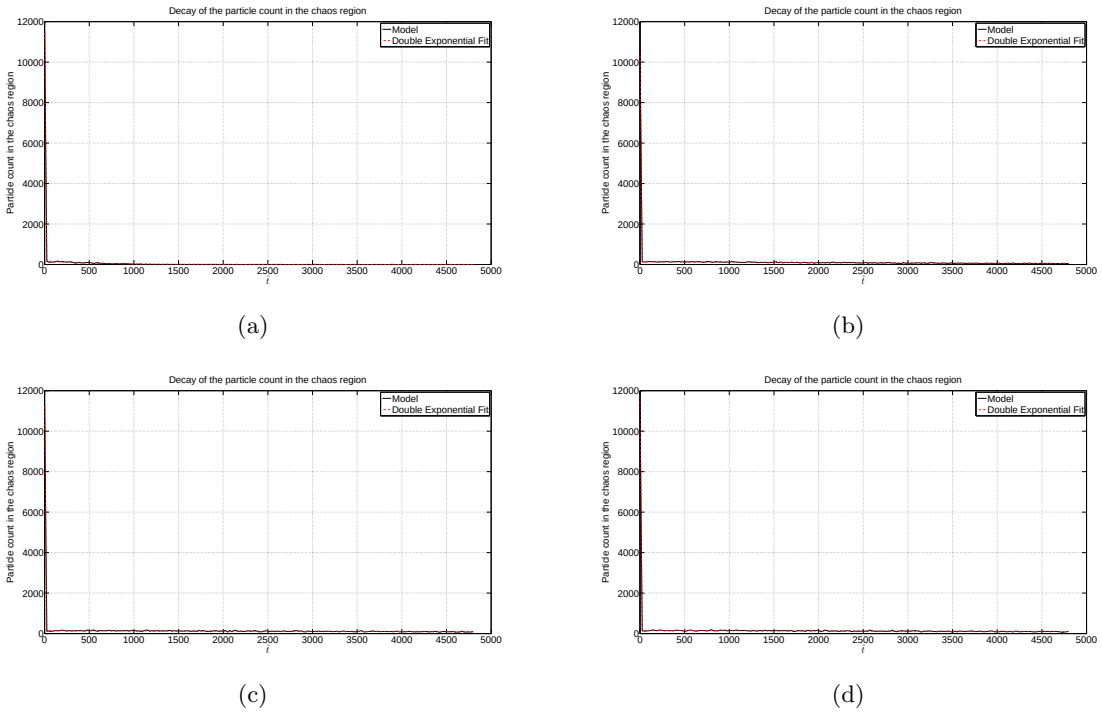

Fig. 6.10: Decay of the number of oxygen ions inside the chaos region. The simulation is started with ≈ 10000 particles. Figures 6.10(a)-6.10(d) are plots for varying electric field E_y. The red curve is a double exponential fit to the data, the fitted numbers of which are given in column 6 of Table 6.1. The exponents from a double exponential decay model of the oxygen ions from the chaos region are tabulated in Table 6.1. The last column indicates the problem with a single exponential fit and that a double exponent gives resistivity that is an order higher than that of proton. The plots were generated using Matlab by following the procedure outlined in Appendix A and the results were fitted by utilizing the curve fitting toolbox included in Matlab.

around the field with a large radius. Note that an electromagnetic drift also occurs in the x direction due to the weak B_z and E_y.

6.6 Summary of the Results Found

The model used for calculating resistivity has been described in section 6.3. Chaos region found from Chapter 4 are found to be centers of accelerating charged particles. Particles remain magnetized upto length scales on the order of the respective gyro radius. This can be seen from the trajectories traced by the charged particles in varying electric and magnetic fields in Appendix B. Since we were interested in the dynamics and resistivity on a

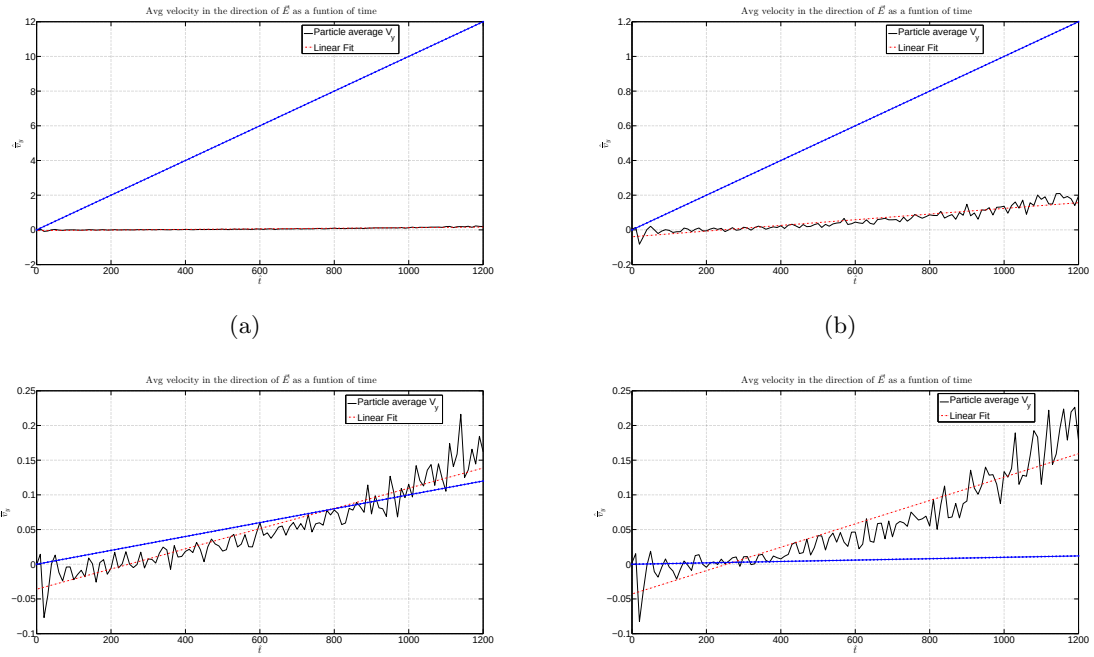

Fig. 6.11: Proton velocity in the direction of applied electric field for the case of BCS. Figures 6.11(a)-6.11(d) are graphs for when $E_y = .01, .001, .0001$, and .00001, respectively. The blue lines indicate free acceleration in absence of a magnetic field. The red lines are linear fits to the given velocity data. Using the procedure outlined in Appendix A, multiple protons were run with different initial velocities and positions, the numbers saved to a file and then averaged and plotted using Matlab. The numbers from fitting the acceleration by a linear fit are given in Table 6.3 and indicates that there is the acceleration does not depend on the electric field. This might be due to a finite B_z being present that could inhibit the acceleration.

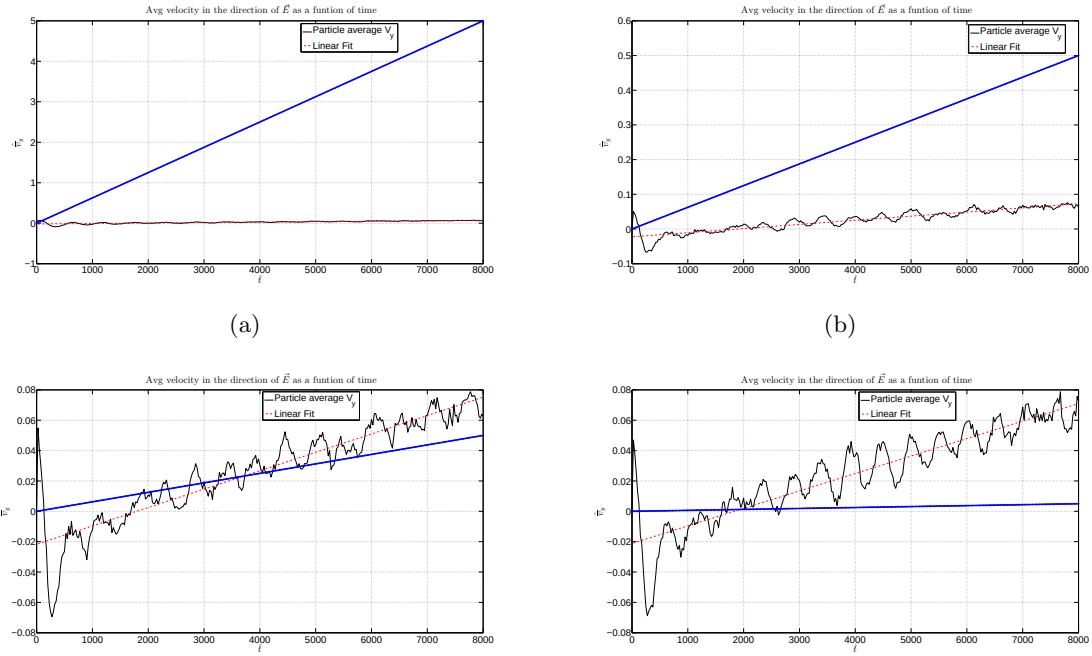

Fig. 6.12: Oxygen ion velocity in the direction of applied electric field for the case of BCS. Figures 6.12(a)-6.12(d) are graphs for when $E_y = .01, .001, .0001$, and $.00001$, respectively. As indicated in Table 6.4, the particle acceleration seems to be independent of the electric field strength. The blue lines indicate free acceleration in absence of a magnetic field. The red lines are linear fits to the given velocity data. Using the procedure outlined in Appendix A, multiple oxygen ions were run with different initial velocities and positions, the numbers saved to a file and then averaged and plotted using Matlab. The diffusion/chaos region size was not scaled w.r.t. the ion (or mass in normalized units). A more linear trend can be seen for the much heavier oxygen ion with oscillations in the average (black lines). The numbers from linear fit are given in Table 6.3.

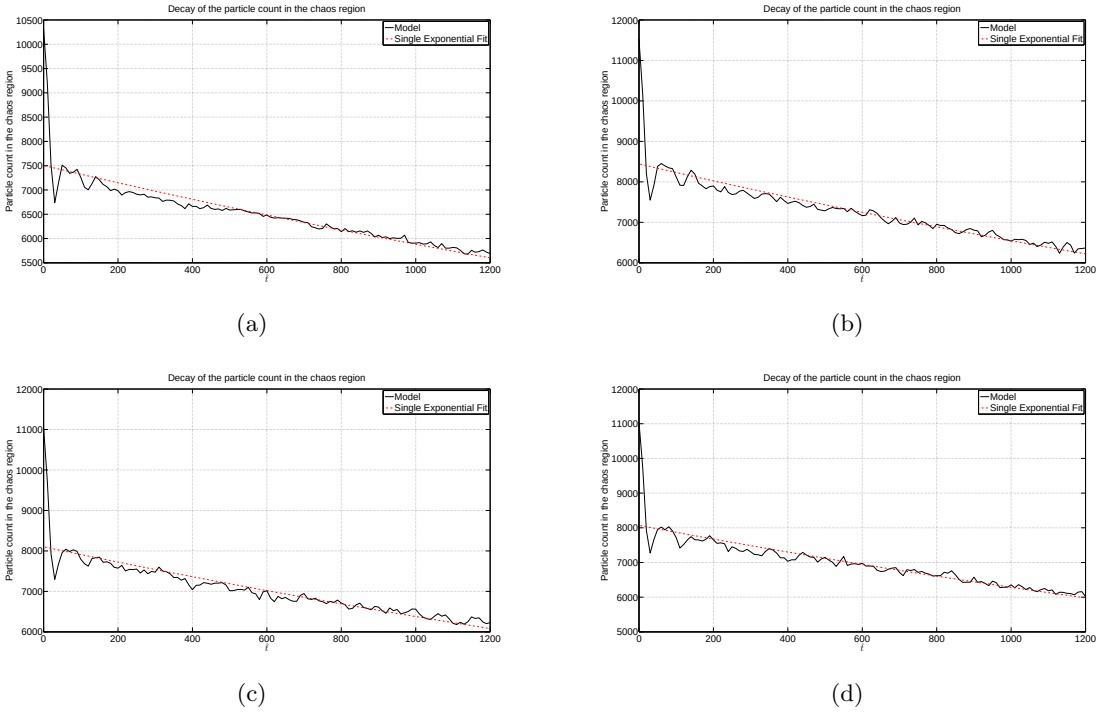

Fig. 6.13: Decay of protons inside the chaos region in a BCS. The simulation is started with ≈ 10000 particles. Figures 6.13(a)-6.13(d) are plots for varying electric field E_y. The red curve is a single exponential fit to the data, the fitted numbers of which are given in column 5 of Table 6.3. When compared to protons in the X-line, a much larger number of particles are left in the chaos region. Numbers from single exponential fits can be seen in Table 6.3. Again, very fast initial decay is followed by a slow decay during later times. The graphs were generated by proceeding according to the steps given in Appendix A and the results were plotted using Matlab and the fits were found by invoking the curve fitting toolbox.

Table 6.3: Results for starting with uniformly distributed velocity distributions for an BCS with varying strengths of E_y. This table is for when $B_z/B_0 = b_n = .2$. The double exponent numbers are for fast intial and slow final decay. The last column is the resistivity value calculated from the collisionless model and that from Spitzer's formula for collisional resistivity. η_{spit}, the Spitzer resistivity for the plasma sheet is 5.4×10^{-6} Ω/m. η_{eff}, η_{eff1} are collisionless resistivities of single and double exponential decays.

E_y	Slope (α)	Exp (β)		$\eta_{eff}, [\eta_{eff1}, \eta_{eff2}](10^3)$ (Ω/m)
		Single exponent	Double exponent	
.01	0.01186	-0.3192	-0.4798 , -0.03182	26.073, [39.19,2.5991]
.001	0.001303	-0.3145	-2.519, -0.003262	23.382, [187.28, .2425]
.0001	0.000168	-0.317	-11.2, -0.0009779	18.279, [645.83, 0.0564]
.00001	9.943e-05	-0.3112	-4.218 , -0.0006957	3.032, [41.1, 0.0068]
.01	0.0003478	NaN	NaN, NaN	NaN, [NaN, NaN]
.001	5.592e-05	-0.2051	-0.2224 , -.0002268	1776.6, [1926.4, 1.9645]
.0001	6.49e-06	-0.2075	-0.228 , -7.05e-05	1548.7, [1701.7, 0.5262]
.00001	1.134e-07	-0.2093	-0.2319, -8.401e-06	8940,[9905.3, 0.35884]

Table 6.4: Percentage number of particles remaining in the chaos region at the end of simulation as compared to the number in the starting of the simulation ($\approx$ 10000) for a BCS.

Particle	B	E_y	Count
Proton	BCS	.01	55.14 %
Proton	BCS	.001	55.27 %
Proton	BCS	.0001	56.42 %
Proton	BCS	.00001	54.49 %
Oxygen	BCS	.01	45.92 %
Oxygen	BCS	.001	46.71 %
Oxygen	BCS	.0001	46.17 %
Oxygen	BCS	.00001	46.17 %

proton diffusion/gyro scales, less number of oxygen ions were found in the chaos region due to gyro scale not being changed with the charged particle species. For an X-line, as discussed in section 6.4, the velocity in the direction of electric field was found to be linearly dependent on time (figs. 6.6 and 6.5) with the slope corresponding to the bulk acceleration. Then the fact that acceleration was calculated over the total number of particles that decayed with time meant that the a large number of particles were lost. This is also evident from the figs. 6.7 and 6.8 which shows that the number of particles decay as an exponential in the chaos region. Fits to acceleration and decay were obtained from Matlab nonlinear fitting toolbox, through which resistivities were calculated for both protons and oxygen ions as shown in Table 6.1. The numbers for resistivity indicated that the faster initial decay gave unphysical resistivity values but was essential for a good overall fit and the slower second exponential decay was responsible for resistivity generation in the X-line as seen in Table 6.1.

Resistivity calculation for the BCS was discussed in section 6.5. Using a model similar to that of an X-line, particles were tracked whenever they were found in the chaos region determined in Chapter 4. Particle average velocity as a function of time was then plotted as seen in figs. 6.11 and 6.12 for protons and oxygen ions, respectively. Although the particle average velocity could be fitted well with a linear polynomial, the figures also suggested that exponential fits to weaker electric fields could also be done. Particle trapping due to the presence of finite B_z was also evident by the periodic variations in the average velocity.

The number of particles decayed with an exponential decay that has a slow and a fast decay as for the X-line. This is shown in figs. 6.14(a)-6.16(d). The faster decay yielded unphysical resistivity values as seen in Table 6.3 but contrary to the X-line, the resistivity values were an the order of magnitude lower and varied with the strength of the electric field. Also, the acceleration scaled as M^2 when compared to X-line where it scaled with the usual M.

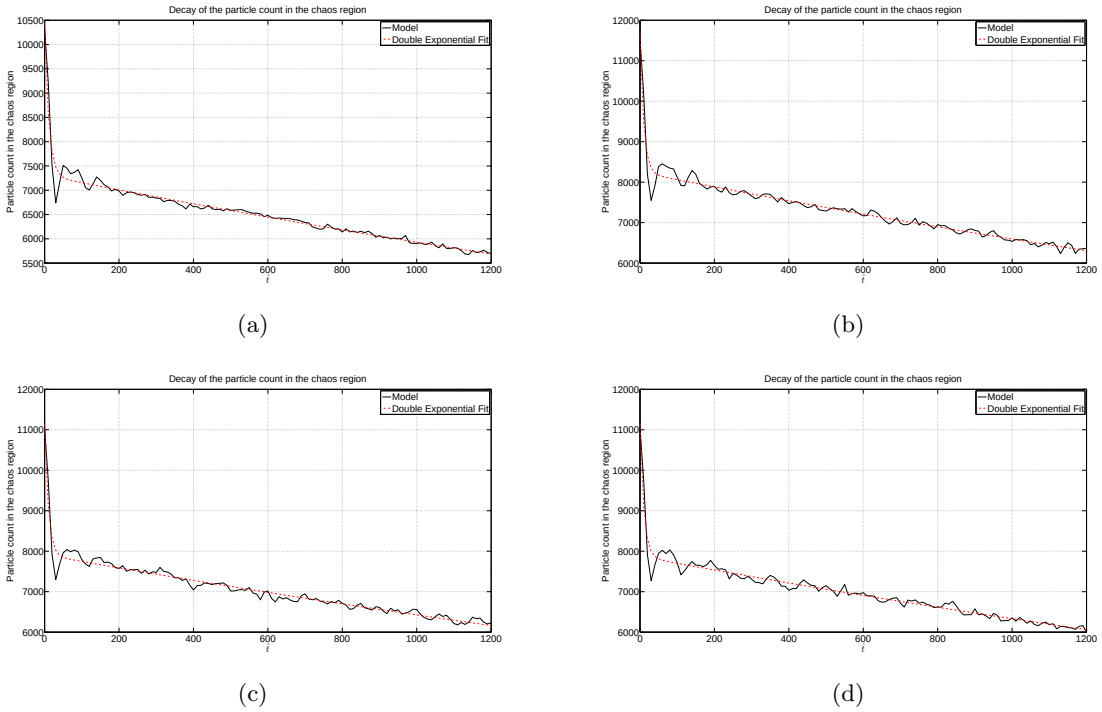

Fig. 6.14: Decay of the number of protons fitted with a double exponential. Figures 6.14(a)-6.14(d) are plots for varying electric field E_y. The red curve is a double exponential fit to the data, the fitted numbers of which are given in column 6 of Table 6.3. The graphs were generated by proceeding according to the steps given in Appendix A and the results were plotted using Matlab and the fits were found by invoking the curve fitting toolbox.

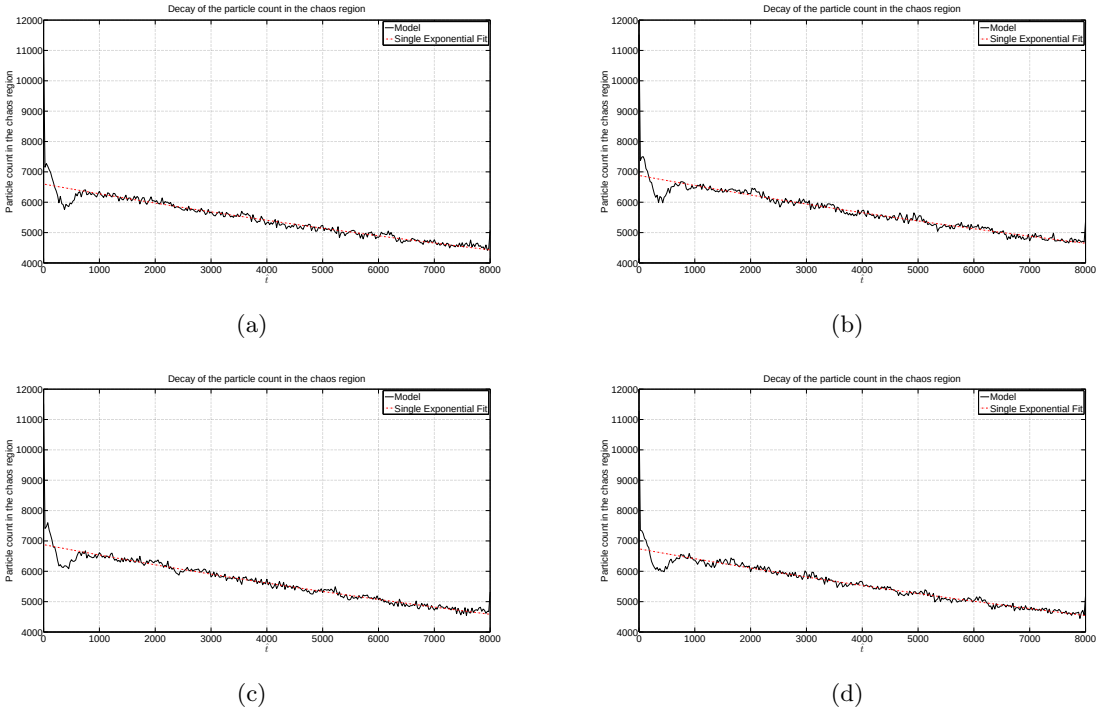

Fig. 6.15: Decay of the number of oxygen ions inside the chaos region with a Matlab fit to single exponent. The simulation is started with ≈ 10000 particles. Figures 6.15(a)-6.15(d) are plots for varying electric field E_y. The red curve is a single exponential fit to the data, the fitted numbers of which are given in column 5 of Table 6.3. The graphs were generated by proceeding according to the steps given in Appendix A and the results were plotted using Matlab and the fits were found by invoking the curve fitting toolbox.

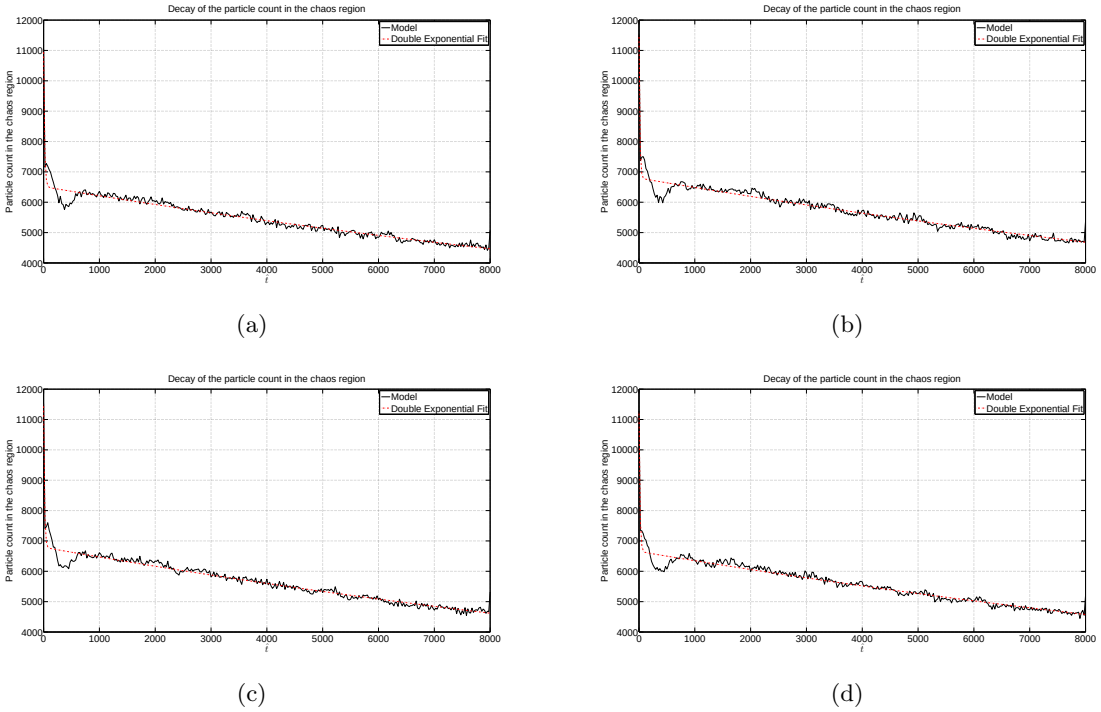

Fig. 6.16: Decay of the number of oxygen ions inside the chaos region. The simulation is started with ≈ 10000 particles. Figures 6.16(a)-6.16(d) are plots for varying electric field E_y. As indicated in the Table 6.3, the decay rate of ions from the chaos region does not change with a change in the strength of electric field. The graphs were generated by proceeding according to the steps given in Appendix A and the results were plotted using Matlab and the fits were found by invoking the curve fitting toolbox.

Chapter 7

Conclusions and Future Work

7.1 Conclusions

The two magnetic field configurations analyzed in the study namely the X-line and the BCS behaved differently with regards to location of the chaos region, types of orbits found, acceleration scaling, and resistivities. The velocity distribution functions of velocities in the three directions for an X-line were found to tend to a Maxwellian with time (Chapter 5). The velocity distribution functions for a BCS behaved differently due to presence of a weak but finite magnetic field normal to the current sheet in the z direction which made the current sheet quasi neutral (Chapter 5). This apparent dissimilarity in the evolution of the distribution functions altered the temperature profiles for the two configurations with temperature anisotropy following the electric field in the X-line but B_z for the BCS. The distributions were found to be different froms Maxwellian in a BCS with a different core temperature. Distribution of velocities in the z direction had a very strong counterstreaming beam like distribution for the oxygen ions in the case of a BCS which was not found for protons. Heavy tail was found in BCS for y directed velocity distribution. The number of particles in the chaos region and their decay was found by using the Lyapunov exponent as an indicator of chaos. While it seemed that the oxygen ions were decaying faster than the protons in the chaos region for both the configurations, it was due to the fact that the region itself was not scaled according to the particle gyro radius and therefore the oxygen ions experienced acceleration by the electric field in the region of the same dimension as the proton gyro radius. The above point implies that we were looking at the proton diffusion region (where most of the dissipation in the magnetotail during active times is supposed to occur) as scaling to a much larger (16 times) oxygen ion diffusion region would already be a macroscopic scale with the parameters of the magnetotail and we were interested in what

happens at the microscopic scales where protons are demagnetized. Particle acceleration scaled with the inertia and protons in all the runs had an average acceleration that was an order of magnitude larger than that for oxygen for the X-line. Particle acceleration scaled with the square of the inertia and protons in all the runs for a BCS and that it was two orders of magnitude larger than that for oxygen for the X-line. Hence, apart from the chaos experienced by the particle at the two current sheets, the rest of the motion is periodic (gyration around the normal magnetic field). Chaos region was found on the two humps around the location of the current sheet.

7.2 Future Work

The fact that velocity distributions in the BCS are far from Maxwellians is an avenue for further investigation. Electrons of high energies play a very important role in the substorm dynamics. Hence, they also need to be analyzed although with the magnetotail parameters, they still follow the guiding center. PIC simulations are also necessary to find the affect self-consistency (magnetic and electric fields produced by the particle interacting with the background fields). Diffusion in terms of pitch angles in the two configurations is also important with regards to observations. Running with initial conditions that depend on pitch angle, phase angle (gyration phase), and in terms of energy needs to be analyzed with regards to pitch angle distribution due to collisionless resistivity. Plasma sheet just before substorm onset is found to be turbulent which can lead to very different motion of the charged particles. Difference in resistivity values with addition of magnetic turbulence would be an important calculation.

References

[1] E. N. Parker, "Sweet's mechanism for merging magnetic fields in conducting fluids," *Journal of Geophysical Research*, vol. 62, no. 4, pp. 509–520, 1957.

[2] P. A. Sweet, "The production of high energy particles in solar flares," *Nuovo Cimento*, vol. 8, no. 2 supplement, pp. 188–196, 1958.

[3] E. Priest and T. Forbes, *Magnetic Reconnection: MHD Theory and Applications*. Cambridge: Cambridge University Press, 1999.

[4] M. Oieroset, T. D. Phan, M. Fujimoto, R. P. Lin, and R. P. Lepping, "In situ detection of collisionless reconnection in the Earth's magnetotail," *Nature*, vol. 412, no. 6845, pp. 414–417, 2001.

[5] T. G. Northrop, "Adiabatic charged-particle motion," *Reviews of Geophysics*, vol. 1, no. 3, p. 283, 1963.

[6] R. Numata and Z. Yoshida, "Chaos-induced resistivity in the magnetic null region: A nonlinear mechanism of collisionless dissipation," *Physical Review Letters*, vol. 68, no. 1, pp. 2–8, 2003.

[7] E. N. Parker, "Extension of the solar corona into interplanetary space," *Journal of Geophysical Research*, vol. 64, no. 11, pp. 1675–1681, 1959.

[8] J. W. Dungey, "Interplanetary magnetic field and the auroral zones," *Physical Review Letters*, vol. 6, pp. 47–48, 1961.

[9] H. Volland, "A semiempirical model of large-scale magnetospheric electric fields," *Journal of Geophysical Research*, vol. 78, no. 1, pp. 171–180, 1973.

[10] J. T. Gosling, D. J. McComas, and J. L. Phillips, "Geomagnetic activity associated with Earth passage of interplanetary shock disturbances and coronal mass ejections," *Journal of Geophysical Research*, vol. 96, pp. 7831–7839, 1991.

[11] W. D. Gonzalez, J. A. Joselyn, and Y. Kamide, "What is a geomagnetic storm?" *Journal of Geophysical Research*, vol. 99, no. A4, pp. 5771–5792, 1994.

[12] R. D. Elphinstone and J. S. Murphree, "What is a global auroral substorm?" *Reviews of Geophysics*, vol. 34, no. 96, pp. 169–232, 1996.

[13] G. Rostoker, S. I. Akasofu, and J. C. Foster, "Magnetospheric substorms - definition and signatures," *Journal of Geophysical Research*, vol. 85, pp. 1663–1668, 1980.

[14] R. L. McPherron, "Substorm related changes in the geomagnetic tail: The growth phase," *Planetary and Space Science*, 1972.

[15] R. Kaufmann, "Substorm currents - Growth phase and onset," *Journal of Geophysical Research*, vol. 92, no. A7, pp. 7471–7486, 1987.

[16] B. Gvozdevsky and V. A. Sergeev, "Long lasting energetic proton precipitation in the inner magnetosphere after substorms," *Journal of Geophysical Research*, vol. 102, pp. 333–338, 1997.

[17] H. J. Opgenoorth, M. A. L. Persson, T. I. Pulkkinen, and R. J. Pellinen, "Recovery phase of magnetospheric substorms and its association with morning-sector aurora," *Journal of Geophysical Research*, vol. 99, pp. 4115–4129, 1994.

[18] T. N. Davis, "Auroral electrojet activity index AE and its universal time variations," *Journal of Geophysical Research*, no. 3, 1966.

[19] D. F. Smart and M. A. Shea, "Magnetospheric models and trajectory computations," *Space Science Reviews*, pp. 305–333, 2000.

[20] E. Spencer, P. Kasturi, S. Patra, and W. Horton, "Influence of solar wind- magnetosphere coupling functions on the Dst index," *Journal of Geophysical Research*, pp. 1–13, 2011.

[21] E. Spencer and W. Horton, "The dynamics of storms and substorms with the WINDMI model," *Advances in Space Research*, vol. 38, pp. 1657–1668, 2006.

[22] A. J. Dessler, "Hydromagnetic theory of geomagnetic storms," *Journal of Geophysical Research*, vol. 64, no. 12, pp. 2239–2252, 1959.

[23] N. Sckopke, "A general relation between the energy of trapped particles and the disturbance field near the earth," *Journal of Geophysical Research*, vol. 71, no. 13, pp. 3125–3130, 1966.

[24] E. Spencer, *Analysis of geomagnetic storms and substorms with the WINDMI model*, Ph.D. dissertation, University of Texas, Austin, 2006.

[25] W. Horton and T. Tajima, "Collisionless conductivity and stochastic heating of the plasma sheet in the geomagnetic tail," *Journal of Geophysical Research*, vol. 96, 1991.

[26] W. Horton, C. Liu, B. Burns, and T. Tajima, "Collisionless plasma transport across loop magnetic fields," *Physics of Fluids B: Plasma Physics*, vol. 3, no. 8, p. 2192, 1991.

[27] D. C. Delcourt, H. V. Malova, and L. M. Zelenyi, "Dynamics of charged particles in bifurcated current sheets: The κ =1 regime," *Journal of Geophysical Research*, vol. 109, no. A01222, pp. 1–10, 2004.

[28] F. L. Scarf, L. A. Frank, K. L. Ackerson, and R. P. Lepping, "Plasma wave turbulence at distant crossings of the plasma sheet boundaries and the neutral sheet," *Geophysical Research Letters*, vol. 1, no. 5, pp. 189–192, 1974.

[29] J. E. Borovsky, M. F. Thomsen, and D. J. McComas, "The superdense plasma sheet: Plasmaspheric origin, solar wind origin, or ionospheric origin?" *Journal of Geophysical Research*, vol. 102, no. A10, pp. 22 089–22 097, 1997.

[30] I. A. Daglis, S. Livi, E. T. Sarris, and B. Wilken, "Energy density of ionospheric and solar wind origin ions in the near-Earth magnetotail during substorms," *Journal of Geophysical Research*, vol. 99, no. A4, pp. 5691–5703, 1994.

[31] K. Stasiewicz, "Finite Larmor radius effects in the magnetosphere," *Space Science Reviews*, vol. 65, pp. 221–252, 1994.

[32] P. B. Dusenbery, R. F. Martin, and G. R. Burkhart, "Particle chaos in the Earth's magnetotail," *Chaos*, vol. 2, no. 3, pp. 427–446, 1992.

[33] S. M. Thompson, M. G. Kivelson, M. El-Alaoui, A. Balogh, H. Réme, and L. M. Kistler, "Bifurcated current sheets: Statistics from Cluster magnetometer measurements," *Journal of Geophysical Research*, vol. 111, no. A3, pp. 1–26, 2006.

[34] G. Lapenta and J. U. Brackbill, "Nonlinear evolution of the lower hybrid drift instability: Current sheet thinning and kinking," *Physics of Plasmas*, vol. 9, no. 5, p. 1544, 2002.

[35] E. Camporeale, "Model of bifurcated current sheets in the Earth's magnetotail: Equilibrium and stability," *Journal of Geophysical Research*, vol. 110, pp. 1–21, 2005.

[36] S. Dalena, A. Greco, G. Zimbardo, and P. Veltri, "The role of oxygen ions in the formation of a bifurcated current sheet in the magnetotail," *Journal of Geophysical Research*, vol. 115, no. A03213, pp. 1–9, 2010.

[37] M. G. Kivelson and C. T. Russell, *Introduction to Space Physics.* Cambridge: Cambridge University Press, 1995.

[38] B. U. Sonnerup, G. Paschmann, I. Papamastorakis, N. Sckopke, G. Haerendel, S. J. Bame, J. R. Asbridge, J. T. Gosling, and C. T. Russell, "Evidence for magnetic field reconnection at the Earth's magnetopause," *Journal of Geophysical Research*, vol. 86, no. A12, pp. 10 049–10 067, 1981.

[39] J. Birn, "Computer studies of the dynamic evolution of the geomagnetic tail," *Journal of Geophysical Research*, vol. 85, no. A3, p. 1214, 1980.

[40] J. Birn and E. W. Hones Jr., "Three-dimensional computer modeling of dynamic reconnection in the geomagnetic tail," *Journal of Geophysical Research*, vol. 86, no. A8, pp. 6802–6808, 1981.

[41] R. Schunk and A. Nagy, *Ionospheres: Physics, Plasma Physics, and Chemistry.* Cambridge: Cambridge University Press, 2009.

[42] N. A. Krall and A. W. Trivelpiece, *Principles of Plasma Physics.* San Francisco: San Francisco Press, 1986.

[43] W. Baumjohann and R. A. Treumann, *Basic Space Plasma Physics*, 6th ed. London: Imperial College Press, 1996.

[44] J. A. Bittencourt, *Fundamentals of Plasma Physics*, 3rd ed. New York: Springer-Verlag, 2004.

[45] W. H. Matthaeus and S. L. Lamkin, "Turbulent magnetic reconnection," *Physics of Fluids*, vol. 29, no. 8, p. 22, 1986.

[46] D. Biskamp, E. Schwarz, and J. F. Drake, "Two-fluid theory of collisionless magnetic reconnection," *Physics of Plasmas*, vol. 4, no. 4, p. 8, 1997.

[47] D. Biskamp, *Magnetic Reconnection in Plasmas.* Cambridge: Cambridge Monographs on Plasma Physics, 1997.

[48] M. A. Shay, J. F. Drake, R. E. Denton, and D. Biskamp, "Structure of the dissipation region during collisionless magnetic reconnection," *Journal of Geophysical Research*, vol. 103, no. A5, pp. 9165–9176, 1998.

[49] J. Jackson, *Classical Electrodynamics*, 3rd ed. London: Wiley, Aug. 1998.

[50] G. Parks, *Physics Of Space Plasmas: An Introduction.* Boulder: Westview Press, 2004.

[51] A. J. Lichtenberg and M. A. Liberman, *Regular and Stochastic Motion.* New York: Springer-Verlag, 1982.

[52] S. M. Stone, *Investigation of the magnetosphere of Ganymede with Galileo's energetic particle detector*, Ph.D. dissertation, University of Kansas, 1999.

[53] G. Benettin, L. Galgani, A. Giorgilli, and J. M. Strelcyn, "Lyapunov exponents for smooth dynamical systems and Hamiltonian systems; a method for computing all of them, Part I: Theory," *Meccanica*, vol. 15, pp. 21–30, 1980.

[54] Z. Yoshida, H. Asakura, H. Kakuno, J. Morikawa, K. Takemura, S. Takizawa, and T. Uchida, "Anomalous resistance induced by chaos of electron motion and its application to plasma production," *Physical Review Letters*, vol. 81, no. 12, pp. 2458–2461, 1998.

Appendices

Appendix A

Procedure to Derive Collective Behavior from Single Particle Motion

As mentioned in Chapter 6, the main aim of this study was to derive the average behavior of particles or the fluid like collective behavior neglecting the self-consistent part. Particles are demagnetized in regions of weak magnetic fields and in presence of an imposed/inductive electric fields (which in the case of the magnetotail can be either in y or z direction), they can be accelerated along the electric field. The process of demagnetization destroys the adiabaticity of the magnetic moment (Chapter 3) and guiding center approximation is no longer valid. This happens in regions where the field line curvature is comparable to the particle gyro radius. Such a condition occurs in the magnetotail during the formation of X-line, Y-line, in parabolic sheet, and BCS.

The inherent nongyrotropic motion can be regarded as chaos in the particle orbit as a result of inhomogeneity in the magnetic field that occurs over a gyro period. Quantification of such chaos can be done by Lyapunov exponents and the ensemble behavior can be studied by evaluating the SOS (Chapter 3). The region around a weak magnetic field is chaotic but the region where most of the chaos is concentrated or where most of the demagnetization occurs will depend on the maximal Lyapunov exponent (Chapter 4). For an even ordered phase space with no external driving, presence of at least one positive exponent indicated chaos in the system. However, certain regions inside the weak field region need to be looked at more carefully with regards to the value of this exponent. For the case of a Y-line, Numata and Yoshida [6] suggested that the exponents need to be run in a circular region of radius R with initial conditions in the xz being determined by the equation $x^2+(z-l)^2 <=> R$ where $l = l_z/l_x$. By running for the exponents, they found that on and inside $R = 1$, maximum sustained chaos occurs, and this was chosen as the region for average particle acceleration

and resistivity production. In the next few sections, we shall discuss the procedure to calculate the parameters needed in eqs. (6.1) and (6.2) to get to collisionless resistivity in eq. (6.8).

The following steps are needed to get the anomalous resistivity for a given magnetotail configuration and electric field.

1. Create/find an approximate model of the magnetic field and of the electric field if it is inhomogeneous, also.

2. Solve the set of differential equations for a few different initial conditions and determine the plane through which most of the trajectories pass (say $z = 0$).

3. Plot SOS for this configuration by reducing the number of state variables (say from x, y, z, v_x, v_y, and v_z to x, z, v_x, and v_z). This is done by finding COMs using the fact that a cyclic variable leads to the conjugate momentum a COM (in this case would be y and v_y). Once done, record the value of x, v_x during the evolution of the reduced set of differential equations when the trajectory in 4D state space crosses $z = 0$. This is plotted for a given constant energy and different initial conditions. Note that since the degrees of freedom for the problem is three but since we only have two COMs (v_y and energy), the problem is essentially nonintegrable.

4. Chaotic and quasi-periodic trajectories will never close on themselves and will be a set of random points and points on a circle, respectively. If one finds that such trajectories do exist (system is ergodic for chaotic trajectories), it means that on kinetic scales (inertial scales for respective charged particles), there will be entropy generation and resistivity due to such motion.

5. To quantify this chaos and to find where in such magnetic and electric field configurations does this chaos occur, and for how much time are the charged particles to be simulated, one then needs to run Lyapunov exponents with initial conditions starting off in the region of interest. The amount of chaos is indicated by the magnitude of the largest positive exponent and one will typically get varying value of the exponent

in different regions. A stable value of this exponent indicates that the particle experiences continuous chaos in such region and this is taken as the time over which the trajectories are to be simulated.

6. After determining the region and amount of chaos, the Newton-Lorentz system of ODEs governing the motion of charged particles in magnetic and electric fields is solved and the trajectories of a larges number of particles is saved for the calculation of macroscopic quantities such as resistivity. We chose this number based on reading multiple papers to be 10000.

7. Once the equations have been solved for the time ascertained by running the Lyapunov exponent, the number of particles in the chaos region and their respective velocities in the direction of the applied electric field (for magnetotail, this would be the dawn dusk direction y) are stored at predetermined times. Along with this, velocities in the other two directions are also stored for finding the distribution function and related moments.

8. Based on these data, a graph of the total count as a function of time and the average velocity is plotted. Hence, the exponent decay of particles and the acceleration (slope of the average velocity), with exponential and linear fits from Matlab toolbox gives the numbers needed to get the collision frequency of the charged particle in an inhomogeneous magnetic field. These numbers are then put into a microscopic equations as seen in section 6.3 to find the collision frequency and collisionless resistivity.

In the next sections, the points mentioned above are enumerated upon with reference to chapters and section where information about the steps can be found.

A.1 Field Models

In this study, we are interested in calculating resistivity produced by individual particles in magnetotail like configurations mention in Chapter 2. These magnetic field topologies are found observationally in the magnetotail during different phases of solar wind driving of

the magnetosphere (i.e., during strong driving or when there is hardly anything in the solar wind with regards to density or magnetic field but only radial velocity). During substorms, the magnetotail goes through dynamic field reconfiguration which through observations indicate to bifurcated structure where instead of current peaking at the center (Harris and modified Harris sheet), it bifurcates and peaks off the center. During reconnection, the field lines look like an X-line. Using the formulations of Numata and Yoshida [6] and Delcourt et al. [27], the field equations can be written as (subsections 2.3.3 and 2.3.4),

$$\vec{\mathbf{B}} = \left[B_0\left(\frac{z \mp l_z}{l_x}\right), B_0\frac{x}{l_x}, 0\right], (|z| > l_z), \tag{A.1}$$

$$\vec{\mathbf{B}} = \left[0, B_0\left(\frac{x}{l_x}\right), 0\right], (|z| \leq l_z), \tag{A.2}$$

and

$$B_x = \frac{B_0}{2}\left(tanh\left(\frac{z + z_c}{L_{left}}\right) + tanh\left(\frac{z - z_c}{L_{right}}\right)\right), \tag{A.3}$$

$$B_y = 0, \tag{A.4}$$

$$B_z = B_n, \tag{A.5}$$

where B_0, l_x, and l_z are constants and signify the magnitude of the magnetic field far from the neutral sheet ($x = 0, |z| \leq l_z$), and the extent of bending or curvature in the magnetic field in eq. (A.1). If one were to substitute $l_z = 0$ in the above equations, we would get an X-line as seen in fig. 2.3. Similarly, $B_0, B_n, L_{right}, L_{left}$, and z_c are all constants in appropriate units in eq. (A.3). Geocentric Solar Magnetospheric (GSM) coordinates are used throughout the study where x axis points from the Earth to the Sun. The y axis is defined to be perpendicular to the Earth's magnetic dipole so that the xz plane contains the dipole axis (`http://www.spenvis.oma.be/help/background/coortran/coortran.html#GSM`). Electric field is constant and only applied along y axis or the cross-tail direction. Strength of this electric field is varied from $0.01 - 0.00001$ $[V_A B_0]$ to see the effect in the magnitude and scaling of resistivity.

A.2 Newton-Lorentz System of ODEs

Once we have a model for electric and magnetic fields, we need to find whether or not particles experience chaotic motion in the inhomogeneous field. In other words, does the guiding center approximation (section 3.2) work for the model. We are interested in looking at proton kinetic scales (which is the scale of thin current sheets during substorms) where protons get demagnetized but electrons are still frozen-in to the magnetic field. Hence, protons and oxygen ions will perform chaotic orbits in such field configurations. For constructing SOS, it is necessary to find a plane through which most or all of the trajectories pass through. This can be done by running a certain number of particles through the model by using Newton's second law and using the fact that the forcing term is due to electric and magnetic field. Using the equations from section 3.6, we have

$$m\frac{d\vec{v}}{dt} = q(\vec{E} + \vec{v} \times \vec{B}), \tag{A.6}$$

$$\frac{d\vec{x}}{dt} = \vec{v}, \tag{A.7}$$

where electric and magnetic fields are substituted for the two models.

A.3 Surface of Section (SOS)

Once the plane through which most trajectories pass is found, we then need to search the state space for what types of orbits that can exist. But since the Newton-Lorentz system has six ODEs coupled nonlinearly to each other, this would be impossible without some manipulations. The form of the equations can be used in such cases to help reduce the number of ODEs to be integrated to a lower number. This can also help in visualizing the phase space behavior on a computer as it is impossible to view the behavior in 6D space than it is on a 3D space (the trajectory would be on a plane that is a solution to the reduced ODE set). Noting that the fields in eqs. (A.1) and (A.3) depend spatially only on x and z, and y is hence the so called cyclic variable (see section 3.3). Hence, the momentum or velocity conjugate to y would be a COM. Then y is the cyclic or invariant variable. For a Harris sheet, invariant tori could be found through parametrization (adiabatic invariant).

The method is based on solving iteratively the functional equations that stand for invariance and reducibility. An approximation of an invariant torus can be found, with a fixed vector of basic frequencies and a basis along the torus that approximately reduces the normal variational equations to constant coefficients. It produces simpler and more constructive proofs that lead to more efficient numerical algorithms for the computation of these objects. Such numerical algorithms are suitable to be adapted in order to perform computer assisted proofs. Invariants that are not strictly COMs but are adiabatic invariants can be found by using such methods and even velocity space distribution functions can be found. Using this information, the ODE set is reduced to

$$\dot{x} = v_x, \tag{A.8}$$

$$\dot{v}_x = -(q_m)^2 x(1+2z), \tag{A.9}$$

$$\dot{z} = v_z, \tag{A.10}$$

$$\dot{v}_z = (q_m)^2(-x^2 - z + z^2), \tag{A.11}$$

where the v_y was integrated and the constants were taken to be zero (translation invariance). The phase space variable y is called the cyclic variable and the momntum conjugate to it is called the COM for the dynamical system. Similarly for an X-line and BCS, the equations of motion can be simplified into four ODEs involving only x, z, v_x, and v_z as $\dot{x} = v_x$, $\dot{z} = v_z$,

$$\dot{v}_x = \begin{cases} -(q_m)^2(x^2/2 - z^2/2 - zl)x, & z > l, \\ -(q_m)^2(x^2/2 - z^2/2 + zl)x, & z <= -l, \\ -(q_m)^2 x^3/2, & \text{otherwise} \end{cases} \tag{A.12}$$

$$\dot{v}_z = \begin{cases} (q_m)^2(x^2/2 - z^2/2 - zl)(z-l), & z > l, \\ (q_m)^2(x^2/2 - z^2/2 + zl)(z+l), & z <= -l, \\ 0, & \text{otherwise} \end{cases} \tag{A.13}$$

and

$$\dot{x} = v_x, \tag{A.14}$$

$$\dot{v}_x = (q_m)^2(bn(-bnx + 5/2z^4 - 3z^5 + z^6)), \tag{A.15}$$

$$\dot{z} = v_z, \tag{A.16}$$

$$\dot{v}_z = (q_m)^2(-z^3(10 - 15z + 6z^2)(-bnx + 5/2z^4 - 3z^5 + z^6))], \tag{A.17}$$

respectively. In the equations, $q_m = Q/M, l = l_z/l_x$ These equations are again solved using ODE solvers and the values of x, v_x are saved every time the trajectories cross $z = 0$. When a sufficient number of initial conditions are run through the solver, one can then construct an SOS as seen in section 4.3. As seen in fig. 4.3, unlike the modified Harris sheet, quasi-periodic orbits are absent from an X-line geometry which indicates that an X-line is strongly chaotic.

A.4 Lyapunov Exponents

To quantify the amount of chaos in a nonlinear dynamical system, Lyapunov exponents are used. Variation principle is used to study the evolution of differential equations along with how variations evolve and whether or not the phase space follows incompressible flow (Louville's theorem). Hamiltonian systems do not have attractors (not dissipative since energy being COM, is conserved) conserve phase space volume. All this information can be derived by looking at Lyapunov exponents. Repeating the example of a chaotic system, the Lorenz system, we have (see section 3.5)

$$\frac{dx}{dt} = \sigma(y - x) = f_x, \tag{A.18}$$

and

$$\frac{dy}{dt} = x(\rho - z) - y = f_y, \tag{A.19}$$

$$\frac{dz}{dt} = xy - \beta z = f_z, \tag{A.20}$$

we can write how variations in one phase space variable effect the other by way of partial derivative as say $\frac{\partial f_x}{\partial z}$. For this system, to find such variations we need 3×3 or in general $n \times n$ of such derivatives. Building up this argument leads us to the so called Jacobian which is written as (section 6.2)

$$D\vec{F} = \begin{pmatrix} \frac{\partial f_x}{\partial x} & \frac{\partial f_x}{\partial y} & \frac{\partial f_x}{\partial z} \\ \frac{\partial f_y}{\partial x} & \frac{\partial f_y}{\partial y} & \frac{\partial f_y}{\partial z} \\ \frac{\partial f_z}{\partial x} & \frac{\partial f_z}{\partial y} & \frac{\partial f_z}{\partial z} \end{pmatrix}. \tag{A.21}$$

Hence, for the Lorenz system, we have the variations as

$$D\vec{F} = \begin{pmatrix} -\sigma & \sigma & 0 \\ \rho - z & -1 & -x \\ y & x & -\beta \end{pmatrix}. \tag{A.22}$$

Also, to record how these variations evolve we would want to set up an ODE system similar to the one which tracks the trajectory in phase space as

$$\begin{pmatrix} \dot{\delta}_{xx} & \dot{\delta}_{yx} & \dot{\delta}_{zx} \\ \dot{\delta}_{xy} & \dot{\delta}_{yy} & \dot{\delta}_{zy} \\ \dot{\delta}_{xz} & \dot{\delta}_{yz} & \dot{\delta}_{zz} \end{pmatrix} = \begin{pmatrix} \frac{\partial f_x}{\partial x} & \frac{\partial f_x}{\partial y} & \frac{\partial f_x}{\partial z} \\ \frac{\partial f_y}{\partial x} & \frac{\partial f_y}{\partial y} & \frac{\partial f_y}{\partial z} \\ \frac{\partial f_z}{\partial x} & \frac{\partial f_z}{\partial y} & \frac{\partial f_z}{\partial z} \end{pmatrix} \begin{pmatrix} \delta_{xx} & \delta_{yx} & \delta_{zx} \\ \delta_{xy} & \delta_{yy} & \delta_{zy} \\ \delta_{xz} & \delta_{yz} & \delta_{zz} \end{pmatrix}. \tag{A.23}$$

To set this up in the code, we need to first evaluate the Jacobian and then evolve the extended set (phase space variables as well as the variations) with prescribed initial conditions. The code used was downloaded from `http://www.math.rsu.ru/mexmat/kvm/matds/`. The setup is such that the initial variations (RHS of eq. (A.23)) are set to unity (i.e., along the n phase space orthonormal directions for a general system). Then an ODE solver is invoked to solve the system and the variations in a given direction are summed (e.g., in the x direction due to variations in x, y, and z are $\delta_{xx}^2 + \delta_{yx}^2 + \delta_{zx}^2$) to find the expansion or contraction along a specific direction. This is the norm of the direction (say

x) that has expanded or contracted.

To get the first basis orthonormal vector for GSR mentioned in subsection 3.5.2, the first variation vector (along x direction say) is divided by the norm just found. This forms the new first vector of the basis set after a certain time step. GSR is invoked during prescribed time steps which for our problem was a fraction (.01-.001) of the gyro time. The other vectors are found using the GSR method with projections of subsequent variations on the just found orthonormal vector. To get the Lyapunov exponents, natural log of these norms are taken and divided by the time at which the normalization was done. The resultant plots of such exponents for the current sheet systems studied in this dissertation are discussed in Chapter 4. This system is a Hamiltonian system which can be proved by adding the exponents the sum of which is close to zero when the exponents are run for a sufficiently long time. By running for these exponents with different initial conditions in various parts of the magnetotail system (specifically places near current sheet where the magnetic field morphs on scales comparable to particle gyro radius), we can get the amount of chaos in the system. As seen in figs. 4.1 and 4.4, we can derive the fact that running the system for around a thousand times (normalized to gyro time) is sufficient to build up a constant amount of chaos. We can safely say that by truncating the simulation at these times can be enough for the study of chaos and resistivity production.

A.5 Evaluation of Macroscopic Quantities

Calculation of the Slope of Average Velocity, α

After finding the region of maximum chaos, macroscopic quantities such as resistivity, heat conduction, and temperature (Chapter 5), are calculated by invoking multiple particles with initial conditions chosen from uniform distributions. Individual particles are then followed through the simulation under the influence of magnetotail type magnetic (spatially inhomogeneous) and electric fields (spatially constant), both of which were time invariant and so did not require solving Maxwell's equations. At predetermined times, particle's location was checked with the region of maximum chaos and if the condition was found true

the velocity in the direction of electric field was stored. After doing this for a number of particles (10000 in number) and for two different ion species, protons and oxygen ions, the velocity was averaged over the number of particles. This was then plotted against time to evaluate the slope or the acceleration of particles as a bulk or collective fluid. The slope was the required number α in eq. (6.1).

Calculation of the Exponent of Decay, β

The procedure to calculate the number of particles in the chaos region at a given instant of time is the same as for that of average velocity. The particles were checked for at given times if they were in the chaos region. If the condition was satisfied, a counter was incremented by one and this was carried through for all the particles. In this way, the number of particles as a function of time was graphed. This curve was then fitted against single and double exponents from Matlab's nonlinear fitting toolbox and the number of the exponential decay was then substituted for as the number β in eq. (6.2).

In subsection 3.6.2, three types of orbits were found namely quasi-periodic, transient/resonant, and chaotic. This was also indicated in the SOS plot (fig. 3.17) where most of the phase space was occupied by chaotic and quasi-periodic orbits.

Appendix B

Particle Trajectories in X-line and BCS

B.1 Particle Trajectories in an X-line

The trajectories of protons for different intensity of electric field are graphed in figs. B.1(a)-B.1(d).

B.2 Charged Particle Trajectory in BCS

BCS is a different magnetotail topology compared to say the X-line. Particle trajectories inside the sheet are shown in figs. B.2(a)-B.3(d) for varying electric and magnetic fields. Figure B.2 indicates the x directed $E \times B$ drift which is due to the particle drifting perpendicular to a y directed electric field and a z directed magnetic field. Also, the magnitude of the drift reduces for a reducing strengths of electric field. For the run, the electric field is kept constant and the value of the normalized magnetic field is changed. From figs. B.3(b) and B.3(d), as B_z increases, the particle tends to get trapped for longer times inside the sheet.

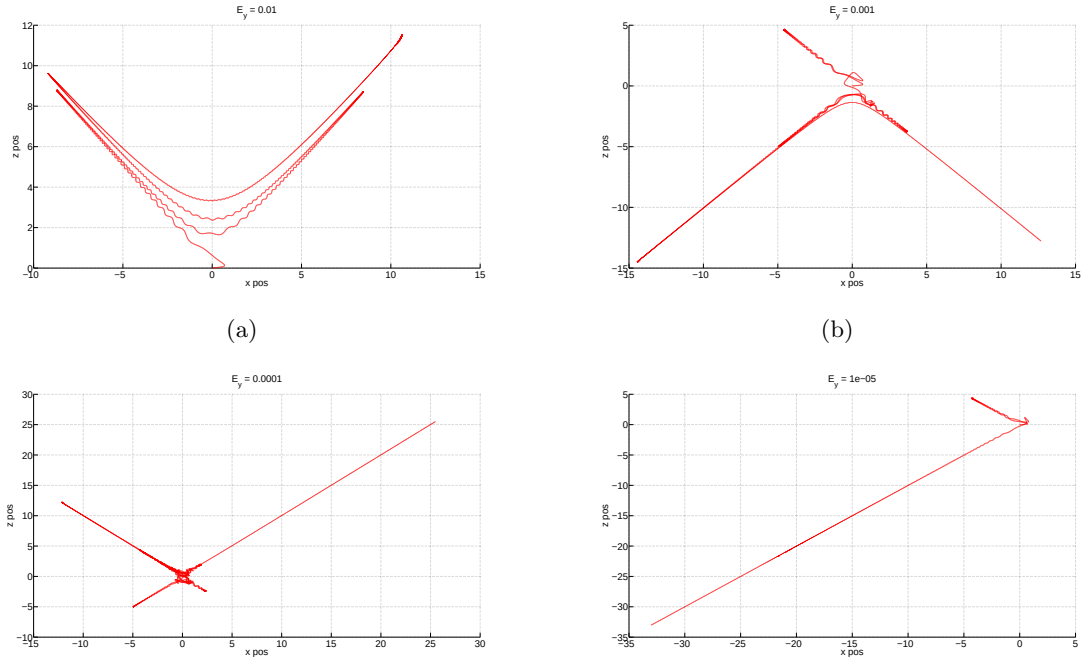

(a) (b)

(c) (d)

Fig. B.1: Typical proton trajectories in an X-line. Figures B.1(a)-B.1(d) are graphs for when $E_y = .01, .001, .0001$, and $.00001$, respectively. The initial conditions were $[\hat{x}, \hat{y}, \hat{z}, \hat{v}_x, \hat{v}_y, \hat{v}_z] = [0, 0, 0, 0.3926, 0.03756, 0.1829]$ for all the orbits. The particle is ejected from the chaos region and gyrates out into the strong field region (lobes) and is mirrored back into the chaos region. The graphs were generated using Matlab to solve the Newton-Lorentz system of equations and the spatial solutions at $y = 0$ plane were plotted using the plot command.

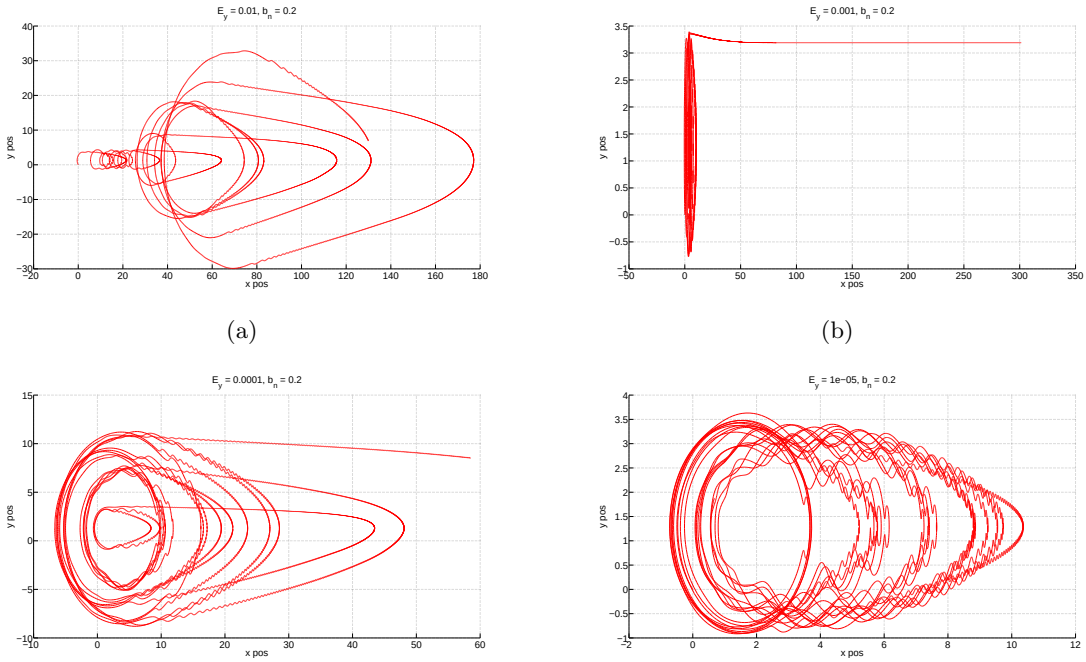

Fig. B.2: Sample proton trajectory in a BCS in the plane perpendicular to the normal magnetic field (B_z). The initial conditions chosen were $[\hat{x}, \hat{y}, \hat{z}, \hat{v}_x, \hat{v}_y, \hat{v}_z] = [0, 0, 0, -0.2584, 0.2715, 0.1997]$ for all the orbits. Figures B.2(a)-B.2(d) are trajectories for $E_y = .01, .001, .0001$, and $.00001$, respectively. The quasi-neutral sheet is where the particle is trapped in the weak North South (B_z) field and performs gyration around the field while being drifted in the direction perpendicular to electric field (i.e., in the x direction). The particle is ejected from the region and gyrates out into the strong field region (lobes) and is mirrored back into the chaos region after some bounce time. The graphs were generated using Matlab to solve the Newton-Lorentz system of equations and the spatial solutions at $z = 0$ plane (to indicate the $E \times B$ drift) were plotted using the plot command.

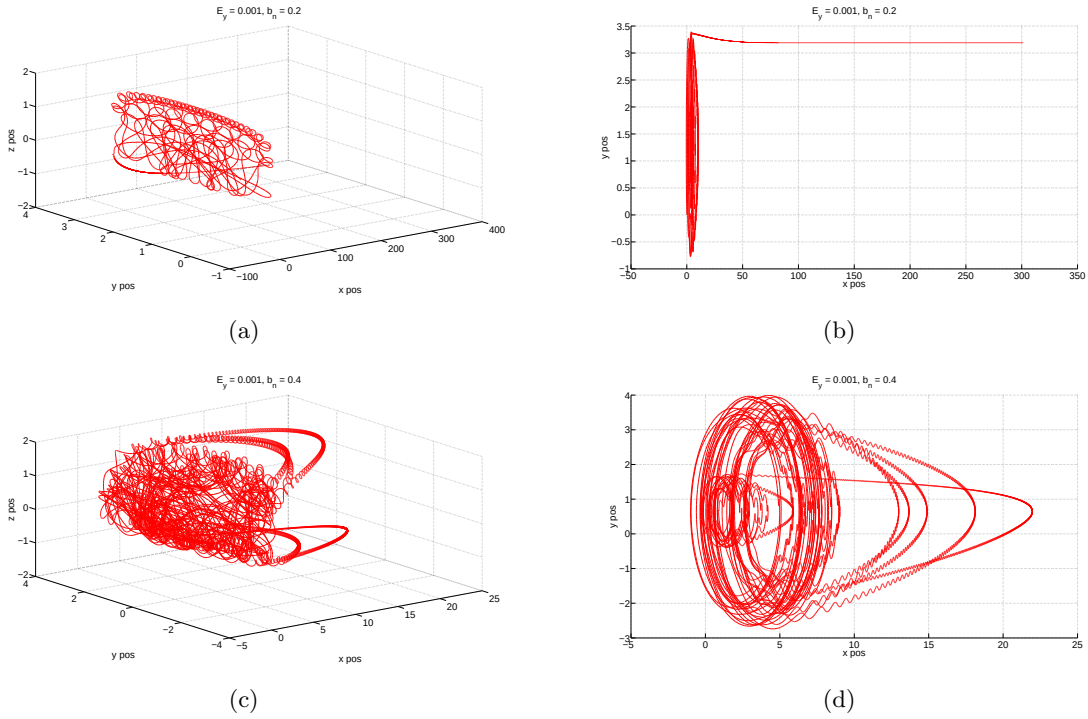

(a) (b)

(c) (d)

Fig. B.3: Sample proton trajectory in a BCS. $E_y = .001$ and the trapping effect of B_z is analyzed. The initial conditions chosen were $[\hat{x}, \hat{y}, \hat{z}, \hat{v}_x, \hat{v}_y, \hat{v}_z] = [0, 0, 0, -0.2584, 0.2715, 0.1997]$ for all the orbits. For the stronger field ($b_n = B_z/B_0 = .4$) however, the particle is trapped for the time the simulation is run and is unable to come out of the region. The graphs were generated using Matlab to solve the Newton-Lorentz system of equations and the spatial solutions (at $z = 0$ plane for figs. B.3(b) and B.3(d) to indicate the $E \times B$ drift) were plotted using the plot command.

Appendix C

Experiment with Different Initial Velocity Distributions and Shear in Magnetic Field Configuration (Initial Results) for X-line

C.1 Distribution Functions for Protons in an X-line with Shear ($B_y \neq 0$)

Protons were intialized from a uniform distribution (between $-.5$ to $.5$) with regards to their velocity in the three directions. The particles tend to settle into Maxwellians as time increases. A shear in the magnetic field configuration means that there is a finite B_y (dawn dusk) apart from x and z fields described in Chapter 2. The distribution functions are shown in figs. C.1(a)-C.1(c).

Count and Average Velocity

The electric field in y direction implies that the particles accelerate in that direction while demagnetized inside the chaos region. This is plotted in fig. C.2(a). The number of particles or the count inside the chaos region also decreases with time due to the action of the electric field. This is evident from figs. C.2(a) and C.2(b).

Fit Results for Count

Fitting numbers by using the nonlinear fitting toolbox of Matlab are given below.

General model: Double exponential f(x) = a*exp(b*x) + c*exp(d*x).

Coefficients (with 95 % confidence bounds): a = 5570 (5336, 5803) b = **-0.1345** (-0.1495, -0.1195) c = 4973 (4846, 5101) d = **-0.00365** (-0.003829, -0.00347).

Goodness of fit: SSE: 2.566e+05 R-square: 0.9971 Adjusted R-square: 0.9968 RMSE: 97.49.

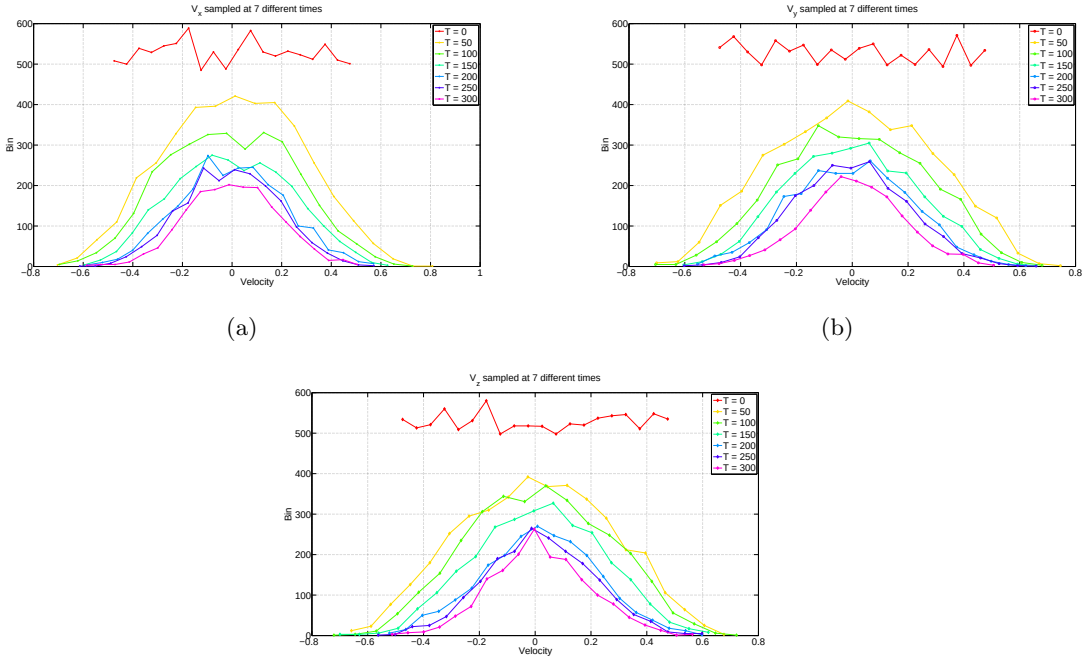

(a) (b)

(c)

Fig. C.1: V_x, V_y, and V_z distribution at different times. As seen in the figures, the initial uniform distributions isotropize to Maxwellians with finite temperatures (not shown) in all the three directions. The isotropization which in Lorentz gas would be due to collisions occurs in this collisionless environment due to inhomogeneities in the magnetic field on the order of particle gyro radius because of which particles are lost from the chaos region. The figures were generated by saving the number of particles at a given time step which are found in the chaos region and then plotting a histogram of the saved particles in Matlab.

The fit indicates that there is a two fold decay with a faster intial and a slower decay of the particles.

Fit Results (Average V)

The fit to the average velocity in the chaos region was calculated in Matlab.

Linear model: Linear polynomial f(x) = p1*x + p2.

Coefficients (with 95 % confidence bounds): p1 = **3.886e-06** (1.361e-06, 6.412e-06) p2 = -0.0002225 (-0.0006636, 0.0002185).

Goodness of fit: SSE: 1.097e-05 R-square: 0.2546 Adjusted R-square: 0.2289 RMSE: 0.0006149.

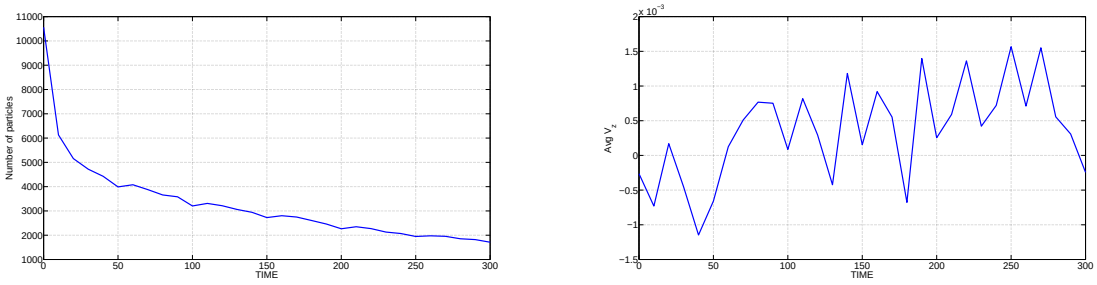

(a) (b)

Fig. C.2: The number of particles in the chaos region as a function of time (started with around 10000 protons) in an X-line with shear in the magnetic topology ($B_y \neq 0$) (fig. C.2(a)). Figure C.2(b) is a plot of the average velocity in the direction of electric field (E_z) of the particles remaining in the chaos region. The plots indicate that the number of particles decay in the chaos region which can be best fitted by an exponential model and that they are accelerated by the electric field during their demagnetization. The plots were generated using the procedure outlined in Appendix A and the results were plotted using Matlab.

The slope of fig C.2(b) which gives the acceleration that the particles as bulk fluid experience is around **3.886e-06** normalized to the appropriate units.

C.2 Oxygen Ions in a Sheared X-line with Initial Uniform Velocity Distributions

Starting again with uniform distributions for velocities, with the heavier oxygen ion, the particle distribution functions can be seen in figs. C.3(a)-C.3(c). The evolution in time shows that the asymptotic distribution is again close to a Maxwellian.

Count and Average Velocity Fits

The electric field in y direction implies that the particles accelerate in that direction while demagnetized inside the chaos region. This is plotted in fig. C.4(a). The number of particles or the count inside the chaos region also decreases with time due to the action of the electric field. This is evident from fig. C.4(a). Figure C.4(b) is a plot of the average velocity in the direction of electric field (E_z) of the particles remaining in the chaos region.

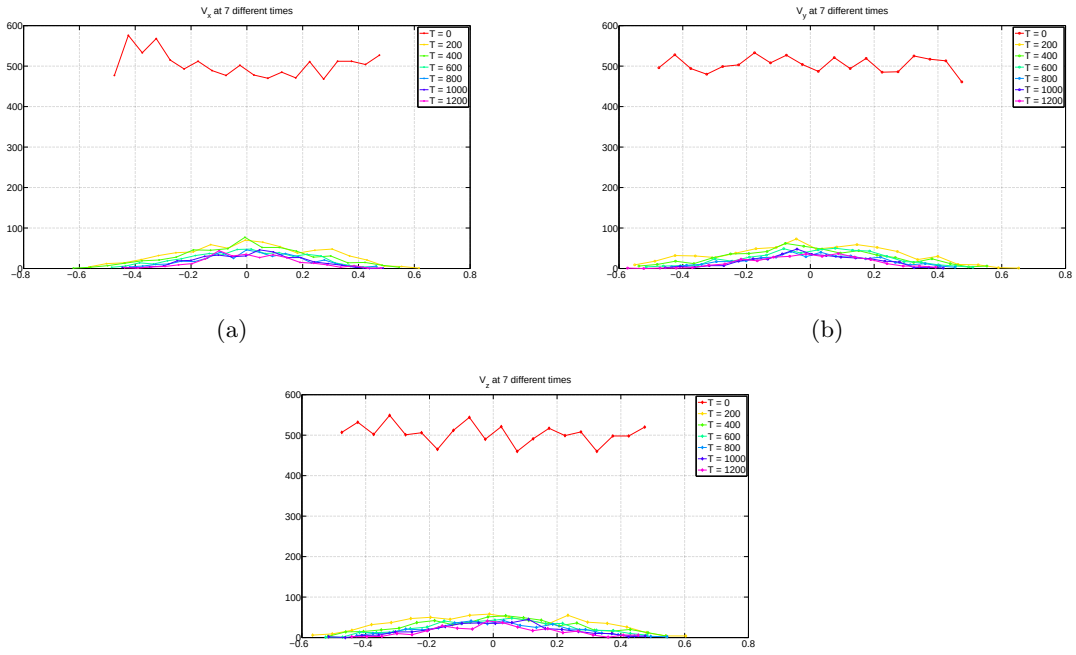

(a) (b)

(c)

Fig. C.3: V_x, V_y, and V_z distributions at different times for oxygen ions. As seen in the figures, the initial uniform distributions isotropize to Maxwellians with finite temperatures (not shown) in all the three directions. The figures were generated by saving the number of particles at a given time step which are found in the chaos region and then plotting a histogram of the saved particles in Matlab.

Fit to Count

The number of particles remaining in the chaos region as a function of time is plotted in fig. C.4(a). Again the decay follows two exponentials with the initial decay faster than that for protons which could indicate towards physics on multiple time scales. The fitted model does an average job.

The exponent numbers are given below.

General model Exp2: f(x) = a*exp(b*x) + c*exp(d*x).

Coefficients (with 95 % confidence bounds): a = 9219 (9153, 9285) b = **-0.08165** (-0.08627, -0.07703) c = 861.1 (829.1, 893) d = **-0.0008811** (-0.0009484, -0.0008138).

Goodness of fit: SSE: 2.154e+04 R-square: 0.9998 Adjusted R-square: 0.9997 RMSE: 28.25.

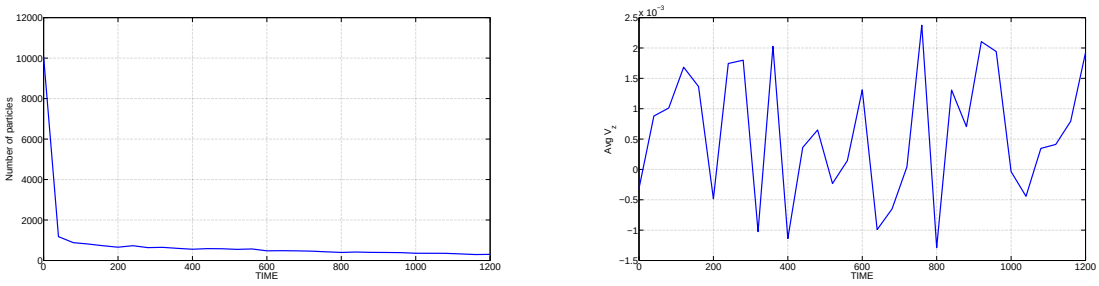

(a) (b)

Fig. C.4: The number of particles in the chaos region as a function of time ($\approx$ 10000 oxygen ions) in an X-line with shear in the magnetic topology ($B_y \neq 0$) (fig. C.4(a)). Figure C.4(b) is a plot of the average velocity in the direction of electric field (E_z) of the particles remaining in the chaos region. The plots indicate that the number of particles decay in the chaos region which can be best fitted by an exponential model and that they are accelerated by the electric field during their demagnetization. The plots were generated using the procedure outlined in Appendix A and the results were plotted using Matlab. Due to a larger inertia, the oxygen ions accelerate to a much weaker value compared to protons.

Average V_z Fit

Due to the oxygen ion being 16 times heavier than the proton, the acceleration is very slow and a linear fit to the average velocity gives a number approximately an order of magnitude lower than that for a proton.

Linear model Poly1: f(x) = p1*x + p2.

Coefficients (with 95 % confidence bounds): p1 = **8.657e-08** (-1.041e-06, 1.214e-06) p2 = 0.0005392 (-0.0002486, 0.001327).

Goodness of fit: SSE: 3.498e-05 R-square: 0.0008494 Adjusted R-square: -0.0336 RMSE: 0.001098.

C.3 Protons in X-line with Counterstreaming Velocity Distributions

This section deals with results from when a different initial distribution was assumed for the velocities. We have experimented with Maxwellians and the one discussed in this section. As seen in figs. C.5(a)-C.5(c), a counterstreaming distribution (beam distribution) has velocities randomly distributed around two Maxwellian distributions.

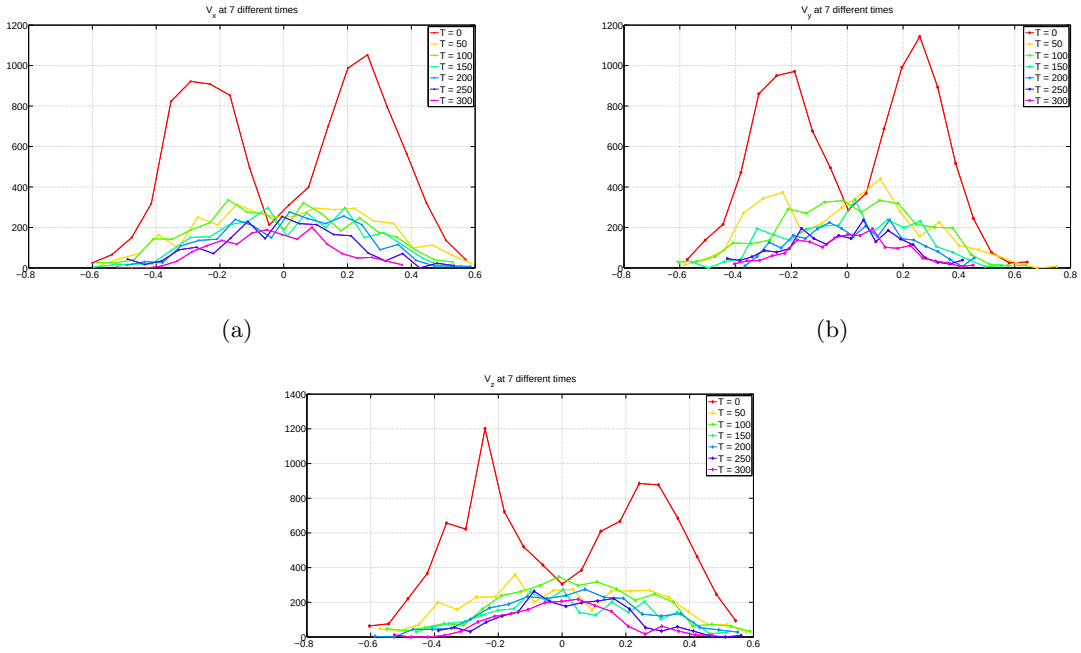

(a) (b)

(c)

Fig. C.5: V_x, V_y, and V_z distribution at different times for protons with counterstreaming beams as initial distribution in the three directions. As seen in the figures, the initial uniform distributions isotropize to Maxwellians with finite temperatures (not shown) in all the three directions. The figures were generated by saving the number of particles at a given time step which are found in the chaos region and then plotting a histogram of the saved particles in Matlab.

Fit to Count

A decay of the initial distribution accompanies decay of particles inside the chaos region. The exponent of the slow decay is around the number found by Numata and Yoshida [6]. Again a double exponential decay seems to fit the decay.

General model Exp2: f(x) = a*exp(b*x) + c*exp(d*x).

Coefficients (with 95 % confidence bounds): a = 5215 (4785, 5645) b = **-0.13** (-0.1581, -0.1019) c = 4838 (4607, 5070) d = **-0.003308** (-0.003632, -0.002983).

Goodness of fit: SSE: 8.821e+05 R-square: 0.9887 Adjusted R-square: 0.9875 RMSE: 180.7.

Average V_z Fit

The protons accelerate in the direction of the electric field as seen from the positive slope of the linear fit p1. This number is an order of magnitude lower than what was found for a uniform distribution. The number of particles in the chaos region as a function of time (started with around 10000 ions) in an X-line with shear in the magnetic topology is shown in fig. C.6(a). Figure C.6(b) is a plot of the average velocity in the direction of electric field (E_z) of the particles remaining in the chaos region. Particle acceleration is not that evident in the figure but decay follows an exponential function with a negative exponent.

Linear model Poly1: f(x) = p1*x + p2.

Coefficients (with 95 % confidence bounds): p1 = **-3.787e-07** (-2.859e-06, 2.101e-06) p2 = 0.0004092 (-2.384e-05, 0.0008423).

Goodness of fit: SSE: 1.057e-05 R-square: 0.003353 Adjusted R-square: -0.03101 RMSE: 0.0006038.

C.4 Oxygen Beam Distributions in an X-line

The oxygen was initialized with the same beam distribution in the three velocity directions as shown in figs. C.7(a)-C.7(c). Again, the beam average velocity was kept at $\pm.3$ V_A. Both the beams have a finite temperature with velocities randomly distributed around the average values.

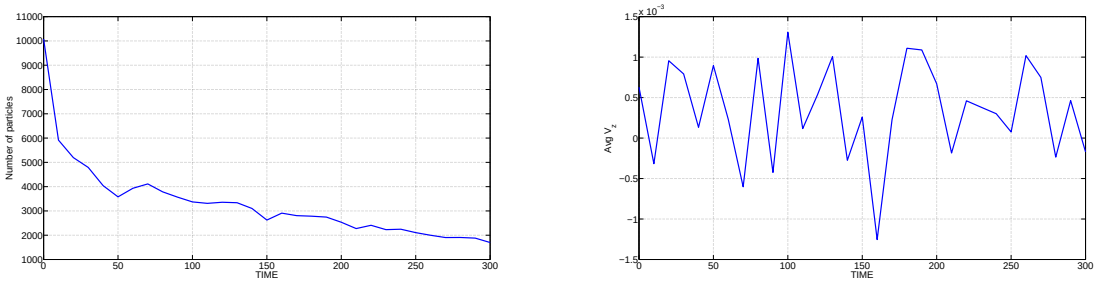

(a) (b)

Fig. C.6: The number of particles in the chaos region as a function of time (started with around 10000 ions) in an X-line with shear in the magnetic topology (fig. C.6(a)). Figure C.6(b) is a plot of the average velocity in the direction of electric field (E_z) of the particles remaining in the chaos region. The plots were generated using the procedure outlined in Appendix A and the results were plotted using Matlab. Compared to fig. C.2, the acceleration appears to be weaker.

Fit to Count

The number of particles in the chaos region as a function of time (started with around 10000 oxygen ions) in an X-line are shown in fig. C.8(a). The number of oxygen ions decay smoothly but with double exponential decay as seen from the numbers given below.

General model Exp2: f(x) = a*exp(b*x) + c*exp(d*x).

Coefficients (with 95 % confidence bounds): a = 9101 (8824, 9377) b = **-0.0289** (-0.03105, -0.02674) c = 938.8 (768.2, 1109) d = **-0.001197** (-0.001536, -0.0008584).

Goodness of fit: SSE: 3.283e+05 R-square: 0.9967 Adjusted R-square: 0.9963 RMSE: 110.3. R-square values indicate that a double exponent models the decay of particles from the choas region very well.

Average V_z Fit

On average the ions are accelerated in the direction of electric field. The jaggedness in fig. C.8(b) suggests that the acceleration is very weak.

Linear model Poly1: f(x) = p1*x + p2.

Coefficients (with 95 % confidence bounds): p1 = **2.746e-07** (-2.535e-07, 8.028e-07) p2 = 5.686e-06 (-0.0003632, 0.0003746).

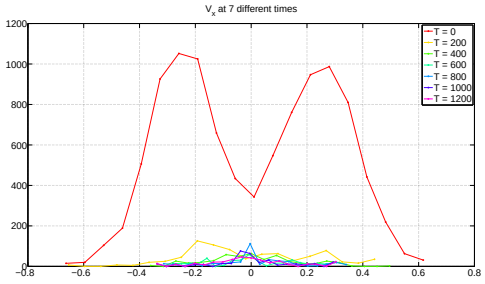

(a)

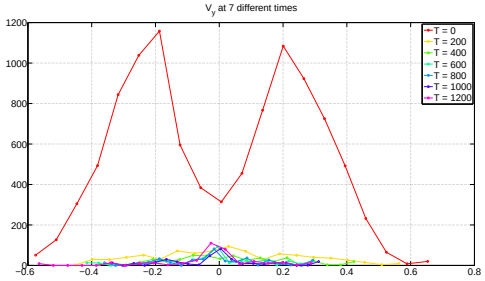

(b)

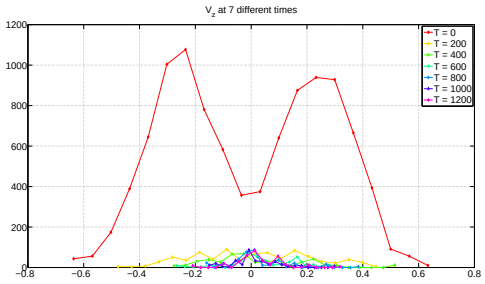

(c)

Fig. C.7: V_x, V_y, and V_z distribution at different times for oxygen ions for a counterstreaming beam like distribution. As seen in the figures, the initial uniform distributions isotropize to Maxwellians with finite temperatures (not shown) in all the three directions. The isotropization which in Lorentz gas would be due to collisions occurs in this collisionless environment due to inhomogeneities in the magnetic field on the order of particle gyro radius because of which particles are lost from the chaos region. The figures were generated by saving the number of particles at a given time step which are found in the chaos region and then plotting a histogram of the saved particles in Matlab. Since the diffusion region (chaos region) does not scale with the particle type, much larger number of oxygen ions are lost from the chaos region as can also be seen in fig. C.8(a).

Goodness of fit: SSE: 7.673e-06 R-square: 0.03754 Adjusted R-square: 0.004356 RMSE: 0.0005144.

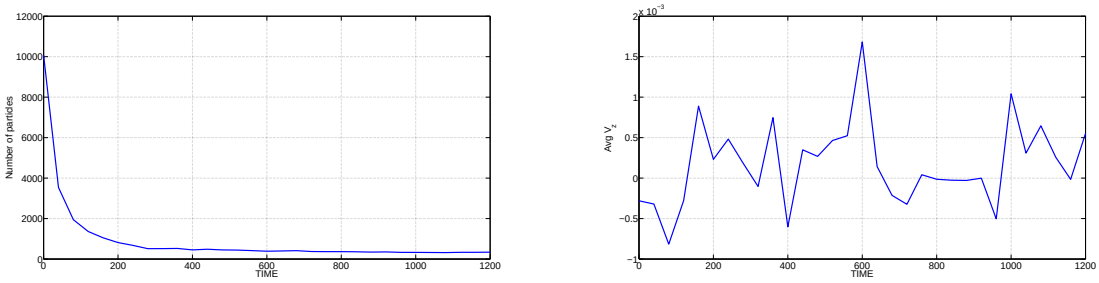

(a) (b)

Fig. C.8: The number of particles in the chaos region as a function of time (started with around 10000 oxygen ions) in an X-line (fig. C.8(a)). Figure C.8(b) is a plot of the average velocity in the direction of electric field (E_z) of the particles remaining in the chaos region. The plots indicate that the number of particles decay in the chaos region which can be best fitted by an exponential model and that they are accelerated by the electric field during their demagnetization. The plots were generated using the procedure outlined in Appendix A and the results were plotted using Matlab.

Appendix D

Experiment with Different Initial Velocity Distributions and Shear in Magnetic Field Configuration (Initial Results) for a BCS

D.1 Convection E (E_y) with Oxygen Ions (Beam Distribution)

BCS configuration is discussed in Chapter 2. With the two humps in the field when compared to the modified Harris sheet, the particle will tend to get demagnetized at and around these humps. When the oxygen ion was initialized with a beam distribution inside the current sheet, we got the velocity distributions shown in figs. D.1(a)-D.1(c). There is a difference from the velocity distributions found in the case of X-line. As the particle gyrates in the direction perpendicular to the magnetic field (which in this case is the z direction), the velocity distribution in that direction tends to and stays at around a distribution with two average velocities.

Fit to Count

As seen in figs. D.2(a) and D.2(b), there are a lot more features in the decay of particles from the current sheet. This apparent jaggedness might be due to the trapping of particles by B_z inside the current sheet. Hence, the particle gyrates and goes out of the sheet to come back periodically into the sheet again. The numbers again point to a two phased decay of the count in the sheet as seen from the numbers in bold.

General model Exp2: f(x) = a*exp(b*x) + c*exp(d*x).

Coefficients (with 95 % confidence bounds): a = 2.489e+13 (-1.815e+22, 1.815e+22) b = **-22.49** (-7.29e+08, 7.29e+08) c = 7601 (7379, 7824) d = **-0.0113** (-0.01289, -0.009716).

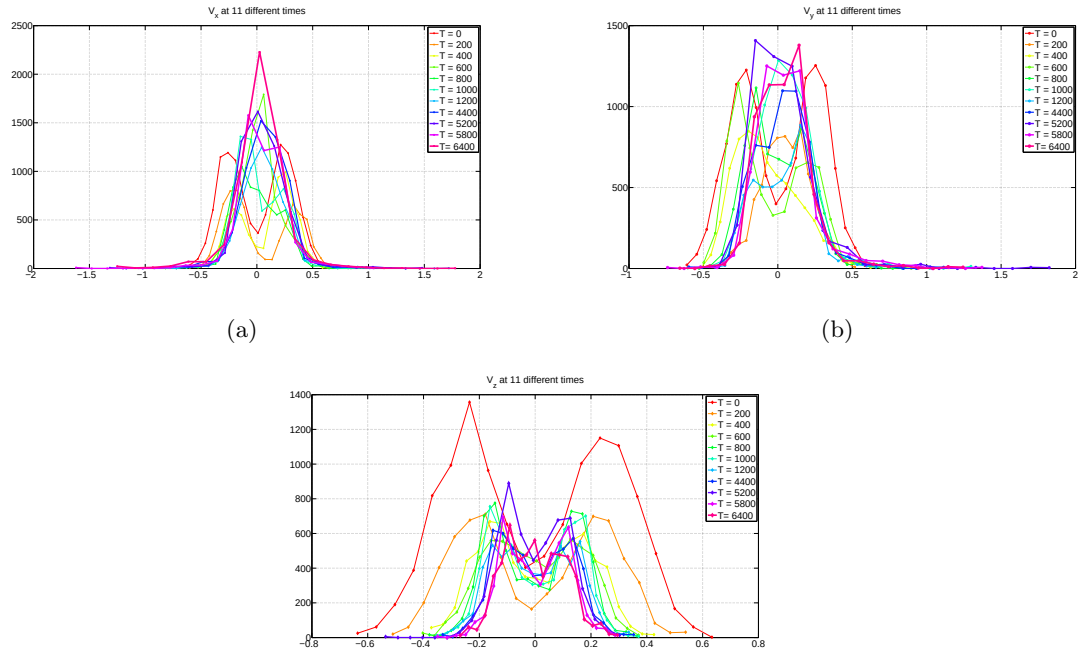

(a) (b)

(c)

Fig. D.1: V_x, V_y, and V_z distribution at different times for oxygen ions initialized from beam distributions in a BCS. As seen in the figures, the initial uniform distributions isotropize to Maxwellians with finite temperatures (not shown) in all the three directions. The isotropization which in Lorentz gas would be due to collisions occurs in this collisionless environment due to inhomogeneities in the magnetic field on the order of particle gyro radius because of which particles are lost from the chaos region. The figures were generated by saving the number of particles at a given time step which are found in the chaos region and then plotting a histogram of the saved particles in Matlab.

Goodness of fit: SSE: 1.659e+06 R-square: 0.9628 Adjusted R-square: 0.959 RMSE: 239.2.

Average V_y Fit

Average velocity in the direction of the electric field has a positive slope as found from the linear fit from Matlab. The particles on average tend to accelerate in the direction of electric field. This is because the particle is free to move in the direction of electric field in a weak field region.

Linear model Poly1: f(x) = p1*x + p2.

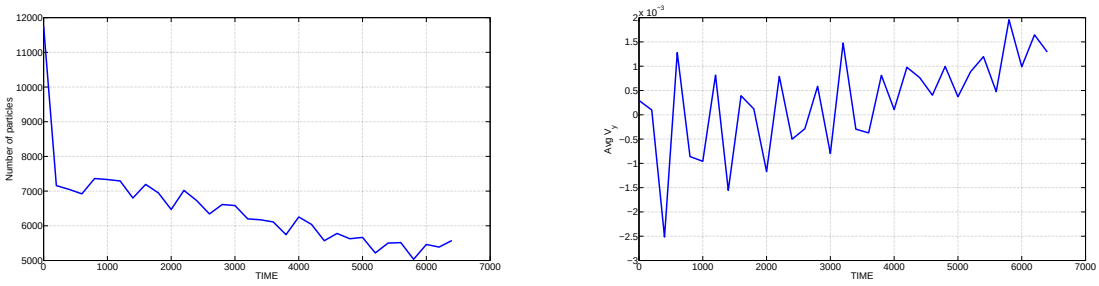

(a) (b)

Fig. D.2: The number of particles in the chaos region as a function of time in a BCS (fig. D.2(a)). Figure D.2(b) is a plot of the average velocity in the direction of electric field (E_y) of the particles remaining in the chaos region. The plots were generated using the procedure outlined in Appendix A and the results were plotted using Matlab. The decay seems to follow a pattern of particles returning after sometime into the chaos region.

Coefficients (with 95 % confidence bounds): p1 = **5.969e-05** (2.938e-05, 9e-05) p2 = -0.0007294 (-0.00132, -0.0001388).

Goodness of fit: SSE: 2.049e-05 R-square: 0.3422 Adjusted R-square: 0.321 RMSE: 0.0008129.

D.2 Convection E (E_y) for Oxygen Ions with Beam Distribution and Shear (Finite B_y) in BCS

A shear in the BCS implies that there is a nonzero magnetic field in the dawn dusk direction (y along with the electric field). A shear in the magnetic field tends to rotate the current sheet by an angle given by $\theta = tan^{-1}(B_z/B_y)$. The particle ejection from the current sheet and the overall phase space dynamics can be altered by the inclusion of a finite shear.

Distribution Function

The velocity distributions tend to follow the results as found before but with one added feature. The velocity distribution in the direction of the shear tends to have an elongated tail. The temperature in the direction (not shown) also suggests that this might be a

nonthermal distribution. Also, as seen in figs. D.3(a)-D.3(c), the distribution tends to remain as a beam like distribution with the reduction indicating that the particles lost.

Fit to Count

The decay in the number of particles can be seen in fig. D.4(a). When compared to the decay when no shear was included, the so called periodicity in the particles ejected and coming back into the sheet seems to be altered by the finite shear.

General model Exp2: f(x) = a*exp(b*x) + c*exp(d*x).

Coefficients (with 95 % confidence bounds): a = 3.708e+15 (-4.908e+26, 4.908e+26) b = **-27.58** (-1.324e+11, 1.324e+11) c = 7501 (7265, 7737) d = **-0.01496** (-0.01671, -0.0132). Goodness of fit: SSE: 1.726e+06 R-square: 0.9663 Adjusted R-square: 0.9628 RMSE: 244.

Average V_y Fit

The slope of the average velocity (fig. D.4(b)) does not seem to be altered by the inclusion of a finite shear as seen from the numbers below.

Linear model Poly1: f(x) = p1*x + p2.

Coefficients (with 95p1 = **6.294e-05** (3.573e-05, 9.014e-05) p2 = -0.0006189 (-0.001149, -8.886e-05).

Goodness of fit: SSE: 1.65e-05 R-square: 0.418 Adjusted R-square: 0.3992 RMSE: 0.0007296.

D.3 Convection E (E_y) for Oxygen Ions with Maxwellian Distributions in BCS

Instead of using a beam or a uniform distribution, we then experimented with a Maxwellian distribution in all the three velocity directions.

Distribution Function

The plots for the evolution of the distributions with time is shown in figs. D.5(a)-D.5(c). There seems to be no change as far as the final distribution is concerned but the temperatures of the initial distribution are different from the final distribution. Also, the

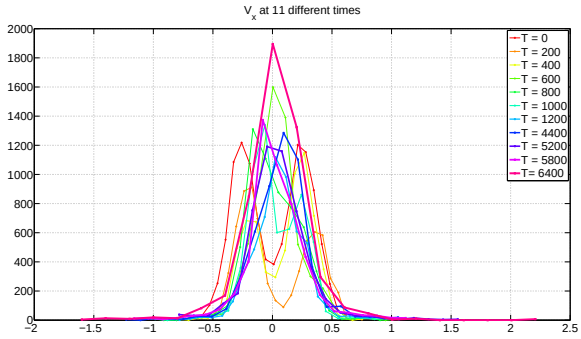

(a)

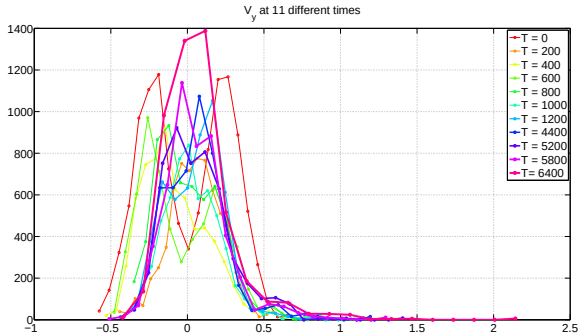

(b)

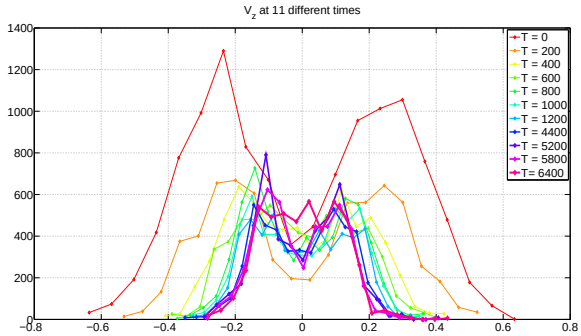

(c)

Fig. D.3: V_x, V_y, and V_z distribution at different times for oxygen ions with initial velocities sampled from a beam distribution and with a finite dawn dusk constant magnetic field, B_y. As seen in the figures, the initial uniform distributions isotropize to Maxwellians with finite temperatures (not shown) in all the three directions. The figures were generated by saving the number of particles at a given time step which are found in the chaos region and then plotting a histogram of the saved particles in Matlab.

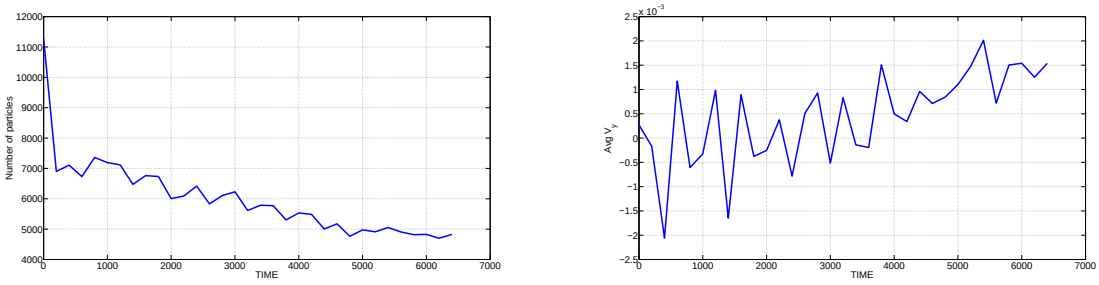

(a) (b)

Fig. D.4: The number of particles in the chaos region as a function of time (started with around 10000 oxygen ions) in a BCS with shear in the magnetic topology ($B_y \neq 0$) (fig. D.4(a)). Figure D.4(b) is a plot of the average velocity in the direction of electric field (E_y) of the particles remaining in the chaos region. The plots were generated using the procedure outlined in Appendix A and the results were plotted using Matlab.

distribution in the z direction (parallel to the magnetic field inside the current sheet) tends to develop is weak beam distribution with counterstreaming beams propagating at $\pm.2 - .3$ V_A. The distribution function in z direction tends to a beam like distribution as seen in fig. D.5(c) while the other two distributions tend to Maxwellians with similar temperatures (not shown).

Fit to Count

The decay of particles inside the current sheet is shown in fig. D.6(a). The periodic increase and decrease in the number can be attributed to the slow gyration around the weak normal magnetic field. Again as before, a double exponent tends to fit the decay well.

General model Exp2: f(x) = a*exp(b*x) + c*exp(d*x).

Coefficients (with 95% confidence bounds): a = 5.167e+04 (-8401, 1.117e+05) b = **-2.485** (-3.652, -1.318) c = 6060 (5886, 6234) d = **-0.007252** (-0.008749, -0.005755).

Goodness of fit: SSE: 1.047e+06 R-square: 0.9646 Adjusted R-square: 0.961 RMSE: 190.

The plots were generated using the procedure outlined in Appendix A and the results were plotted using Matlab. Trapping by the weak B_z can be seen in the figures with

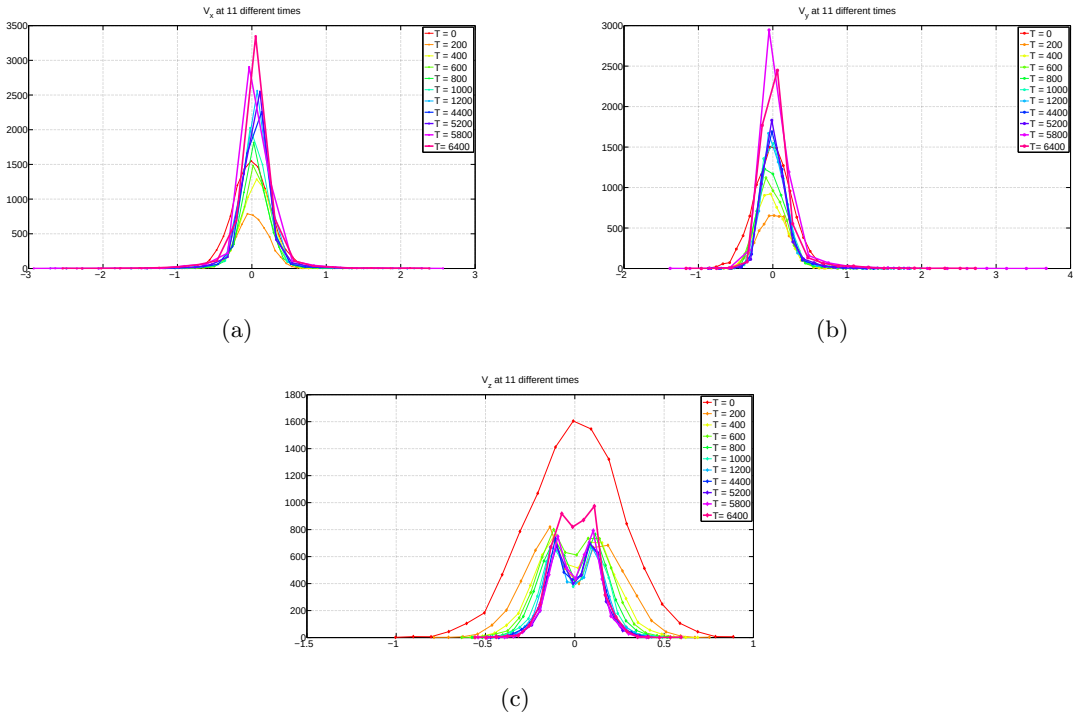

(a) (b)

(c)

Fig. D.5: V_x, V_y, and V_z distribution at different times for oxygen ions initialized from a Maxwellian distribution in all three directions in a BCS. As seen in the figures, the initial uniform distributions isotropize to Maxwellians with finite temperatures (not shown) in all the three directions. The figures were generated by saving the number of particles at a given time step which are found in the chaos region and then plotting a histogram of the saved particles in Matlab.

the oscillatory behavior an indication of the same. A Fourier analysis of the time series generated from the decay curve could tell if the oscillation was an artifact of measuring particle chaos (number of particles) or was some mode of the gyro frequency in the weak B_z magnetic field.

Average V_y Fit

Choosing a different initial velocity distribution does not seem to alter the average particle acceleration (see fig. D.6(b)) in the direction of the electric field as seen from the number next to the slope p1. Acceleration might also be aided numerically by the decay of the number of particles over which the average is taken.

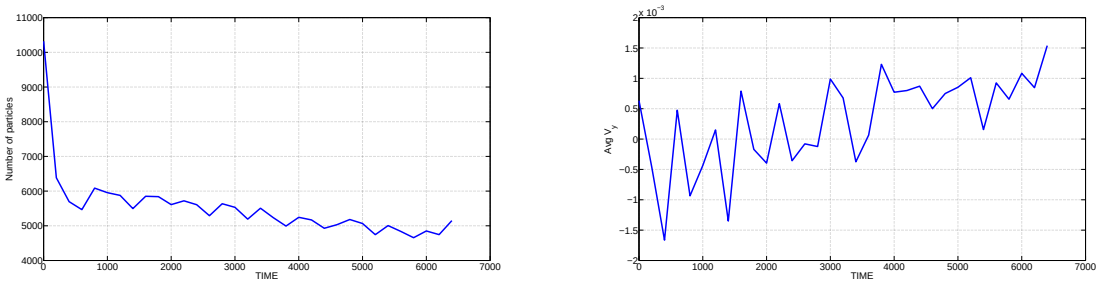

(a) (b)

Fig. D.6: The number of particles in the chaos region as a function of time (started with around 10000 oxygen ions) in a BCS (fig. D.6(a)). Figure D.6(b) is a plot of the average velocity in the direction of electric field (E_y) of the particles remaining in the chaos region. The plots were generated using the procedure outlined in Appendix A and the results were plotted using Matlab. Trapping by the weak B_z can be seen in the figures with the oscillatory behavior an indication of the same.

Linear model Poly1: f(x) = p1*x + p2.

Coefficients (with 95 % confidence bounds): p1 = **5.105e-05** (2.966e-05, 7.244e-05) p2 = -0.0005646 (-0.0009814, -0.0001477).

Goodness of fit: SSE: 1.02e-05 R-square: 0.4331 Adjusted R-square: 0.4149 RMSE: 0.0005737.

D.4 Convection E (E_y) with Oxygen Ions and Initial Maxwellian Distributions in BCS with Shear ($B_y \neq 0$)

When initialized with a Maxwellian distribution in a BCS with an added shear (finite y directed magnetic field), the results found are discussed in the next few sections.

Distribution Function

The distributions in the three directions are shown in figs. D.7(a)-D.7(c). The y directed distribution tends to develop a finite tail while the distribution in the z direction tends to have a very strong counterstreaming beam distribution (fig. D.7(c)). The temperature also seems to drastically change with time. This could be due to the presence of a weak but finite magnetic field in the z direction.

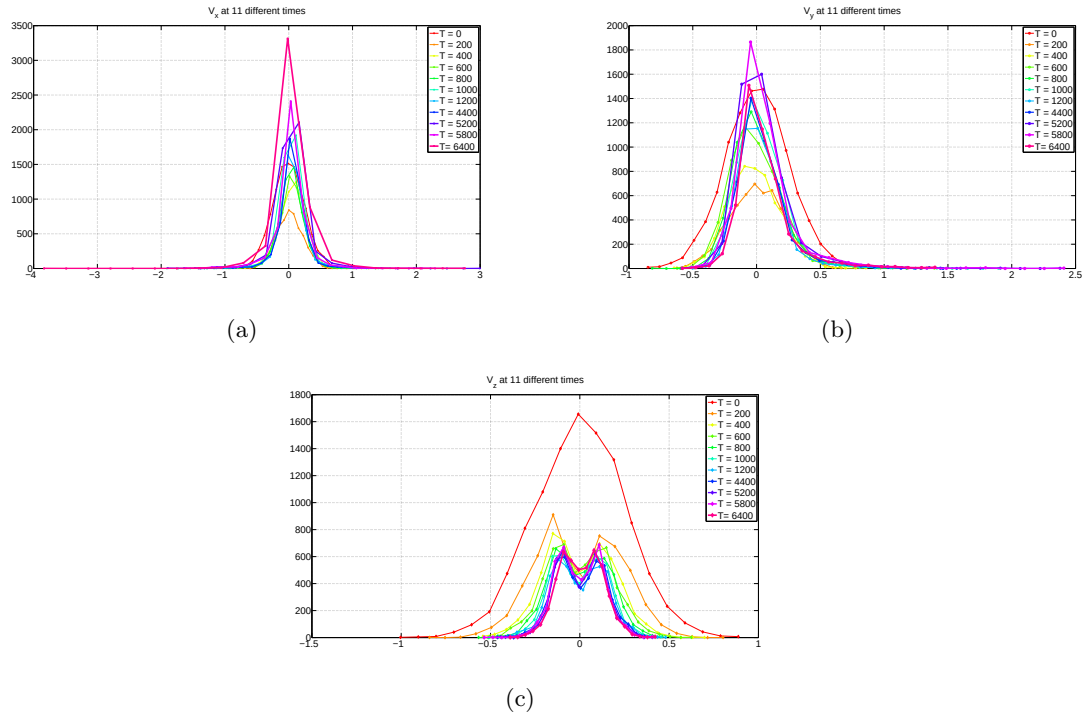

(a) (b)

(c)

Fig. D.7: V_x, V_y, and V_z distribution at different times for oxygen ions initially sampled from a Maxwellian distribution in all the three directions. As seen in the figures, the initial uniform distributions isotropize to Maxwellians with finite temperatures (not shown) in all the three directions. The isotropization which in Lorentz gas would be due to collisions occurs in this collisionless environment due to inhomogeneities in the magnetic field on the order of particle gyro radius because of which particles are lost from the chaos region. The figures were generated by saving the number of particles at a given time step which are found in the chaos region and then plotting a histogram of the saved particles in Matlab.

Fit to Count

The decay of oxygen ions from the current sheet follows an exponential with an initial fast and a final slow decay as seen in fig. D.8(a). The slow exponent has around the same order of magnitude as for the cases discussed before. Also, the periodicity of particle entry and ejection from the current sheet seems to be broken because of inclusion of a finite shear.

General model Exp2: f(x) = a*exp(b*x) + c*exp(d*x).

Coefficients (with 95 % confidence bounds): a = 7.535e+04 (-5.433e+04, 2.05e+05) b = **-2.851** (-4.58, -1.122) c = 6022 (5839, 6204) d = **-0.009168** (-0.01077, -0.007561).

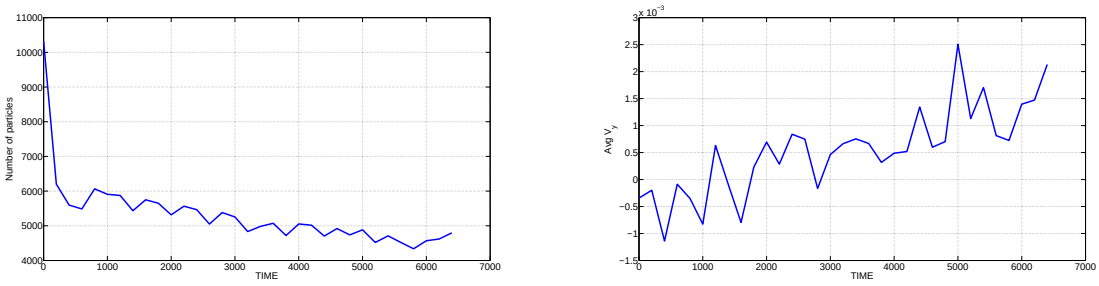

(a) (b)

Fig. D.8: The number of particles in the chaos region as a function of time in a BCS with shear in the magnetic topology ($B_y \neq 0$) (fig. D.8(a)). Figure D.8(b) is a plot of the average velocity in the direction of electric field (E_y) of the particles remaining in the chaos region. The plots were generated using the procedure outlined in Appendix A and the results were plotted using Matlab. Again the trapping effect of B_z (B_y is still a fraction of B_z) can be seen in the oscillatory nature of the two graphs.

Goodness of fit: SSE: 1.123e+06 R-square: 0.9665 Adjusted R-square: 0.963 RMSE: 196.8.

Average V_y Fit

The positive slope of average velocity in the direction of electric field (fig. D.8(b)) is an indication of the particles on average being accelerated in the direction of electric field. The numbers also tend to agree with the ones for uniform distribution.

Linear model Poly1: f(x) = p1*x + p2.

Coefficients (with 95 % confidence bounds): p1 = **6.677e-05** (4.844e-05, 8.509e-05) p2 = -0.0005947 (-0.0009517, -0.0002376).

Goodness of fit: SSE: 7.487e-06 R-square: 0.6405 Adjusted R-square: 0.6289 RMSE: 0.0004915.

D.5 Convection E (E_y) with Oxygen Ions Sampled from Uniform Distributions with Shear ($B_y \neq 0$)

This section discusses the results for when the initial velocity distribution was taken as uniform distribution.

Distribution Function

As found in the previous results, we found that the distribution in the x direction seems to tend to a Maxwellian distribution with time. The y velocity distribution has a finite tail with velocities reaching to fluid velocities ($\approx 2\ V_A$) in the direction shear. The z directed velocity distribution also has the same beam like distribution with counterstreaming beams around average velocity of $\pm.3\ V_A$ (figs. D.9(a)-D.9(c)).

Fit to Count

With the uniform distribution the particle decay rate is not changed in any way and the same features are again found as discussed before.

General model Exp2: f(x) = a*exp(b*x) + c*exp(d*x).

Coefficients (with 95 % confidence bounds): a = 4.198e+04 (2896, 8.107e+04) b = **-2.247** (-3.181, -1.313) c = 7173 (6979, 7366) d = **-0.01237** (-0.01382, -0.01091).

Goodness of fit: SSE: 1.137e+06 R-square: 0.9763 Adjusted R-square: 0.9739 RMSE: 198. Again, a double exponent fits the decay of particles with time very well as indicated by the R-square value.

Average V_y Fit

The average velocity and count in the direction of electric field has a positive slope as seen in figs. D.10(a) and D.10(b). The number in bold suggests that the acceleration of the particles on average is an order of magnitude larger than that found for when shear was not included.

Linear model Poly1: f(x) = p1*x + p2.

Coefficients (with 95 % confidence bounds): p1 = **6.953e-05** (5.381e-05, 8.526e-05) p2 = -0.0008192 (-0.001126, -0.0005129).

Goodness of fit: SSE: 5.51e-06 R-square: 0.7242 Adjusted R-square: 0.7153 RMSE: 0.0004216. R-square value is relatively low but higher order polynomial fits overfitted the model data and so were not used.

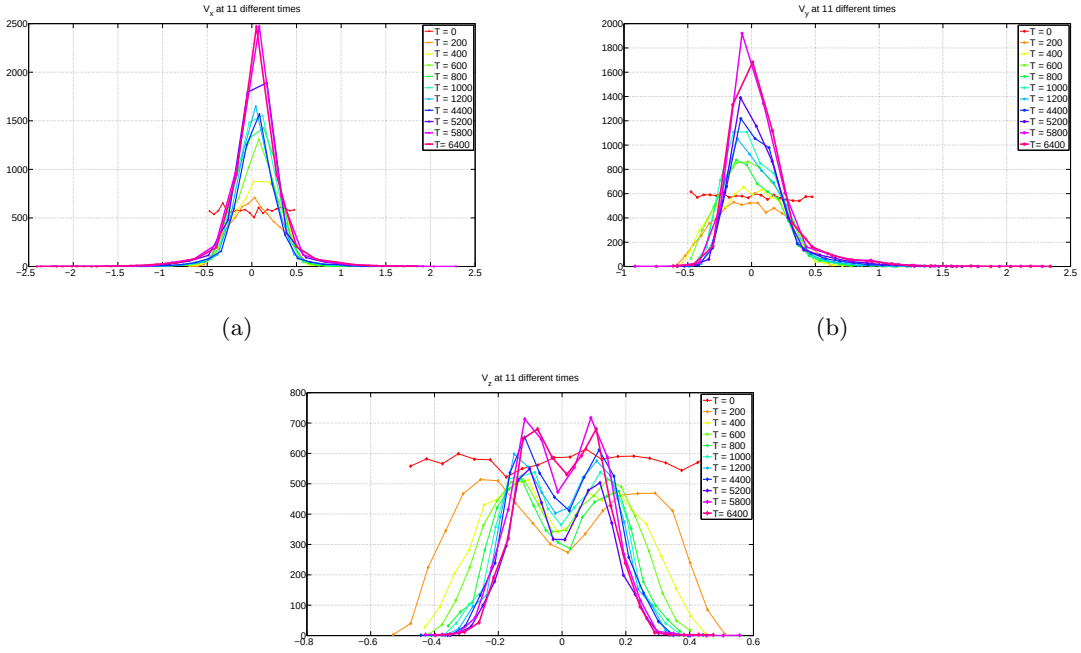

(a) (b)

(c)

Fig. D.9: V_x, V_y, and V_z distribution at different times for oxygen ions initialized from uniform distributions and with a constant shear in the magnetic topology. As seen in the figures, the initial uniform distributions isotropize to Maxwellians with finite temperatures (not shown) in all the three directions. The figures were generated by saving the number of particles at a given time step which are found in the chaos region and then plotting a histogram of the saved particles in Matlab.

D.6 Convection E (E_y) with Protons Sampled from Beam Distribution

Initialization of velocity distribution for the proton is done in the same fashion as done for oxygen ion. The initial distribution is randomly distributed from $-.5\ V_A$ and $.5\ V_A$ in all the three directions. The lighter protons compared to the oxygen ions are accelerated to much higher velocities. The temperatures (not shown) are also different from the ones found for oxygen ions since protons are more mobile when compared with oxygen ions.

Distribution Function

The distributions tend to evolve in the same way as for the oxygen ions but with a few dissimilarities (figs. D.11(a)-D.11(c)). The finite tail of the y distribution is not evident as

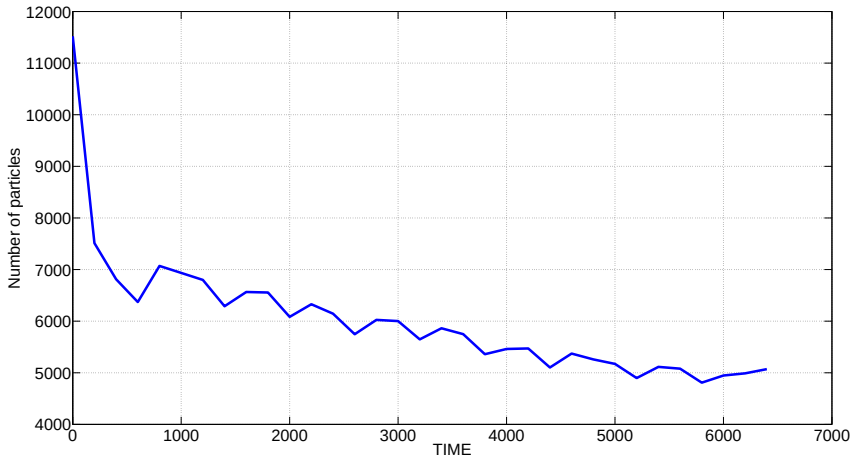

(a)

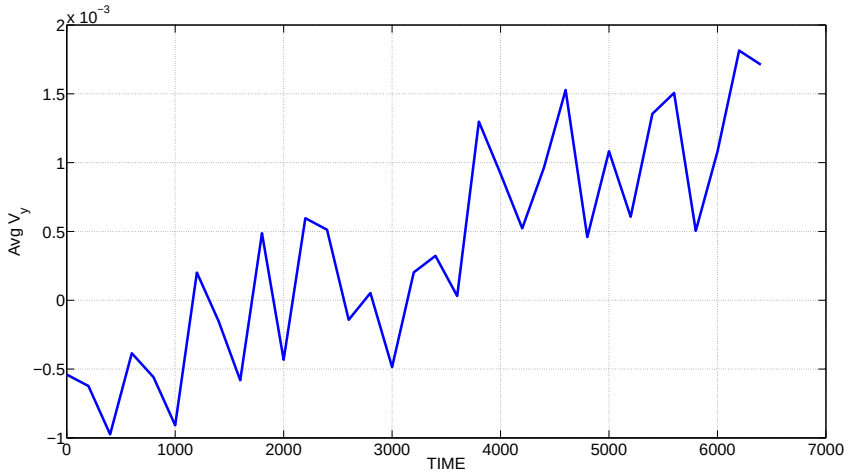

(b)

Fig. D.10: The number of particles in the chaos region as a function of time (started with around 10000 oxygen ions) in a BCS with shear in the magnetic topology ($B_y \neq 0$) (fig. D.10(a)). Figure D.10(b) is a plot of the average velocity in the direction of electric field (E_y) of the particles remaining in the chaos region. The plots indicate that the number of particles decay in the chaos region which can be best fitted by an exponential model and that they are accelerated by the electric field during their demagnetization. The plots were generated using the procedure outlined in Appendix A and the results were plotted using Matlab. Particles on an average are linearly accelerated in the chaos region which can be seen in fig. D.10(b).

seen in fig. D.11(b). The beam like final distribution found for oxygen is not found in the case of protons. The lighter mass of protons although tends to accelerate them to much higher Alfven speeds than for a oxygen ion. This is also seen in the bulk scaling where the aceeleration rate of a charged species scales with particle mass.

Fit to Count

The decay of protons from the chaos region (current sheet) follows an exponential with two decay rates (fig. D.12(a)). The faster rate will give a very high resistivity and is not physical but it tends to bring the number for the slow decay down. The slow decay exponent on the other hand is around the same number as for the oxygen ions.

General model Exp2: f(x) = a*exp(b*x) + c*exp(d*x).

Coefficients (with 95 % confidence bounds): a = 5.855e+13 (-1.744e+23, 1.744e+23) b = **-23.65** (-2.979e+09, 2.979e+09) c = 7483 (7277, 7690) d = **-0.006182** (-0.0077, -0.004663).

Goodness of fit: SSE: 1.361e+06 R-square: 0.9292 Adjusted R-square: 0.9213 RMSE: 224.5.

Average V_y Fit

Due to the scaling of mass of the proton ion compared to the oxygen ion, the acceleration which is dependent on the inertia, does have a number lower than what was found for the oxygen ion. The jagged features of the average velocity can also be found for the proton (fig. D.12(b)). These jagged features are a result of the statistical averaging on the number of particles in the chaos region at a given time.

Linear model Poly1: f(x) = p1*x + p2.

Coefficients (with 95 % confidence bounds): p1 = **0.0001195** (3.663e-05, 0.0002025) p2 = -0.0008994 (-0.002419, 0.0006205).

Goodness of fit: SSE: 0.0001182 R-square: 0.2307 Adjusted R-square: 0.2041 RMSE: 0.002019.

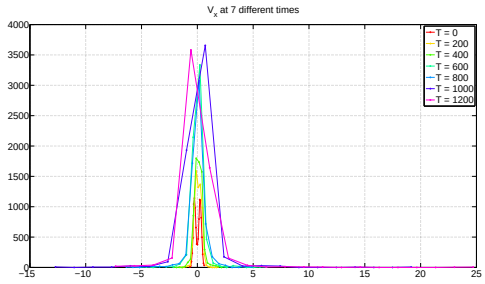

(a)

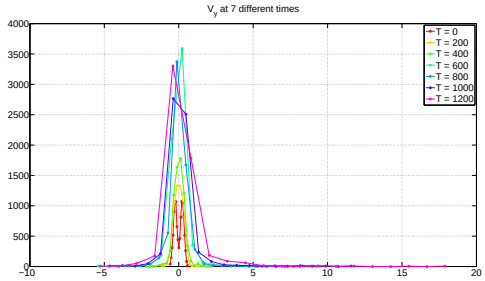

(b)

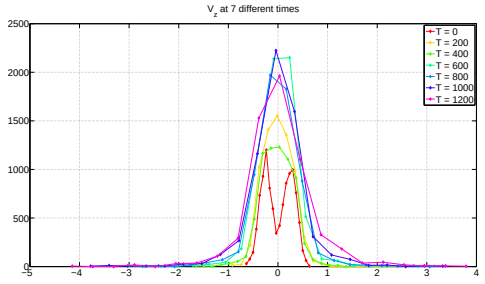

(c)

Fig. D.11: V_x, V_y, and V_z distribution at different times for protons in a BCS. As seen in the figures, the initial uniform distributions isotropize to Maxwellians with finite temperatures (not shown) in all the three directions. The isotropization which in Lorentz gas would be due to collisions occurs in this collisionless environment due to inhomogeneities in the magnetic field on the order of particle gyro radius because of which particles are lost from the chaos region. The figures were generated by saving the number of particles at a given time step which are found in the chaos region and then plotting a histogram of the saved particles in Matlab. Temperatures in x, y directions seem to differ from that in the z direction (also the direction of B_z).

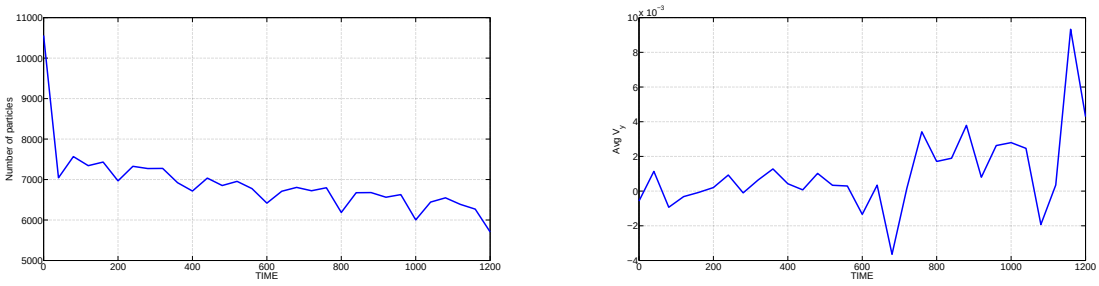

(a) (b)

Fig. D.12: The number of particles in the chaos region as a function of time (started with around 10000 protons initialized from beam distributions in all three directions) in a BCS (fig. D.12(a)). Figure D.12(b) is a plot of the average velocity in the direction of electric field (E_y) of the particles remaining in the chaos region. The plots indicate that the number of particles decay in the chaos region which can be best fitted by an exponential model and that they are accelerated by the electric field during their demagnetization. The plots were generated using the procedure outlined in Appendix A and the results were plotted using Matlab.

D.7 Convection E (E_y) with Protons Initialized from Beam Distributions Including Shear ($B_y \neq 0$)

Distribution Function

The distributions tend to evolve in the same way as for the oxygen ions but with a few dissimilarities (see fig. D.13(a)). The finite tail of the y distribution is not evident as seen in fig. D.13(b). The beam like final distribution found for oxygen is not found in the case of protons. The lighter mass of protons although tends to accelerate them to much higher Alfven speeds than for a oxygen ion. Starting with a beam distribution still does not produce a final beam distribution in the z direction as seen in fig. D.13(c).

Fit to Count

The decay of protons from the chaos region (current sheet) follows an exponential with two decay rates (fig. D.14(a)). The faster rate will give a very high resistivity and is not physical but it tends to bring the number for the slow decay down. The slow decay exponent on the other hand is around the same number as for the oxygen ions.

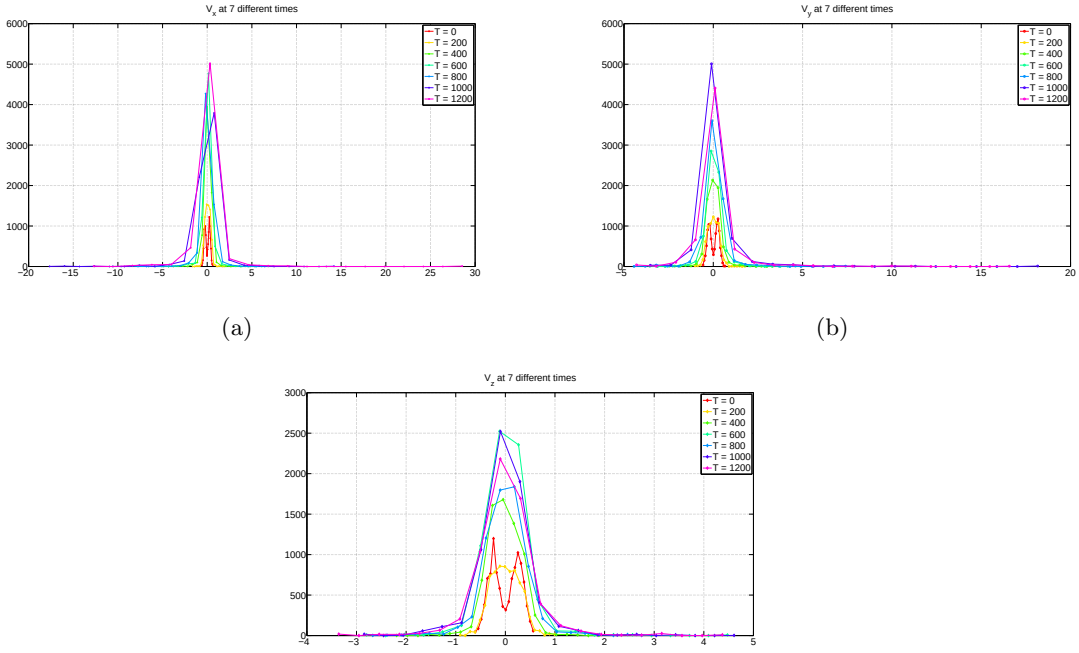

(a) (b)

(c)

Fig. D.13: V_x, V_y, and V_z distribution at different times for protons sampled from beam distribution in a BCS with shear. As seen in the figures, the initial uniform distributions isotropize to Maxwellians with finite temperatures (not shown) in all the three directions. The figures were generated by saving the number of particles at a given time step which are found in the chaos region and then plotting a histogram of the saved particles in Matlab. Also, note the scale of x axis in figs. D.13(a) and D.13(b) compared to D.13(c).

General model Exp2: f(x) = a*exp(b*x) + c*exp(d*x).

Coefficients (with 95 % confidence bounds): a = 1.118e+13 (-8.921e+21, 8.921e+21) b = **-22.07** (-7.983e+08, 7.983e+08) c = 7687 (7438, 7936) d = **-0.005005** (-0.006776, -0.003235).

Goodness of fit: SSE: 2.032e+06 R-square: 0.8774 Adjusted R-square: 0.8638 RMSE: 274.4.

Average V_y Fit

Due to the scaling of mass of the proton ion compared to the oxygen ion, the acceleration which is dependent on the inertia, does have a number lower than what was found

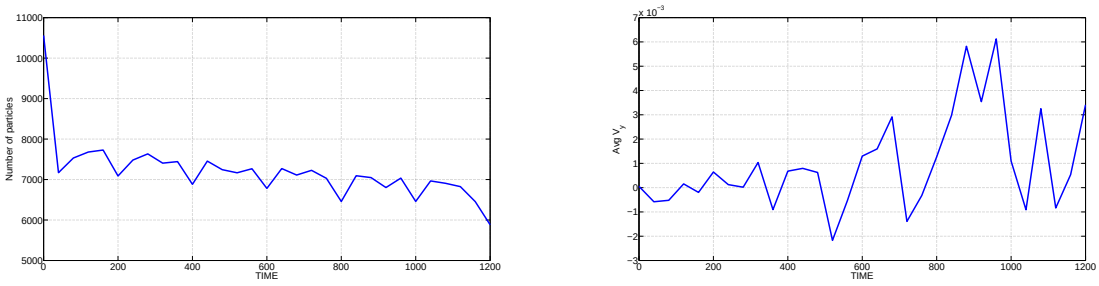

(a) (b)

Fig. D.14: The number of particles in the chaos region as a function of time in a BCS with shear in the magnetic topology ($B_y \neq 0$) (fig. D.14(a)). Figure D.14(b) is a plot of the average velocity in the direction of electric field (E_y) of the particles remaining in the chaos region. The plots were generated using the procedure outlined in Appendix A and the results were plotted using Matlab. Trapping by $B_z \gg B_y$ can e seen in the jagged oscillatory nature of fig. D.14(a).

for the oxygen ion (fig. D.14(b)). The jagged features of the average velocity can also be found for the proton. These jagged features are a result of the statistical averaging on the number of particles in the chaos region at a given time. The slope of the average velocity is an order of magnitude higher than that for oxygen ion.

Linear model Poly1: f(x) = p1*x + p2.

Coefficients (with 95 % confidence bounds): p1 = **9.656e-05** (2.32e-05, 0.0001699) p2 = -0.0005908 (-0.001935, 0.000754).

Goodness of fit: SSE: 9.253e-05 R-square: 0.1999 Adjusted R-square: 0.1723 RMSE: 0.001786.

D.8 Convection E (E_y) with Protons Initialized from Maxwellian Distributions with Additional Shear ($B_y \neq 0$)

This section reports the results of experiment done with an initial Maxwellian distribution for velocities and magnetic field topology that supports a finite shear $B_y \neq 0$.

Distribution Function

The distributions tend to evolve in the same way as for the oxygen ions but with a

few dissimilarities. The finite tail of the x and y distributions is not evident as seen in figs. D.15(a) and D.15(b). The beam like final distribution found for oxygen is not found in the case of protons. The lighter mass of protons although tends to accelerate them to much higher Alfven speeds than for a oxygen ion. Starting with a beam distribution still does not produce a final beam distribution in the z direction as seen in fig. D.15(c). This could be due to the fact that protons are not sufficiently accelerated before being ejected and that a finite B_z does not allow the particle to meander too far out into the lobes.

Fit to Count

The decay of protons from the chaos region (current sheet) follows an exponential with two decay rates (fig. D.16(a)). The faster rate will give a very high resistivities and is not physical but it tends to bring the number for the slow decay down. The slow decay exponent on the other hand is around the same number as for the oxygen ions. The percentage number of particles remaining in the current sheet does not seem to be affected by the presence of a shear (Table 6.4).

General model Exp2: f(x) = a*exp(b*x) + c*exp(d*x).

Coefficients (with 95a = 7.992e+13 (-4.036e+23, 4.036e+23) b = **-24.02** (-5.05e+09, 5.05e+09) c = 7646 (7419, 7872) d = **-0.004825** (-0.006438, -0.003212).

Goodness of fit: SSE: 1.68e+06 R-square: 0.8958 Adjusted R-square: 0.8842 RMSE: 249.4.

Average V_y Fit

Due to the scaling of mass of the proton ion compared to the oxygen ion, the acceleration which is dependent on the inertia, does have a number lower than what was found for the oxygen ion. The jagged features of the average velocity can also be found for the proton.

These jagged features are a result of the statistical averaging on the number of particles in the chaos region at a given time. The slope of the average velocity is an order of magnitude higher than that for oxygen ion as seen in fig. D.16(b).

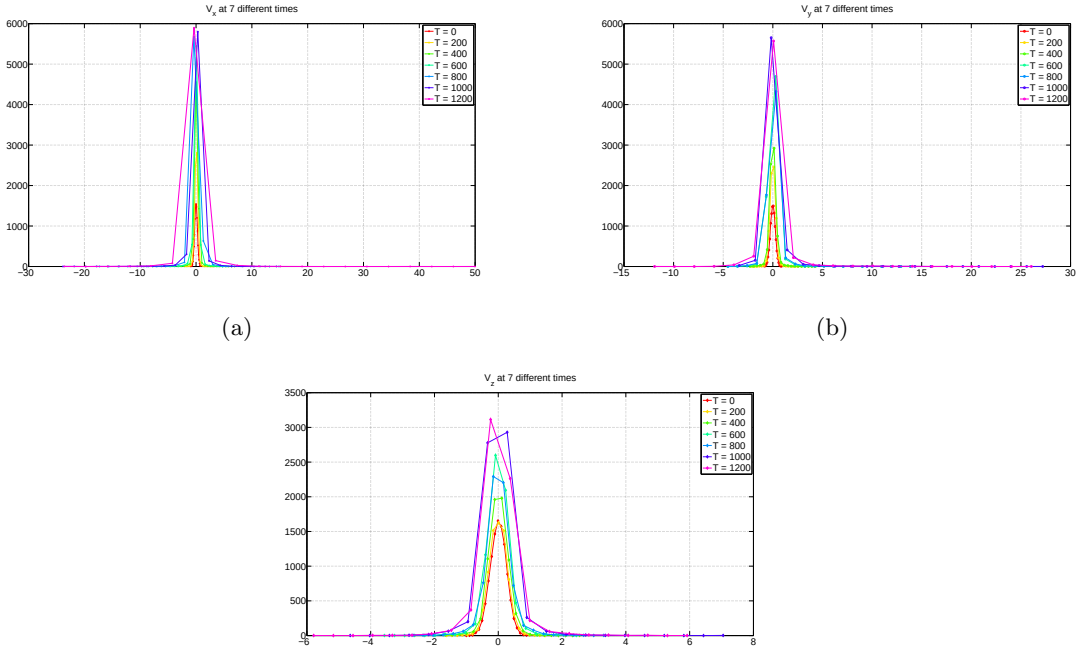

(a) (b)

(c)

Fig. D.15: V_x, V_y, and V_z distribution at different times for protons in a BCS with shear in magnetic topology. As seen in the figures, the initial uniform distributions isotropize to Maxwellians with finite temperatures (not shown) in all the three directions. The isotropization which in Lorentz gas would be due to collisions occurs in this collisionless environment due to inhomogeneities in the magnetic field on the order of particle gyro radius because of which particles are lost from the chaos region. The figures were generated by saving the number of particles at a given time step which are found in the chaos region and then plotting a histogram of the saved particles in Matlab.

Linear model Poly1: f(x) = p1*x + p2.

Coefficients (with 95p1 = **7.821e-05** (2.512e-05, 0.0001313) p2 = -0.0005656 (-0.001539, 0.0004075).

Goodness of fit: SSE: 4.846e-05 R-square: 0.2384 Adjusted R-square: 0.2121 RMSE: 0.001293.

Matlab nonlinear fitting tool does not do a good job at fitting the average series as indicated by the numbers from the fit above. The fitting also suggests that a nonlinear model like a rising exponential or a polynomial might well be able to fit the curve. But the physical interpretation of the fitting would be a lot difficult in that case.

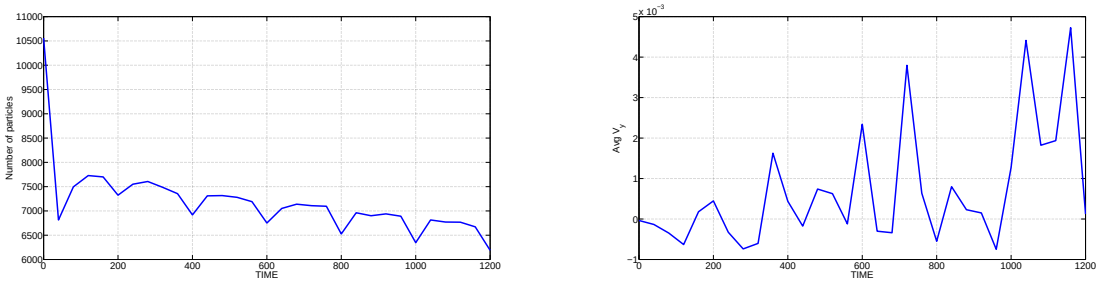

(a) (b)

Fig. D.16: The number of particles in the chaos region as a function of time (started with around 10000 protons with initial velocities sampled from a Maxwellian distribution) in a BCS with shear in the magnetic topology ($B_y \neq 0$) (fig. D.16(a)). Figure D.16(b) is a plot of the average velocity in the direction of electric field (E_y) of the particles remaining in the chaos region. The plots indicate that the number of particles decay in the chaos region which can be best fitted by an exponential model and that they are accelerated by the electric field during their demagnetization. The plots were generated using the procedure outlined in Appendix A and the results were plotted using Matlab. Clear indication of trapping can be seen in fig. D.16(a).

D.9 Convection E (E_y) with Protons Sampled from Uniform Distribution in BCS with Shear ($B_y \neq 0$)

The distribution functions in x, y, and z directions are plotted in fig. D.17(a)-D.17(c), respectively.

D.10 Fit to Count

The decay of protons from the chaos region (current sheet) follows an exponential with two decay rates (fig. D.18(a)). The faster rate will give a very high resistivities and is not physical but it tends to bring the number for the slow decay down. The slow decay exponent on the other hand is around the same number as for the oxygen ions.

General model Exp2: f(x) = a*exp(b*x) + c*exp(d*x).

Coefficients (with 95 % confidence bounds): a = 3.472e+13 (-8.302e+22, 8.302e+22) b = **-23.23** (-2.391e+09, 2.391e+09) c = 8028 (7801, 8256) d = **-0.006096** (-0.007657, -0.004535).

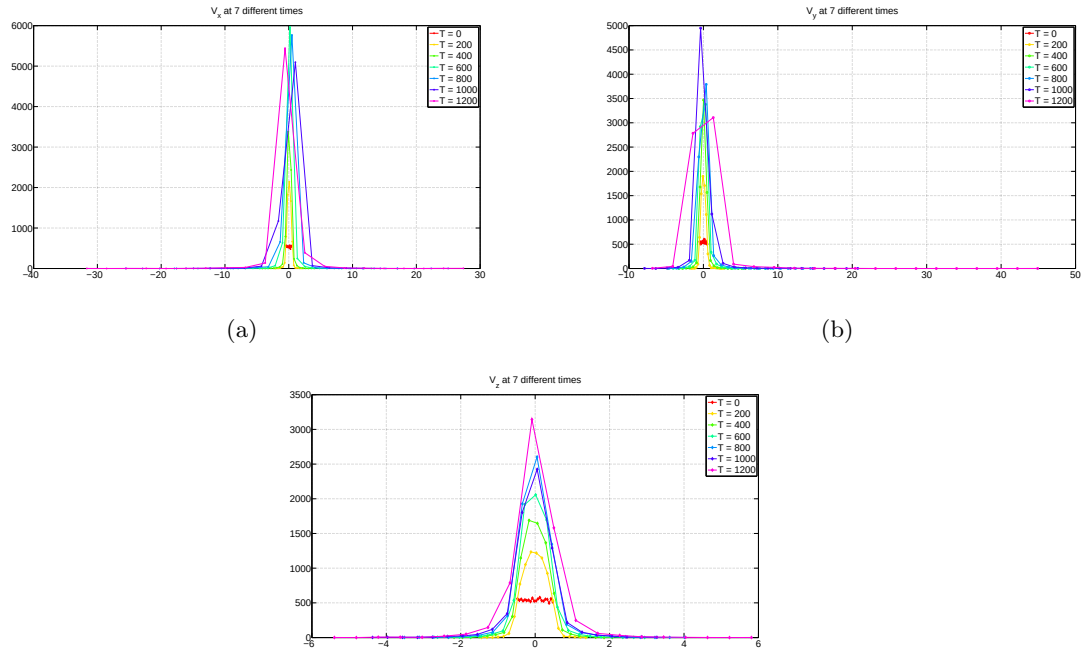

Fig. D.17: V_x, V_y, and V_z distribution at different times for protons in a BCS with shear and initial velocities sampled from uniform distribution. As seen in the figures, the initial uniform distributions isotropize to Maxwellians with finite temperatures (not shown) in all the three directions. The isotropization which in Lorentz gas would be due to collisions occurs in this collisionless environment due to inhomogeneities in the magnetic field on the order of particle gyro radius because of which particles are lost from the chaos region. The figures were generated by saving the number of particles at a given time step which are found in the chaos region and then plotting a histogram of the saved particles in Matlab.

Goodness of fit: SSE: 1.66e+06 R-square: 0.9086 Adjusted R-square: 0.8985 RMSE: 247.9.

D.11 Average V_y Fit

The jagged features of the average velocity can also be found for the proton. These jagged features are a result of the statistical averaging on the number of particles in the chaos region at a given time. The slope of the average velocity is an order of magnitude higher than that for oxygen ion as seen in fig. D.18(b).

Linear model Poly1: f(x) = p1*x + p2.

Coefficients (with 95 % confidence bounds): p1 = **9.723e-05** (4.741e-05, 0.000147) p2 = -0.0006253 (-0.001538, 0.0002879).

Goodness of fit: SSE: 4.267e-05 R-square: 0.3546 Adjusted R-square: 0.3323 RMSE: 0.001213. Exponential also fits well to the average velocity.

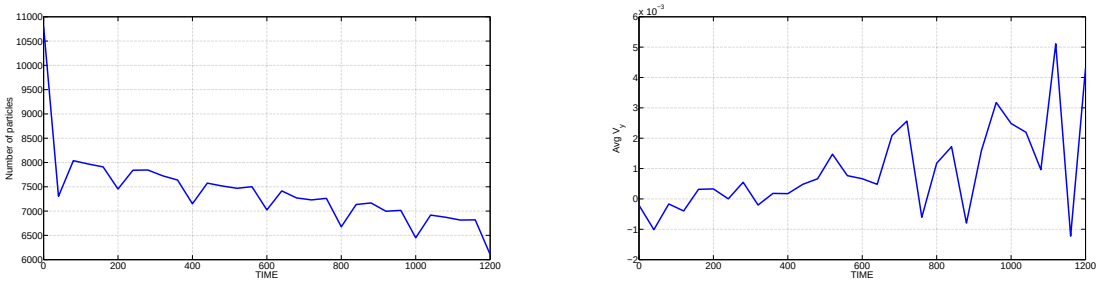

(a) (b)

Fig. D.18: The number of particles in the chaos region as a function of time (started with around 10000 protons with initial velocity sampled from uniform distribution in) in a BCS with shear in the magnetic topology ($B_y \neq 0$) (fig. D.18(a)). Figure D.18(b) is a plot of the average velocity in the direction of electric field (E_y) of the particles remaining in the chaos region. The plots indicate that the number of particles decay in the chaos region which can be best fitted by an exponential model and that they are accelerated by the electric field during their demagnetization. The plots were generated using the procedure outlined in Appendix A and the results were plotted using Matlab.

Vita

Tushar Andriyas

Education

PhD, Electrical and Computer Engineering — May 2013

Utah State University, Logan, Utah, USA

Major: Space Physics

Dissertation Title: Particle dynamics and resistivity characteristics in Bifurcated Current Sheets

Major Professor: Dr. Edmund Spencer

Master of Science, Electrical Engineering — July 2009

Utah State University, Logan, Utah, USA

Thesis Title: Surface Wave Propagation in a Dielectric Waveguide Loaded with an Anisotropic, Conductive, and Spatially Dispersive Substrate

Major Professor: Dr. Edmund Spencer

Bachelor of Technology, Electronics and Communication Engineering — June 2000

United College of Engineering and Research, U.P., India

Project Title: Telephone switching module for household electrical appliances

Research Interests

- Dissipation mechanisms in different magnetic field topologies
- Machine learning /Evolutionary algorithms techniques for geomagnetic storm prediction

- Understanding heliophysics through numerical simulations

Published Journal Articles

- T. Andriyas, E. Spencer, A. Raj, L. Mays, J. Sojka, Dst Prediction from CIR Events During 2008 Using Synthesized Signals Derived from SOHO and ACE Observations, JGR Space Physics, In Press, December 30, 2011.

- E. Spencer, S. Patra, T. Andriyas, C. Swenson, J. Ward, A. Barjatya, Absolute Electron Density and Electron Neutral Collision Frequency in the Ionosphere from Plasma Impedance Probe Measurements, J. Geophysical Research VOL. 113, A09305 doi:10.1029/2007JA013004, 2008.

Talks and Presentations at Scientific Conferences

- E. Spencer, T. Andriyas, J. Sojka, M.L. Mays, Dst Prediction from CIR Events During 2008 Using Synthesized Signals Derived from SOHO and ACE Observations, presented at the AGU Fall Meeting 2011.

- E. Spencer, P. Wheeler, S. Kaveri, T. Andriyas, B. Beardall, Acoustic Coupling between Drumset Cymbals, Acoustical Society of America Meeting, Salt Lake City, June 2007.

- T. Andriyas, E. Spencer, W. Horton, Interplay of Kelvin Helmholtz and Tearing Mode Instability during High Speed Stream (HSS) Events, AGU Meeting Fall 2011.

- T. Andriyas, E. A. Spencer, Numerical simulation of surface waves in a stratified magnetoplasma using a Plasma Fluid Finite Difference Time Domain Simulation, AGU Fall Meeting, 2009.

- T. Andriyas, S. Patra, E. Spencer, J. Ward, Aerodynamic Influence on Plasma Impedance Probe Measurements in Sounding Rocket Missions, AGU Fall Meeting, 2008.

- E. Spencer, S. Patra, T. Andriyas, C. Swenson, J. Ward, Plasma Impedance Probe Analysis with a Finite Difference Time Domain Simulation, Pulsed Power and Plasma Science Conference, July 2007
- S. Patra, E. Spencer, T. Andriyas, C. Swenson, J. Ward, Determination of Absolute Plasma Electron Density and Electron Neutral Collision Frequency from Plasma Impedance Probe Measurements, AGU Fall Meeting, 2007

Workshops Attended and Affiliations

- Heliophysics Summer School in Colorado - 2011
- Santa Fe CEDAR/GEM Workshop in New Mexico - 2011
- American Geophysical Union Member
- IEEE Member